Shielding Aspects of Accelerators, Targets and Irradiation Facilities – SATIF-11

Workshop Proceedings
Tsukuba, Japan
11–13 September 2012

OECD
BETTER POLICIES FOR BETTER LIVES

NEA
NUCLEAR ENERGY AGENCY

Nuclear Science

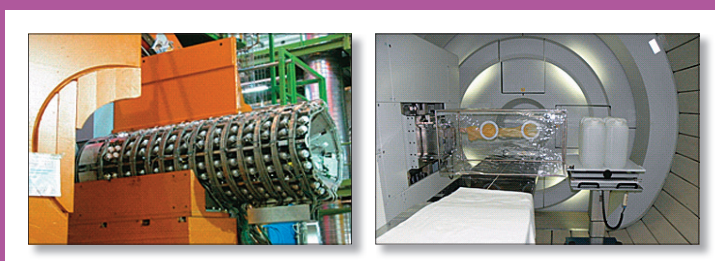# Shielding Aspects of Accelerators, Targets and Irradiation Facilities – SATIF-11 Workshop Proceedings

Tsukuba, Japan
11-13 September 2012

Hosted by the
High-energy Accelerator Research Organisation (KEK)

ORGANISATION FOR ECONOMIC CO-OPERATION AND DEVELOPMENT

The OECD is a unique forum where the governments of 34 democracies work together to address the economic, social and environmental challenges of globalisation. The OECD is also at the forefront of efforts to understand and to help governments respond to new developments and concerns, such as corporate governance, the information economy and the challenges of an ageing population. The Organisation provides a setting where governments can compare policy experiences, seek answers to common problems, identify good practice and work to co-ordinate domestic and international policies.

The OECD member countries are: Australia, Austria, Belgium, Canada, Chile, the Czech Republic, Denmark, Estonia, Finland, France, Germany, Greece, Hungary, Iceland, Ireland, Israel, Italy, Japan, Luxembourg, Mexico, the Netherlands, New Zealand, Norway, Poland, Portugal, the Republic of Korea, the Slovak Republic, Slovenia, Spain, Sweden, Switzerland, Turkey, the United Kingdom and the United States. The European Commission takes part in the work of the OECD.

OECD Publishing disseminates widely the results of the Organisation's statistics gathering and research on economic, social and environmental issues, as well as the conventions, guidelines and standards agreed by its members.

> *This work is published on the responsibility of the OECD Secretary-General.*

NUCLEAR ENERGY AGENCY

The OECD Nuclear Energy Agency (NEA) was established on 1 February 1958. Current NEA membership consists of 31 countries: Australia, Austria, Belgium, Canada, the Czech Republic, Denmark, Finland, France, Germany, Greece, Hungary, Iceland, Ireland, Italy, Japan, Luxembourg, Mexico, the Netherlands, Norway, Poland, Portugal, the Republic of Korea, the Russian Federation, the Slovak Republic, Slovenia, Spain, Sweden, Switzerland, Turkey, the United Kingdom and the United States. The European Commission also takes part in the work of the Agency.

The mission of the NEA is:

– to assist its member countries in maintaining and further developing, through international co-operation, the scientific, technological and legal bases required for a safe, environmentally friendly and economical use of nuclear energy for peaceful purposes, as well as

– to provide authoritative assessments and to forge common understandings on key issues, as input to government decisions on nuclear energy policy and to broader OECD policy analyses in areas such as energy and sustainable development.

Specific areas of competence of the NEA include the safety and regulation of nuclear activities, radioactive waste management, radiological protection, nuclear science, economic and technical analyses of the nuclear fuel cycle, nuclear law and liability, and public information.

The NEA Data Bank provides nuclear data and computer program services for participating countries. In these and related tasks, the NEA works in close collaboration with the International Atomic Energy Agency in Vienna, with which it has a Co-operation Agreement, as well as with other international organisations in the nuclear field.

Foreword

The transport of radiation through shielding materials is a major consideration in the safety design studies of nuclear power plants, and the modelling techniques used may be applied to many other types of scientific and technological facilities. Accelerator and irradiation facilities represent a key capability in R&D, medical and industrial infrastructures, and they can be used in a wide range of scientific, medical and industrial applications. High-energy ion accelerators, for example, are now used not only in fundamental research, such as the search for new super-heavy nuclei, but also for therapy as part of cancer treatment.

While the energy of the incident particles on the shielding of these facilities may be much higher than those found in nuclear power plants, much of the physics associated with the behaviour of the secondary particles produced is similar, as are the computer modelling techniques used to quantify key safety design parameters, such as radiation dose and activation levels. Clear synergies exist, therefore, with other technical work being carried out by the OECD Nuclear Energy Agency (NEA), and its Nuclear Science Committee continues to sponsor activities in this domain.

One of these activities concerns "Shielding Aspects of Accelerators, Targets and Irradiation Facilities" (SATIF). A series of workshops have been held over the last 18 years: SATIF-1 was held on 28-29 April 1994 in Arlington, Texas; SATIF-2 on 12-13 October 1995 at CERN in Geneva, Switzerland; SATIF-3 on 12-13 May 1997 at Tohoku University in Sendai, Japan; SATIF-4 on 17-18 September 1998 in Knoxville, Tennessee; SATIF-5 on 17-21 July 2000 at the OECD in Paris, France; SATIF-6 on 10-12 April 2002 at the Stanford Linear Accelerator Center (SLAC), Menlo Park, California; SATIF-7 on 17-18 May 2004 at ITN, Sacavém, Portugal; SATIF-8 on 22-24 May 2006 at the Pohang Accelerator Laboratory in the Republic of Korea; SATIF-9 on 21-23 April 2008 at Oak Ridge National Laboratory (ORNL), Oak Ridge, Tennessee; SATIF-10 on 2-4 June 2010 at CERN in Geneva, Switzerland.

The 11th workshop on Shielding Aspects of Accelerators, Targets and Irradiation Facilities took place in Tsukuba, Japan and was jointly organised by the following bodies:

- Expert Group on Radiation Transport and Shielding (EGRTS) of Working Party on Scientific Issues of Reactor Systems (WPRS) of OECD/NEA;

- High Energy Accelerator Research Organisation (KEK);

- Technical Divisions of Radiation Science and Technology of the Atomic Energy Society of Japan.

The workshop was sponsored by the OECD/NEA and its Nuclear Science Committee (NSC) and co-sponsored by the Technical Divisions of Radiation Science and Technology of the Atomic Energy Society of Japan and the Radiation Safety Information Computational Center (RSICC).

The current proceedings provide a summary of the discussions, decisions and conclusions as well as the text of the presentations made at the 11th workshop.

Acknowledgements

Table of Contents

Executive Summary

The 11th workshop on Shielding Aspects of Accelerators, Targets and Irradiation Facilities (SATIF-11) took place at the High Energy Accelerator Research Organization (KEK) in Tsukuba, Japan on 11-13 September 2012, following the 12th International Conference on Radiation Shielding (ICRS12), which was held in Nara, Japan the previous week. The workshop was chaired by Syuichi Ban and was attended by 36 participants representing 21 organisations located in 8 countries.

Support for the SATIF workshop is now part of the mandated activity of the Expert Group on Radiation Transport and Shielding (EGRTS, chaired by R. Grove from ORNL) of the Working Party on Scientific Issues of Reactor Systems (WPRS) of the OECD/NEA Nuclear Science Committee (NSC). The EGRTS also co-ordinates maintenance and development of the SINBAD database of Reactor Shielding, Fusion Neutronics and Accelerator Shielding benchmark experiments. The SATIF internet forum has been reactivated and will be used to distribute information to members. An overview of WPRS activities can be found at: *www.oecd-nea.org/science/wprs/index.html*.

The main objectives of the SATIF workshops are to:

- promote the exchange of information among experts in the field of accelerator shielding and in other related areas;

- identify areas where international co-operation could be fruitful;

- identify a programme of work in order to achieve progress in specific priority areas.

SATIF-11 is sponsored by the OECD/NEA and its Nuclear Science Committee (NSC) and co-sponsored by the Technical Divisions of Radiation Science and Technology of the Atomic Energy Society of Japan (AESJ) and the Radiation Safety Information Computational Center (RSICC). The meeting consisted of five technical sessions and a wrap-up session summarising achievements and defining further work for the next two years. The highlight of the meeting was a trip to the J-PARC facility at the Tokai site, which included visits to the Materials and Life Science Experimental Facility (MLF), the neutrino beam line and Hadron Hall. The facility is very impressive and the participants noted in particular the facility's astonishingly quick recovery from the earthquake.

The five technical sessions were as follows:

- Session 1: Induced radioactivity;

- Session 2: Present status of codes and data libraries;

- Session 3: Dosimetry, medical and industrial accelerators;

- Session 4: Benchmarking code/code and code/experimental data;

- Session 5: Source term and related themes.

The first session, during which five presentations were made, was dedicated to activation data, predictions of radioactive nuclides, and predictions of residual dose rates. The session was chaired by Heinz Vincke from the European Organization for Nuclear Research (CERN).

The second session was dedicated to recent developments in simulation codes, data for accelerator shielding, and integral experiments databases. Five presentations were made during this session, which was chaired by Nikolai Mokhov (Fermilab). At the end of the session, participants commented that, while damage can be measured, Displacement per Atom (DPA) cannot, and therefore validation of DPA against experiments cannot be carried out directly. It was also noted that quantitative confidence bounds cannot be attached to results for high energy simulations. Uncertainty analysis due to different models is therefore "next to impossible," and only comparisons of a qualitative nature can be proposed in practice.

During the third session, issues related to calculation of dosimetric quantities, shielding, secondary dose to patients, and dose delivery were explored, with Syuichi Ban (KEK) acting as chair of the session. Three presentations were made during this session. The chair added some comments for future studies, noting that there are many medical electron linear accelerators. Beam energies were mainly at E=10, 15, and 18 MeV, and the amount of activity in the air and water was small and difficult to measure. Some benchmark studies were carried out, but the components of these accelerators are not well known; nor are the actual beam energy or energy spreads during the operations because medical staff generally have no interest in these issues. This is an important problem and further studies, including experiments and benchmarks, are needed.

The fourth session was dedicated to thick-target yield experiments, shielding and deep penetration, neutron spectra-experiments and calculation, energy deposition, and high-energy reference fields. Four presentations were given, with the session chaired by Hiroshi Nakashima, Japan Atomic Energy Agency (JAEA).

The fifth session focused on hadron production, electron-photon production, photo-neutron production, radioactive ion production, and spallation neutron sources. Six presentations were given, with Hideo Hirayama (KEK) chairing the session. It was noted during this session that code inter-comparison activities within SATIF are crucial, especially for the growing number of heavy-ion facilities.

The main outcomes of the meeting were summarised during the last session where areas of co-operation for the next two years and actions required to achieve progress in the different research areas were identified. Several comments and suggestions were made by participants, and by N.V. Mokhov in particular, and are included herein. In many talks, a systematic underestimation of code-computed results compared to experimental results was revealed with the underestimation factors ranging from 2 to 10. It was recommended that the authors perform further analyses to better understand the reasons for the underestimations and inform the community on their findings. Without a safety factor, regulatory limits may otherwise be exceeded.

Hideo Hirayama proposed a computational benchmark to compare code performance for neutron production by high-energy protons. In a previous benchmark for medium energy neutron attenuation in iron and concrete, large discrepancies among the codes were found. The new proposal would use incident proton energies of 1, 3, 10, 50, and 100 GeV. The materials would be C, Al, Cu and W with target dimensions of 1 interaction length and 1 cm in diameter. The angular neutron spectrum would be examined at various angles and compared to determine the differences resulting from the code and model used. A detailed specification for the computational benchmark will be prepared as well. Some participants suggested making comparisons against experiments, since unpublished data from SATURNE exists that could be included in SINBAD. Thick target experiments from CERN and a 50 GeV experiment at Protvino are additional candidates. It was agreed that comparison against experiments could be part of a second benchmark phase, but the proposed computational benchmark is appropriate for the first phase. In the meantime, Hideo Hirayama asked for comments from participants on the proposed computational benchmark.

It was suggested that the NEA Secretariat arrange for the OECD-NEA Expert Group on Radiation Transport and Shielding (EGRTS) to discuss the different tasks agreed upon at the SATIF-11 workshop. It was also suggested that the NEA SATIF listserver be used for this purpose. New experimental data, to be compiled, evaluated and reviewed for the SINBAD database, should be identified and collected by EGRTS and the NEA Secretariat.

It was suggested that the next SATIF meeting (SATIF-12, also celebrating the 20th anniversary of the first meeting held in Arlington, Texas in 1994) would be held in 2014 in the USA, following the tradition of rotating the venue between America, Europe and Asia. The suggested venue is Fermilab in Batavia, Illinois; the tentative date would be Spring or Autumn 2014, depending upon the dates of the RPSD Topical meeting. It was suggested that SATIF-12 not be held in conjunction with the RPSD Topical. N. V. Mokhov of Fermilab agreed to explore this possibility of holding the meeting at this time, and indicated that final confirmation would be provided well in advance of the next meeting. Participants thanked the General Chair, Syuichi Ban, and KEK for hosting SATIF-11 and for their kind hospitality. The chair adjourned the meeting.

The members of the Scientific Committee of SATIF-11 were: S. Ban (KEK, the general chairman of SATIF-11), M. Brugger (CERN), R. Grove (ORNL), J. Gulliford (OECD/NEA), H. Hirayama (KEK), H.S. Lee (PAL), N. Mokhov (Fermilab), G. Muhrer (LANL), T. Nakamura (U. Tohoku), H. Nakashima (JAEA), S. Roesler (CERN), S. Rokni (SLAC), M. Silari (CERN), T. Valentine (ORNL), and P. Vaz (ITN).

The members of the Local Organising Committee were: S. Ban (KEK), H. Hirayama (KEK), K. Masumoto (KEK), S. Sasaki (KEK), T. Sanami (KEK), H. Iwase (KEK), H. Nakamura (KEK), N. Toyoshima (KEK), and H. Nakashima (JAEA).

Session I: Induced Radioactivity

Chair: Heinz Vincke

Shielding and activation studies for the design of the MYRRHA proton beamline

Anna Ferrari[1], Jean-Luc Biarrotte[2],
Luc Perrot[2], Hervé Saugnac[2], Dirk VandePlassche[3]
[1]Institute of Radiation Physics, Dresden, Germany
[2]CNRS-IN2P3, Université Paris Sud, IPNO, Orsay, France
[3]SCK·CEN, Mol, Belgium

Abstract

Accelerator-driven systems require the use of high energy Mega-Watt proton beams, in combination with a nuclear reactor core operating in subcritical mode. Between the challenges in the design, key points are the radiation shielding and the minimisation of the induced activation. The present study has been done to optimise the design of the MYRRHA facility at SCK•CEN in Mol (Belgium), where a 600 MeV, 4 mA proton beam will be produced and transported through a linear accelerator up to a LBE spallation target, located inside the core of a LBE-cooled reactor, operating at 94 MW when coupled with the proton accelerator. To assess some aspects of the shielding of the proton beamline, as well as to fix the activation problems that heavily influence the design, extensive simulations have been performed with the FLUKA Monte Carlo code. In the first part of this work a systematic study has been finalised to estimate the neutron production and the radioactivity induced by the MYRRHA proton beam in typical materials used in the accelerator structures. The results of this study allow optimising the design of the elements devoted to the total or partial beam absorption (beam dump, collimators). It will be shown, in particular, how a suitable material configuration can improve the accessibility and the long-term treatment of the irradiated elements.

Introduction

Accelerator-driven systems (ADS) are one of the options studied for the transmutation of nuclear waste in the European Community. With the aim of demonstrating efficient transmutation of high-level waste and associated ADS technology, the FP7 European project Central Design Team (CDT) has worked from 2009 to 2012 to design the FAst Spectrum Transmutation Experimental Facility (FASTEF), on which the MYRRHA research facility [1] at SCK·CEN in Mol (Belgium) will be based. The heart of the system is a lead-bismuth eutectic (LBE)-cooled reactor, working both in critical and in sub-critical operation modes. The neutrons needed to sustain fission in the subcritical mode are produced via spallation processes by a 600 MeV, 4 mA proton beam, which is provided by a linear accelerator and hits a LBE spallation target located inside the reactor core (see Figure 1). The use of high energy/high current proton beams itself presents many challenges for various aspects of the design, as already pointed out in the SATIF-10 Workshop [2]. The combination with a nuclear reactor core operating in subcritical mode with 94 MW power, or in critical mode with 100 MW power when not coupled with the proton beam, makes the shielding problem an issue: thick shielding for the prompt radiation, high target/dump activation, spent beam handling are the main points. Figure 1 shows that the general problem of the radiation containment can be divided into two parts: the shielding of the accelerator tunnel and the shielding of the reactor building. The present work focuses on the first problem, while the second one, still under investigation, has been treated elsewhere (for example in [3]). Two main points will be analysed as follows: the shielding and the activation of the element devoted to the full beam absorption (beam dump), and the activation of the materials, along the beam-line, where beam losses occur. To address these problems, an extensive simulation analysis with the FLUKA Monte Carlo code [4] [5] has been performed, as shown in the next two sections.

Double differential neutron yields, residual dose rates and specific activities from irradiated thick reference materials

As a first step, a systematic study has been finalised to estimate the neutron production and the radioactivity induced by a proton beam – with the energy and the current foreseen at MYRRHA – in five typical materials used in the accelerator structures: carbon (a candidate material for the core structure of the dump); stainless steel (used in pipe, magnets and eventually as a part of the dump structure around the carbon core); copper (possible solution for the dump, but also present in magnet coils and cavities); aluminium (foreseen in some points of the beam-line instead of the stainless steel); iron (alternative material in the dump structure around the carbon core). This study, which aims to represent a natural extension of the work presented at the SATIF-10 Workshop [6] from lower proton energies up to the MYRRHA energy range, is intended to provide a simple database, useful to drive the choice of the main structural materials and to assess an approximate estimate of the radiological risk to be expected when interventions on the accelerator components are needed.

All the simulations have been carried out with the FLUKA Monte Carlo code, version 2011.2. A precious advantage of FLUKA is the possibility to evaluate, in the same simulation, not only the particle fluences and the ambient dose equivalent, H*(10), due to all the components of the prompt radiation field, but also the time evolution of the activation products and the transport of their emitted radiation.

Figure 1: Layout of the last part of the FASTEF-MYRRHA proton beamline, until the spallation target inside the reactor core
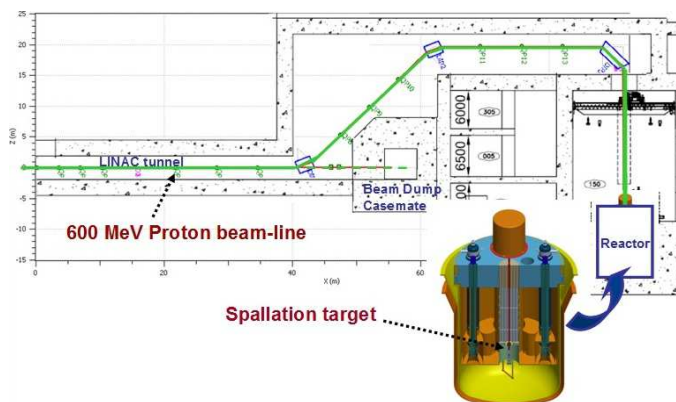
Given an irradiation pattern, the time evolution of the system (the time dependency of the isotopic densities, N_i, in the irradiated material) is evaluated run-time via the exact analytical solution of the Bateman equations, for which a particle fluence rate, $\varphi(E)$, constant during each considered time interval can be written as:

$$\frac{dN_i}{dt} = -\sum_{j \neq i} \left[\lambda_{ji}^d + \overline{\sigma}_{ji}\overline{\varphi} \right] N_i + \sum_{j \neq i} \left[\lambda_{ij}^d + \overline{\sigma}_{ij}\overline{\varphi} \right] N_j \tag{1}$$

where λd_{ji} is the decay probability of the radionuclide i in the radionuclide j and σ_{ji} is the particle induced cross-section for transmutation from the isotope i to the isotope j, and where the average spectrum, $\overline{\varphi}$, and the spectrum averaged, particle induced cross-section, $\overline{\sigma}_{ji}$, have been introduced:

$$\overline{\varphi} = \int \varphi(E)\,dE \qquad \overline{\sigma}_{ji} = \frac{1}{\overline{\varphi}} \int \varphi(E)\sigma_{ji}(E)\,dE \tag{2}$$

In Equation (1) the number of isotopes of species i decayed in other isotope species or transmuted via a nuclear reaction with the incoming beam, and the number of isotopes i produced via the decay of other radionuclides or via nuclear reactions are therefore taken into account.

At the same time FLUKA can perform the generation and transport of the residual radiation (in the used version of the code extended to γ, β+, β-, X-rays and conversion electron emissions). This means that in the same run we can obtain the production of the residuals, their time evolution and the residual dose due to their decay.

Double differential neutron yields

First, we want to evaluate the neutron yield during the operation and the residual dose in the points where the beam can be completely absorbed (also with the goal to study suitable materials for the beam dump optimisation), so that the geometry structure of the irradiated materials has been considered as a thick target: for each sample a cylindrical structure has been chosen, with the height slightly exceeding the corresponding proton range (by a factor 1.2), the diameter equal to its height and the center of the coordinate system located at the center of the upstream face (in Table 1 the values are reported). A 600 MeV proton pencil beam, with a 4 mA current (2.497 10^{16} p/s) has been simulated, hitting the center of the cylinder and directed along the z axis. The double differential yields of neutrons escaping from the target have been calculated in six angular bins with respect to the axis of the impinging proton beam: 0°-15°, 15°-45°, 45°-75°, 75°-105°, 105°-135° and 135°-180°. Figures 2 and 3 show the neutron spectra for

carbon, AISI-316L and copper, together with a picture of the neutron fluence in and around the target in the case of carbon. The high energy spallation peak, which decreases at large angles and is strongly suppressed in the backward direction, is well visible in all cases. The evaporation peak at around 1 MeV is important (in terms of neutron yield) in the high-Z materials, and in the neutron distributions of stainless steel is also clearly visible the resonance structure, mainly due to the iron component. The neutron distributions from the carbon target show the typical moderation peak. In Table 2 the total neutron yields and the yields for the very forward (0°-15°) and backward (135°-180°) components of the radiation are summarised. They give a first quantitative indication about the advantage in using soft materials (carbon) as main components of the structures that are directly hit by the proton beam.

Table 1: Dimensions and densities of the sample targets

	Sample height (cm)	Sample radius (cm)	Material density (g/cm³)
Carbon	105	52.5	2.0
Copper	30.5	15.25	8.98
AISI-316L	35	17.5	8.0
Aluminium	87.5	43.75	2.70
Iron	35	17.5	7.87

Residual dose rates

The analysis of the dose rates due to the residual radiation and of the activation products has been performed on the same samples by studying two irradiation patterns. A short-term irradiation has been simulated in the most conservative beam conditions during the commissioning: 24 hours continuous operation at the maximum beam energy and intensity. Cooling times have been analysed between the end of irradiation (EOI) and the following 24 hours. Moreover, a long-term irradiation has been simulated by considering 2 years of commissioning and 5 years of normal operation and adopting the scheme, motivated by the need to operate also in critical mode, of 1 months of operation at 6 hours/day followed by 3 months of stop, considered as a continuous time interval. Cooling times have been analysed, in this case, until one year after the EOI. The ambient dose equivalent rates due to the residual radiation around the samples are shown in Figures 4 and 5 for copper and carbon in the case of short-term irradiations. We observe that for the copper, as well as for the AISI-316L sample, the residual dose rates are very high (at the level of some tens of Sv/h) already after short irradiations and considering a reasonable cooling time of 24 hours. In Figure 6 the evolution of the H*(10) at 50 cm from the front side of the target is reported as a function of the cooling time, for both the irradiation patterns and for the samples in copper, carbon and stainless steel. We can observe that the high-Z materials exhibit very high dose rates also after long cooling times: in particular the activated radionuclides in copper still give around 20 Sv/h after 5 years from the end of the long-term irradiation. This analysis suggests the use of innovative, combined solutions, with soft (low-Z) materials inserted, where possible, in the parts of the accelerator that are directly hit by the full beam, as is the case of the beam dump.

Figure 2: Neutron double differential spectra from the target in carbon (left) and neutron fluence in and around the same sample (right)
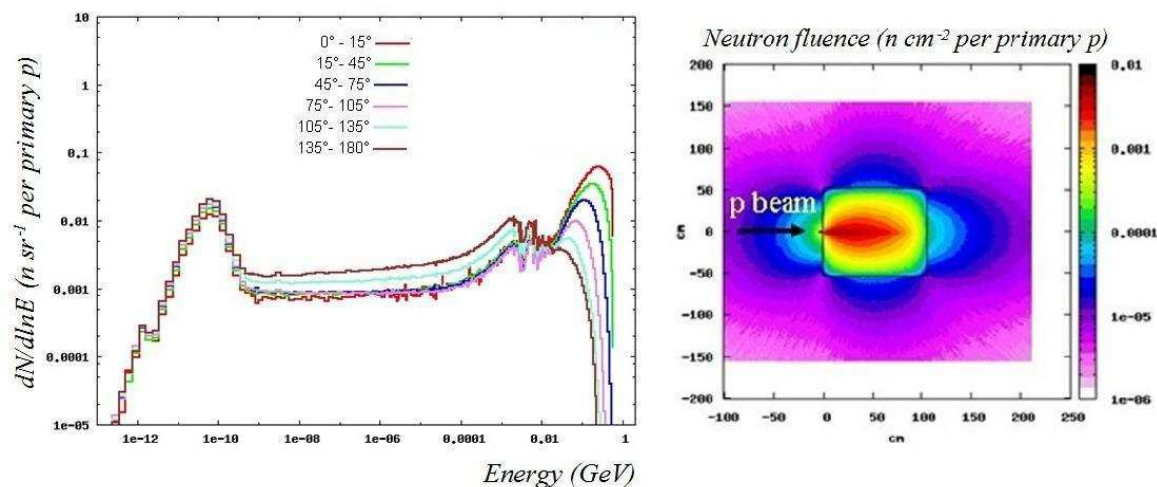
Figure 3: Neutron double differential spectra from the targets in stainless steel (left) and in copper (right)
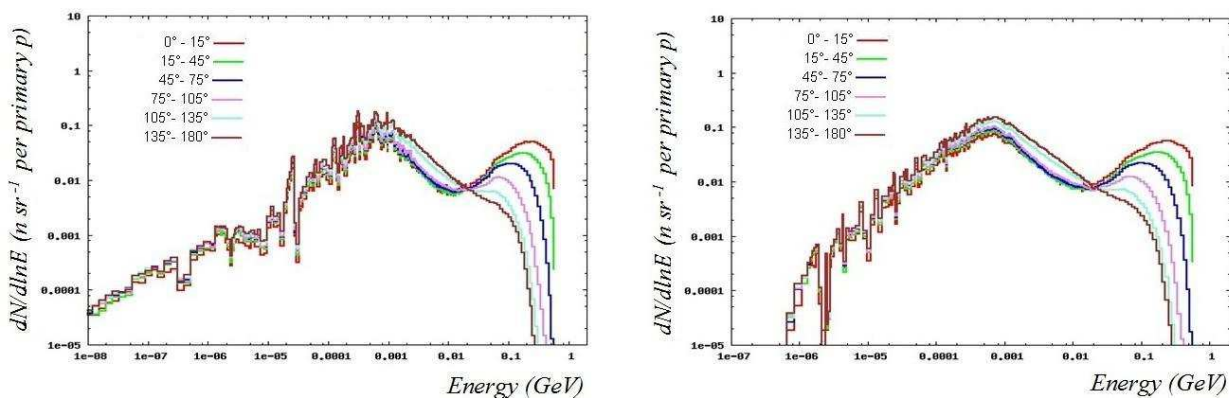
Table 2: Neutron yields computed for the sample targets

	Neutron yield (n/p)					
	Forward direction (0°-15°)		Backward direction (135°-180°)		Total	
	Full energy spectrum	E_n>100 keV	Full energy spectrum	E_n>100 keV	Full energy spectrum	E_n>100 keV
Carbon	0.036	0.029	0.190	0.068	1.195	0.554
Copper	0.067	0.062	0.747	0.684	3.989	3.625
AISI-316L	0.055	0.052	0.619	0.569	3.308	3.021
Iron	0.059	0.056	0.663	0.585	3.478	3.215
Aluminium	0.048	0.038	0.376	0.261	2.161	1.439

Note: The values in the region of the neutron energy spectrum > 100 keV are also reported.

Specific activities

As a last step, the specific activity of the irradiated samples has been evaluated, putting in evidence the contribution of the single radionuclides. In all of the Monte Carlo calculations the statistical error has been kept at the level of few percent. In Figures 7 and 8 the radionuclide composition of the activated samples is shown in the copper and in the carbon case, for short-and long-term-irradiations. In the copper case a total specific activity of $2.27 \ 10^{11}$ Bq/cm^3 is evaluated after 24 hours irradiation and 8 hours cooling, the main contributors (also under the point of view of radiological importance) being? the cobalt products as ^{56}Co, ^{57}Co, ^{58}Co and ^{60}Co. After a long-term irradiation and 10 years cooling the copper sample still exhibits a total specific activity of $1.2 \ 10^{10}$ Bq/cm^3, mainly due to long-life radionuclides like ^{60}Co ($t_{1/2}$=5.27 years), which is the dominant isotope, ^{63}Ni ($t_{1/2}$=100.1 years) and ^{55}Fe ($t_{1/2}$=2.737 years). The graphite sample shows a specific activity of $4.0 \ 10^7$ Bq/cm^3 after 24 hours irradiation and 8 hours cooling, mainly due to the ^{7}Be and tritium contributors. After a long-term irradiation and 10 years cooling the carbon total specific activity is at the level of $4.1 \ 10^8$ Bq/cm^3 and is completely dominated by tritium. The results for the stainless steel sample in the case of a long-term irradiation are shown in Figure 9, where the behaviour of all contributors is shown for cooling times up to 5 years: the total specific activity is around $8 \ 10^{10}$ Bq/cm^3 and is dominated by ^{55}Fe. It must be stressed, however, that in the present calculation the sample of AISI-316L has been simulated in the ideal situation where cobalt impurities are not present: such impurities have to be foreseen and they should be maintained at the lowest reasonable level (typical values are fractions of 0.1-0.5 per-mille in volume).

Figure 4: H*(10) Residual dose rate around the copper target, at different cooling times after a 24 h irradiation
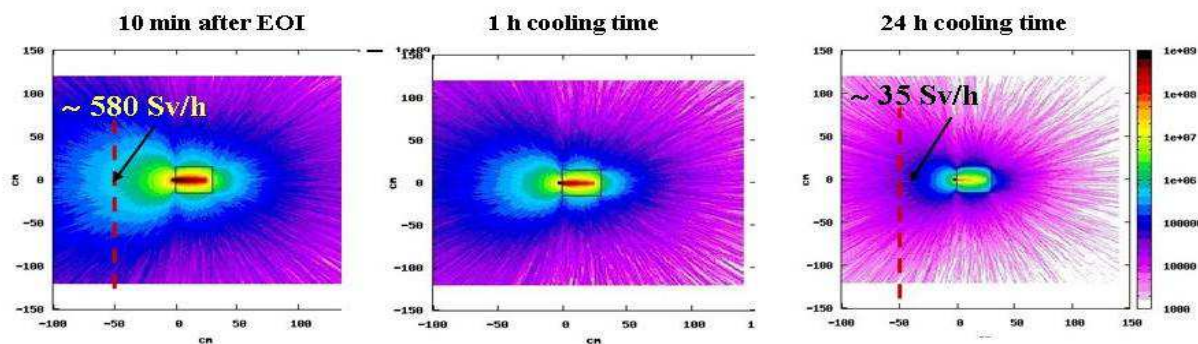
Figure 5: H*(10) Residual dose rate around the carbon target, at different cooling times after a 24 h irradiation
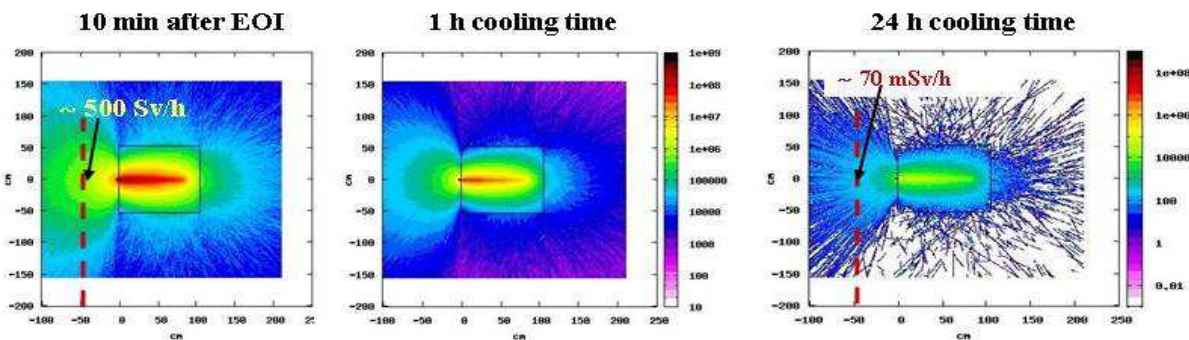
Figure 6: H*(10) Residual dose rate evaluated at 50 cm from the front of the target samples as a function of the cooling time, for short-(left) and long-term (right) irradiations
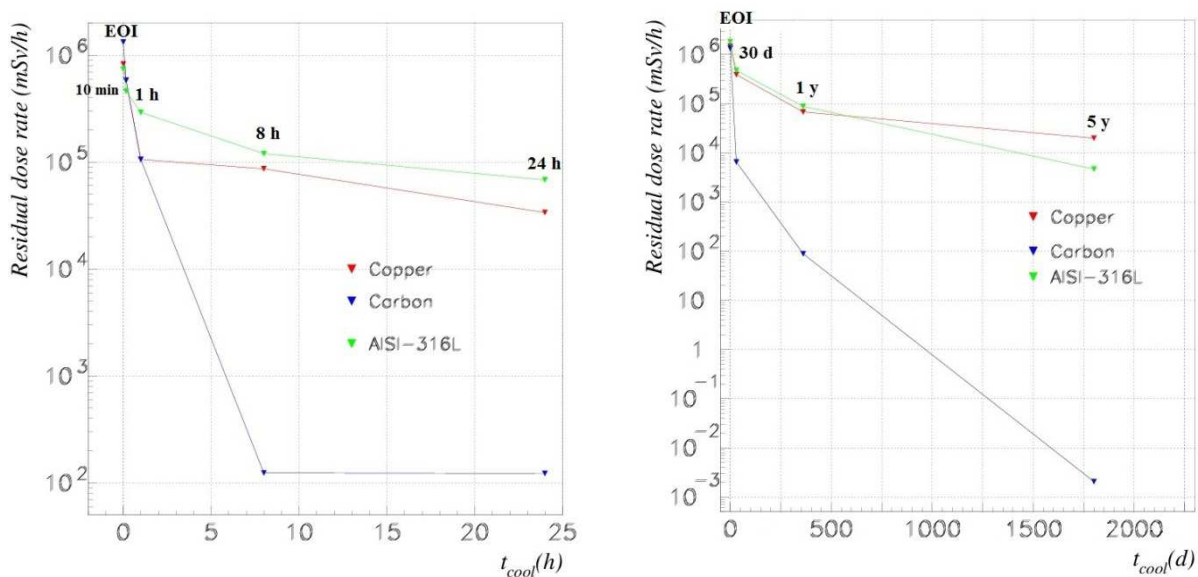
Figure 7: Specific activity (in Bq/cm³) of the copper and carbon samples in the case of short-term irradiation, after 8 hours cooling
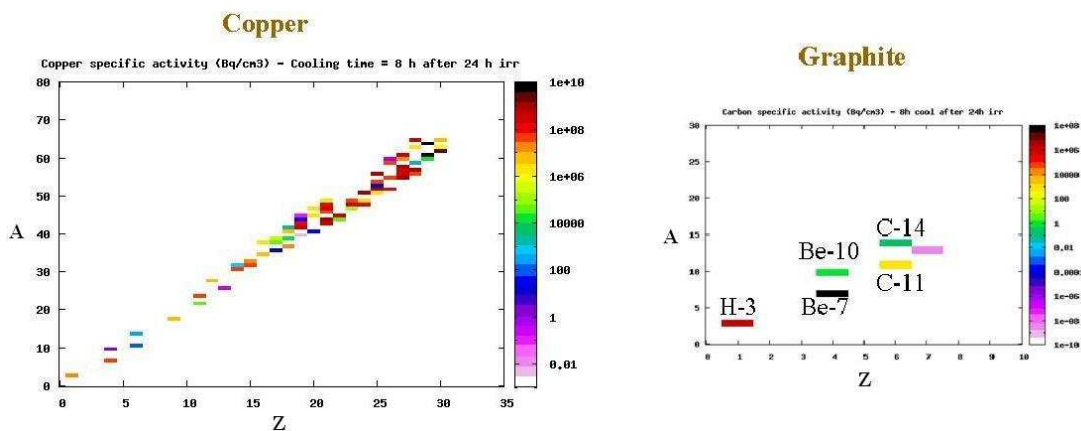
It is represented in the Z-A plane to show the contribution of the single radionuclides.

Figure 8: Specific activity (in Bq/cm³) of the residual radionuclides evaluated in the samples of copper and carbon in the case of a long-term irradiation, after 10 year cooling
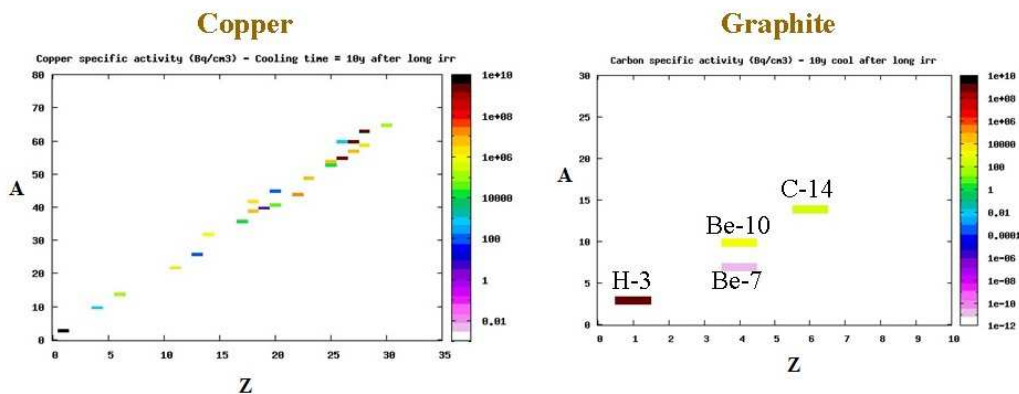
Figure 9: Behaviour of the total specific activity (in Bq/g) of the stainless steel sample in the case of the long-term irradiation, for different cooling times up to 5 years
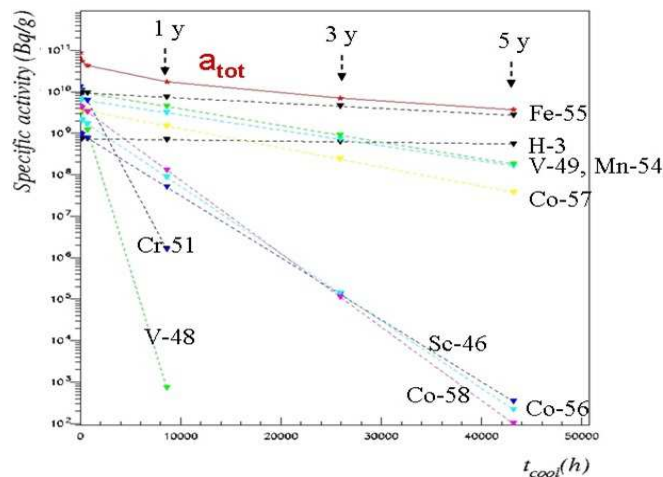
The contribution of the main radionuclides is reported.

Optimisation study of the beam dump

The beam dump will always absorb the beam completely during the period of the accelerator commissioning, and for accelerator tuning purposes during the operation time. It will be, therefore, the "hottest" part of the accelerator beam-line. The first solution thought for the beam dump is based on the model adopted at PSI for the High Intensity Proton Accelerator Facility [7], because the beam characteristics (590 MeV proton beam energy and maximum beam current of 2 mA, corresponding to a full power of 1.2 MW) are very close to the MYRRHA requirements. The PSI beam dump is composed of 4 copper blocks (see Figure 10), cooled with water and placed in a parallelepiped-shaped vacuum chamber. Each copper block extends to a stainless steel block, ~3 m long. A preliminary upgrade of the PSI solution has been evaluated to fit the MYRRHA requirements and foresees the use of 5-6 copper elements. This solution, which presents the advantage of a consolidated know-how, does not exhibit, however, the best performances under the point of view of the radiation protection. As it can be argued from the studies presented in the previous section, with this solution quite a high-yield

of secondary neutrons and serious activation problems are to be expected. For this reason two approaches have been followed in parallel: to quantify and possibly to limit the main problems in the copper dump design and, on the other hand, to propose and to explore an alternative solution. This one has been identified in a bi-material structure, with a suitable soft material as dump core, surrounded by a high-Z shielding structure. As already pointed out elsewhere [8] [9], advantages of this concept are a smaller neutron yield, an energy deposition over a wider range and consequently considerable less activation problems, especially in terms of residual ambient dose equivalent rate. A key point that drives the choice in favour of a soft material core is that in this case the build-up region of the secondary radiation moves from the front part towards the central part of the dump, with a very effective auto-shielding effect: the "hottest" part of the dump is not anymore close to the dump surface but is deeper inside the material, minimising the H*(10) rate outside the dump.

Figure 10: The PSI 1.2 MW beam dump
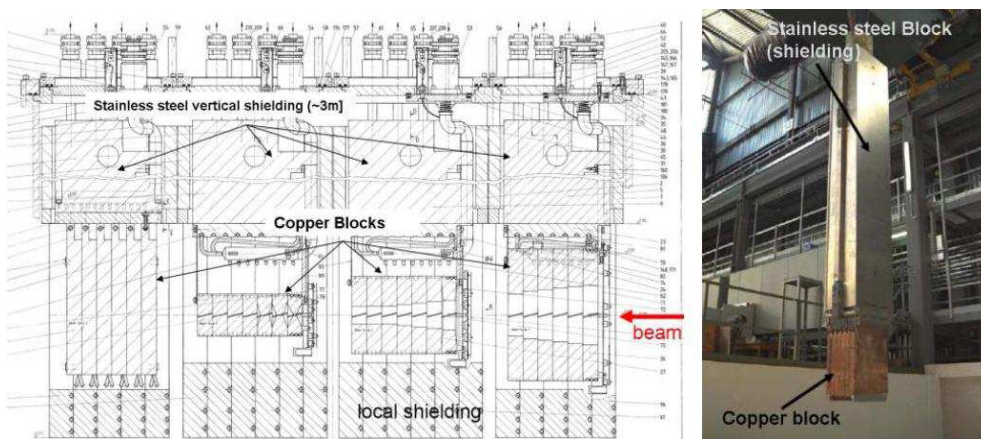
Figure 11: The FASTEF-MYRRHA beam dump casemate along the proton beamline
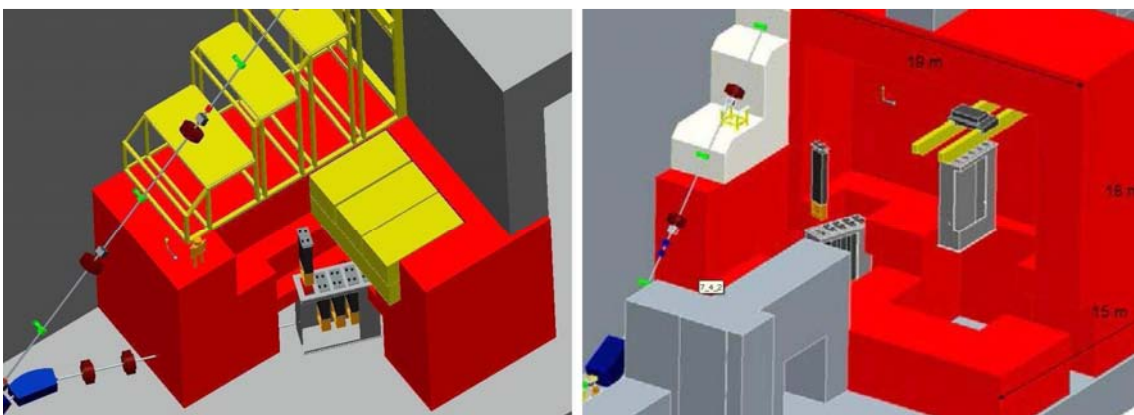
Left: the simulated design of the irradiated cell. Right: a possible design with a second cell for maintenance and a crane for remote handling.

A bi-material solution in carbon (graphite for shielding, with a density of ~ 2.0 g/cm³) and stainless steel (AISI-316L) has been studied. The dimensions assumed for the carbon core are 50 cm in radius and 180 cm in length, while for the high-Z part a radius of 140 cm and a length of 330 cm have been set. The model implemented in FLUKA also includes the whole concrete cage, with walls ~5 m thick, and the last part of the proton beam-line. Parallel simulations of a complete model of the beam dump in copper, with 5 copper elements and their extensions in stainless steel, have been also performed. Figure 12 shows a comparison between the two models in terms of neutron fluence. Firstly, it should be stressed that the casemate in concrete contains the radiation in a very satisfactory way in both cases. The average neutron fluence inside the concrete cage, however, is in the bi-material case ~100 times lower. Moreover, if the neutron secondary radiation emitted in the backward direction is studied (see Figure 13), it can be observed that the bi-material solution minimises the part of the spectrum from the epithermal up to the fast and the high energy neutrons. This result is also more interesting if in this sample the neutrons that pass through the pipe channel and come out from the shielding wall are selected: the spectra of these neutrons (in red in Figure 13) show that the backscattered neutron radiation reaching the beamline is bigger in the copper case and is never negligible. For this reason, with the aim of protecting the instrumentation close to the dipole at 45° positioned at the beginning of the vertical beamline, together with the horizontal beam tube before, the portion of the proton line between this dipole and the dump has been rotated of 20° with respect to the horizontal beamline, as illustrated in Figure 11.

Figure 12: Neutron fluence (n/cm² per primary proton) in the dump concrete cage in the case of the dump in copper (left) and of the bi-material dump in carbon and stainless steel (right)
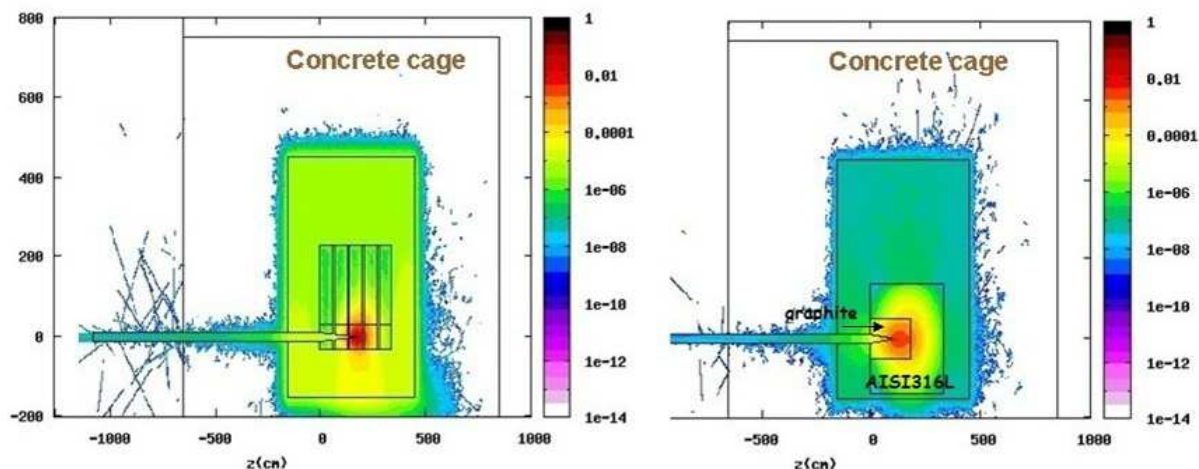
Figure 13: Spectra of the neutrons (neutrons sr⁻¹ per primary proton) coming out from the dump in the backward direction, for the two studied models of the beam dump
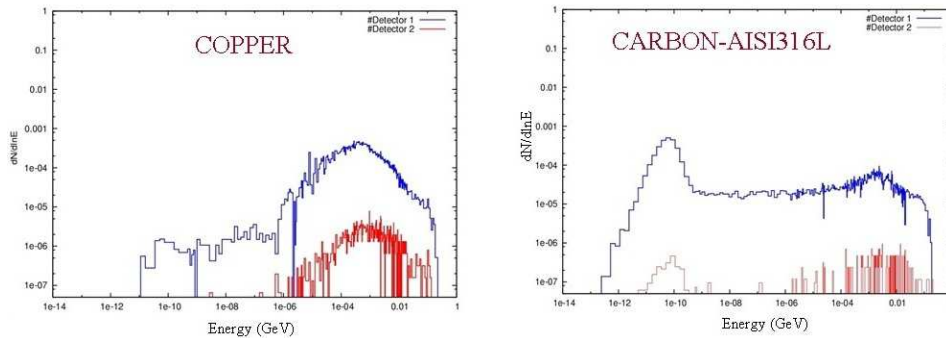
In blue all the backward neutrons from the copper structure (left) and from the graphite/stainless steel structure (right) are computed. In red, the neutrons are reported that, going in the backward direction, cross the shielding walls along the beam-line tunnel and reach the accelerator hall.

Residual dose rates and specific activities

A special study has been dedicated to the evaluation of the residual dose rates expected inside the concrete cage and on the roof for the two models of the beam dump. The special capability of the FLUKA code has been used to perform a simulation in a condition of variable geometry: the geometry of the problem can vary from the transport of the prompt radiation to the transport, during the cooling, of the residual one. In the latter case, the concrete blocks that in the roof of the dump casemate are removable have also been also removed in the simulation during the cooling time, and replaced with air.

The FLUKA model used in the case of the copper beam dump is shown in Figure 14. The two usual irradiation patterns have been studied, for short- and long-term irradiations. The results for the two beam dump models are reported in Figures 15 and 16. In the case of the beam dump in copper, the H*(10) rate due to the residual radiation over the roof is at the level of 1 Sv/h after the 24-hour cooling that follows or follow 24-hour irradiation. This very high value definitely requires a better protection against the dose from activation, to make the area over the roof accessible for the maintenance, even with the opportune restrictions. This better protection could come from additional local shielding – for example with concrete slabs – around the copper structure in the dump casemate. In the case of the bi-material dump the H*(10) over the roof due to the activated materials in the dump is at the level of 10 mSv/h after the 24 hours of cooling that follows the short-term irradiation. This value, which is already two orders of magnitude lower with respect to the previous case, can be lowered further by using a proper shielding against the radiation coming from the activation: experience at high-energy accelerators shows, for example, that quite narrow slabs of marble around the dumps are highly effective[1]. The picture of the residual H*(10) rate 30 days after the long-term irradiation, moreover, shows how well, with this beam dump choice, the residual radiation is contained in the inner part of the dump, allowing the access to the roof.

As a last step, a study of the residual specific activity in the dump materials has been done. In Figure 17 the residual specific activities in the carbon core and in the "hottest" part of the stainless steel are reported for the bi-material dump, after a long-term irradiation and for a cooling time of 30 days. The total specific activity for the stainless steel is at the level of 10^9 Bq/cm³, while in the carbon core is around 10^3 Bq/cm³.

---

[1] A. Fasso private communication.

Figure 14: FLUKA model of the copper beam dump
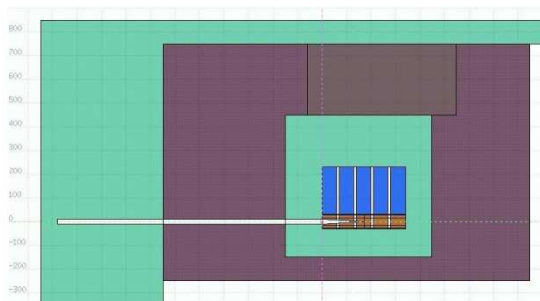
The concrete cage around the beam dump is described, with the last meters of the beam-line and, on the roof, the concrete blocks that are removable when the accelerator is not in operation.

Figure 15: Residual H*(10) rate (in mSv/h) in the concrete cage and over the cage roof in the case of the dump in copper, for two typical cooling times after a short-and a long-term irradiation
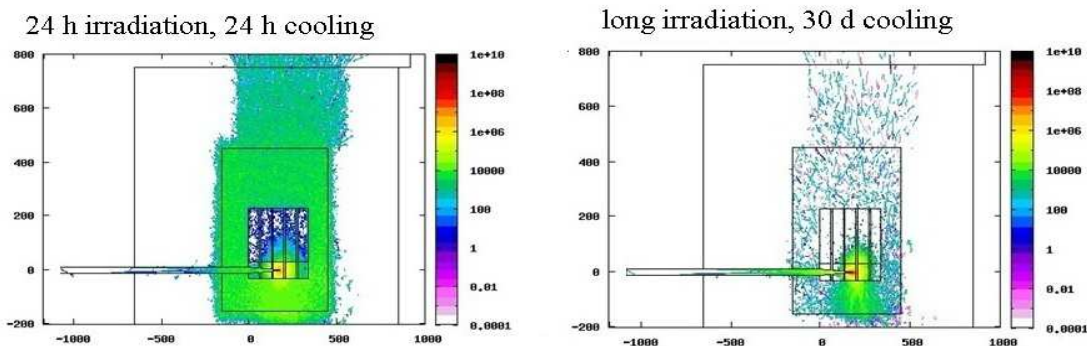
Figure 16: Residual H*(10) rate (in mSv/h) in the concrete cage and over the cage roof in the case of the bi-material dump, 24 hours after a 24 hours irradiation and 30 days after a long-term irradiation
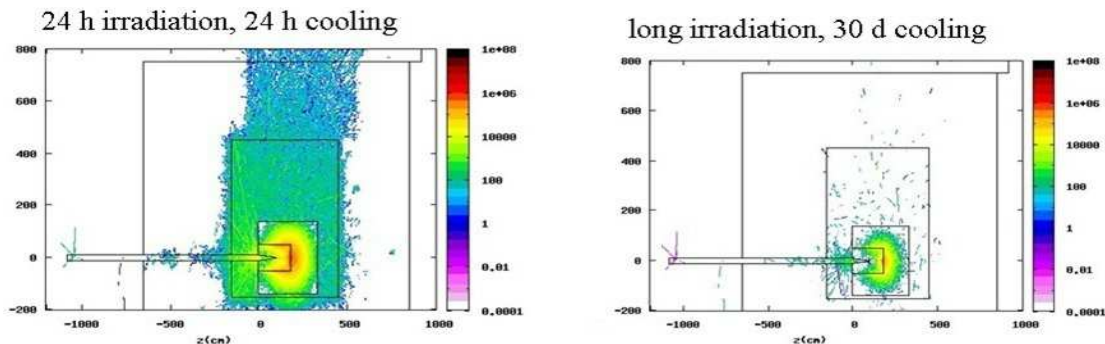
Figure 17: Specific residual activity of the carbon core and the stainless steel "hottest" part in the case of the bi-material dump, after a long-term irradiation and a cooling time of 30 days
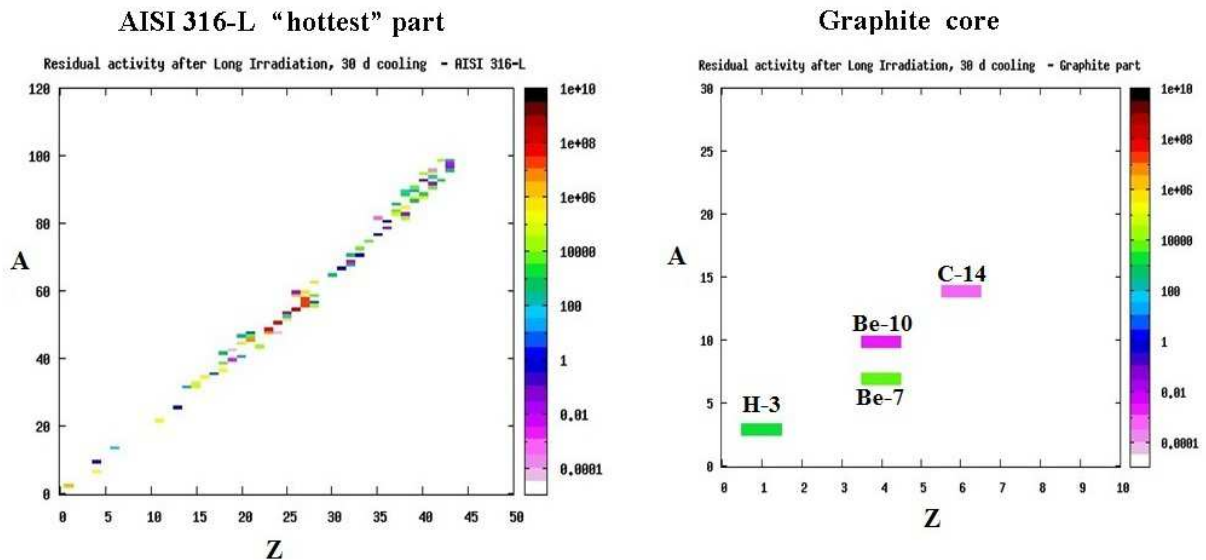
In the Z-A plane the main radionuclides that contribute to the activity are shown.

In the case of the copper dump the results for the "hot" part of the dump are those of the left sides of Figures 7 and 8: it can be observed that a value of 1.2 10^{10} Bq/cm^3 is still present at the end of the 10 years of cooling that follows the long-term irradiation.

Residual dose rates due to the beam losses along the beam-line

Beam losses along the beam-line have to be minimised to keep activation at an acceptable level for hands-on maintenance and to protect equipment. Operational results from the Spallation Neutron Source at ORNL show that an uncontrolled beam loss level of about 1 W/m is fully consistent with a hands-on maintenance philosophy [10]. To check the validity of this assumption in the case of MYRRHA, an additional Monte Carlo study with the FLUKA code has been performed. The last 100 meters of the LINAC horizontal tunnel have been simulated, including the pipe of the beam-line in stainless steel and 10 collimators in copper, one every 10 m. The concrete walls along the tunnel have been also included and described with the first 30 cm of their thickness, in order to take into account the backscattered component of the neutron radiation. A continuous beam loss of 1 nA/m has been then assumed and a continuous, linear distributed proton source corresponding to this loss has been described. In order to take into account the realistic behaviour of the proton beam, the proton energy has been described in the model as linearly increasing along the line. The two irradiation patterns studied in the analysis in the previous sections have been assumed, for short-and long-term irradiations. In the case of the short-term (24 h) irradiation the initial residual dose rate of about 200 µSv/h at EOI at the distance of 1 m goes down, after the first 24 hours cooling, to ~ 10-30 µSv/h, depending on the position along the line. Therefore, a human intervention on the line seems possible in a reasonable time after the end of the irradiation. After a long-term irradiation and the first 30 days cooling the ambient dose equivalent residual rate varies from few up to ~ 50 µSv/h, still a limited value, which seems low enough to allow a human intervention.

In addition to these simulations, a second study has been performed with the aim of evaluating the radiological impact of eventual "hot spot losses" of 100 nA due to the collimators. Figure 18 shows the results of this simulation for a short-term irradiation. In the top picture, which shows the behaviour of the residual H*(10) rate at EOI, the effect of

the collimators and the effect of the increasing proton energy are clearly visible. The high dose rate of few mSv/h at the end of the short-term irradiation goes down to values between 100 µSv/h up to several hundreds µSv/h after 24 hours. A similar result, which should be seen as a superior limit due to the pessimistic value of the assumed "hot spot" losses, would require a longer waiting time before an eventual access close to the line.

Figure 18: Residual H*(10) rates (in µSv/h) around the last 100 m of the horizontal beamline, for two representative cooling times (EOI and 24 h) after a 24 h irradiation, with the hypothesis (100 nA) of hotspot losses due to the collimators
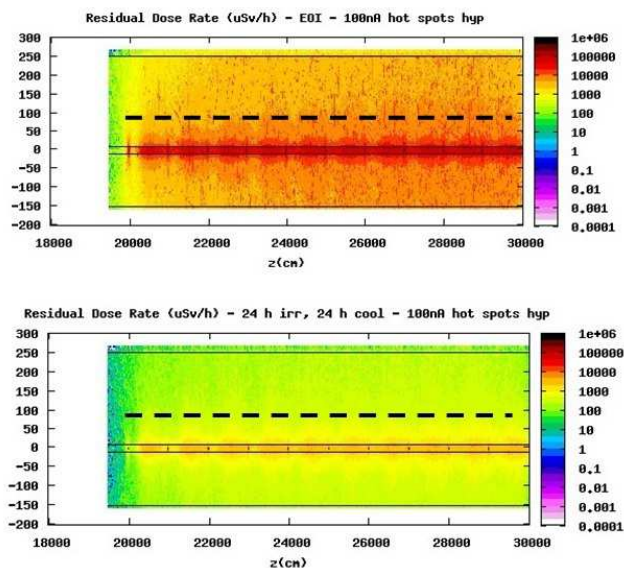
Conclusions

Firstly, a general Monte Carlo study has been presented, with the aim of optimising some aspects of the shielding of the MYRRHA proton beamline, as well as quantifying the activation problems that heavily influence the design. Results about neutron double differential yields and induced radioactivity from irradiated thick samples of carbon, aluminium, iron, stainless steel and copper are intended to be a simple database, to address the choice of the main structural materials. The optimisation study of the beam dump showed that, besides a first design of a beam dump in copper, a beam dump solution with a soft, low Z material for the core, surrounded by a medium-high Z material is optimal under the point of view of the induced activation, improving the accessibility and the long-term treatment of the irradiated elements. Detailed thermal and mechanical studies will be needed to better assess the feasibility of all the proposed solutions.

Acknowledgements

References

[1] D. De Bruyn, H. Aït Abderrahim, P. Baeten, R. Fernandez (2011), MYRRHA, the Multi-purpose Hybrid Research Reactor for High-tech applications, Proc. of the International Congress on Advances in NPPs (ICAPP '11), Nice, France 2-6 May 2011, France Omnipress, 472-478.

[2] N.V. Mokhov (2010), Dealing with MegaWatt beams, *Proc. of the SATIF-10 Workshop,* CERN 2-4 June 2010, OECD/NEA publication 6898, 105-111.

[3] A. Ferrari, S. DiMaria, M. Sarotto, A. Stankovskiy (2012), Shielding and activation calculations for the MYRRHA ADS design in the sub-critical operation mode, *ICRS12 Conference*, Nara, Japan 2-7 September 2012.

[4] A. Ferrari, P. Sala, A. Fassò, J.Ranft (2005), FLUKA: A multi-particle transport code, CERN-2005-10, INFN/TC_05/11, SLAC-R-773.

[5] G. Battistoni *et al.* (2007), The FLUKA code: description and benchmarking, *Proceedings of the Hadronic Shower Simulation Workshop 2006,* Fermilab 6-8 September 2006, AIP Conference Proceedings, 896, 31-49 (2007).

[6] F. Cerutti, N. Charitonidis, M. Silari (2010), Neutron double differential distributions, dose rates and specific activities from accelerator components irradiated by 50-400 MeV protons, *Proc. of the SATIF-10 Workshop,* CERN 2-4 June 2010, OECD/NEA publication 6898, 139-155.

[7] http://aea.web.psi.ch/Urs_Rohrer/MyWeb/pkanal.htm.

[8] A. Ferrari, T. Cowan, D. Margarone, J. Prokupek, B. Rus (2010), Shielding assessment for the ELI high-intensity laser beamline facility in the Czech Republic, *Proc. of the SATIF-10 Workshop,* CERN, 2-4 June 2010, OECD/NEA publication 6898, 105-111.

[9] A. Ferrari, E. Amato, D. Margarone, T. Cowan, G. Korn (2012), Radiation field characterization and shielding studies for the ELI Beamlines Facility, Applied Surface Science, http://dx.doi.org/10.1016/j.apsusc.2012.09.105.

[10] J. Galambos (2008), Operational experience with high power beams at the SNS superconducting LINAC, *Proc. of the LINAC2008 Conference,* Victoria, Canada.

Induced radioactivity and residual dose rates in the LHC experiments

I. Kurochkin[1,2], S. Roesler[1], C. Theis[1], C. Urscheler[1], H. Vincke[1]
[1]CERN, CH-1211 Geneva 23, Switzerland, [2]IHEP, Protvino, Russian Federation

Abstract

The Large Hadron Collider (LHC) at CERN started beam operations in 2008 and has clearly outperformed initial expectations. At the two biggest LHC experiments, ATLAS and CMS, the delivered integrated luminosity (which refers to the number of inelastic interactions during a certain time interval) for 2011 has been exceeded by a factor of almost 6 compared with its initial goal given at the beginning of 2010. LHCb and ALICE are operating already at their nominal luminosities and even above.

Consequently, radiation levels in the LHC experiments are increasing. Further, the amount of radioactive material inside the experiments is becoming larger. Predictions of the expected residual dose rate during accesses are necessary in order to plan and co-ordinate work activities inside the experimental caverns. The Monte-Carlo particle transport code FLUKA was used to assess the expected prompt and residual dose rates at the LHC experiments. Further, the code was used to calculate the amount of material which would become radioactive and therefore requires special treatment and alertness when being handled, modified, stored or shipped. Estimates of radiation levels are presented and compared with the first measurements. An outlook of the expected radiation levels after several additional years of LHC operation is also given.

Introduction

The superconducting Large Hadron Collider (LHC) [1] is the world's largest and highest-energy particle accelerator and is located deep underground below the Franco-Swiss border near Geneva, Switzerland, (see Figure 1). The LHC consists of a 14 TeV (centre-of-mass energy) accelerator (presently operated at 8 TeV) and is installed in a 27 km long tunnel. This tunnel was originally constructed for the Large Electron Positron (LEP) collider at CERN which operated from 1989 to 2000 before liberating the tunnel for the LHC. Two transfer lines (TI 2 and TI 8) are acting as injectors to the LHC and connect the LHC to CERNs accelerator complex. At present, seven experiments have been approved for the LHC. Four of them, ALICE [2], ATLAS [3], CMS [4] and LHCb [5], are large experiments, LHCf [6], MoEDAL [7] and TOTEM [8] and are much smaller.

LHC operation started in 2008 and has achieved exceptional performance clearly outperforming initial expectations. As a consequence, dose rates in the LHC experiments are increasing as well as the amount of activated material is becoming larger. The Monte-Carlo particle transport code FLUKA [9] [10] was used for predications of prompt and residual dose rates and for the activation of material at the LHC experiments.

Figure 1: Location of the LHC
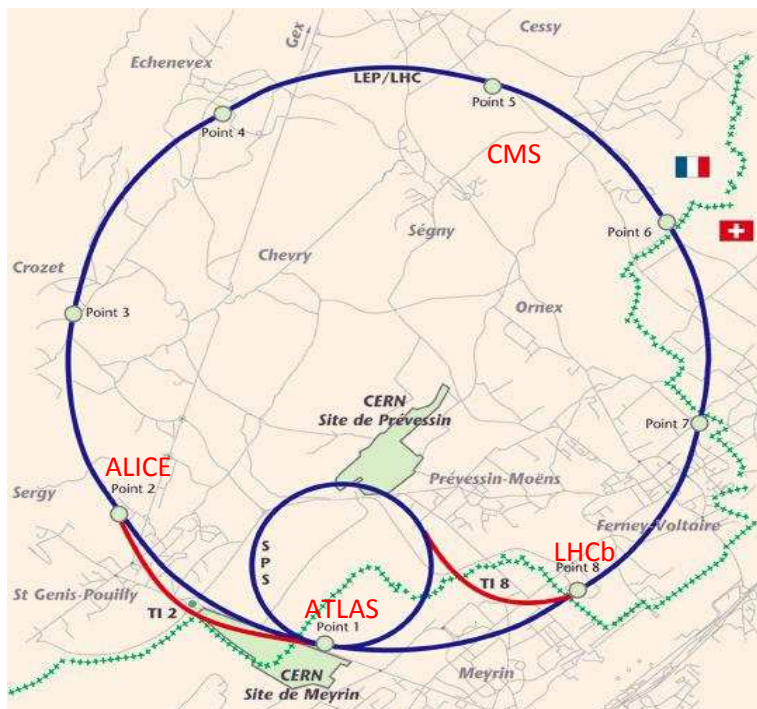
The four major LHC experiments

Four major experiments are installed at the LHC. Two of them, namely ATLAS and CMS are so called high luminosity[1] experiments. LHCb is operated at peak luminosities about a factor of 50 lower than in ATLAS or CMS whereas the peak luminosity in ALICE is about hundred times lower than in LHCb. Two counter-rotating beams are crossing each other at the 4 experiments roughly 11 000 times per second where they can be brought into collisions to study fundamental questions/laws of particle physics at high energy.

---

[1] Luminosity refers to the number of inelastic interactions during a certain time interval.

No access into the experimental caverns is possible during beam periods because the prompt dose rate is by far too high. Only well-shielded service areas and counting rooms in the underground are accessible during beam time.

Figure 2: The LHC and the 4 major experiments
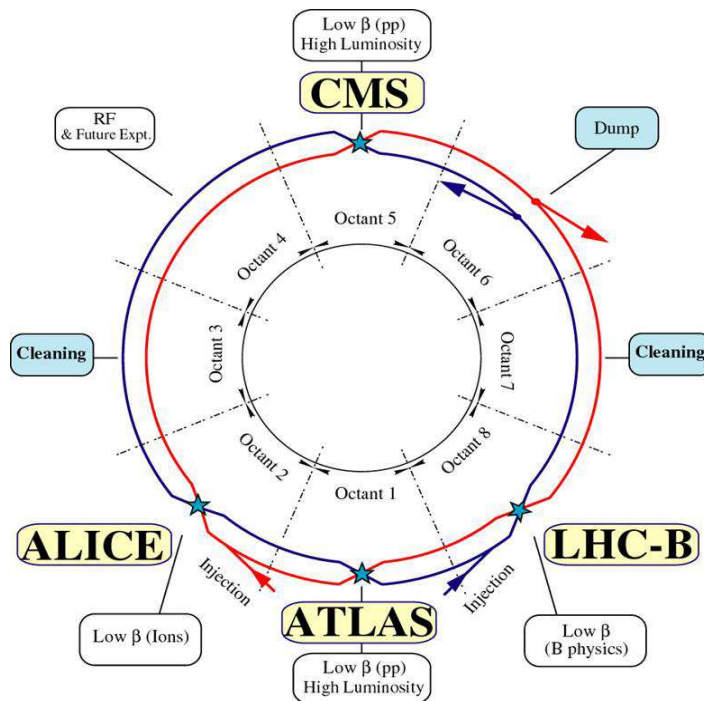
LHC performance

The LHC is presently operating at performances well beyond first expectations. Estimates given in January 2010 about the integrated luminosity for 2011 were exceeded by a factor of 6. The LHC has delivered almost 6 fbarn^{-1} by the end of 2011 to ATLAS and CMS, (see Figure 3). In 2012 (not adding up the values from the past) the delivered luminosity is expected to reach ~ 25 fbarn^{-1} (by beginning of September 2012 almost 14 fbarn^{-1} were delivered already, see also Figure 3). In 2012, the peak luminosity has reached nearly 80% of the nominal luminosity of 1.0×10^{34} cm^{-2} s^{-1} with an average integrated luminosity of 1 fbarn^{-1} per week to ATLAS and CMS. ALICE and LHCb are operating already at nominal luminosities and even above.

Figure 3: Luminosities delivered to the LHC experiments in 2011 and 2012, respectively
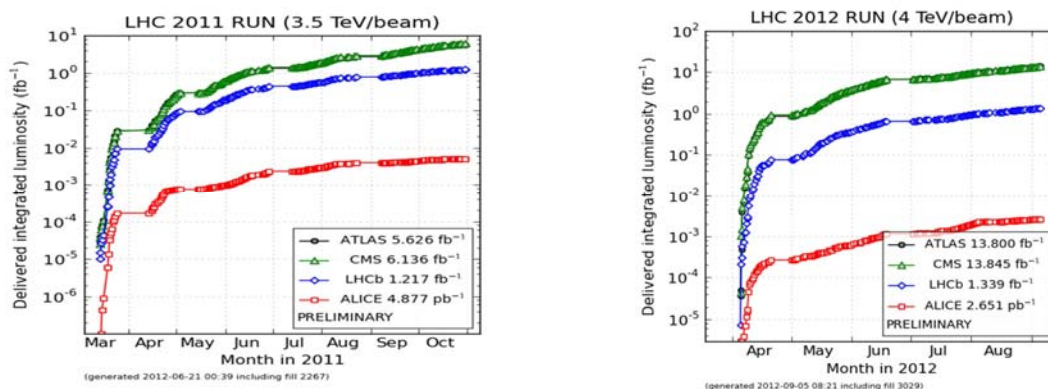
Radiological assessments for the LHC

Many radiological studies have been performed for the LHC experiments. This paper reports on residual dose rate up to 2022 inside the experimental cavern to which personnel could be exposed during access and maintenance work of detector components. An activation chart is also presented indicating which parts of the detectors are radioactive according to CERNs radiation protection legislation and therefore, require special treatment and alertness when being handled, modified, stored or shipped.

FLUKA simulations

All four major experiments have been modelled in detail with FLUKA, (see Figure 4). It should be mentioned that these geometries are very complex and are partially derived from work developed and updated by several contributors[2]. Magnetic fields inside the magnets of the experiments were also well described and modelled within FLUKA.

Figure 4: FLUKA geometry of the ALICE experiment (shown with FLAIR[3])
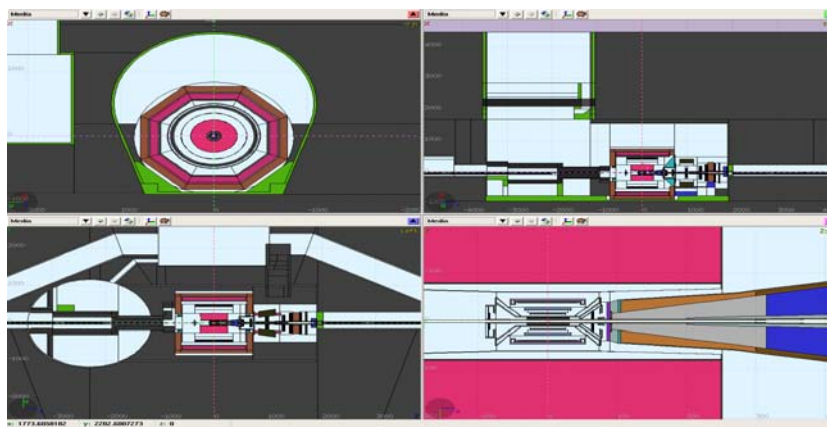
An important input for the radiological calculations is the proper description of beam intensities as well as beam operation and cool-down periods. Table 1 represents the

---

[2] Contributors: I. Dawson, A. Ferrari, A. Morsch, M. Huhtinen, L. Shekhtman, M. Karacson, Z. Zajacova, N. Ludovic, M. Guthoff, S. Mueller, M. Brugger, R. Veenhof and others.

[3] http://www.fluka.org/flair/index.html.

beam operation schedule for ATLAS[4] up to 2021/2022. In general, LHC operation starts in March/April with proton-proton (p-p) runs until end of October. Afterwards, the LHC programme continues with a heavy ion period of about 4 weeks followed by either a winter shutdown period (winter SD) for ~4 month or a so-called long shutdown (LS) which can last up to 2 years. These LSs are used for major upgrade activities of the LHC accelerator as well as for upgrade activities of detectors of the LHC experiments. It should be noted that the luminosity during the ion operation is considerable lower than during p-p operation. Consequently, the radiological conditions are dominated by the p-p run periods (with the exception of ALICE). Peak luminosity during the p-p collisions is up to a factor 1×10^7 higher in ATLAS and CMS than during Pb-Pb collisions periods.

Table 1: ATLAS beam operation schedule

Year	Period Run/SD/LSx	Peak luminosity $cm^{-2} s^{-1}$	Period length (months)	Efficiency	Collect $fbarn^{-1}$/period	Integrated $fbarn^{-1}$	Cooling (months)
2011	run	3E+33	3	0.25	5.8E+00	5.8	0
2011/2012	Winter SD	0	5	0.25	0.0E+00	5.8	5
2012	run	6.00E+33	8	0.2	2.5E+01	30.7	0
2012	LS1	0	2	0.2	0.0E+00	30.7	2
2013	LS1	0	12	0.2	0.0E+00	30.7	12
2014	LS1	0	12	0.2	0.0E+00	30.7	12
2015	run	1.00E+34	10	0.2	5.2E+01	82.6	0
2015/2016	Winter SD	0	4	0.2	0.0E+00	82.6	4
2016	run	1.00E+34	8	0.2	4.1E+01	124.0	0
2016/2017	Winter SD	0	4	0.2	0.0E+00	124.0	4
2017	run	1.00E+34	8	0.2	4.1E+01	165.5	0
2017/2018	LS2	0	16	0.2	0.0E+00	165.5	15
2019	run	2.00E+34	8	0.2	8.3E+01	248.4	9
2019/2020	Winter SD	0	4	0.2	0.0E+00	248.4	4
2020	run	2.00E+34	8	0.2	8.3E+01	331.4	0
2020/2021	Winter SD	0	4	0.2	0.0E+00	331.4	4
2021	run	2.00E+34	8	0.2	8.3E+01	414.3	0
2021/2022	LS3	0	24	0.2	0.0E+00	414.3	0

Residual dose rates in the experimental caverns

Detector equipment as well as beam line components located close to the beam pipe will get significantly activated in the high-luminosity experiments ATLAS and CMS. Therefore, significant shielding was placed aside these components in order to allow access into the cavern while preventing unjustified exposure. Both ATLAS and CMS have enough shielding around the beam pipe to reduce the radiation levels outside shielded areas to acceptable levels. For example, if an access is required to the cavern, the radiation level immediately after the beam stop at the end of 2012 will be below 1 µSv/h in the ATLAS cavern outside of the shielded areas, (see Figure 5). The highest dose rate of 10 to 20 µSv/h, in accessible detector areas of the four major LHC experiments, is being measured at the VELO location of LHCb shortly after a beam stop. Very similar values have been predicted also with FLUKA, (Figure 6). The radiation levels at ALICE are considerably lower than in all other experiments.

---

[4] Provided by the ATLAS Radiation Safety Officer.

**Figure 5: Ambient dose equivalent rate in ATLAS
(only the upper part of the detector is shown, symmetric layout)**
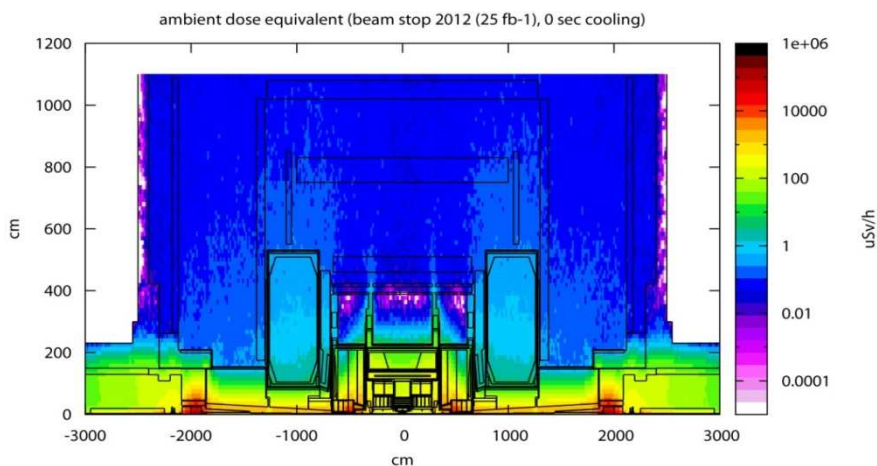
Figure 6: Ambient dose equivalent rate in LHCb
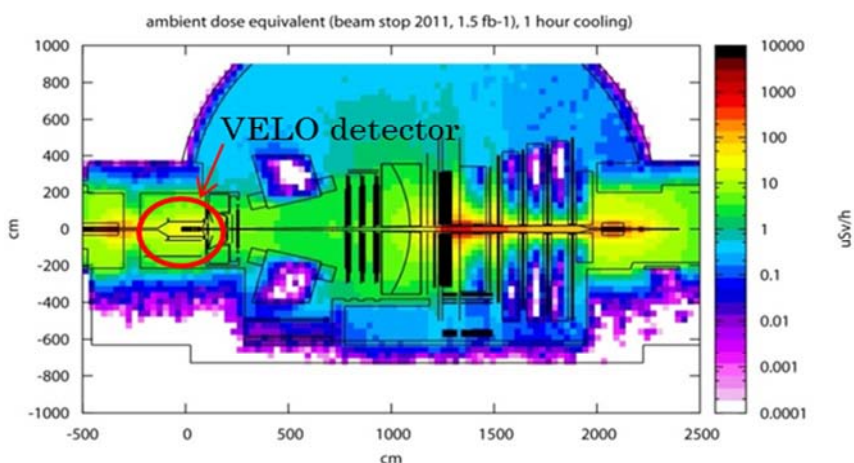
As shown in Figure 5, the radiation levels outside of the shielded components are small. However, this changes as soon as the shielding is opened to allow for access and the repair of components. This is illustrated in Figure 7, which shows the dose rate averaged over the first 14 cm around the beam line as a function of cooling time after the beam stop in 2012. It can be seen that the dose rate is about a factor of 100 lower at the end of LS1 (after 2 years of cool down) compared to the time when the beam will be stopped at the end of 2012 and about a factor of 50 lower compared to a cool down time of 1 week. It should be noted here, that the heavy ion run (due to the low luminosity) does not contribute significantly to the activation levels and can be considered as cool down time for ALTAS, CMS and LHCb.

A similar plot is shown in Figure 8, here, for a cool down time of 1 month following the beam stops in 2012, 2015, etc. up to the stop for the long shutdown 3 (LS3) at the end of 2021. It can be seen that the dose rate in LS2 (end of 2017) will be ~2 times higher than in LS1 and ~3 times lower than in LS3. The high dose rates at the Target absorber for secondaries (TAS) and the forward calorimeter FCAL are values inside the opening for the beam pipe and are normally not accessible unless being dismantled.

**Figure 7: Ambient dose equivalent rate around the beam pipe of ATLAS
(detector and shielding closed, averaged over 14 cm radius from the beam line)**
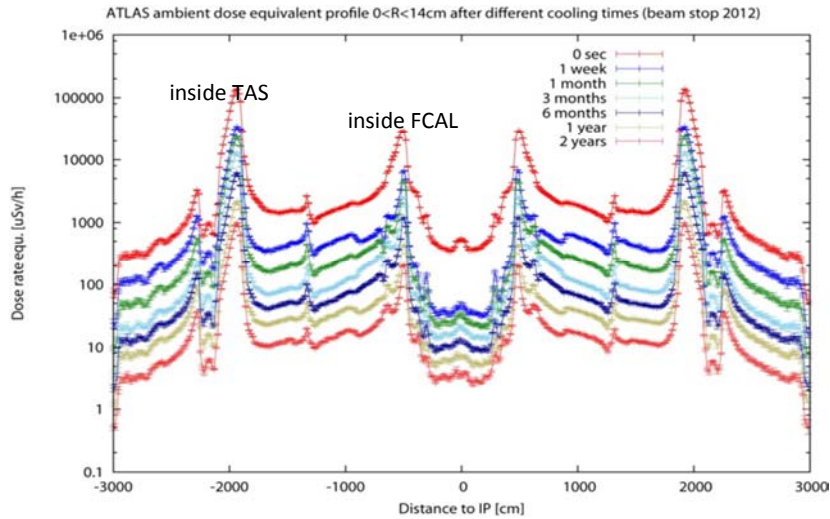
Figure 8: Ambient dose equivalent rate around the beam pipe of ATLAS
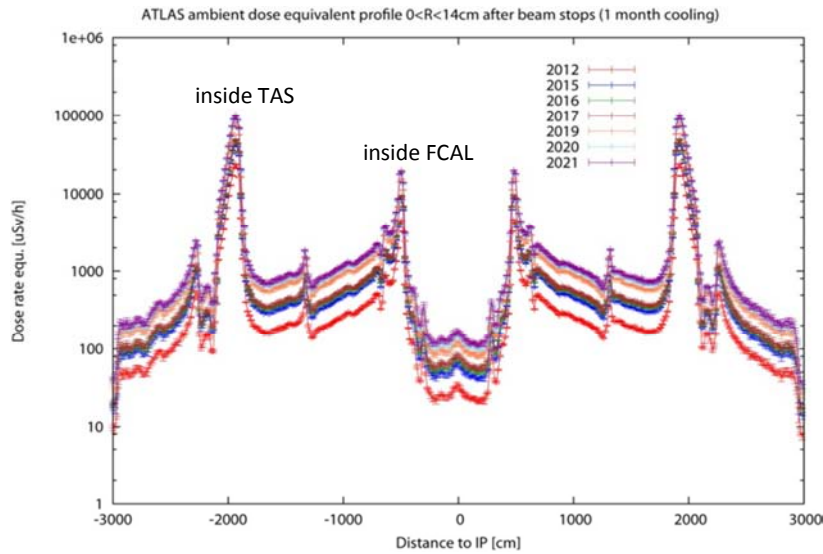
Calculation of specific activities inside the experimental caverns

FLUKA was also used to calculate the specific activity of components inside the detector and shielding material and these activities were compared afterwards with Swiss exemption limits. The following sum rule was used;

$$\sum_i \frac{a_i}{LE_i} \geq 1 \qquad (1)$$

where a_i is the specific activity of the i-th radionuclide in the material and LE is the specific exemption limit given in Bq/kg for the corresponding radionuclide. In order to avoid over-conservative classification for very small quantities of material, the same ratio is also calculated based on total activity and the exemption limit in terms of Bq. As soon as the sum is greater or equal to 1 for both results (specific and total activity), the

material is considered as radioactive according to CERNs legislation (this is in line with the Swiss regulation). It should be emphasised that the specific activity is just one criterion for the classification of a material as radioactive. The two others are dose rate and surface contamination.

Figure 9 shows the "activation" chart for CMS which was used in 2011 to assess the boundary of radioactive *vs.* conventional material, as shown here, for a cool down time of 4 months. As said before, values above 1 indicate radioactive material.

Figure 9: Specific activities/LE ratios at CMS
(4 month after beam stop in 2011)
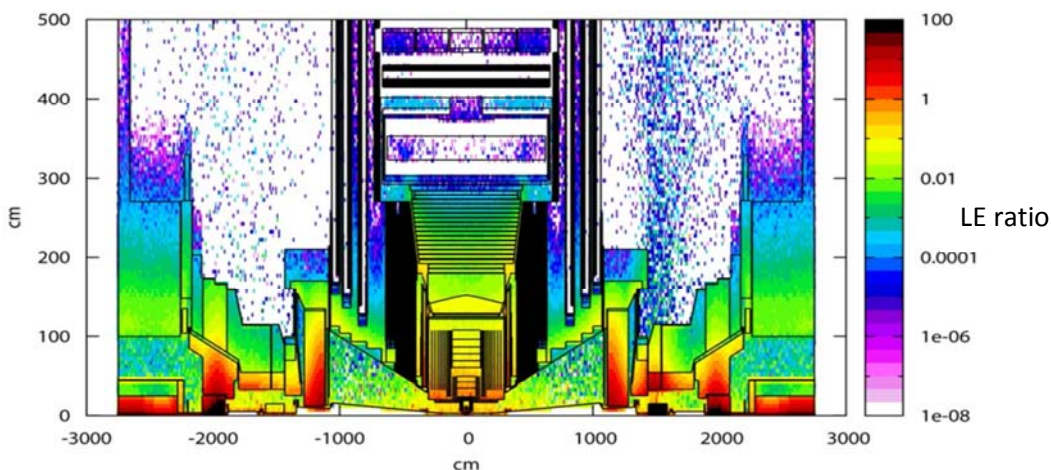
Measurements and comparison with calculations

Measurements at CASTOR

The removal of the CASTOR detector at CMS has provided a good opportunity to verify the estimates of residual dose rate with real measurements taken during the removal of the detector. The CASTOR detector was taken out in March 2012, 149 days after the end of the p-p run in 2011. CASTOR itself has a cylindrical shape and consists of 2 half cells which were removed separately from the beam line, (see Figure 10). Ambient dose equivalent rate measurements were performed after the removal of CASTOR. The dose rate was measured at 5 positions around one half cell of the cylinder, (see Figure 10). These results are shown in Table 2 together with the FLUKA estimates. Although the detector was not modelled in detail, the results are rather good. For example, the measurement at location E (on contact) showed 100 µSv/h whereas we predicted 89 µSv/h.

Table 2: Ambient dose equivalent rate at CASTOR (measurement and calculation)

Position	Measurement in · Sv/h	Calculation in · Sv/h
F on contact	35	30
F at 100 cm	3	3
G on contact	14	11
G at 40 cm	5	4
G at 100 cm	2.5	2
E on contact	100	89
E at 10 cm	53	40
E at 40 cm	16	10
E at 100 cm	3.5	2.4

Figure 10: Specific activities/LE ratios at CMS
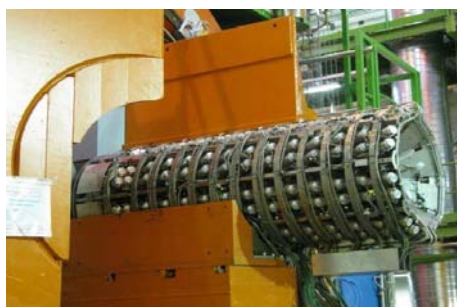
CASTOR detector at CMS.
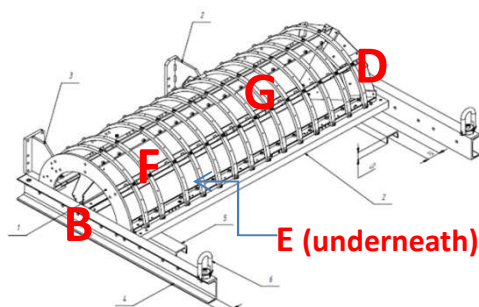
Measurement locations.

Material samples

Different material samples were placed next to the CASTOR detector for another benchmark experiment. A similar set of samples were also placed on the opposite side of the CMS detector (here called "no-castor-side") since CASTOR is installed only on one side of the CMS detector. The samples were Cu, Al, Pb and stainless steel with a well-known chemical composition and were put in place from the beginning of 2009 and were retrieved from their locations after the winter shutdown in 2011. Due to time constraints, only stainless steel samples could be taken out and were analysed with a Gammaspectrometer. The dominating 3 isotopes in the stainless steel samples are ^{54}Mn, ^{58}Co and ^{60}Co. With the exception of the ^{60}Co sample on the "no-castor" side the ratio between the FLUKA results and the measurements is very close to one, indicating a very good agreement, (see Table 3). Because ^{60}Co is produced by thermal neutron capture, a possible reason for the divergence of ^{60}Co production might be an underestimation of the low-energy neutrons in the "no-castor" side due to simplified geometry implementation.

Table 3: Measured and calculated activity in stainless steel samples

Sample	Radionuclide	Measured activity in Bq/g	Ratio FLUKA/measurement
Samples on the CASTOR side	^{54}Mn	7.3 ± 3.3	1.0 ± 0.5
	^{58}Co	6.1 ± 2.8	0.9 ± 0.4
	^{60}Co	0.7 ± 0.2	0.9 ± 0.3
Samples on the "no – castor" side	^{54}Mn	77 ± 35	0.9 ± 0.3
	^{58}Co	68 ± 24	0.9 ± 0.3
	^{60}Co	24 ± 7	0.3 ± 0.1

Summary

The LHC at CERN has produced sensational performance and is operating at almost nominal luminosities at ATLAS and CMS and even above at ALICE and LHCb. The Monte-Carlo particle transport code FLUKA was used extensively for radiation protection studies. A few of them, the ambient dose equivalent rates during beam down times, as well as charts, show which parts of the detector will become radioactive or not. Dose rates inside the experiment cavern are (and will be even in the future) reasonably low during accesses as long as the detectors are closed. As soon as the detectors are opened, the radiation levels are considerably higher and will reach mSv/h levels at the high luminosity experiments of ATLAS and CMS. Benchmark experiments showed very good agreement between calculated and measured values.

References

[1]   LHC design report (CERN-2004-003-V-1), http://cdsweb.cern.ch/record/782076.

[2]   ALICE collaboration, ALICE: Technical proposal for a Large Ion collider Experiment at the CERN LHC, CERN-LHCC-95-71, http://cdsweb.cern.ch/record/293391.

[3]   http://cdsweb.cern.ch/record/290968 ATLAS Collaboration, ATLAS: technical proposal for a general-purpose pp experiment at the Large Hadron Collider at CERN, CERN-LHCC-94-43.

[4]   http://cdsweb.cern.ch/record/290969, CMS collaboration, CMS technical proposal, CERN-LHCC-94-38.

[5]   http://cdsweb.cern.ch/record/622031, LHCb collaboration, LHCb technical proposal, CERN-LHCC-98-004.

[6]   LHCf collaboration, Technical Proposal for the CERN LHCf Experiment, CERN-LHCC-2005-032, LHCC-P-007, 12 October 2005, http://cdsweb.cern.ch/record/887108.

[7]   MoEDAL Collaboration (2010), Technical design report of the MoEDAL experiment, CERN-LHC-2009-006, MoEDAL-TDR-1, 27 February 2010.

[8]   W. Kienzle *et al*. TOTEM collaboration, Total cross section, elastic scattering and diffractive dissociation at the LHC: Technical Proposal, CERN-LHCC-99-007, http://cdsweb.cern.ch/record/385483.

[9]   G. Battistoni, S. Muraro, P.R. Sala, F. Cerutti, A. Ferrari, S. Roesler, A. Fasso`, J. Ranft (2006), The FLUKA code: Description and benchmarking, *Proceedings of the Hadronic Shower Simulation Workshop 2006,* Fermilab 6--8 September 2006, M. Albrow, R. Raja (2007), eds., *AIP Conference Proceeding* 896, 31-49.

[10]   A. Ferrari, P.R. Sala, A. Fasso, J. Ranft, (2005), FLUKA: a multi-particle transport code*,* CERN-2005-10, INFN/TC_05/11, SLAC-R-773.

New capabilities of the INCL4.6 model implemented into high-energy transport codes

S. Leray[1], A. Boudard[1], B. Braunn[1], J. Cugnon[2],
J.-Ch. David[1], A. Leprince[1], D. Mancusi[1]
[1]CEA, Centre de Saclay, Gif-sur-Yvette, France
[2]University of Liège, Liège, Belgium

Abstract

High-energy reactions in spallation targets produce a large number of radioactive isotopes that are a concern for radioprotection in normal conditions (gas release, waste disposal), in case of accident and in view of the decommissioning. Transport codes are essential, because they are able to predict reliably the production of radioactive isotopes in spallation targets. Recently, the INCL4.6-Abla07 combination of models, which was proven to have a very good predictive power of spallation residue production in the IAEA benchmark of spallation models, has been implemented in a MCNPX2.7 and PHITS. Examples of simulations done with this code will be presented. The first example concerns the European Spallation Source (ESS) tungsten target. A careful benchmarking of the code on W elementary cross-sections (excitation functions) allows assessing the uncertainty on the predictions of the most hazardous isotopes. The second one is devoted to the production of astatine (Z=85) isotopes in the ISOLDE (CERN) lead-bismuth target. Our model, thanks to the coalescence mechanism in the intranuclear cascade model and to an improved handling of low-energy helium-induced reactions, correctly predicts the astatine yields. The recent extension of the model to light ion induced reactions and its implementation into GEANT4 is also discussed.

Introduction

The Liège Intranuclear Cascade model, INCL4 [1], has originally been developed to describe spallation reactions, i.e. nucleon and light charged particle induced collisions in the 100 MeV-3 GeV energy range. The main motivations for the work on spallation reaction models were the development of spallation neutron sources, projects of accelerator-driven subcritical reactors (ADS) that could be used to transmute long-lived radioactive waste and radioactive ion beam facilities. Other applications of high-energy reactions involving also sometimes light-ion induced reactions are nowadays also raising a lot of interest: for instance, hadron therapy, radioprotection of astronauts and radiation damage to microelectronics circuits near accelerators or in space missions, and simulation of detector set-ups in nuclear and particle physics experiments. As such, there is a need for models, to be used in high-energy transport codes, with a scope large enough to cover all these applications.

Coupled with the ABLA de-excitation code from GSI [2], INCL4 has been extensively compared with experimental data covering all possible reaction channels and continuously improved during the last ten years, part of the work being done in the framework of the HINDAS [3] FP5 and EUROTRANS/NUDATRA [4] FP6 EC projects, whose objective was to provide improved simulation tools for the design of ADS transmuters. The combination of versions developed in this framework, INCL4.5 [5] and ABLA07 [6], has been shown [7] [8] to be one of the models giving the best overall agreement with experimental data in the benchmark of spallation models organised recently under the auspices of IAEA [9]. A new version, INCL4.6, very similar to INCL4.5 for nucleon-induced reaction above 100 MeV but improved for composite particle and energies below 100 MeV, has been recently released [10].

This version is now implemented into PHITS [11], in which it is coupled with the GEM de-excitation model. The same version, coupled to ABLA07, is available in a version of MCNPX [12]. A version fully re-written in C++, INCL++, extended to light-ion collisions up to ^{18}O has also been developed and is included into GEANT4 [13].

In this paper, we discuss the present capabilities of the new versions through comparisons with some elementary experimental data and examples of calculations with the model implemented into high-energy transport codes, in particular MCNPX and GEANT4, focusing on applications related to radioprotection and shielding issues.

Simulations for the ESS target station

In the IAEA benchmark of spallation models, the main success of INCL4.5-ABLA07 compared the other participating models was encountered in the prediction of isotopic distributions of spallation residues. It is therefore likely that our model implemented into MCNPX will provide reliable calculations of spallation target radioactive inventories. An example of a simulation done recently with INCL4.6-ABLA07 implemented into MCNPX concerns the helium cooled, rotating tungsten target foreseen for the ESS facility, in which the radioactive inventory has been estimated and the major contributors to the radiotoxicity identified [14].

Validation of the model for the elementary reaction channels

Since the benchmark did not contain any experimental data on tungsten, we have first checked that our model gives a reasonable agreement on available excitation functions concerning isotopes appearing as main contributors to the radioactivity of the ESS target. Examples of such excitation functions are displayed in Figure 1 for some of most problematic nuclides for radioprotection, ^{148}Gd, which is an alpha emitter and tritium, which is a gas and can therefore easily escape. In all the cases where

experimental data were available, the model reproduces data generally within a factor smaller than 2.

Figure 1: Experimental production cross-sections of ^{148}Gd (left) and tritium (right) in p+W reactions compared with INCL4.6-Abla07 (lower part: ratio calculation/measurement [14])
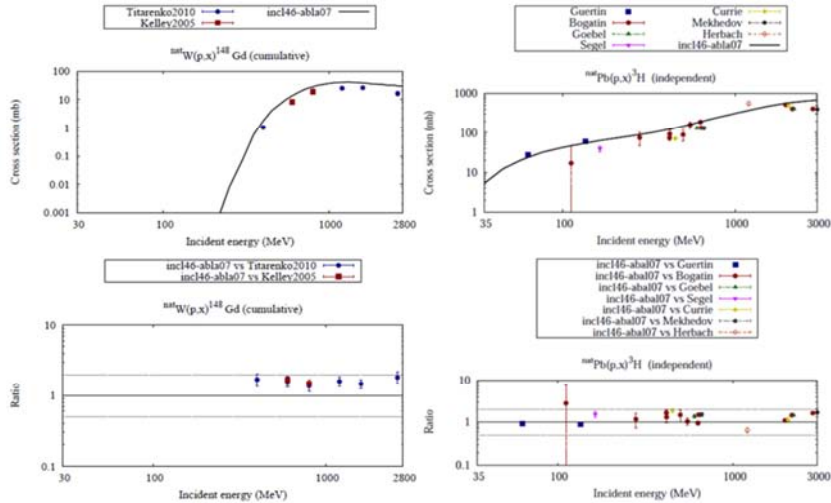
Full simulation

The ESS target is composed of 11 tungsten layers of different thicknesses surrounded by 2 mm of helium [15]. The detailed geometry of the target and surrounding materials has been simulated with MCNPX and CINDER'90 has been used to take into account the production by low-energy neutrons and decay of the different isotopes. Figure 2 represents, on a chart of nuclides, the activity at the end of an irradiation time of 3.6 years (left) and after a cooling time of 156 days (right), due to the different spallation products generated in the tungsten.

Figure 2: Nuclide activity (Bq) in the ESS tungsten target irradiated during 3.6 years, just after shutdown (left), after 156 days off beam (right), obtained by INCL4.6-Abla07 in MCNPX+CINDER'90 on a chart of nuclides [14]
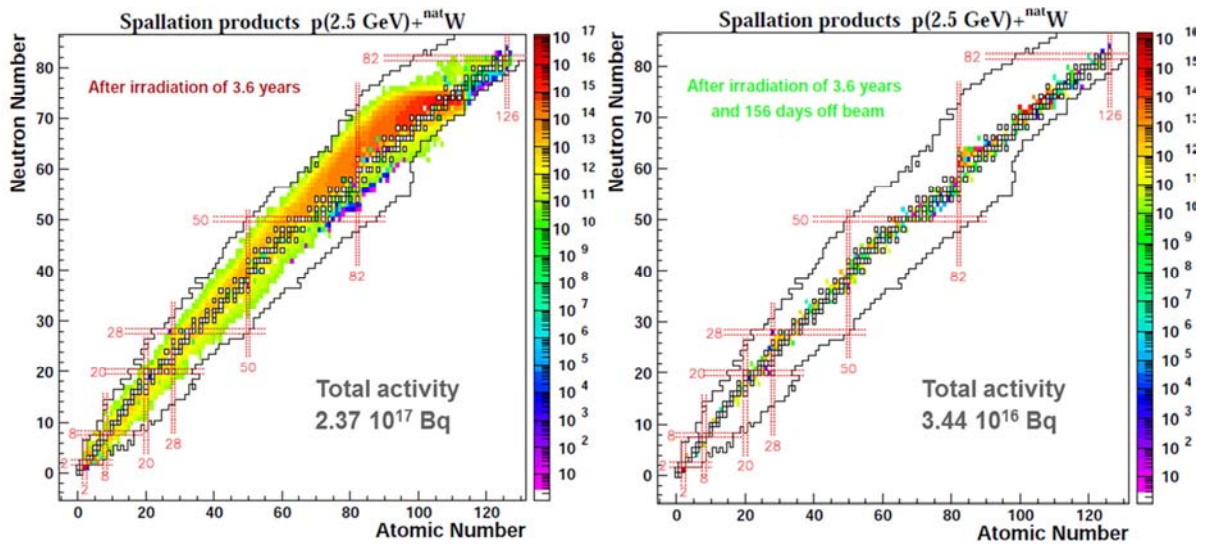
The left panel illustrates a very large number of radioactive nuclei produced in spallation reactions and the high level of the induced radioactivity. Although most of the generated nuclides are short-lived and have disappeared after 6 months (right panel), the total activity has been reduced by a factor of 6 – this is due to a small number of major contributors, among which is tritium.

As stressed in the preceding section, the fact that elementary reactions have been shown to be well predicted by our model gives confidence in the full simulation.

Production of astatine isotopes in the ISOLDE target

Recently, the IS419 experiment at the ISOLDE facility at CERN measured the production and release rates of volatile elements from a liquid lead-bismuth eutectic (LBE) target irradiated by a proton beam of 1 and 1.4 GeV [16]. Among others, the production of At isotopes was investigated. Although the production of astatine isotopes is relatively modest and these isotopes are generally short-lived, they could be a radioprotection issue since astatine is highly volatile and its isotopes decay to polonium isotopes. In [16], the experimental results were compared to simulations with different high-energy transport codes, none of which were able to predict neither the order of magnitude of the measured astatine production nor the shape of the isotopic distribution. In [17], we have investigated astatine production channels in LBE and used our model in MCNPX to simulate the ISOLDE experiment.

Protons irradiating a LBE target can produce astatine isotopes through the following mechanisms: $^{209}Bi(p,\pi^-xn)^{210-x}At$, i.e. double charge exchange in primary reactions; secondary reactions induced by helium nuclei produced in primary collisions, $^{209}Bi(^3He,xn)^{212-x}At$ and $^{209}Bi(^4He,xn)^{213-x}At$. Contributions from other secondary reactions have been checked to be negligible. Actually, a first simulation of the ISOLDE experiment with MCNPX has revealed that isotopes with mass larger than 209 are produced only through secondary helium-induced reactions, ^4He playing a larger role and leading to higher masses. On the other hand, both mechanisms populate the other isotopes, the very lightest ones preferentially originating from double charge exchange reactions.

Validation of the model for the elementary reaction channels

In order to estimate the reliability of our model regarding astatine production in LBE targets a careful validation on the involved elementary channels has been done. Concerning production of the light isotopes through double charge exchange reactions, the predictions of the model, not shown here, can be considered as correct within a factor of 2.

Since secondary reactions of helium nuclei play an important role, it is necessary to have a model able to correctly predict helium production in spallation reactions. In most models, helium is produced only in the de-excitation stage, which cannot account for the high-energy tail (above around 50 MeV) observed in the experimental spectra. Actually, only models which have a specific mechanism to produce high-energy clusters of nucleons can aspire to reproduce this tail. In INCL4, a mechanism based on surface coalescence in phase space has been introduced and leads to a very good agreement with experimental data all along the energy spectrum [10].

The treatment of secondary reactions induced by helium nuclei of energies below 100 MeV is also important. Although from the origin, the INCL4 model was designed to handle reactions with composite particle up to alpha, little attention had been paid to those up to recently. In addition, secondary reactions occur at low energies, generally below the alleged theoretical limit of validity of INC models. In the last version, the treatment of low-energy composite particle induced reactions has been significantly improved. Details of the modifications brought to the model are discussed in [10]. Let us say here that the composite projectile is now described as a collection of off-shell

independent nucleons with Fermi motion, ensuring full energy and momentum conservation and that a phenomenological prescription has been added in order to lead to complete fusion at low energies. With these modifications, the model is able to predict rather well the helium-induced total reaction cross-sections and the individual channels, corresponding to the evaporation of x neutrons after fusion, which leads to the production of astatine nuclei, as can be seen in Figure 3.

Figure 3: ^{209}Bi(α,xn) (left) and ^{209}Bi(^{3}He,xn) (right) cross-sections for x=1 to 6 as a function of the helium incident kinetic energy compared to the predictions of the INCL4.6+ABLA07 model
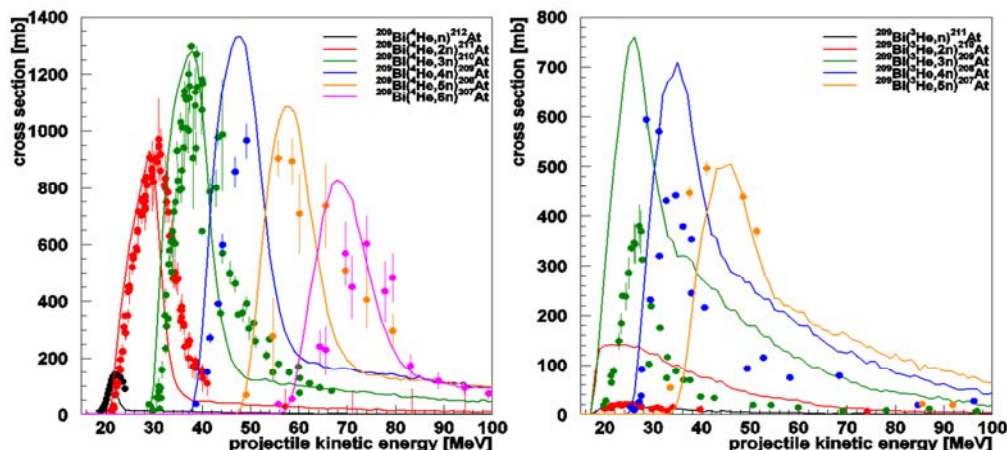
Experimental data come from the experimental nuclear reaction database EXFOR [17].

Actually, the situation is better in the case of ^{4}He than for ^{3}He, for which the x=1 and x=2 channels are largely overestimated, the agreement being restored only for the largest x values. However, in the ISOLDE target secondary reactions induced by ^{3}He are much less numerous than those due to ^{4}He for the channels with the smallest x-values. Since our model agrees well with the experimental data for ^{4}He for all x-values and for ^{3}He for x>2, we can expect the overall prediction to be reliable within a factor definitely smaller than 2.

Astatine production yields in the ISOLDE target

Figure 4 shows the result of the MCNPX simulation with INCL4.6-ABLA07 compared to the ISOLDE data at 1.4 GeV for the total production yields of astatine isotopes. An average release time from the liquid metal of 10 hours has been assumed during which the radioactive decay of the different isotopes is taken into account. A remarkable agreement between the calculation and the experiment is observed, regarding not only the shape of the isotopic distribution but also the absolute release rates. Clearly, all the new features discussed in the preceding sections, in particular the better handling of low energy helium-induced reactions, have considerably improved the predictive capability of our model compared to the version used in [16].

In order to emphasise the importance of the secondary reactions induced by the clusters produced during the cascade stage through our coalescence mechanism, a calculation has been performed switching off this mechanism. The result is presented as the green curve and exhibits a severe deficit of heavy isotopes. Obviously, a model unable to emit high-energy helium nuclei cannot be expected to correctly predict astatine production in a LBE target, since only a small fraction of the heliums produced in the evaporation stage have enough energy to undergo a reaction before being stopped. This was the case of our first version INCL4.2, which is more or less mimicked by INCL4.6 without clusters, but also of the MCNPX default model option, Bertini-Dresner.

Figure 4: Astatine release rates from [16] at 1.4 GeV compared to MCNPX simulations, assuming an average release time of 10 hours, with INCL4.6-ABLA07 (red line), INCL4.6-ABLA07 in which the cluster production in the INC model was switched off (green line) and CEM03 (blue line) [17]
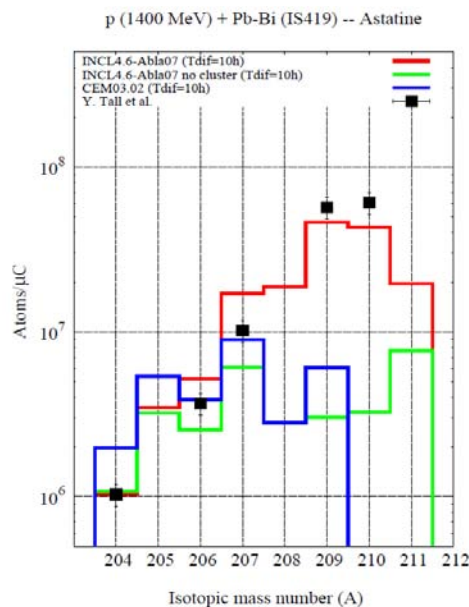
In the same figure, the results are also compared with CEM03 [18], which is also available in MCNPX2.7b (blue line), using the same assumption on the release time. It is interesting to note that this model is not able to account for the measured yield of the heavy astatine isotopes. In fact, CEM03 does have mechanisms to produce high-energy heliums but does not produce isotopes with mass larger than 209 probably because of an inappropriate treatment of low-energy helium induced reactions.

This study on astatine isotopes suggests that the production of isotopes due to secondary reactions can easily be severely underestimated by usual models used in transport codes and that our model, thanks to the attention paid to the emission of high-energy clusters and to low-energy cluster induced reactions, can be considered as having a good predictive power for these isotopes.

Extension to light-ion induced reactions

The idea to extend our model to heavy-ion reactions has arisen from the need of predictive transport codes for applications such as hadron therapy and protection against radiation in space or near accelerators. Since the model is very successful in nucleon and composite particle induced reactions, it seemed natural to try to extend it to heavier projectiles. It is clear, however, that our model cannot aspire to describe collisions of two very heavy nuclei since it does not have physics ingredients allowing for instance the prediction of important collective effects. Therefore, we have limited the extension to ^{18}O projectiles. The goal is to provide an event-generator for high-energy transport codes, being able to calculate the characteristics of all particles and nuclei generated in a particular application, with a main focus on hadron therapy.

The model

The first INCL light ion extension [19] [20], based on the INCL4.2 version of the nucleon-induced reaction model, consisted of two main parts: handling of the projectile as a collection of individual nucleons and de-excitation of the projectile fragments after the reaction. The main cascade in the target nucleus is treated following the standard INCL cascade procedure as described in [1]. This version, translated to C++ and coupled with ABLA, has been included in GEANT4 [21]. In this approach, clearly the target and projectile are not treated symmetrically. If we try to interpret the reaction in the framework of a participant-spectator picture, the treatment of the target spectator and participant zone (where NN collisions happen) is satisfactory while the projectile spectator is obviously not correctly handled. When one is interested in fragments of the projectile, this deficiency is circumvented by reversing the reaction (i.e. the target impinging on the projectile) and then boosting it back to the laboratory frame.

Recently, the model has been revisited on the basis of the INCL4.6 version and totally re-written in C++. This light-ion extended version is denoted as INCL++ and has been implemented in the latest GEANT4 beta release (v9.6 beta).

Let us briefly describe its main features. The projectile is described as a bulk of (N, Z) nucleons in the ion rest frame whose positions and momenta are randomly chosen in a realistic r and p space density (gaussian), with the constraint that the vectorial sum equal to zero in both spaces, and then Lorentz-boosted. For each configuration the depth of a binding potential is determined so that the sum of the nucleon energies is equal to the tabulated mass of the projectile nucleus. The nucleons are no more on mass shell but the sum of energies and vector momenta are correct. The ion follows globally a classical Coulomb trajectory until one of its nucleon impinges on a sphere of calculation around the target nucleus, large enough to marginally neglect nuclear interactions. Considering the collective cluster velocity, some of the nucleons will never interact with this sphere and will be combined together in the "projectile spectator". All other nucleons are entering the calculation sphere. They move globally (with the beam velocity) until one of them interacts, being close enough to a target nucleon. The NN interaction is then computed with the individual momenta, and Pauli blocking is tested. Nucleons crossing the sphere of calculation without any NN interaction are also combined in the "projectile spectator" at the end of the cascade.

The projectile spectator nucleus is kinematically defined by its nucleon content and its excitation energy obtained by an empirical particle-hole model based on the energy configuration of the current projectile and the removed nucleons (interacting with the target). This nucleus is then given to a de-excitation model. It is quite clear that this "projectile spectator" has not received any explicit contribution from the zone of interaction which is entirely contained in the target remnant with two consequences: the calculation is not symmetric and the residue of the target should be more realistic than the "projectile spectator" at this stage of the model. In this model, energy and momentum are always conserved.

Comparison with elementary experimental data

In order to compare with experimental data, the INCL++ model has to be coupled to a de-excitation model. Our standalone version has been coupled to the Abla07 model [6], as the INCL4.6 fortran model. In Geant4, it is linked with the native de-excitation handler [22]. This handler, depending on the mass and the excitation energy of the excited nuclei provided by the cascade, chooses between three different statistical de-excitation models (a Fermi break-up model, an evaporation model or a multifragmentation model) to bring back the nuclei to their fundamental state. This allows comparing the respective merits of Abla07 and Geant4 de-excitation.

Neutron production

The calculation is still not symmetric although the projectile spectator is better treated than in the first version of our model. This means that, depending on the observable that one is interested in, the calculation should be done either in direct or in inverse kinematics. In Figure 5, left panel, we compare the model with neutron production cross-sections measured in the $^{12}C+^{12}C$ system at 290 MeV by Iwata *et al*. [25]. Calculations done using either inverse or direct kinematics are plotted. High-energy neutrons in direct kinematics are mostly arising from NN collisions in the INC model plus neutrons from the de-excitation of the projectile spectator, while in inverse kinematics they result from the de-excitation of the target remnant or are the low-energy partner in NN collisions. Globally, the inverse kinematics gives a better agreement.

Figure 5: Neutron production double differential cross-sections in the $^{12}C+^{12}C$ system at 290 MeV/u from [25] compared to INCL++ in Geant4 in direct and inverse kinematics (left) and to the former version, INCL4.3 and BIC, all coupled to the GEANT4 de-excitation handler
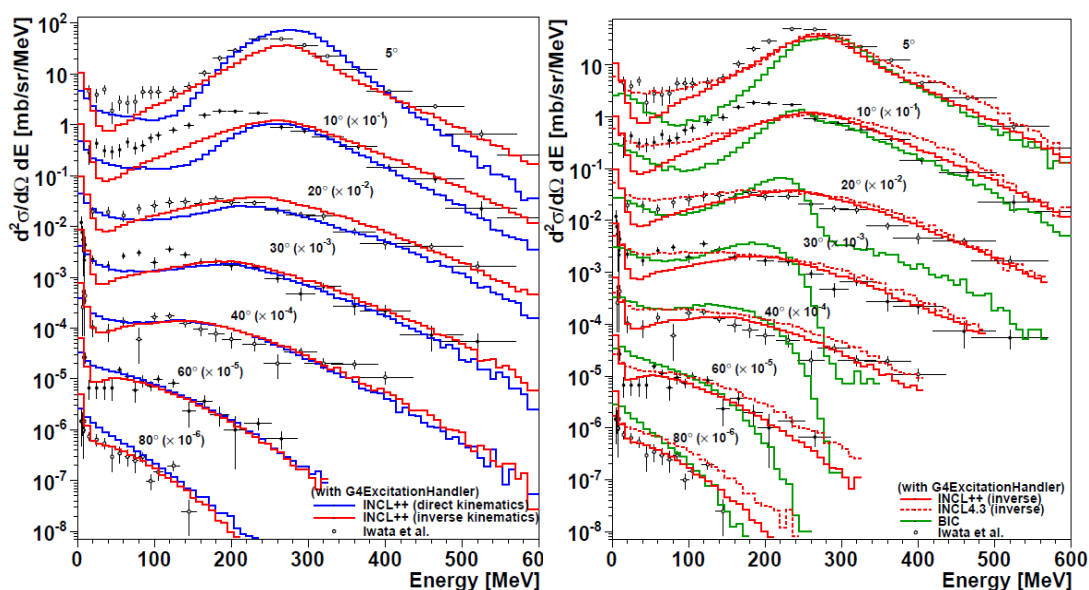
Figure 5, right panel, shows the comparison of the data with the present model, the former version INCL4.2, both in inverse kinematics, and to the binary cascade (BIC) from Folger *et al*. [23] also available in Geant4, all models being coupled to the Geant4 de-excitation handler. It can be observed that the new version of our model better reproduces the data than the former version and that BIC is definitely less good.

Residue production

Results on residue production are generally more sensitive to details of the models than particle production. In Figure 7, top panels, several sets of data concerning charge changing cross-sections from [26] are compared to our model, present and former versions, and to BIC. All are linked to the GEANT4 de-excitation handler. The experiment was devoted to the study of iron projectile fragmentation on a carbon target. Since the model is available only up to oxygen projectiles, the calculations have been performed in inverse kinematics. As said before, we expect our model to be better for the target remnant, i.e. precisely for projectile fragments in inverse kinematics. Generally, our model gives a better agreement with the data than BIC. However, some significant discrepancies can be noticed, especially for the lightest residues.

Figure 6: Charge changing cross-sections in the Fe+C system at 3 000 (left) and 500 MeV/u (right) from [26] compared with INCL++, INCL4.3 and BIC (top) and with INCL++ coupled to two different de-excitation models, ABLA07 and Geant4 de-excitation handler
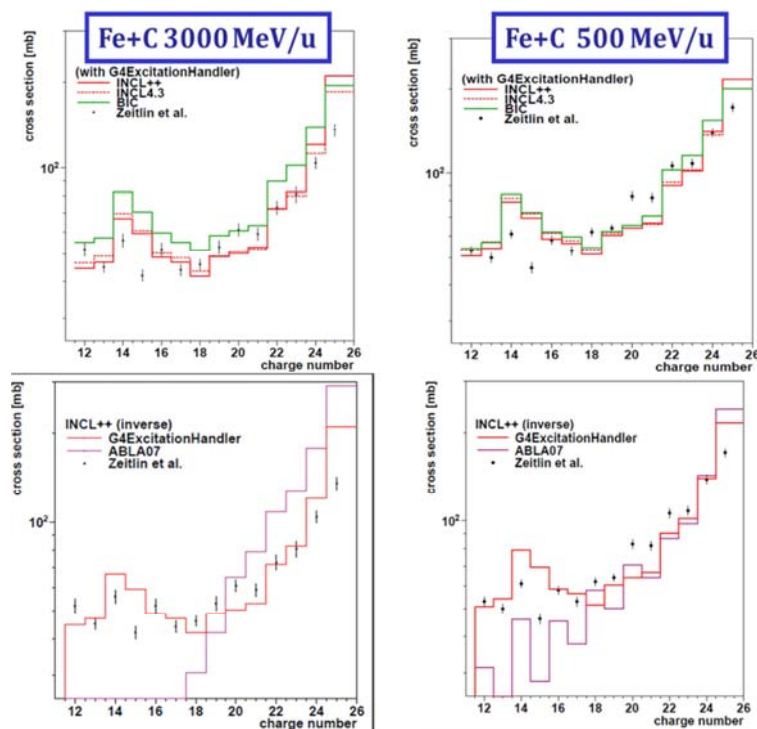
We have also compared the effect of the choice of the de-excitation model. This can be seen in Figure 7, bottom panels. Clearly the results are largely dependent on the choice: the Geant4 de-excitation gives the best fit to the experimental data while Abla07 has a problem in predicting light nuclei. This may be due to the fact that the model was up to now mainly tested, and therefore adjusted, on systems with excitation energies much smaller than the values reached in the cases studied here.

Comparison with thick target data

With the model implemented into Geant4, it is possible to perform simulations of experiments done with thick targets. In Figure 7, data from B. Braunn *et al.* [27], in which nuclear charge distributions from the fragmentation of a ^{12}C beam at 95 MeV/u as projectile have been measured with different thicknesses of PMMA targets are presented. We here only show the comparison of production rates for the 5 mm target at three different angles.

It can be observed that our model reproduces rather well the light ion cross-sections (up to Z=4) but tends to underestimates higher charges at forward angles while BIC overestimates these elements at 10° and 20°. Calculations done with the Geant4 Quantum Molecular Dynamic model (QMD) developed by Koi [24] are also shown and seem to give globally a slightly better agreement with the data. It should be stressed, however, that the CPU time needed to perform the simulation of the experiment is much longer in the case of QMD than with our model.

Figure 7: Nuclear charge distributions at different angles from a ^{12}C beam at 95 MeV/u interacting with a 5~mm PMMA target from [27] (red triangles) compared with INCL++ (blue crosses), BIC (blue circles) and QMD (blue squares)
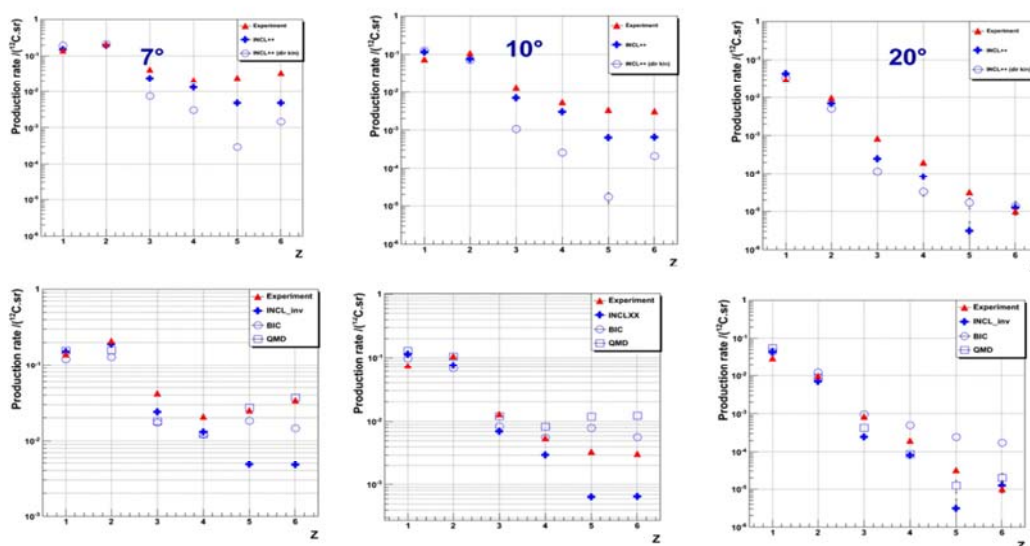
Conclusions

This paper presents the new capabilities of the Liège Intranuclear Cascade model, INCL4, which is now implemented into several high-energy transport codes. This allows the simulation of spallation targets. The example of the European Spallation Source (ESS) tungsten target was shown, for which a careful benchmarking of the code on W elementary cross-sections (excitation functions) allows assessing the uncertainty on the predictions of the most hazardous isotopes.

A study of the production of astatine (Z=85) isotopes in the ISOLDE (CERN) lead-bismuth target shows that our model, thanks to the coalescence mechanism in the intranuclear cascade model and to an improved handling of low-energy helium-induced reactions, correctly reproduces the measured astatine yields. More generally, this indicates that it is well-suited for predicting isotopes generated in secondary reactions.

The recent extension of the model to light ion induced reactions was also discussed. Although the treatment of target and projectile is not fully symmetric, but provided that the model is used with the kinematics (direct or inverse) most appropriate to the considered observables, it gives very satisfactory results when compared to different sets of experimental data. Being included in Geant4, it can be used to simulate thick target problem and gives results generally better than BIC and comparable or only slightly less good than QMD, but with a much shorter CPU time. Further improvements, in particular to make the model symmetrical for projectile and target, are in progress.

An extension to energies up to 10 GeV, which requests the adding of multipion [28] and strangeness production channels, is also in progress.

References

[1]   A. Boudard *et al.* (2002), *Phys. Rev. C* 66, 044615.

[2]   A.R. Junghans *et al.* (1998), *Nucl. Phys. A*, 629, pp. 635-655.

[3]   HINDAS. EC contract FIKW-CT-2000-00031, Final report. ed. J.P. Meulders, A. Koning, S. Leray, 2005.

[4]   FP6 Euratom Project EUROTRANS/NUDATRA (2004), EC contract number FI6W-CT-2004-516520.

[5]   A. Boudard, J. Cugnon (2008), *Proc. of the ICTP-IAEA Advanced Workshop on Model Codes for Spallation Reactions*, IAEA INDC(NDS)-0530, Vienna, August 2008, p. 29. http://www-nds.iaea.org/reports-new/indc-reports/indc-nds/indc-nds-0530.pdf.

[6]   A. Kelic et al. (2008), *Proc. of the ICTP-IAEA Advanced Workshop on Model Codes for Spallation Reactions*, IAEA INDC(NDS)-0530, Vienna, August 2008, p. 181.

[7]   J.C. David *et al.* (2010), Shielding Aspects of Accelerators, Targets and Irradiation Facilities, *SATIF 10 Workshop Proceedings*, Geneva, Switzerland 2-4 June 2010, p. 273.

[8]   S. Leray *et al.* (2011), *Journal of the Korean Physical Society*, Vol. 59, No. 2, August 2011, p. 791.

[9]   http:/www-nds.iaea.org/spallation.

[10] A. Boudard *et al.* accepted for publication in Phys. Rev. C.

[11] K. Niita *et al.* (2010), JAEA-Data/Code 2010-022.

[12] D.B. Pelowitz *et al.* (2009), MCNPX 2.7.B extensions, Los Alamos Report LA-UR-09-04130.

[13] S. Agostinelli *et al.* (2003), *Nucl. Instrum. Meth. A* 506, 250 – 303.

[14] A. Leprince *et al.* (2012), *Proceedings of the ICRS12 Conference*, Nara, 2-7 September 2012.

[15] D. Ene (2011), ESS Proposal for the source term definitions nuclides break down lists, private communication.

[16] Y. Tall *et al. Proceedings of the International Conference on Nuclear Data for Science and Technology,* 22-27 April 2007, Nice, France, Ed. O. Bersillon, F. Gunsing, E. Bauge, R. Jacqmin, S. Leray, EDP Sciences, 2008, p.1069.

[17] J.C. David *et al.* (2012), *Proceedings of the ICRS12 conference*, Nara, 2-7 September 2012.

[18] S.G. Mashnik *et al.* (2006), *J. Phys., Conf. Ser. 41, 340. Conf. on Physics of Reactors (PHYSOR96)*, Mito, Japan, 16-20 September 1996, pp. E161.

[19] A. Boudard et al. (2009), Proc. Int. Topical Meeting on Nuclear Research Applications and Utilization of Accelerators, Vienna, Austria, 5-8 May 2009.

[20] P. Kaitaniemi *et al.* (2011), *Progress in Nuclear Science and Technology*, Vol. 2, pp.788.

[21] A. Heikkinen, P. Kaitaniemi, A. Boudard (2008), *J. Phys. Conf. Ser.,* 119, 032024.

[22] J.M Quesada et al. (2011), Progress in Nuclear Science and Technology, Vol. 2, pp.936-941.

[23] G. Folger, V.N. Ivanchenko, J.P. Wellisch (2004), *Eur. Phys. J. A* 21(3), 407–417.

[24] T. Koi (2008), *Proc. IEEE 2008 Nuclear Science Symposium,* Dresden, Germany, 19-25 October 2008.

[25] Y. Iwata *et al.* (2001), *Phys. Rev. C* 64, 034607.

[26] C. Zeitlin *et al.* (2008), *Phys. Rev. C* 77, 034605.

[27] B. Braunn *et al.* (2011)*, Nucl. Instrum. Meth. B* 269, 2676.

[28] S. Pedoux *et al.* (2011), *Nucl. Instrum. Meth. B* 269, 2676.

Design of an experimental method for measurement of isotopic fragmentation cross-section energy dependence of nucleus-nucleus collisions

Tatsuhiko Ogawa[1], Morev N. Mikhail[2], Tatsuhiko Sato[1]
[1]Japan Atomic Energy Agency
[2]Science and Engineering Center for Nuclear and Radiation Safety, Russian Federation

Abstract

We have developed a method to measure isotopic fragmentation reaction cross-sections as excitation functions in a single heavy ion irradiation experiment. The method consists of measurement of velocity, dE/dx and kinetic energy of projectile fragments originated in a thick target bombarded by mono-energetic heavy ions. Identifying isotopic identity by ΔE-E method and measuring kinetic energy by TOF method, isotopic fragmentation cross-sections are obtained as a function of energy. This method was tested against the simulation by FLUKA for a bombardment of 400 MeV/u ^{16}O on a thick carbon target. The result shows cross-sections for production Li, Be, B, and C from ^{16}O are successfully obtained above about 50 MeV/u as a function of energy.

Introduction

Heavy ion accelerators are becoming more and more important in the field of material science, medicine, etc. Their growing importance is particularly valuable in cancer therapy. Many hospital-based intermediate energy (a few hundreds of MeV/u) heavy ion accelerators are operated or constructed for application in cancer radiation therapy worldwide[1]. One of the key issues in the application of intermediate- or high-energy heavy ions is fragmentation reactions. In heavy ion radiotherapy, fragments of primary ions are transmitted beyond the range of primary ions, giving undesired doses to healthy tissues. Therefore, fragmentation reactions of light nuclei are the key to the precise evaluation of particle therapy dose.

A lot of experiments to measure fragmentation cross-sections with respect to mass yield and charge distribution have been published[2-7]. However, some data on energy dependence of fragmentation reaction cross-sections is available[8-9]. The stacked-foil method is commonly used to obtain fragmentation cross-section as a function of energy in interactions of protons with various materials[10]. Unfortunately, the stacked-foil method cannot be applied to the fragmentation of light nuclei because most light nuclei are gas at room temperature and the activation products are short-lived.

In this study we developed a method to measure fragmentation reaction cross-sections as a continuous function of energy using a scintillator telescope consisting of three scintillators. In order to validate the performance of the telescope detector, radiation transport simulation was carried out with FLUKA[11,12] in a system including a thick carbon target irradiated with 400 MeV/u ^{16}O ions and a telescope detector. By analysing the energy deposition in the scintillators by fragments of ^{16}O, charge and mass of the fragments are identified. Furthermore, by converting the TOF spectra of each fragment species, fragmentation cross-sections are obtained as a function of energy.

Method

Theoretical basis of detection

In fragmentation reactions, the part of the nucleus involved in the collision with another nucleus is referred to as a participant, while the rest is referred to as a spectator. Because the projectile spectators do not directly interact with the target nucleus, the momenta of nucleons in the projectile spectator are mostly conserved. In addition, the stopping power of the projectile fragments is also smaller than that of the projectiles. Furthermore, in a target bombarded by mono-energetic ion beam, projectile beam is quasi-mono-energetic at arbitrary depths because of little statistical fluctuation of the stopping power. Assuming that the projectiles and fragments have no energy straggling, and the average momentum of the nucleons in the projectile spectators is completely conserved before and after fragmentation, the energy of projectiles at fragmentation reaction E_r satisfies the formula:

$$t = \int_{E_r}^{E_0} \frac{1}{s_p(E)} dE \; + \; \int_{E_e}^{E_r} \frac{1}{s_f(E)} dE \tag{1}$$

where t is the thickness of the target, E_0 is the kinetic energy of incident primary ions, s_p is the stopping power of primary ions in the target, E_e is the fragment energy after penetrating the target and s_f is the stopping power of fragments in the target. By solving the Equation (1), E_r is obtained as a function of E_e.

By measuring the kinetic energy of each fragment behind the target (E_e) and using Equation (1), one can obtain fragmentation cross-section as a function of energy:

$$\phi\sigma_f\left(E_f\right)\frac{dE_f}{dz}dz\,Exp\left(-n\int_{E_f}^{E_0}\sigma_{l,p}\left(E\right)\frac{1}{s_p\left(E\right)}dE-n\int_{E_e}^{E_f}\sigma_{l,f}\left(E\right)\frac{1}{s_f\left(E\right)}dE\right)=\frac{dN\left(E_e\right)}{dE_e}\frac{dE_e}{dE_f}dE_f$$

(2)

where φ is the incident primary ion flux, σf is the fragmentation cross-section, Ef is the energy at fragmentation reaction, z is the depth inside the target, n is the atomic density of the target, σl,p is the total reaction cross-section of primary ions, sp is the stopping power of projectiles, σl,f is the total reaction cross-section of fragments, sf is the stopping power of fragments, N(E) is the number of fragments with kinetic energy E behind the target, and Ee is the energy of the fragments behind the target.

It should be noted that the conversion described as Equation (2) has to be applied to each fragment isotopic species (i.e. fragment charge and mass have to be distinguished prior to the conversion). Therefore the detection system has to be capable of detecting (a) kinetic energy, (b) charge, and (c) mass of the fragments behind the target. The detector system which satisfies the above performance requirements is illustrated in Figure 1.

Figure 1:Schematic diagram of the detector system configuration
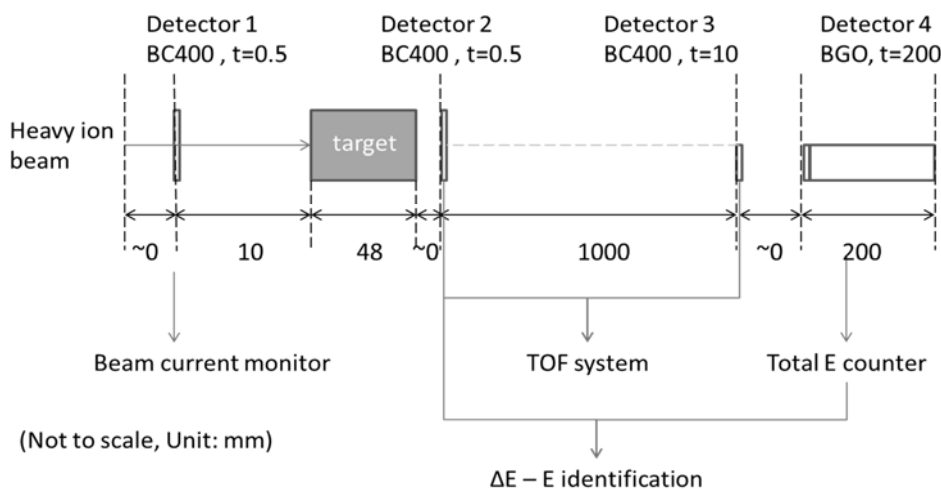
The most upstream detector serves as a beam current monitor to normalise the measured quantities by the primary ion beam intensity. The second most upstream detector placed just downstream the target is used as TOF start detector. The signal from the third detector is used as both a TOF end signal and a dE/dx signal. The most downstream thick BGO detector is used to measure total kinetic energy of the fragments. The properties of the detectors are summarised in Table 1.

Table.1 Properties and functions detector

	Detector type	Thickness (mm)	Function
Detector #1	Plastic (BC400)	0.5	Beam current monitor
Detector #2	Plastic (BC400)	0.5	TOF start detector
Detector #3	Plastic (BC400)	10	TOF end detector/ ΔE counter
Detector #4	BGO	200	Total E counter

From the second and third detector outputs, the kinetic energy of fragments in MeV/u is obtained by TOF method. The signals from the third and fourth detector outputs are used for isotope identification by ΔE-E method. Although it is often the case that more

than one projectile fragments reach detectors, the largest fragment among all the projectile fragments is focused.

Validation simulation

In order to verify the performance of the telescope detector explained above, energy deposition by fragments in the scintillators was simulated by FLUKA-2011 and the energy depositions in each event were analysed to obtain the kinetic energy, mass and charge of the fragment. The obtained excitation functions of fragmentation reactions (referred to as telescope cross-sections hereafter) were compared with the cross-sections directly calculated with FLUKA (referred to as FLUKA cross-section hereafter). The method of calculating the telescope cross-sections is described below.

In the simulation, a carbon (density: 2.00 g/cm^3) target with a thickness of 4.8 cm was irradiated by 400 MeV/u ^{16}O ions (the geometry is shown in Figure 2). BC400 plastic scintillator of 0.5 mm thickness (counter 1) was placed immediately downstream the target and 20 cm thick BGO detector (counter 2) was placed 1 m downstream counter 1. Nucleus-nucleus interaction model RQMD[13] and the statistical decay model of PEANUT was applied to simulate fragmentation reactions.

Because the stopping power of nitrogen fragments is so close to that of primary ^{16}O ions, E_e calculated with Equation (1) is close to zero. Therefore, the method was not applied for N isotopes. In addition, helium and hydrogen fragments are so penetrating and have such a large angular spread that the total energy cannot be measured by counter 2. Therefore, their production cross-sections were not analysed.

The timing of the TOF end signal was defined to be the peak of signal in counter 2 to detect the largest projectile fragment. The peak signal is insensitive to unimportant fragments such as light projectile fragments and evaporated fragments.

In order to take into account the losses of the projectile fragments by inelastic reactions inside target, fragmentation cross-sections were corrected for the secondary reaction losses by substituting $\sigma_{l,p}$ and $\sigma_{l,f}$ in Equation (2) with the total fragmentation cross-section parameterised as Kox's formula[14]. The stopping power and the range of the fragments in Equation (2) were calculated by SPAR[15]. For simplification, the energy straggling and the range straggling of neither primary ions nor the fragments were taken into account.

Figure 2: Schematic diagram of the simulation geometry
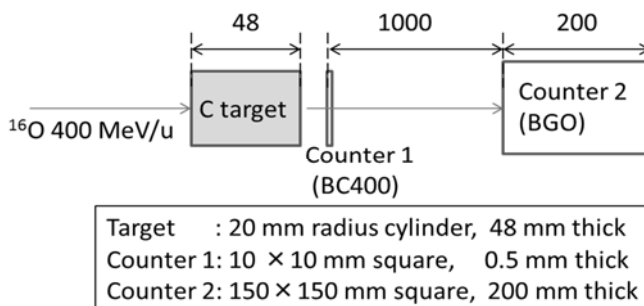
Results

Figure 3 shows a three-dimensional scatter plot of kinetic energy obtained from TOF, ΔE counter output and the total E counter output. This result shows charge can be clearly identified by this method and mass is also identified subject to a few % of energy resolution. It is also shown that 200 mm thick BGO cannot stop some portion of helium fragments.

Figure 3: TOF, ΔE counter signal and total E counter signal output
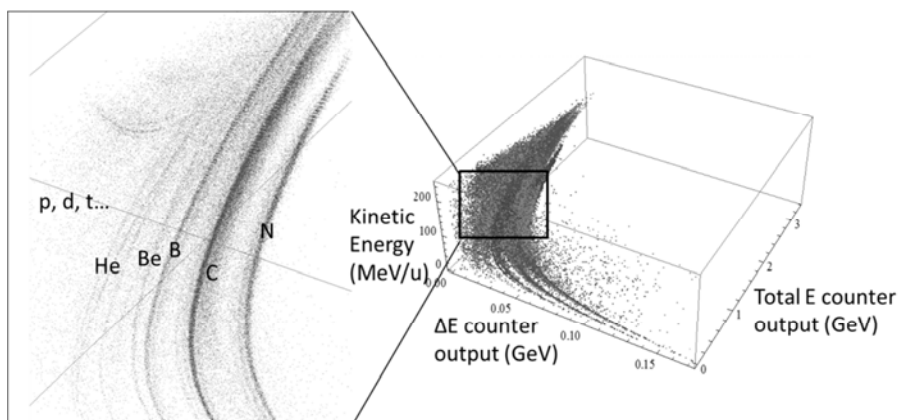
To obtain telescope cross-sections, the kinetic energy of fragments behind the target measured by TOF was converted to reaction energy by Equation (2) for each isotope species. Some typical excitation functions are plotted in Figures 4-7. The fluctuation of telescope cross-sections is attributed to statistical uncertainty.

Figure 4: Calculated fragmentation cross-sections for ^{13}C production
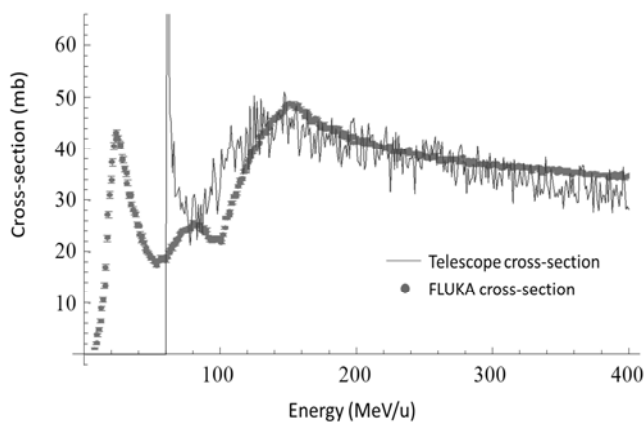
Figure 5: Calculated fragmentation cross-sections for ^{11}B production
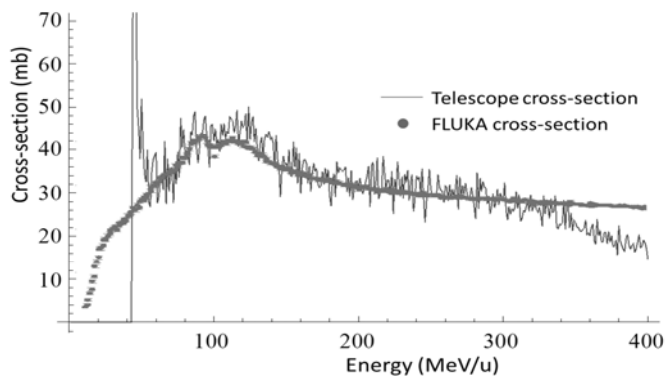
Figure 6: Calculated fragmentation cross-sections for ^{9}Be production
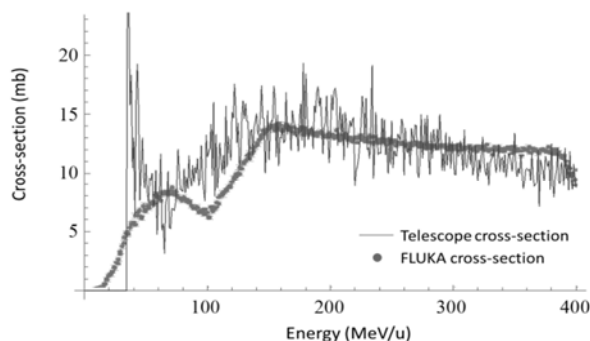
Figure 7: Calculated fragmentation cross-sections for ^{6}Li production
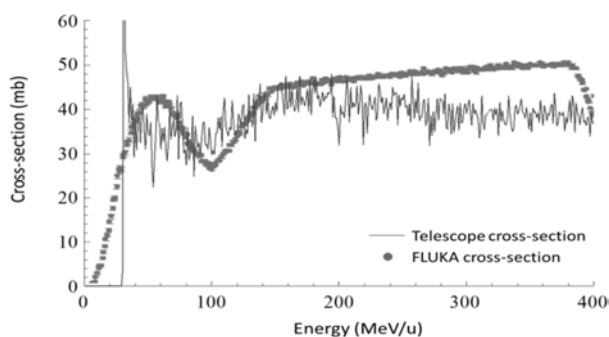
The telescope cross-sections well agree with FLUKA cross-sections down to a few 10 MeV including the fluctuating structure near 100 MeV/u. All the telescope cross-sections have a sharp rise and drop near the detection low-energy threshold, which are not seen in the FLUKA cross-sections.

Discussion

The truncation of cross-sections at a few tens of MeV is attributed to the stopping of fragments by counter 1 and air along the TOF path. In the case of ^{11}B production, correlation between reaction energy and energy behind the target calculated by Equation (1) is shown in Figure 8.

Figure 8: Reaction energy and ^{11}B fragment kinetic energy behind the target
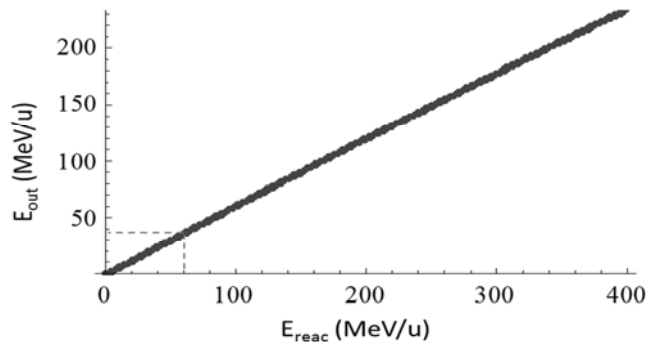
The horizontal axis and vertical axis show the kinetic energy of fragment at the time of fragmentation reaction and the kinetic energy of fragment behind the target, respectively. According to Figure 8, ^{11}B fragments produced at 80 MeV/u have a kinetic energy of about 40 MeV/u after penetrating the target. Because the stopping power of the air and that of counter 1 is large enough to stop 40 MeV/u ^{11}B, scintillation signals are not invoked in counter 2. As a result, ^{11}B production events below 80 MeV/u are not detected. By this mechanism, telescope cross-sections are truncated below fragment specific threshold energies.

In Figures 4-7, a discontinuous rise of cross-sections is observed just above the detection threshold in all the cases. This rise is attributed to evaporated fragments. In general, fragments evaporated inside the target have such small kinetic energy that they cannot reach the counters. However, near the end of the target, evaporated fragments escaping from the downstream surface of the target can reach the counters. Furthermore, the counters cannot distinguish evaporated fragments from projectile fragments. Therefore, projectile fragments and corresponding cross-sections are overestimated near the detection threshold.

The underestimation of cross-sections near 400 MeV/u typically seen in Figure 7 is attributed to the energy spread of fragments. The kinetic energy of projectiles and that of fragments averaged over constituent nucleons is ideally equal, however, due to the Fermi motion of nucleons in the projectiles and the interaction between nucleons during fragmentation reactions, fragment kinetic energy deviates from the projectile kinetic energy[13]. One example of energy scattering is illustrated in Figures 9 and 10. The production of fragments with kinetic energy less than 10 MeV/u is attributed to evaporation, which are beyond the scope of this study. On the other hand, the fragments with energy close to the projectile energy are projectile fragments. The mean energy of projectile fragments is almost equal to the projectile energy. However, the distribution of projectile fragment kinetic energies has a noticeable variation. Therefore, some of the projectile fragments produced from 400 MeV/u projectile have a kinetic energy less than 400 MeV/u and they do not contribute to cross-sections at 400 MeV/u. As a result, cross-sections are underestimated near 400 MeV/u due to the variation of the fragment kinetic energy.

**Figure 9: Projectile kinetic energy and fragment (^{8}B) kinetic energy
in 400 MeV/u ^{16}O ion irradiation to a thick carbon target**
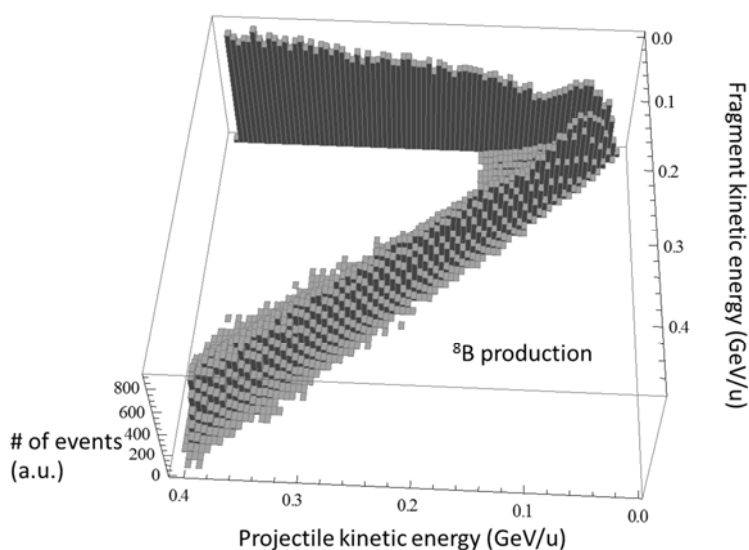
Figure 10: 2D projection of projectile kinetic energy and fragment (^{8}B) kinetic energy in 400 MeV/u ^{16}O ion irradiation to a thick carbon target
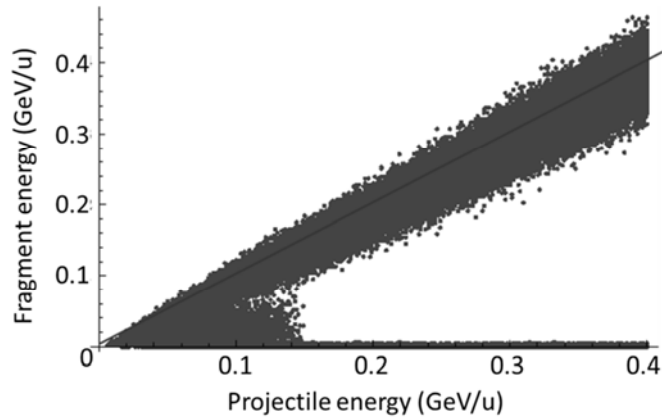
As shown in Figures 11 and 12, production cross-sections for neutron deficient fragments and ^{12}C are underestimated by a factor of more than three due to coincidence with ^{4}He fragments.

Figure 11: Calculated fragmentation cross-sections for ^{13}N production
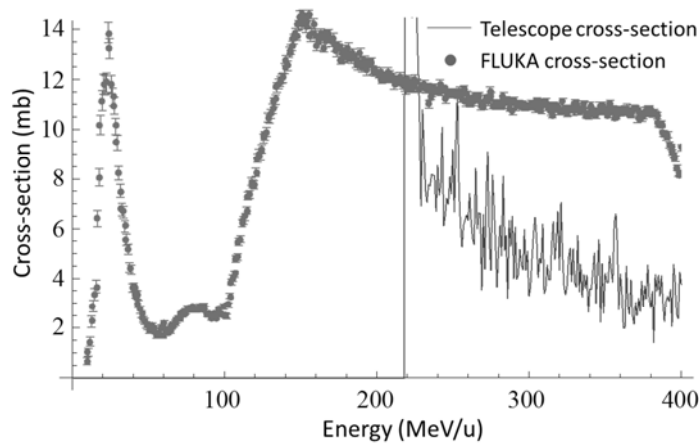
Figure 12: Calculated fragmentation cross-sections for ^{12}C production
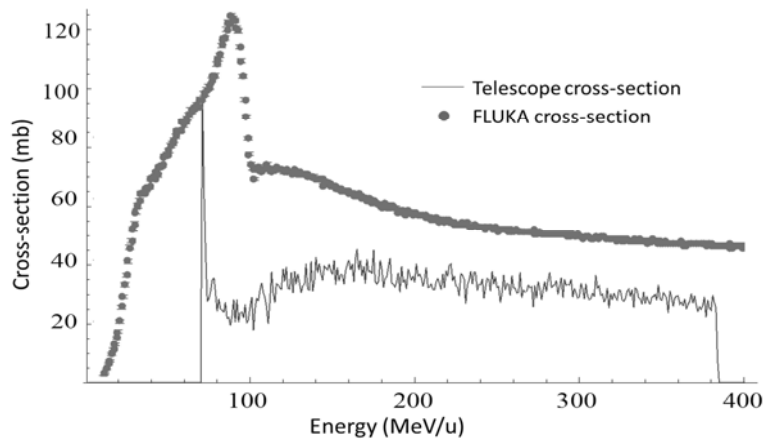
The mechanism of the coincidence loss is briefly illustrated in Figure 13. The coincidence is attributed to the fragmentation reaction channel expressed as $^{16}O(^{Nat}C, \alpha$ x)X (both α and x are projectile fragments). In this type of reaction, fragments of interest are fragments denoted as x (adjoint fragment, hereafter) which has the largest mass and charge among the projectile fragments. Transmitting the target and TOF path, the ^{4}He ions deposit their energy in counter 2. In the meantime, the adjoint fragments also travel inside the target and the TOF path. Because ^{12}C or neutron deficient fragments produced as adjoint fragments lose energy much more than ^{4}He ions, the total energy deposition in counter 2 is dominated by ^{4}He. As a result, energy deposition by the adjoint fragment cannot be identified and adjoint fragments are underestimated. As illustrated in Figure 13, adjoint fragments cannot be observed regardless of the trigger condition in counter 2. According to FLUKA simulation, this coincidence is meaningful for ^{13}N, ^{12}C, ^{11}C and ^{10}C, which have (1) a neutron number smaller than the proton number and (2) a proton number greater than 6. The reason why ^{12}C is significantly affected by the coincidence with ^{4}He is projectile fragmentation reaction $^{16}O \rightarrow ^4He + ^{12}C$. In addition to the above nuclei, cross-sections for nuclei lighter than ^{9}C and those lighter than ^{13}N are probably affected by the coincidence with ^{4}He, however, it was unclear due to large statistical uncertainty. Coincidence loss of similar mechanism by other light charged particles (e.g. ^{3}H, d, etc) was not observed probably because of their small production cross-sections or small energy deposition.

Figure 13: Example of coincidence loss of projectile fragment with ^{4}He; X denotes the adjoint fragment
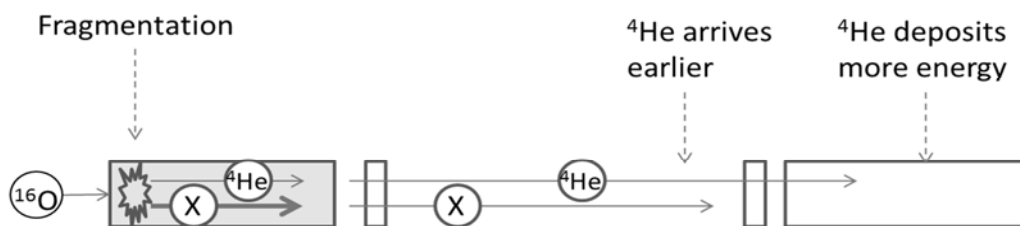
Conclusion

An experimental technique to measure excitation functions of nucleus-nucleus fragmentation reaction was developed in this study. By bombarding a thick target with relativistic energy projectiles and detecting the projectile fragments escaping from the target using a scintillator telescope, the isotopic identity of fragments and projectile energy at the reaction can be determined.

Measurement of $^{16}O(^{Nat}C, X)$ fragmentation cross-sections by this method was simulated with FLUKA. By simulation, fragment charge and mass are distinguished subject to energy resolution better than 10% and cross-sections are obtained generally within a few 10%.

The cross-sections are underestimated in three cases: (1) cross-sections below isotope-dependent detection threshold, (2) production of light fragments near incident energy and (3) fragments with charge larger than 5 and neutrons less than protons due to different mechanisms. Therefore, the cross-sections for fragments not affected by the above underestimation mechanism can be measured by the method developed in this study.

References

[1]   A. Kitagawa *et al*. (2010), "Review on heavy ion radiotherapy facilities and related ion sources (invited)", *Review of Scientific Instruments* 81, 02B909.

[2]   G. D. Westfall *et al*. (1979), "Fragmentation of relativistic 56 Fe", *Phys. Rev*. C, 19, 1309-1323.

[3]   N. T. Porile *et al*. (1979), "Nuclear reactions of silver with 25.2 GeV 12 C ions and 300 GeV protons", *Phys. Rev*. C, 19, 2288-2304.

[4]   J. R. Cummings *et al*. (1990), "Determination of the cross sections for the production of fragments from relativistic nucleus-nucleus interactions. I. Measurements", *Phys. Rev*. C, 42 2508-2529.

[5]   J. Benlliure *et al*. (1998), "Production of medium-weight isotopes by fragmentation in 750 A MeV 238 U on 208 Pb collisions", *Euro. Phy. J. A*, 2 193-198.

[6]   S. Cecchini *et al*. (2002), "Fragmentation cross sections of 158 A GeV Pb ions in various targets measured with CR-39 nuclear track detectors", *Nucl. Phys. A*, 707, 513-524.

[7]   C. Scheidenberger *et al*. (2004), "Charge-changing interactions of ultrarelativistic Pb nuclei", *Phys. Rev. C*, 70, 014902.

[8]   J. R. Cummings *et al*. (1990), "Determination of the cross-sections for the production of fragments from relativistic nucleus-nucleus interactions. II. Parametric fts", *Phys. Rev. C*, 42, 6, 2530-2545.

[9]   H. Yashima *et al*. (2002), "Projectile dependence of radioactive spallation products induced in copper by high-energy heavy ions", *Phys. Rev. C,* 66 044607.

[10] R. Michel *et al*. (1997), "Cross sections for the production of residual nuclides by low-and medium-energy protons from the target elements C, N, O, Mg, Al, Si, Ca, Ti, V, Mn, Fe, Co, Ni, Cu, Sr, Y, Zr, Nb, Ba and Au", *Nucl. Instr. Meth. B*, 129, 2, 153-193.

[11] A. Ferrari *et al*. (2005), "FLUKA: a multi-particle transport code", CERN 2005-10, INFN TC 05/11, SLAC-R-773.

[12] G. Battistoni *et al*. (2007), "The FLUKA code: Description and benchmarking", Proceedings of the Hadronic Shower Simulation Workshop 2006, 31-49.

[13] A. S. Goldhaber (1974), "Statistical models of fragmentation processes", *Physics Letters B*, 53, 306.

Origin and chemical behaviour of radionuclides observed in the cooling water for magnetic horns at the J-PARC Neutrino Experimental Facility

**Kotaro Bessho, Hiroshi Matsumura, Masayuki Hagiwara, Kazutoshi Takahashi,
Asako Takahashi, Hiroshi Iwase, Kazuyoshi Masumoto, Hideaki Monjushiro,
Yuichi Oyama, Tetsuro Sekiguchi, Yoshikazu Yamada**
High Energy Accelerator Research Organization, KEK, Japan

Abstract

Radionuclides, including ^{3}H, ^{7}Be, and ^{22}Na, are produced by high-energy nuclear reactions in the cooling water used to cool magnetic horns at the Japan Proton Accelerator Research Complex (J-PARC) Neutrino Experimental Facility. The origin of each nuclide is discussed by comparing the experimentally determined concentrations with results from PHITS calculations. The chemical behaviour of the radionuclides in water is dependent on the element being considered. Certain nuclides exhibit complex behaviour and become distributed inhomogeneously in the water-circulation system. In particular, ^{7}Be nuclides, dominant gamma-ray emitters in the cooling-waters, exist in the water as both water-soluble ions and colloidal species. After passing through the deionizer, some amount of ^{7}Be remains in the water, mainly as colloidal species. In addition, ^{7}Be tends to adsorb on the metal piping and metallic components of the circulation system. The behaviour of ^{7}Be contrasts with that of ^{3}H (or T), which exists as tritiated water (HTO) and distributes homogeneously throughout the water cooling system.

Introduction

The T2K experiment is a long-baseline neutrino oscillation experiment carried out using the neutrino beam produced at the Japan Proton Accelerator Research Complex (J-PARC), Tokai, Japan [1] [2]. The experiment is designed to investigate how neutrons change from one flavour to others as they travel [3]. In this experiment, an artificial neutrino beam produced at the J-PARC Neutrino Experimental Facility is shot towards the neutrino observatory Super-Kamiokande, which is 295 km away in Gifu, Japan. At the neutrino experimental facility, a graphite target (26 mm x 900 mm) is bombarded with 30-GeV protons. Secondary charged-pions are focused using three types of magnetic horn. A schematic diagram of the first magnetic horn and the graphite target is shown in Figure 1 [4]. The magnetic horns consist of two coaxial (inner and outer) conductors made of aluminum alloy A6061. Cooling water is sprayed through the enclosed region between the two coaxial conductors, as indicated in Figure 1. Intense high-energy protons, neutrons, and pions produce various radionuclides in the cooling water as a result of high-energy nuclear reactions.

At the J-PARC Neutrino Experimental Facility, the cooling water for the magnetic horns is refreshed every 1 to 2 months, after each experimental run. The concentrations of radionuclides in the drainage water are monitored to ensure that levels are below the regulatory limits [5]. To keep the levels of radionuclides low, it is important to understand their behaviour in water and reduce their radioactivity.

In this work, the production and behaviour of radionuclides in the cooling water for magnetic horns were examined by experiments and calculations. The specific activities of γ-emitting nuclides and ^{3}H in the cooling water were measured. The chemical behaviour of ^{7}Be was also investigated. The production of various radionuclides in the cooling water and in the metal components was estimated using the multi-purpose Monte Carlo Particle and Heavy Ion Transport code System, PHITS [6]. The concentrations of individual nuclides observed in the circulating cooling water were compared with estimations from PHITS calculations in order to understand the origin and behaviour of nuclides in the cooling water system.

Figure 1: Schematic diagram of the first magnetic horn and graphite target used at the J-PARC Neutrino Experimental Facility
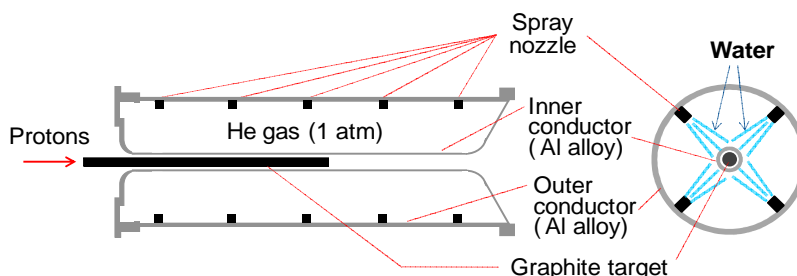
Radioactivity measurements of the cooling water

Magnetic horn cooling water system

A schematic diagram of the cooling water system used to cool the magnetic horns at the J-PARC Neutrino Experimental Facility is shown in Figure 2. Highly purified water passes through three types of magnetic horns, a surge tank (900 L), and heat-exchanger units as it circulates around the cooling water system at 160 L/min. The total volume of water circulating is 2 700 L. The cooling system is equipped with a deioniser which contains a mixture of cation and anion-exchange resins. During beam operation, the water path through the deioniser is closed. When the beam is not in operation, a part of water flows through the deioniser at a rate of 16 L/min. This flow removes macroscopic

amounts of ionic impurities and trace amounts of radionuclides including [7]Be by the ion-exchange process.

Figure 2: Schematic diagram of the cooling water system used in the magnetic horns at the J-PARC Neutrino Experimental Facility
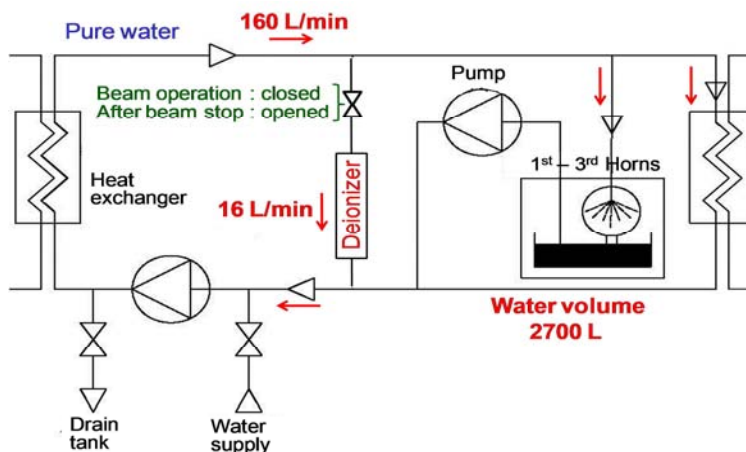
Sampling of cooling water

Cooling water samples were collected in polyethylene bottles immediately after two experimental runs. The first collection was carried out in December 2010 (Run 36), and the second, in February 2011 (Run 37). The number of protons incident on the graphite target (pot) was 4.27×10^{19} and 5.77×10^{19} for Runs 36 and 37, respectively. The maximum power of the proton beam during the two experimental runs was 150 kW.

Measurements of radioactivities in the cooling water

Determination of γ-ray emitting nuclides was carried out on 50 mL samples, which had been acidified with 0.1%(v/v) sulfuric acid. The samples were placed in plastic containers (inner diameter (ID) = 50 mm, height of water = 25 mm). Measurements of the γ-ray spectra were carried out using a high-purity germanium (HPGe) detector. The counting efficiency of the detector was calibrated using a mixed γ-ray source.

The concentration of ^{3}H was determined using a liquid scintillation counter and 1 ml of the sample was mixed with 7 to 20 ml of the scintillation cocktail for the measurements.

Radionuclides observed in the cooling water

Gamma-ray measurements of the cooling water were carried out immediately after the beam operation had stopped. Figure 3 shows the gamma-ray spectrum for cooling water measured 11.7 h after the beam was turned off (Run 37). Strong γ-ray peaks were observed at 478 keV and 511 keV. These peaks correspond to [7]Be and annihilation γ-rays result from short-lived nuclides e.g. [11]C and [13]N. Many other γ-ray peaks were also detected. The γ-emitting nuclides (half-life > 1 h) observed in the spectra of Figure 4 are [7]Be, [24]Na, [56]Mn, [52]Mn, [42]K, [58]Co, [22]Na, [28]Mg, [43]K, [54]Mn and [110m]Ag. The specific activities of the detected γ-nuclides and ^{3}H are summarised in Table 1. The activity of each nuclide is corrected according to the time at which the beam was turned off (beam-stop time).

**Figure 3: Gamma-ray spectrum of the cooling water from Run 37
at the J-PARC Neutrino Experimental Facility**
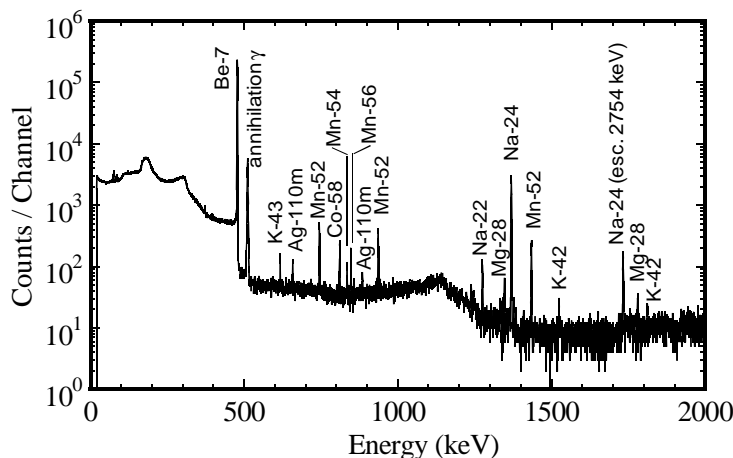
The measurement was carried out on 2011/2/28 at 16:43 (Live time: 2 171 s). The beam (pot 5.77 × 10^{19}) was stopped at 05:00 on 28/2/2011.

**Table 1: Specific activities of γ-emitting radionuclides and ^{3}H observed in the cooling water after
it had passed through the magnetic horns at the J-PARC Neutrino Experimental Facility**

Radionuclide	Half-life	Specific activity*(Bq/ml)
^{7}Be	53.3 d	9 100
^{3}H	12.3 y	2 000
^{24}Na	15.0 h	94
^{56}Mn	2.58 h	34
^{52}Mn	5.59 d	5.2
^{42}K	12.4 h	4.5
^{58}Co	70.9 d	1.8
^{22}Na	2.60 y	1.5
^{28}Mg	20.9 h	1.6
^{43}K	22.2 h	0.9
^{54}Mn	312 d	0.6
^{110m}Ag	250 d	0.5

* Corrected to the beam-stop time (2011/2/28 5:00).

The specific activities of ^{3}H and ^{7}Be are exceptionally high compared to other nuclides. The ^{3}H and ^{7}Be are produced by spallation of O atoms in water molecules. Other nuclides are produced in the metal components and then transferred to the water phase by chemical processes such as corrosion or dissolution of the solid surfaces, and/or physical processes such as recoil reactions. The metal components in contact with the water include the Al alloy A6061 horn (Al ~97%, Mg, Si, Fe, Cu, Mn, Cr, Ti), water pipes made from SUS 304 stainless steel (Fe, Cr, Ni), the SUS 316 stainless steel (Fe, Cr, Ni, Mo) heat-exchanger, and silver (Ag) and copper (Cu) plating and coatings.

Chemical behaviour of ^{7}Be in the cooling water

The chemical form of ^{3}H (or T) observed in the cooling water at the accelerator facilities has been found to be tritiated water (HTO) which behaves the same as ordinary water (H_2O) molecules. In contrast to ^{3}H, the form of ^{7}Be in the cooling water has not been previously clarified experimentally. In the planning and construction of experimental facilities, it is assumed that all the ^{7}Be produced in the cooling water exists in the form of cations [Be^{2+}, Be (OH)$^+$], which adsorb on the ion-exchange resins. In order to study the

adsorption behaviour of ^{7}Be on the ion-exchange resins, the cooling water was sampled at appropriate time intervals as it passed through the deioniser, and the ^{7}Be activities in the water were measured.

Figure 4 shows the relationship between the circulation time through the deioniser and the specific activity of ^{7}Be in the water measured after Runs 36 and 37. Initially, the specific activities of ^{7}Be decrease exponentially in accordance with the expectation function. This implies that most of the ^{7}Be is collected by the deioniser at the beginning of the water circulation cycle. After 90% of the ^{7}Be is removed from the water (circulation >10 h), the decreasing slope becomes more shallow. After several tens of hours of circulation, small amounts of ^{7}Be remain in the water. This implies that adsorptivity of ^{7}Be on ion-exchange resins becomes weak after long hours of circulation through the deioniser.

In order to understand the behaviour of ^{7}Be in deionisation processes, the soluble and colloidal fractions of ^{7}Be in water were determined using ultrafiltration experiments. In these experiments, very fine filters (pore size ≈ 3 nm) were used. After the beam has stopped, but before deionisation has started, the colloidal fractions of ^{7}Be are less than 1%. This increases to 15–40% after several tens of hours of deionisation, where the percentage depends on the beam operation and water-circulation conditions. These results imply that the adsorptivity of ^{7}Be on the ion-exchange resin is closely related to the formation of ^{7}Be colloids and that the removal of colloidal ^{7}Be by the deioniser does not progress efficiently compared to the removal of soluble ^{7}Be ions by the deioniser. Thus, the formation of radionuclide colloids in the cooling water is an important subject in radiation control at high-energy accelerator facilities. At present, further experimental studies are being carried out to clarify the mechanisms involved in colloid formation in intense radiation environments.

Figure 4: Specific activity of ^{7}Be in the cooling water for magnetic horns at the J-PARC Neutrino Experimental Facility as a function of circulation time through the deionisation unit
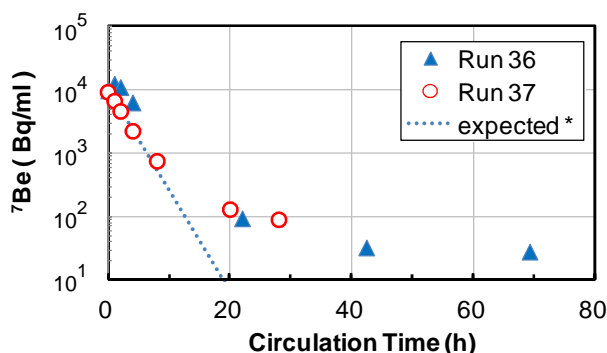
(* line) The expected concentration dependence of ^{7}Be, assuming that all the ^{7}Be in the water is removed when it passes through the deioniser.

PHITS calculations

Calculation method

The water passing between the inner and outer conductors of the first magnetic horn is exposed to intense high-energy particles originating from the graphite target. Therefore, most of the radionuclides can be expected to be produced in the water in the first magnetic horn. The spatial distribution of high-energy hadrons inside and near the first magnetic horn, the energy spectra of the hadrons, and the production of radionuclides in the water and surrounding experimental apparatus were calculated using the PHITS calculation code [6]. Figure 5 shows the simplified model used in the calculations. In the experimental system, water was sprayed into the inner conductor from nozzles placed on the outer conductor. The gap between the two conductors was filled with helium gas saturated with water vapour (Figure 1). As a result, defining the geometry and the amount of water in the system became difficult. Hence, it was assumed that a uniform water layer forms, which covers the outside surface of the inner conductor. The amount of water was estimated from the water-circulation conditions. The water-layer thickness was set to be 4 mm, which corresponds to 1 125 g of water. Most of the calculation parameters were set to the default settings adopted in PHITS/Windows Ver. 2.30 (Cascade model; n, p: Bertini <3.5 GeV <JAM, pions: Bertini <2.5 GeV<JAM; evaporation model: GEM; Cut-off; n, p, pions: 1 MeV). The nuclear production cross-section data, included in the PHITS code, were used to calculate the nuclear reactions induced by the protons and neutrons projected on the light-element targets. In the present calculations, cross-section data corresponding to the following reactions were used [6]: $^{4}He(n,x)^{3}H$, $^{4}He(p,x)^{3}H$, $^{16}O(n,x)^{3}H$, $^{16}O(p,x)^{3}H$, $^{16}O(n,x)^{7}Be$, $^{16}O(p,x)^{7}Be$.

Figure 5: Simplified model of the graphite target and first magnetic horn used in the PHITS calculations
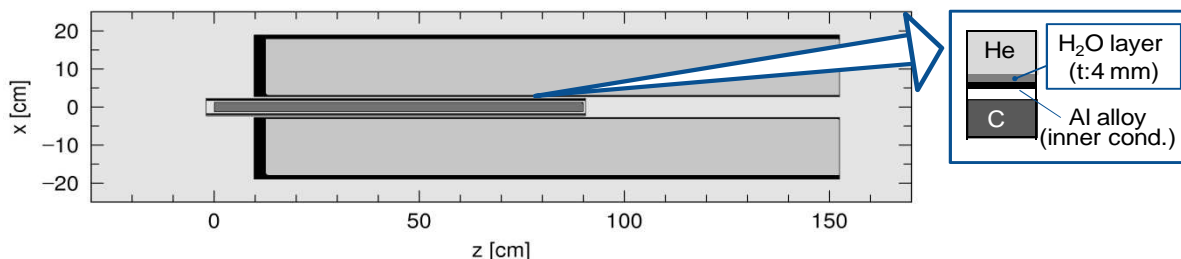
The sizes of the components are as follows: C target (Diameter(Φ) 26 x 900 mm). Inner conductor (ID: 54 mm, thickness (t): 3 mm). Outer conductor (ID: 360 mm, t: 10 mm). Water layer covering the surface of the inner conductor (t: 4 mm, 1125 g of H_2O). Beam window: Ti-6Al4V (t: 0.3 mm). Gas phase: He (1.0 atm) + H_2O (0.03 atm). Projectile: 30-GeV protons (Gaussian, σ = 4.2 mm).

High-energy hadrons irradiating on the water layer

Spatial distribution profiles show that the water layer covering the inner conductor of the first magnetic horn is exposed to intense high-energy protons, neutrons, and charged pions (π+ and π-). Figure 6 shows the energy spectra of protons, neutrons, and charged pions injected into this water layer. The energy spectra of the protons, neutrons, and pions have similar characteristics. High-energy particles (>100 MeV) are dominant and are most likely responsible for the production of radionuclides in the cooling water. Thermal neutrons and epi-thermal neutrons may also induce nuclide production, e.g. of ^{24}Na, ^{56}Mn, and ^{110m}Ag, through (n, γ) reactions.

Figure 6: Energy spectra of protons, neutrons, and charged pions (π^+ and π^-) injected into the water layer covering the inner conductor of the first magnetic horn
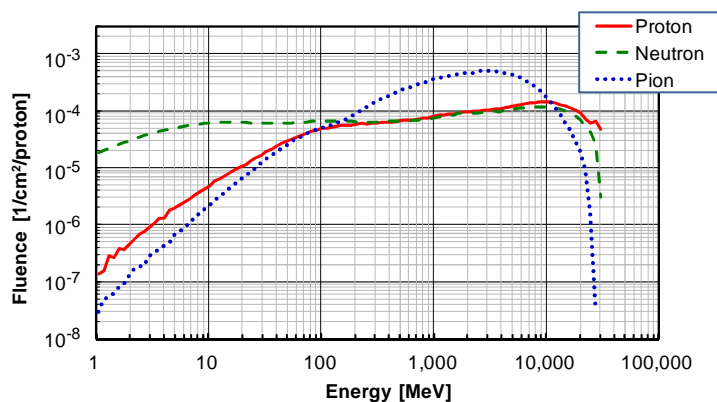
PHITS calculation on radionuclide production and comparison with experimental results

Production of radionuclides in the cooling water, in He gas saturated with water vapour, and in metallic components of the experimental set-up, was estimated using PHITS calculations. Among the long-lived nuclides (half-life >1 h), ^{3}H and ^{7}Be are produced in the water and He gas phase directly. Table 2 summarises the production of ^{3}H and ^{7}Be in water layer and in the He gas phase. The results show that the production of ^{3}H and ^{7}Be occurs mainly in the water layer attached to the inner conductor. Therefore, production of ^{3}H and ^{7}Be in the He gas phase can be neglected. The geometry of the water layer and the amount of water are ambiguous in the present calculation-geometry, meaning that absolute activities of the radionuclides cannot be discussed. Instead, the activity ratio of ^{7}Be/^{3}H is calculated and compared to the activities measured in the cooling water. The activity ratio of ^{7}Be/^{3}H observed in the cooling water is smaller than that predicted by the calculations. In the cooling water at accelerator facilities, ^{3}H exists as tritiated water (HTO) molecules and distributes homogeneously throughout the circulating water. The small observed activity ratio of ^{7}Be/^{3}H implies that some of the ^{7}Be is removed as the water circulates in the loop. Removal of ^{7}Be has previously been observed at other accelerator facilities [7] [8] due to adsorption on water pipes, filters, and other components in the water circulation systems.

Table 2: Radioactivities of ^{3}H and ^{7}Be, produced in the water layer and He-water gas phase, estimated using PHITS calculations

			Observed in the cooling water	
		PHITS Calculation	Run 36 (Pot = 4.27 × 10^{19})	Run 37 (Pot = 5.77 × 10^{19})
			Activity (Bq/proton)	
^{3}H	Water layer	3.7E-11	8.9E-11	9.4E-11
	He-Water gas	2.1E-13		
	Total	**3.7E-11**		
^{7}Be	Water layer	6.4E-10	6.2E-10	4.3E-10
	He-Water gas	5.0E-14		
	Total	**6.4E-10**		
Activity ratio (^{7}Be / ^{3}H)		**17.1**	**7.0**	**4.6**

The experimental activities were measured using the cooling water from Runs 36 and 37.

The activities of the nuclides produced in the first magnetic horn are summarised in Table 3. Most of the nuclides observed in the cooling water (Table 1), with the exception of [110m]Ag, are reproduced in the magnetic horn by PHITS calculations. The predicted activities of nuclides produced in the magnetic horn are compared with the experimental measurements of the activities in the cooling water. In order to investigate the rate at which nuclides are transferred to the water from the magnetic horn, the experimental/PHITS activity ratio is determined. For long-lived nuclides, this activity ratio should be corrected by considering the beam-operation history, which takes into account the accumulation of nuclides inside the horn material. For ^{3}H and [7]Be the experimental/PHITS activity ratio is exceptionally high compared to that measured for the other nuclides. Large differences in this ratio demonstrate that the formation processes of ^{3}H and [7]Be, which are produced in water directly, are different from those of other nuclides. For the nuclides produced in the metallic components of the magnetic horn, the experimental/PHITS activity ratio can be used to probe the transfer rates of nuclides from the horn to the water. For example, if the produced radionuclides are assumed to be distributed homogeneously throughout the horn components, the history-corrected activity ratio of 9×10^{-5} for [22]Na corresponds to the elution of 0.3 μm of aluminum alloy from the surface of the inner conductor (t = 3 mm). Some of the nuclides described in Table 3, along with [110m]Ag, are also produced in other metal materials, such as stainless steels, silver plating and copper coatings. However, this was not considered here and requires further considerations for more reliable and reasonable discussions.

Table 3: Comparison of nuclide activities from PHITS calculations of the magnetic horn and experimental measurements of the cooling water

		Activity (Bq/proton)		Activity ratio (experimental / PHITS)	
Nuclide	Half-life	PHITS Calculation	Observed in CW (Run 37)	Original ratio	Corrected considering the operation history
[3]H	12.3 y	1.2E-10	9.4E-11	0.76	0.33
[7]Be	53.3 d	1.2E-09	4.3E-10	0.37	0.28
[22]Na	2.60 y	2.3E-10	7.E-14	3.E-04	1.E-04
[52]Mn	5.59 d	2.7E-10	2.E-13	9.E-04	9.E-04
[54]Mn	312 d	1.7E-11	3.E-14	2.E-03	8.E-04
[58]Co	70.9 d	1.2E-11	8.E-14	7.E-03	5.E-03
[24]Na	15.0 h	3.4E-07	4.E-12	1.E-05	
[28]Mg	20.9 h	5.1E-11	7.E-14	1.E-03	
[42]K	12.4 h	6.7E-10	2.E-13	3.E-04	
[43]K	22.2 h	6.4E-10	4.E-14	7.E-05	
[56]Mn	2.58 h	2.6E-05	2.E-12	6.E-08	

Summary

Production of radionuclides in the cooling water, which passes through the magnetic horns at the J-PARC neutrino experimental facility, was investigated by experiments and calculations. The main radionuclides observed were ^{3}H and [7]Be, and other γ-emitting nuclides were also detected. Calculations using the PHITS code demonstrate that ^{3}H and [7]Be were directly produced in the cooling water, while the other nuclides were produced in the metal components of the system and transferred to the water via chemical and/or physical processes.

The chemical behaviour of [7]Be in the cooling water was also investigated. After several tens of hours of circulation through the deioniser, small amounts of [7]Be remained

in the circulating water. In the water, ^{7}Be was observed to exist as both water-soluble ions and colloidal species. The results imply that colloid formation of ^{7}Be in water affects the adsorptivity on the deioniser installed in the water circulation system. The formation process of radionuclide colloids in the cooling water should be clarified for radiation control at high-energy accelerator facilities.

The PHITS calculations were used to study the spatial distribution and energy spectra of protons, neutrons, and pions inside and near the first magnetic horn. The water layer and horn materials were exposed to high-energy protons, neutrons, and pions (>100 MeV), which resulted in the production of various nuclides in both the water and metal components. Comparison of the calculations and experimental results was used to investigate the inhomogeneous distributions of the radionuclides and the transfer rates of nuclides to the water from the metal components.

In future work, more reliable theoretical and experimental data, especially for high-energy nuclear reactions concerned with light elements, would be imperative for an accurate determination of the behaviour of radionuclides in water. Furthermore, simulations that take into consideration the movement of nuclides in materials, accompanied by physical and/or chemical processes, would be highly useful for understanding the behaviour of radionuclides in various environments and various media at high-energy accelerator facilities.

References

[1]   K. Abe *et al.* (2010), (T2K collaboration), "The T2K experiment", *Nucl. Instrum. Meth. A*, 659, 106.

[2]   Accelerator Group JAERI/KEK Joint Project Team, (2003), "Accelerator technical design report for high-intensity proton accelerator facility project, J-PARC", KEK Report 2002-13, JAERI Tech 2003-044, J-PARC 03-01.

[3]   K. Abe *et al.* (2011), (T2K collaboration), "Indication of electron neutrino appearance from an accelerator-produced off-axis muon neutrino beam", *Phys. Rev. Lett.*, 107, 041801.

[4]   N. Ichikawa, T. Sekiguchi, T. Nakadaira, (2010), "Neutrino production facility at the T2K experiment (in Japanese)", *High Energy News*, 28, 246.

[5]   M. Hagiwara, K. Takahashi, A. Takahashi, T. Miura, A. Kanai, F. Kouno, Y. Oyama, T. Ishida, Y. Yamada, (2011), "Radiation protection study for the J-PARC neutrino experimental facility", *Sixth International Symposium on Radiation Safety and Detection Technology (ISORD-6)*, Langkawi, Malaysia, July 12–14, 2011.

[6]   K. Niita, N. Matsuda, Y. Iwamoto, H. Iwase, T. Sato, H. Nakashima, Y. Sakamoto, L. Sihver, (2010), "PHITS: Particle and Heavy Ion Transport code System, Version 2.23", *JAEA-Data/Code*, 2010-022.

[7]   S. Itoh, T. Miura, S. Yasui, Y. Ogawa, Y. Kiyanagi, S. Sasaki, K. Iijima, (1998), "Behavior of ^{7}Be in the moderator cooling system at the pulsed neutron source, KENS", *Proc. ICANS-XIV*.

[8]   H. Matsumura, S. Sekimoto, H. Yashima, A. Toyoda, Y. Kasugai, N. Matsuda, K. Oishi, K. Bessho, Y. Sakamoto, H. Nakashima, D. Boehnlein, G. Lauten, A. Leveling, N. Mokhov, K. Vaziri, "Radionuclides in the cooling water systems for the NuMI beamline and the antiproton production target station at Fermilab", *12th International Conference on Radiation Shielding (ICRS-12)*, Nara, Japan, 2-7 September 2012.

Session II: Present Status of Data and Code Libraries

Chair: Nikolai Mokhov

Hadron production model developments and benchmarking in the 0.7 – 12 GeV energy region

Nikolai Mokhov[1], Konstantin Gudima[2], Sergei Striganov[1]
[1]Fermi National Accelerator Laboratory, Batavia IL, US,
[2]Institute of Applied Physics, Academy of Sciences of Moldova

Abstract

Driven by the needs of the intensity frontier projects with their Megawatt beams, e.g. ESS, FAIR and Project X, and their experiments, the event generators of the MARS15 code have been recently improved. After thorough analysis and benchmarking against data, including the newest ones by the HARP collaboration, both the exclusive and inclusive particle production models were further developed in the projectile energy region of 0.7 to 12 GeV crucial for the above projects – but difficult from a theoretical standpoint. At these energies, the modelling of prompt particle production in nucleon-nucleon and pion-nucleon inelastic reactions is now based on a combination of phase-space and isobar models. Other reactions are still modelled in the framework of the Quark-Gluon String Model. Pion, kaon and strange particle production and propagation in nuclear media are improved. For the alternative inclusive mode, experimental data on large-angle (>20 degrees) pion production in hadron-nucleus interactions are parameterised in a broad energy range using a two-source model. It is mixed-and-matched with the native MARS model, which successfully describes low-angle pion production data. Predictions of both new models are – in most cases – in good agreement with experimental data obtained at CERN, JINR, LANL, BNL and KEK.

Introduction

Fermilab, and US HEP in general, is moving to the Intensity Frontier, constructing/planning neutrino experiments (NOVA, LBNE, NuSTORM and Neutrino Factory), rare decay and high-precision experiments (Mu2e, g-2, ORKA, etc.) along with upgrades of the existing accelerators and planning for a Megawatt-scale multi-purpose Project X. Besides new challenges in the material and shielding aspects of these projects, all of the above requires reliable predictions of particle production at beam energies of 1 to 120 GeV, crucial for pions at $1 < E_p < 10$ GeV, the region where theoretical models traditionally have problems and existing experimental data contradict each other. The status of the models and recent developments of the MARS15 code event generators [1] [2] are described in this paper. The focus is on pion production in the difficult intermediate energy range – as a primary need of the above experiments – although new calculations for secondary protons and kaons are also shown.

Issues with low-energy pion production

General purpose particle transport codes such as Geant4, FLUKA and MARS15 use event generators based on the intra-nuclear cascade models at energies below a few GeV and quark-parton models at higher energies. Both groups have difficulties in the intermediate energy range of 1 to 10 GeV. To describe a low-energy particle production, a "formation length" should be introduced and determined from experimental data. To describe a large-angle particle production, interactions of a projectile with a multiple-particle bag should be taken into account. There are also difficulties specific to the models. In particular, descriptions of baryon resonance production cross-sections and interactions are needed, but these were never measured. At low projectile energies, an invariant mass of a chain (string) stretched between the quarks is so small that it is unclear how to transform it to real hadrons in a quark-parton model.

Experimental data on pion production are quite sparse. At small angles (<10 degrees), only spectra of fast pions (p >500 MeV/c) were measured. Backward pion production was studied in detail in [3-5]. There are several measurements of negative pion production in a broad angular range, but only for a limited number of target nuclei and few primary proton momenta [6-8]. Recently, the HARP collaboration has partially closed the gap between the small- and large-angle measurements. The large-angle study [9] covers pion angles from 20° to 123° and momenta from 0.1 to 0.7 GeV/c for primary proton and pion momenta 3, 5, 8 and 12 GeV/c. A part of the collaboration, HARP-CDP, has published similar data [10] based on a calibration different from that used by the main HARP collaboration. The cross-sections measured are not that different for negative pions, but for the positive pions the difference between the HARP and HARP-CDP results reach 60%.

The HARP collaboration performed comprehensive comparison of their large-angle data with Geant4 and MARS15 calculations [9]. The issues with both codes were revealed. The HARP-CDP group has also compared its measurements with the FLUKA and Geant4 simulations [11]. The Geant4 version 4.9.3 was found not to reproduce the energy dependence of pion production measured at the intermediate (20-50 degrees) and large (50-125 degrees) angles, while the FLUKA simulations agree with the data within 30%.

The HARP measurements [9] were fitted using a two-fireball approximation described in the next section. The HARP cross-sections were obtained by integration of this approximation into the HARP-CDP cuts. The HARP-CDP and HARP cross-sections are presented in Figure 1 in comparison with LAQGSM and FLUKA calculations. It is seen that the difference between results obtained by the two HARP groups is not large. The LAQGSM calculations agree with the data rather well. In a recent Geant4 version, the event generators were significantly improved and two new models, INCL and UrQMD,

were included [12]. Results with UrQMD and FTFB are closer to the HARP-CDP data, while INCL produces results closer to the HARP data.

Figure 1: π^- (left) and π^+ (right) production cross-sections on Be, Cu and Ta nuclei *vs* proton momentum
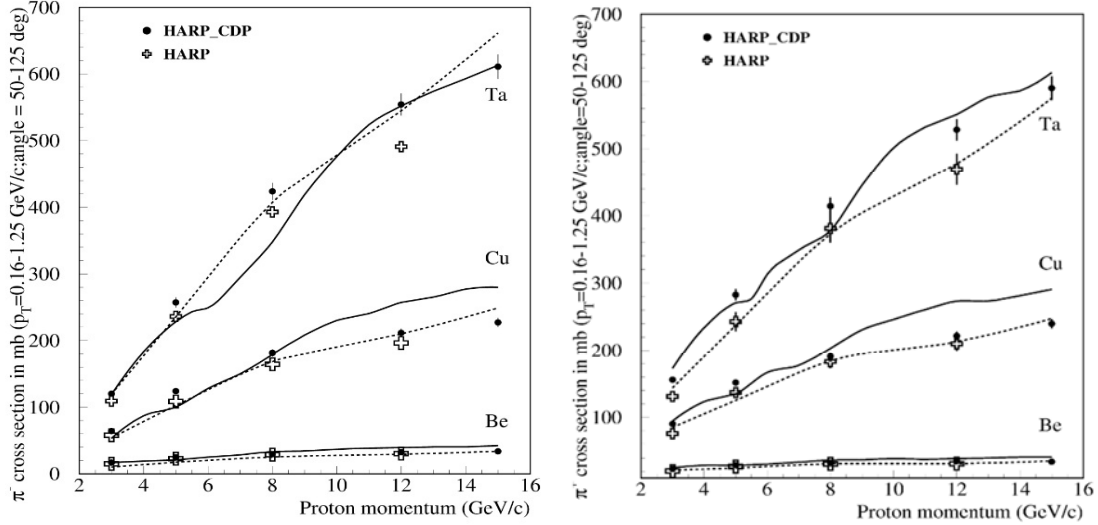
Open symbols are approximation of HARP data [9], full symbols are HARP-CDP data [10], solid lines are FLUKA results from [11], and dotted lines are LAQGSM results.

MARS15 inclusive pion production model development

The main features of charged pion production at low and intermediate energies could be successfully described by a fireball model. In this model, the invariant cross-section of pion production reads:

$$E\frac{d^3\sigma}{dp^3} \propto \exp(-\frac{T_{cm}}{T_0}) \propto \exp(-\frac{E - p\beta\cos(\theta)}{T_0\sqrt{1-\beta^2}}) \,, \tag{1}$$

where T_{cm} is pion energy in the fireball rest-frame, E, p, θ are pion energy, momentum and angle in laboratory system, β is fireball velocity. The low-statistic JINR bubble chamber data [6] [7] was fitted with a good χ^2 by a relativistic form of the above formula ($E \approx p$). It turns out that to describe more precise measurements of negative pion production obtained by the KEK counter experiment for proton momenta of 3 and 4 GeV/c, one needs a two-source model [8]. At the same time, such a model fails to reproduce the LANL measurements [13] of pion production cross-sections at the proton energy of 730 MeV, especially at medium angles (15 – 60 degrees). To improve the model at such a low energy, one of the fireball sources can be changed to a term similar to the Fermi distribution. The resulting invariant cross-section can then be written as:

$$E\frac{d^3\sigma}{dp^3} = p_1(1 + p_7\cos\theta)\exp(-\frac{T(1 - p_2\cos\theta)}{p_3}) + \frac{p_9(1 + p_8\cos\theta)}{1 + p_4\exp(T(1 - p_6\cos\theta)/p_5)} \tag{2}$$

For $p_4 \gg 1$ this is similar to the relativistic two-fireball model [8], but now it fits the LANL data [13] with χ^2/n =2.4. Figure 2 (left) illustrates the quality of the formula (2). It agrees with data [13] even better at larger angles.

Figure 2: π^- production cross-sections in proton-lead interactions at 730 MeV (left) and 3 GeV/c (right)
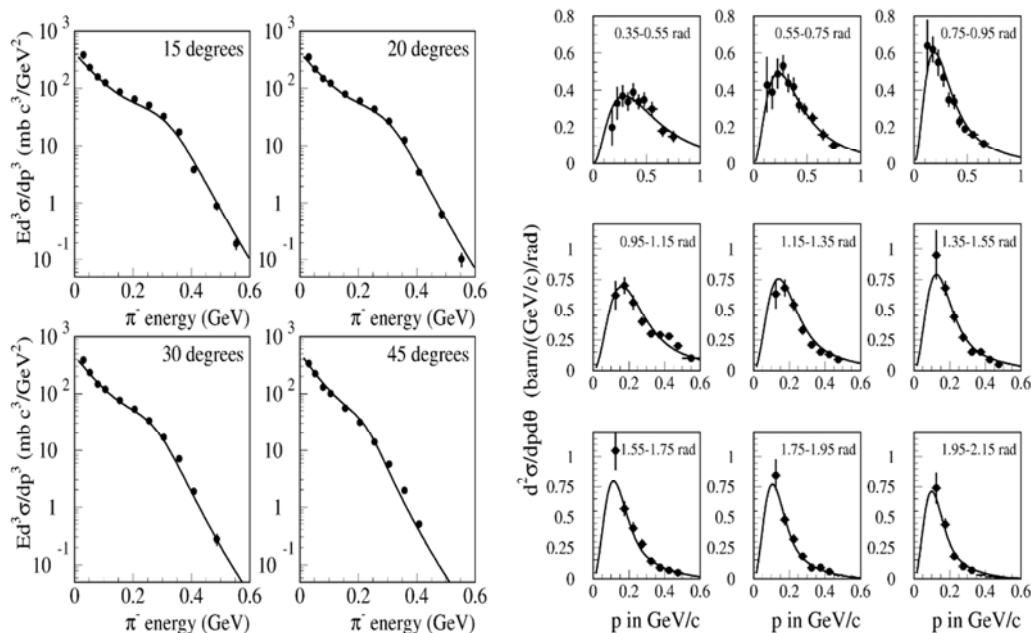
Solid curves are according to formula (2), symbols are experimental data [13] (left) and [9] (right).

Experimental data of the HARP collaboration [9] covers angles from 20° to 123°. This data is also successfully fitted by the two-source model (2) with $x^2/n \sim 1$ for all the HARP projectile momenta (3, 5, 8 and 12 GeV/c) and nuclei. A typical comparison is shown in Figure 2 (right). The other measurements [3-5] at large angles (90, 119, 168 and 180 degrees) can also be included into the fitting procedure. The quality of the fit becomes slightly worse ($x^2/n \sim 2$) but is still quite acceptable. Figure 3 (left) shows the comparison of the two-source model (2) with data at 180 degrees in a broad range of proton momenta. It is seen that the pion yield at 180 degrees grows with the proton momentum up to 5 GeV/c and remains constant after that for pions with a kinetic energy ≥ 150 MeV. The energy dependence of the negative pion spectra (normalised to the primary proton kinetic energy T_0) at the fixed angles is presented in Figure 3 (right). The low-energy parts of the normalised spectra are independent of T_0, i.e. the yield of low-energy pions (< 150 MeV) grows with T_0 nearly linearly for $1 < T_0 < 7$ GeV.

The native inclusive MARS model [1] successfully describes the low-angle HARP data for primary protons with $3 < p_0 < 12$ GeV/c [14] [15]. A typical comparison for secondary pions and protons is presented in Figure 4. A mix-and-match of the newly developed two-source description (2) and the native MARS model provides the complete description of pion production in proton- and pion-nucleus interactions.

Figure 3: π⁻ production in proton-lead interactions as calculated according to formula (2) *vs* pion kinetic energy
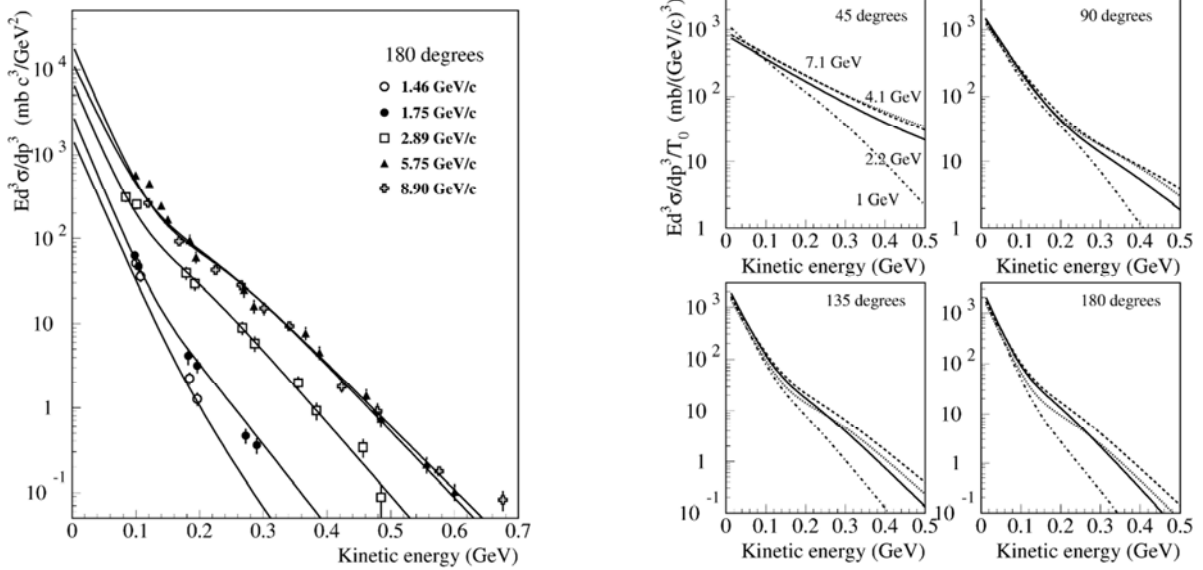
Left: invariant cross-sections at the fixed angle of 180 degrees for proton momenta from 1.46 GeV/c to 8.9 GeV/c in comparison with data (see text). Right: invariant cross-sections (normalised to proton energy T_0) at various angles for $1 < T_0 < 7.1$ GeV.

Figure 4: MARS inclusive model *vs* 8 GeV/c HARP data [9]
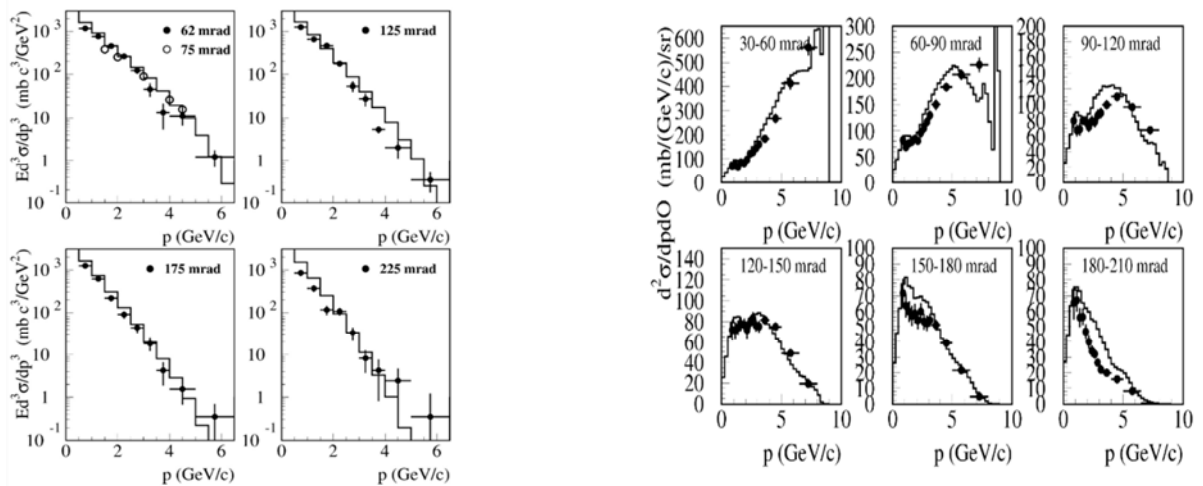
Left: π⁻ production cross-section at various angles in p+Ta interactions. Right: proton production differential cross-section at various angles in p+Be interactions.

Quark-gluon string model developments

The Quark-Gluon String Model, the LAQGSM code [2], is used in MARS15 for photon, hadron and heavy-ion projectiles at projectile energies from a few MeV/A to 1 TeV/A. This provides a power of full theoretically consistent modelling of exclusive and inclusive distributions of secondary particles, spallation, fission, and fragmentation products. The newest developments include: new and better approximations for elementary total, elastic, and inelastic cross-sections for NN and πN interactions; several channels implemented for the explicit description with use of experimental data: N+N→N+N+mπ, π+N→N+mπ (m<5), B+B→B+Y+K, π+B→Y+K, π+B→B+K+Kbar, B+B→B+B+K+Kbar, Kbar+B→Y+π, and K+Kbar, N+Nbar pair production for the cms energy $s^{1/2}$<4.5 GeV; a combination of the phase space and isobar models for N+N and π+N one pion production; γA reactions extended down to the Giant Dipole Resonance energies and below; and an arbitrary light nuclear projectile (*e.g.* d) and nuclear target (*e.g.* d or He).

A mix-and-match is used in the transition region of 0.8 < T_1 < 4.5 GeV to link the above explicit description and the QGSM. Here, T_1 is the kinetic energy of the projectile in the rest frame of the collision partner. The code considers that the nuclear reaction goes through three stages: intra-nuclear cascade, pre-equilibrium emission and evaporation/fission from the excited and thermally equilibrated residual nuclei. The nucleons with close momenta produced in the first stage can form fast light fragments (d, t, ^{3}He and ^{4}He) via the coalescence mechanism. Low-energy neutrons, protons, nuclear fragments, de-excitation photons and fission products are generated in the last two stages. In the newest version, the extension of heavy-ion collisions to low energies (below $4V_c$, where V_c is the Coulomb barrier) is done by replacing the cascade stage with the formation of a compound nucleus followed by the pre-equilibrium and equilibrium evaporation/fission processes.

Results of the first comparison with the HARP data [9] of the MARS15-LAQGSM calculations of large-angle pion production on heavy nucleus are shown in Figure 5 (left). Calculations according to the formula (2) are also shown in the figure for this 8 GeV/c p+Pb reaction. One can see the perfect agreement with the data for negative pions with p> 200 MeV/c. At the same time, the QGSM model overestimates the data by up to 50% for lower pion momenta. Attempts to fix the problem just by increasing the pion absorption cross-section have had a limited success so far. The aim of the ongoing work is to improve the model in this important region.

Figure 5 (right) shows the comparison of the MARS15-LAQGSM calculations of small- and intermediate-angle pion and proton production with the HARP data [14] [15] for the 8 GeV/c p+Cu interactions. The agreement is good for most of the momentum-angle space but in some regions the model underestimates the data by a factor of two (or even bigger for protons). It is clear that additional efforts are needed here to verify the code in complementary cases and – if needed – to further improve the model in this energy domain.

Double-differential cross-sections of the 730-MeV p+Pb →π$^±$X reaction at angles from 15° to 150° are presented in Figure 6. Keep in mind that such a low projectile energy is below the lower limit of 3 GeV for the LAQGSM use in MARS15. With this note, one can consider the agreement with data as satisfactory. The most noticeable problem in the model is still with the excessive yield of low-energy pions.

Figure 5: Left: π⁻ production in p+Pb interactions at 8 GeV/c calculated with inclusive (solid) and LAQGSM (dashed) models *vs* HARP data [9]
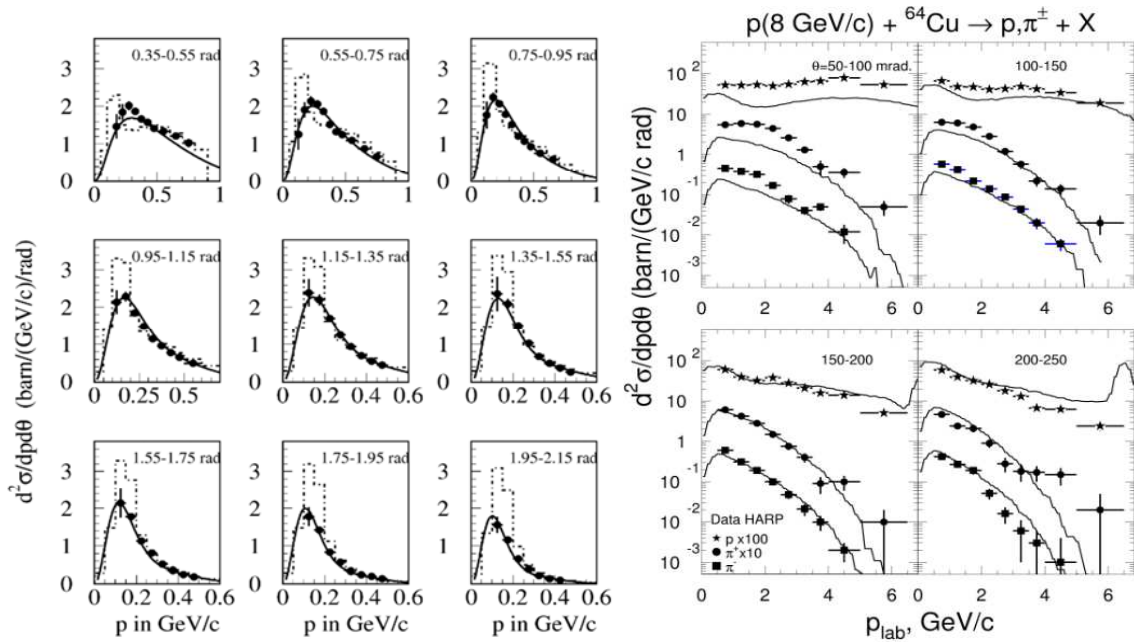
Right: proton and pion production in p+Cu reaction at 8 GeV/c calculated with LAQGSM model *vs* HARP data [14] [15].

Figure 6: Positive (left) and negative (right) pion production in p+Pb interactions at 730 MeV calculated with LAQGSM model *vs* LANL data [13]
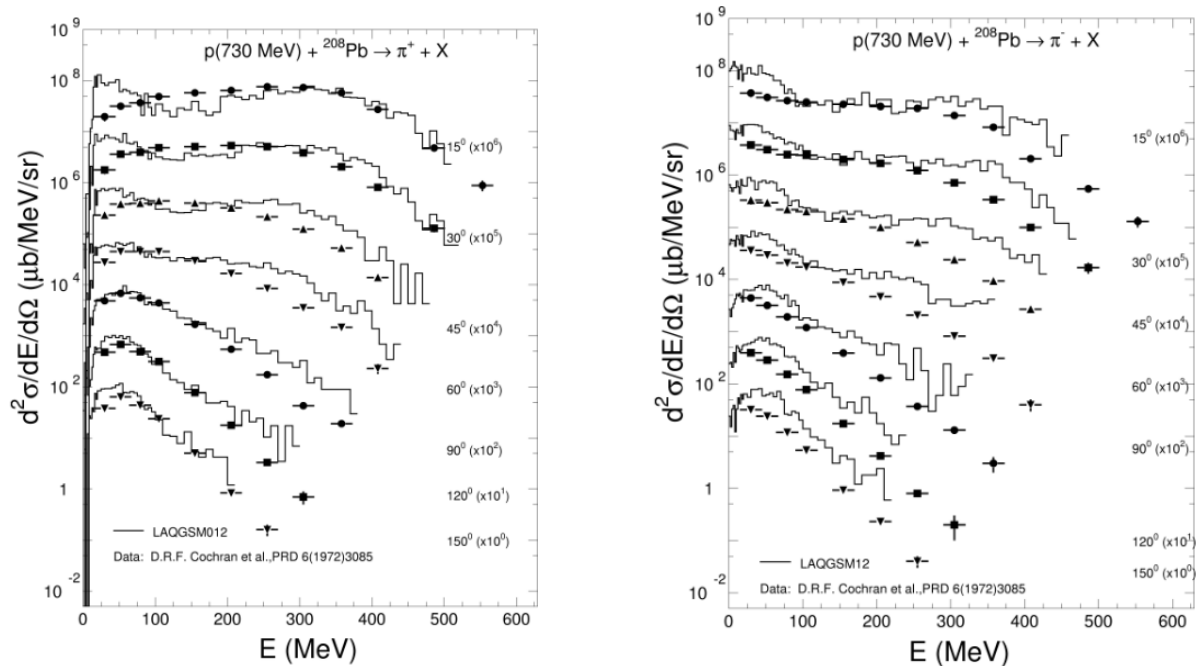
Figure 7 shows the double-differential cross-sections of positive and negative pions produced at four fixed angles in p+Be and p+Au interactions at 12.3 GeV/c. The MARS15-LAQGSM calculations are in very good agreement with the BNL data [16].

Figure 7: Pion production in p+Be (left) and p+Au (right) interactions at 12.3 GeV/c calculated with LAQGSM model *vs* data [16]
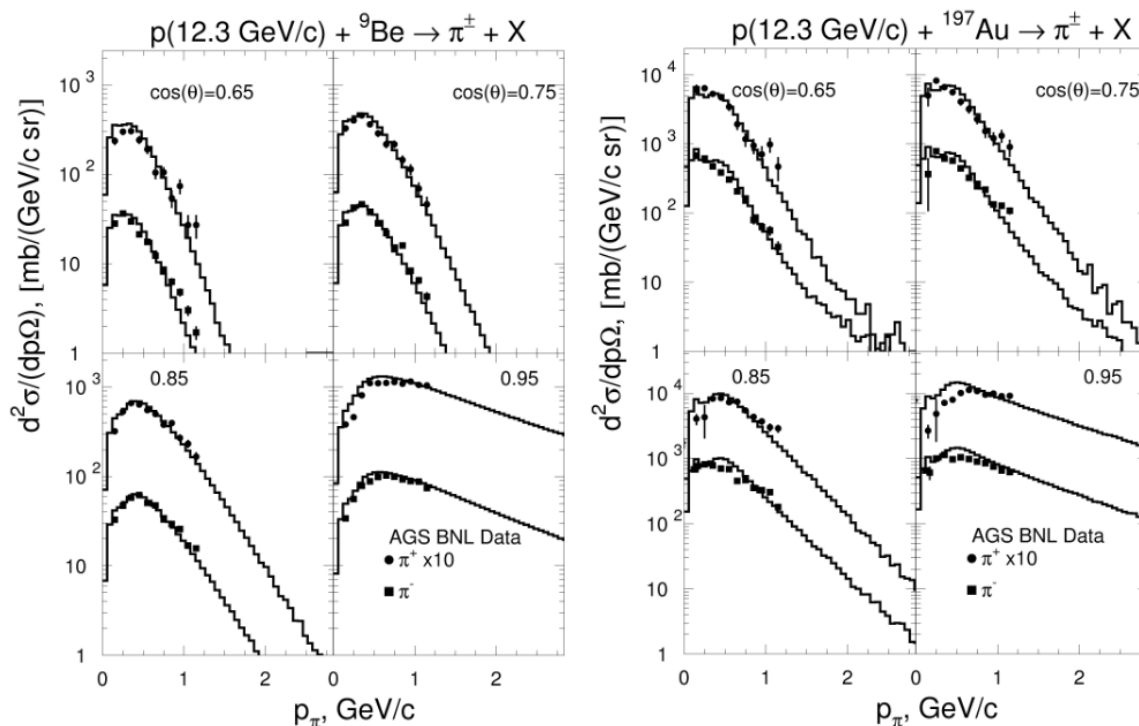
The previous comparisons in this paper were all presented for the proton-induced reactions. Double-differential cross-sections of pions and protons produced at large angles in the π^- interactions with a lead nucleus at 3 and 5 GeV/c are shown in Figure 8. The LAQGSM calculations are in good agreement with the HARP-CDP data [17] for all the energies and angles.

Motivated by the plans for the next generation of rare-decay experiments in the Project X era, the MARS15-LAQGSM model for kaon production was substantially improved [18]. The proton kinetic beam energy (T_p) threshold for producing kaons is 1.7 GeV (on protons) and the kaon yield fraction grows with the increasing number of exclusive production channels that open and saturate around T_p of 6 GeV. The efforts were specifically put on the model development in the near-threshold region. As a result, the improved model predictions were found in excellent agreement with experimental data from the ANKE spectrometer at COSY-Julich [19] for T_p near 2 GeV.

Figure 9 (left) shows the double-differential cross-section of the 2.3-GeV p+C →K$^+$X reaction for forwardly-produced kaons. As in [18], excellent agreement between the data and calculations done with the newest LAQGSM model in MARS15 is observed. Comparison of the new model with data [20] reveals good agreement for K$^\pm$ large-angle production for the 3.5-GeV proton interactions with the gold nucleus.

Figure 8: Proton and pion production in π⁻ +Pb interactions at 3 GeV/c (left) and 5 GeV/c (right) calculated with LAQGSM model *vs* HARP-CDP data [17]
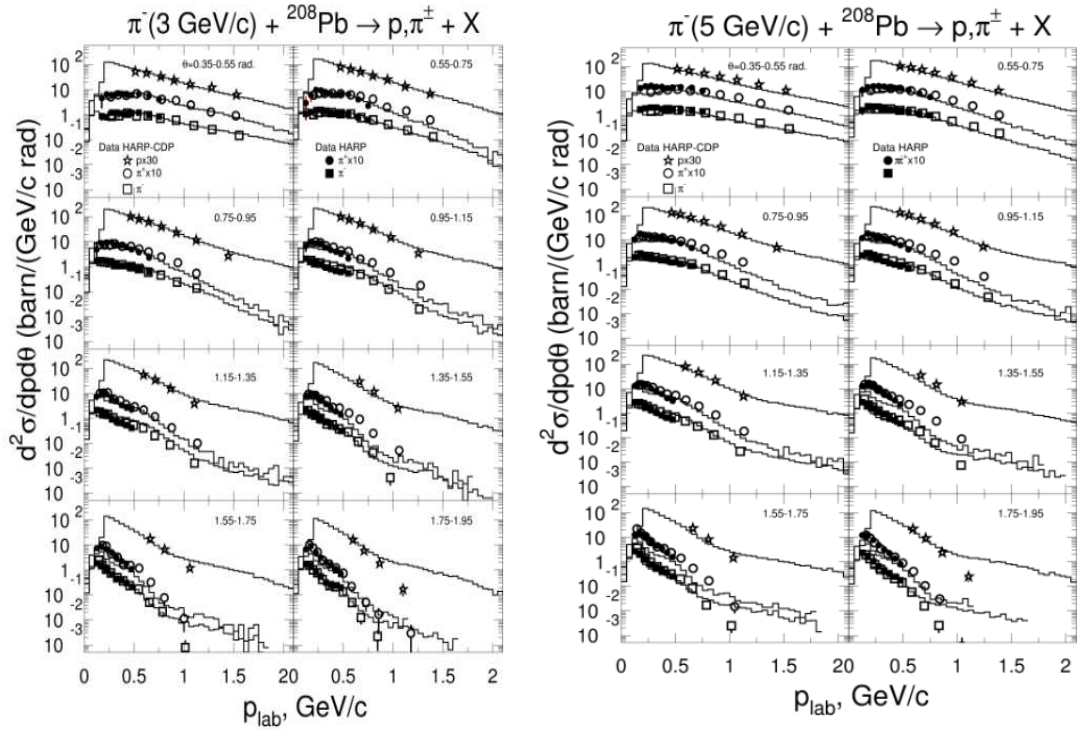
Figure 9: Kaon production in p+C interactions at 2.3 GeV (left) and p+Au interactions at 3.5 GeV (right) calculated with LAQGSM models *vs* data [19] and [20], respectively
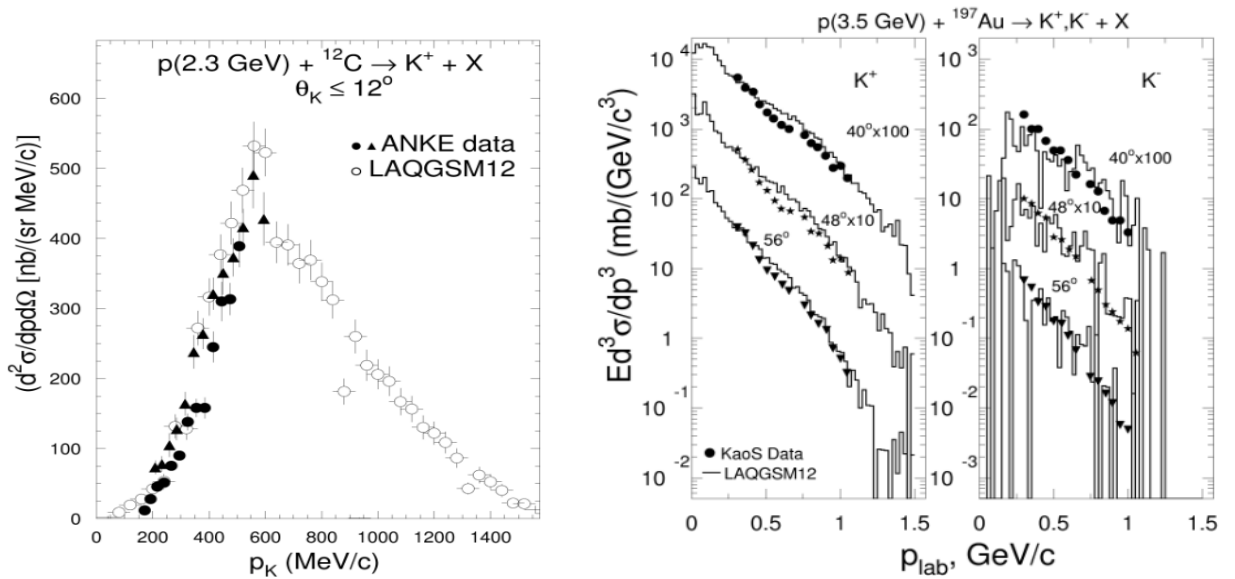
Conclusions

Despite the boost the HARP experiment made to the status of data on particle yields in nuclear reactions in the 2 to 12 GeV energy range, there is still a lack of data in some phase-space regions. Moreover, in some cases there is an inconsistency between the new data and the data measured over the last decades. Also, and this is especially unfortunate, there is an inconsistency between the two HARP subgroups'data. There is certainly noticeable progress with the theoretical models capable of an accurate prediction of particle production at intermediate energies. The phenomenological inclusive model and improved LAQGSM model described in this paper are an example. The agreement of both models with data is good for most of the momentum-angle space, but in some regions the new LAQGSM disagrees with the data by up to a factor of two. Additional efforts are still needed to further improve the model in this intermediate energy region, which is difficult from all prospects but is crucial for numerous applications.

Acknowledgements

References

[1] N.V. Mokhov (1995), The Mars Code System User's *Guide, Fermilab-FN-628,* and N.V Mokhov, S.I. Striganov, "MARS15 Overview", in *Proc. of Hadronic Shower Simulation Workshop*, Fermilab, September 2006, AIP Conf. Proc. 896, pp. 50-60 (2007); http://www-ap.fnal.gov/MARS/.

[2] S.G. Mashnik *et al.* (2008), CEM03.03 and LAQGSM03.03 Event Generators for the MCNP6, MCNPX and MARS15 Transport Codes, *LANL Report LA-UR-08-2931,* arXiv:0805.0751v1, [nucl-th] 6 May 2008.

[3] A.M. Baldin *et al.* (1975), "Experimental investigation of cumulative meson production", *Sov. J. Nucl. Phys.*,20, 1201.

[4] A.M. Baldin *et al.* (1982), "Experimental data on inclusive cross section for cumulative production of pions, kaons, antiprotons and the quark-parton structure of nuclei", *JINR preprint E1-82-472.*

[5] L.S. Schroeder *et al.* (1979), "Energy Dependence of Charged Pions Produced at 180º in 0.8-4.89 GeV Proton-Nucleus Collisions", *Phys. Rev. Lett., 43, 1787.*

[6] G.N. Agakishiev *et al. (1975),* "Dependence of π- Meson Spectra at Fixed Angles on the Atomic Weight of Projectile in Interactions Between Light Nuclei (p, d, α, C) and Carbon Nucleus at 4.2-GeV/c per Nucleon", *Sov. J. Nucl. Phys., 20,1201.*

[7] D. Armutliiski *et al.* (1991), "Hadron Spectra in Hadron-Nucleus Collisions", *JINR preprint P1-91-191.*

[8] K. Nakai *et al.* (1983), "Stopping and energy deposition of GeV particles in target nuclei", *Phys. Lett., 121B, 373.*

[9] M.G. Catanesi *et al.* (2008), "Large-angle production of charged pions with 3-12.9 GeV/c incident protons on nuclear targets", *Phys. Rev., C77, 055207.*

[10] A. Bolshakova *et al.* (2009), "Cross-sections of large-angle hadron production in proton-nucleus and pion-nucleus interactions I: beryllium nuclei and beam momenta of +8.9 GeV/c and -8.0 GeV/c", *Eur. Phys. J., C62, 293.*

[11] A. Bolshakova *et al.* (2010), "HARP-CDP hadroproduction data: comparison with FLUKA and GEANT4 simulations", *Eur. Phys. J., C70, 543.*

[12] K. Abdel-Waged *et al.* (2011), "GEANT4 hadronic cascade models analysis of proton and charged pion transverse momentum spectra from p + Cu and Pb collisions at 3,8 and 15 GeV/c", *Phys. Rev., C84, 014905.*

[13] D.R.F. Cochran *et al.* (1972), "Production of Charged Pions by 730-MeV Protons from Hydrogen and Selected Nuclei", *Phys. Rev., D6, 3085.*

[14] M. Apollonio *et al.* (2009), "Forward proton production of charged pions with incident protons on nuclear targets at the CERN PS", *Phys. Rev., C82, 035208.*

[15] M. Apollonio *et al.* (2010), "Measurements of forward proton production with incident protons and charged pions on nuclear targets at the CERN Proton Synchrotron", *Phys. Rev., C82, 045208.*

[16] I. Chemakin *et al.* (2002), "Inclusive soft pion production from 12.3 and 17.5 GeV/c protons on Be, Cu, and Au", *Phys. Rev., C65, 024904.*

[17] A. Bolshakova *et al.* (2010), "Cross-sections of large-angle hadron production in proton- and pion-nucleus interactions V: lead nuclei and beam momenta from ±3 GeV/c to ±15 GeV/c", *Eur. Phys. J. C66, 57.*

[18] K.K. Gudima, N.V. Mokhov, S.I. Striganov (2009), Kaon yields for 2 to 8 GeV proton beams, *Fermilab-Conf-09-647-APC.*

[19] M. Buscher *et al.* (2004), "Inclusive K^{+} meson production in proton-nucleus interactions", *Eur. Phys. J., A22, 301.*

[20] W. Scheinast *et al.* (2006), "First observation of in-medium effects on phase distribution of antikaons measured in proton-nucleus collisions", *Phys. Rev. Lett., 96, 072301.*

Geant4 Results for "inter-comparison problems of neutron attenuation"

Tatsumi Koi

SLAC National Accelerator Laboratory, Menlo Park US

Abstract

Geant4 is a toolkit for the simulation of the passage of particles through matter. To demonstrate its capability in shielding applications, we have submitted Geant4 results to the SATIF "Inter-comparison Problems of Neutron Attenuation" since 2006. Because Geant4 takes the toolkit approach, the user is allowed flexibility in choosing not only geometry but also physics processes as implemented in a physics list. For the benefit of users, the "Shielding" physics list, which we used in the comparison, is included in the release of Geant4. The latest Geant4 result obtained by using this physics list is measured against the experimental data of the BNL AGS benchmarks and presented in this paper. The agreement with data was found to be slightly worse than that for SATIF-10. After a detailed investigation, we found that the difference is mainly caused by the change of internal nucleon-nucleon cross-section in a cascade model. We confirmed that by switching back to the original cross-section, the agreement with data returns to the level of SATIF-10. Besides this physics list, the current Geant4 provides about 20 so-called reference physics lists and the results from these, together with brief explanations about the character of each list, are also presented.

Introduction

The Geant4 toolkit [1] provides a complete set of class libraries for Monte Carlo simulations of particle interactions in matter. Geant4 is used in many research fields, such as high-energy physics, nuclear physics, astrophysics, space engineering, non-destructive inspection, detector development, environmental research, and medical physics. In order to demonstrate Geant4 capability in radiation protection and shielding calculations, we have participated in the "Inter-comparison of Medium-Energy Neutron Attenuation in Iron and Concrete" project since SATIF-8 [2] [3] [4]. Because Geant4 is designed as a toolkit, it does not include a default application. Users must implement a few classes to build a fully integrated application. One such mandatory class is the "Physics List" where users assemble the physics processes required for the simulation. However, preparing a proper physics list for an application is not an easy task even for experienced users; therefore several "reference" physics lists have been provided as part of the release. One of these, the "Shielding" physics list which has been in the release since v9.4 was used in this comparison.

While preparing the Geant4 result for the SATIF-11 comparison, two problems were noticed. One is related to scoring and the other is associated with physics performance. In this paper, we will explain these problems and their solutions, and show the results of the Geant4 in comparison to the experimental data in the BNL AGS benchmarks. Results from using other reference physics lists in Geant4 are also presented with brief explanations about the character of each list.

Calculation of BNL AGS benchmarks

Comparisons were made to the data from the BNL AGS shielding experiment. 2.83 GeV and 24 GeV protons beams irradiate a mercury target and secondary neutron fluences in the shielding material of concrete and iron were measured. Details of the experiment are available in [5]. The reaction rates of $^{209}Bi(n,4n)^{206}Bi$ and $^{209}Bi(n,6n)^{204}Bi$ were provided by the co-ordinator of the inter-comparison.

The problem in weight calculation

While performing the comparison, we observed unexpected bumps in the result mainly in the deep penetration region. After some investigation, we found that the latest version of Geant4 (v9.5.p01) has a problem in the weight calculation. Analogue calculations (every particle has weight = 1) return correct answers but once we activate variance reduction techniques such as geometrical importance biasing, weight windows and Russian roulette, strange results appear. The problematic code was identified and a fix was also provided. However, to maintain to ability of users to reproduce our result we decided to do our calculation using Geant4 v9.6 beta which does not have the problem. The fix will be included in a future patch release of Geant4.

Results from Geant4 9.6 beta

Figure 1 shows Geant4 results of the comparison with the benchmark. The solid lines are results from Geant4 v9.6 beta with the shielding physics list and the broken lines are Geant4 results with some modification of the original version. We will describe the modification later. Reasonable agreement can be seen in the plots. We defined a quantitative measure representing the level of agreement between data and simulation. The value (X) is defined by the following equation:

$$X = \sum_{i=1}^{n} abs\left(\log\left(\frac{x_{sim\_i}}{x_{data\_i}} \right) \right) \tag{1}$$

In Figure 2 we compare the Geant4 results to the SATIF-10 benchmarks. It shows that the original result from Geant4 9.6 beta becomes worse than the result at SATIF-10 especially in the steel case.

While checking for possible changes which may have caused this difference, we found that internal nucleon-nucleon cross-sections in the Bertini-style cascade were modified. They were changed from their original values to the free-space PDG values. The code was then modified to switch back to the original values. Broken lines in Figure 1 and bars filled by checker board pattern in Figure 2 represent the results of this modification. In steel shielding cases, the agreement with data improves, returning to its previous level or even improving slightly at 24 GeV. In the concrete shielding cases, there is no improvement in the new result; however, the absolute agreement is much better than in the steel cases. Several other developments may potentially impact the results, but we conclude that most of the difference comes from the change of the internal cross-sections. The modification will be included in the next release of Geant4.

Figure 1: Geant4 result for inter comparison of BNL AGS benchmark
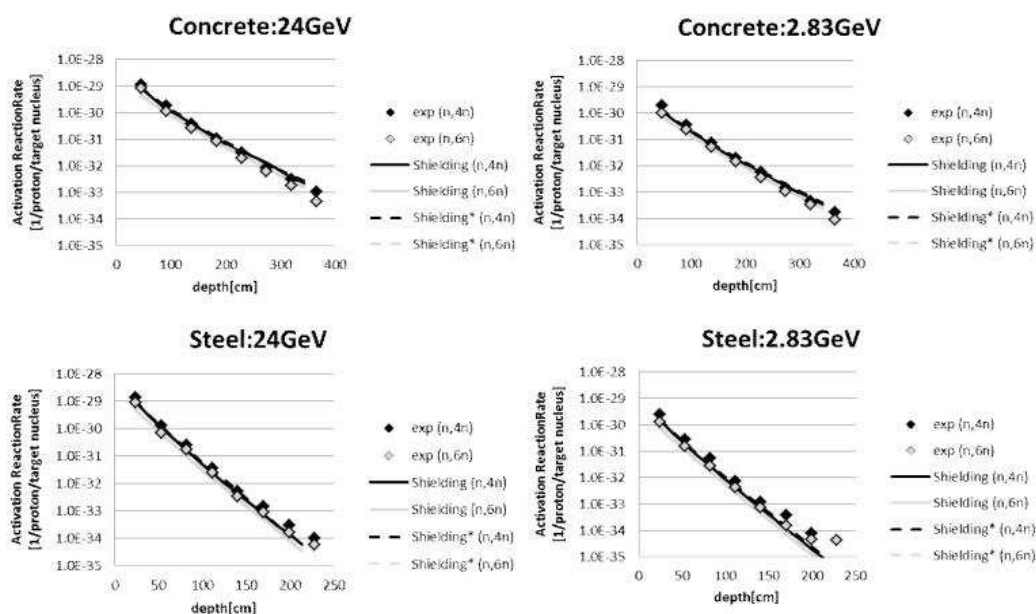
Results from other reference physics lists

Many reference physics lists are provided in the Geant4 release. One of them is the shielding physics list, which we have already discussed. We also compare to the BNL AGS benchmark several other reference physics lists and test their X values. FTFP_BERT, QGSP_BERT, QGSP_BIC and QBBC were selected for the test. FTFP_BERT uses the Fritiof string model at high energies and the Bertini-style cascade at medium energies, that is, below the string formation energy, and at low energies below the resonance region. This physics list is quite similar to the shielding physics list, differing mainly in the selection of cross-section data sets [6] and in the use of neutron HP model for neutrons below 20 MeV. The Quark Gluon String model is used for high-energy interactions in QGSP_BERT, QGSP_BIC and QBBC physics lists. The former two physics lists use the Bertini-style cascade and the Binary cascade for the medium- and low-energy interactions respectively. QBBC uses the Bertini-style cascade at medium energies and the Binary cascade at low energies. None of these physics lists use Neutron HP model for low-energy neutron transportation below 20 MeV, which the Shielding physics list uses, but because the thresholds of the reactions

^{209}Bi(n,4n)^{206}Bi and ^{209}Bi(n,6n)^{204}Bi, are 22.6 and 38.1 MeV, respectively, this is not important in the comparison. Figure 3 shows X values from these physics lists together with results from shielding physics list. The result from the shielding physics list is better than most of the others, but QBBC gives comparable results and even better ones in concrete shielding cases.

Figure 2: The X values of the Geant4 results for BNL AGS benchmark at SATIF-10 and v9.6 beta
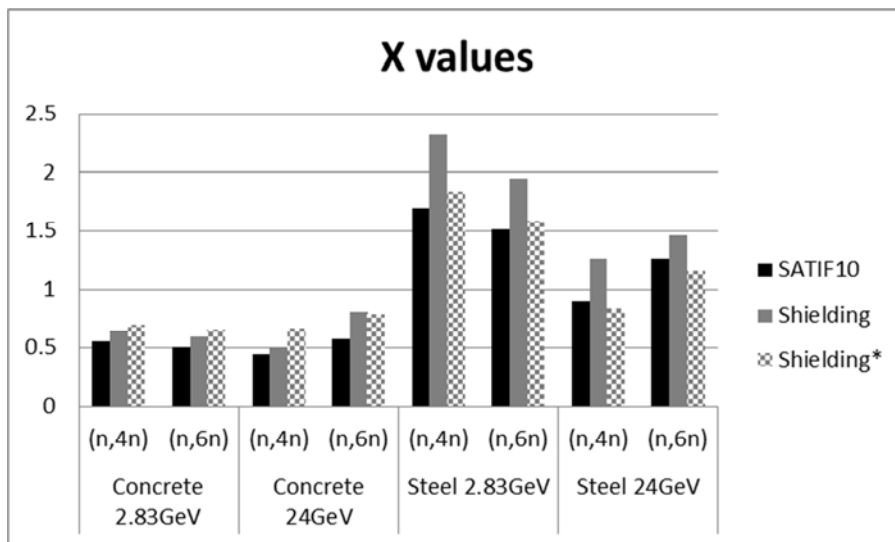
Figure 3: The X values among reference physics lists in Geant4
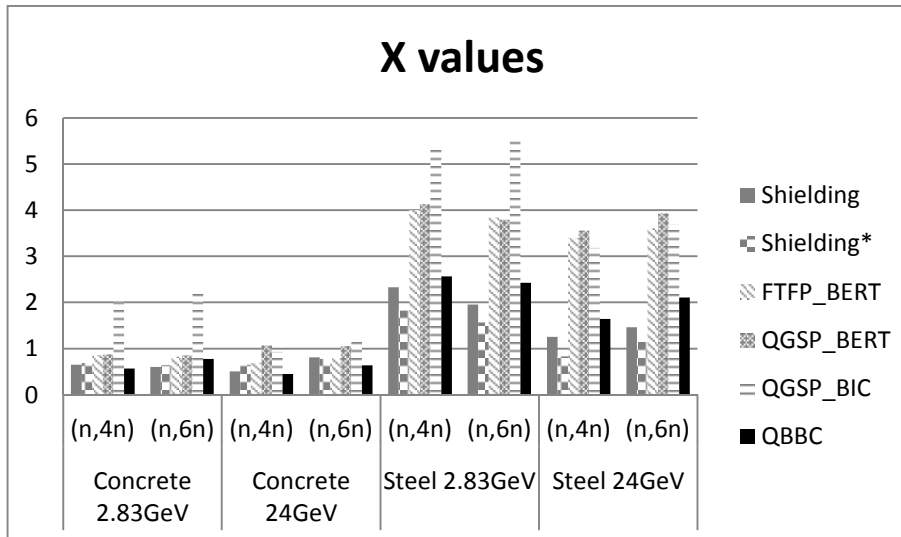
Conclusion

The Geant4 result for the inter-comparison is presented. Because of weight calculation problems in the latest official release of Geant4 v9.5.p01, we use Geant4 v9.6 beta with its shielding physics list for the comparison. BNL AGS benchmark results become slightly worse than the result at SATIF-10. The differences come mainly from the change of internal nucleon-nucleon cross-sections in the Bertini-style cascade and once the cross-sections are returned to their original values, most differences disappear. We also calculate the benchmark for several other reference physics lists. The agreement to the data becomes worse than the shielding physics list in most cases. However, comparable results are achieved when using the QBBC physics list. These changes will be reflected in the future development of Geant4.

References

[1]   S. Agostinelli *et al.* (2003), "Geant4: a Simulation Toolkit", *Nucl. Instrum. Meth.* A 506 250.*J. Allison et al.* (2006), "Geant4 Developments and Applications", *IEEE Transactions on Nuclear Science* 53 No. 1, 270-278.

[2]   H. Hirayama *et al.* (2006), "Inter-comparison of the Medium-Energy Neutron attenuation in Iron and Concrete (6)", *Proceedings of the Shielding Aspects of Accelerators, Targets and Irradiation Facilities – SATIF8*, Pohang Accelerator Laboratory, Republic of Korea, 22-24 May 2006, pp.237-250.

[3]   H. Hirayama *et al.* (2010), "Inter-comparison of the Medium-Energy Neutron attenuation in Iron and Concrete (7)", *Proceedings of the Shielding Aspects of Accelerators, Targets and Irradiation Facilities – SATIF-9*, ORNL, USA, 21-23 April, 2008, OECD/NEA, pp. 261-274.

[4]   H. Hirayama *et al.* (2010), "Inter-comparison of the Medium-Energy Neutron attenuation in Iron and Concrete (8)", *Proceedings of the Shielding Aspects of Accelerators, Targets and Irradiation Facilities – SATIF10*, CERN, Switzerland, 2-4 June 2010, OECD/NEA, pp. 217-233.

[5]   N. Matsuda *et al.* (2008), "Analyses of Benchmark Problems for the Shielding Design of High Intensity Proton Accelerator Facilities", *JAEA-Technology* 2008-030.

[6]   T. Koi (2010), "A Geant4 physics list for shielding calculation", *Proceedings of the Shielding Aspects of Accelerators, Targets and Irradiation Facilities – SATIF10*, CERN, Switzerland, 2-4 June 2010, OECD/NEA, pp 407-412.

Development of displacement damage model in PHITS and comparison with other codes in a high-energy region

Yosuke Iwamoto[1], Koji Niita[2], Tomotsugu Sawai[1], R.M. Ronningen[3], Thomas Baumann[3]
[1]Japan Atomic Energy Agency, Japan
[2]Research Organisation for Information Science and Technology, Japan
[3]National Superconducting Cyclotron Laboratory, Michigan State University, US

Abstract

The PHITS code (Monte Carlo Particle and Heavy Ion Transport code System) was further developed to include the displacement damage model. The screened Coulomb scattering and the nuclear reaction model was used to evaluate the energy of the target PKA (Primary Knock on Atom) created by the projectile and the secondary particles. These latter include all particles created from the sequential nuclear reactions. It was found that the PKA created by the secondary particles is more dominant than a target PKA created by the projectile in DPA (Displacement per Atom) calculations for proton and neutron induced reactions at energies above 20 MeV. Recently, radiation damage models in other codes such as FLUKA, MARS and MCNP have also been developed. As there is little experimental data in this high-energy region, an intercomparison among Monte Carlo codes such as FLUKA, MARS and MCNP used in the radiation damage calculation is one way to improve models or have a consistent approach. As an example, for the reactions between 130 MeV/u ^{76}Ge ions and tungsten, it was found that DPA values calculated with the PHITS are in good agreement with those of SRIM, which is one of the major codes used to estimate radiation damage in the low-energy region and MARS. For the neutron and proton beams in the energy range from 10 MeV to 1 GeV, the PHITS results agree with those of FLUKA within a factor of two. Further intercomparison among the codes such as MARS, FLUKA, MCNP and PHITS should be carried out, as well as measurements of displacement damage cross-sections.

Introduction

As the power of proton and heavy-ion accelerators increases, the prediction of the structural damage to materials under irradiation is essential. Radiation damage of materials is usually measured as a function of the average number of displaced atoms per all atoms in a material, DPA. For example, ten dpa means each atom in the material has been displaced from its lattice site of the material an average of ten times. DPA serves as a quantitative measure of damage: $DPA = \phi t \sigma_{damage}$; σ_{damage} is the displacement cross-section; and ϕt is the irradiation fluence, i.e. the product of the ion beam flux and the bombardment time. The level of the radiation damage in DPA units is used, for example, to estimate radiation damage of those materials experiencing significant irradiation by primary and "secondary particles" which include all particles created from the sequential nuclear reactions at high-energy, high-intensity facilities such as the Facility for Rare Isotope Beams (FRIB) [1], J-PARC facility [2], European Spallation Source (ESS) [3], and others. The DPA value is a useful measure in correlating results determined by different particles and fluxes in an irradiation environment. However, it is difficult to measure the DPA value in high-energy reactions and the relationships between DPA and material property are at present unclear.

SRIM [4] is one of the major codes used to estimate radiation damage in the low-energy region. SRIM treats the transport of projectile with its Coulomb scattering and makes an approximation of cascade damage. As SRIM does not treat nuclear reactions, the calculated damage is that produced by the primary knock-on atom, PKA, because damage created by the "secondary particles" produced in nuclear reactions is not considered. On the other hand, the nuclear reaction models in the advanced Monte Carlo particle transport code systems such as PHITS [5], MARS15 [6], FLUKA [7] and MCNP [8] have been developed for the calculation of radiation shielding and protection. These codes treat nuclear reactions and create the "secondary particles". Recently, these codes were enhanced with the capability of making realistic predictions of radiation induced damage to materials for the high-energy heavy ion region.

In this paper, we describe the radiation damage model which includes Coulomb scattering and the nuclear reaction in the improved PHITS and compare the improved PHITS results with the prediction of the FLUKA, MARS15 and SRIM. The details (incident particle, energy, target, and Monte Carlo code) of the different calculations are given in Table 1.

Table 1: Calculations performed with Monte Carlo codes

Case	Incident particle	Energy (MeV/nucleon)	Target	Monte Carlo code
A	proton	14,50,200,800	^{63}Cu	PHITS, FLUKA
B	neutron	14,50,200,800	^{63}Cu	PHITS, FLUKA
C	^{76}Ge	130	^{184}W	PHITS, MARS15, SRIM

DPA calculation in PHITS

Overview of DPA calculation in PHITS

High-energy ions travelling through a target lose their energy in three ways; nuclear reaction, electron excitations and Coulomb scatterings. The lower the projectile energy is, the higher the energy transfer to the target atom via Coulomb scattering is. The target atom directly hit by the projectile has usually much lower energy than the projectile itself and, therefore, has a larger cross-section for Coulomb scattering with other target atoms. Thus, the primary knock-on atom (PKA) creates localised cascade damage where many target atoms are displaced from their original lattice site and the number of interstitials

will be equal to the number of vacancies. These point defects and their clusters affect the macroscopic properties, such as hardness.

The conditions of various irradiations will be described by using the damage energy to characterise the displacement cascade. This is defined as the initial energy of target PKA, corrected for the energy lost to electronic excitations by all of the particles composing the cascade. There are mainly two processes to produce the target PKA for heavy-ions and proton incident reactions, as shown in Figure 1. One is the Coulomb scattering due to PKA's directly created by the projectile, and the other is that due to PKA's created by the secondary particles. In this work, the energy of the secondary charged particles is obtained by PHITS calculations using the nuclear reaction model of JQMD and Bertini for heavy-ion and proton, respectively, and the evaporation model of GEM [5]. Details of the model are presented in our previous paper [9].

Figure 1: Overview of DPA calculations in PHITS
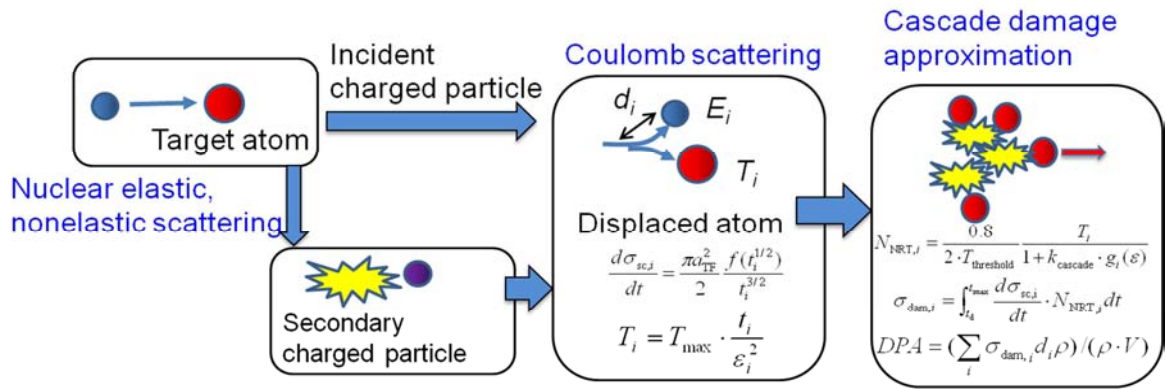
Coulomb scattering with target atom

To simplify differential cross-section calculations even further, J. Lindhard, V. Nielsen, and M. Scharff [10] introduced a universal one-parameter differential scattering cross-section equation in reduced notation:

$$d\sigma_{sc} = \frac{\pi a_{TF}^2}{2} \frac{f(t^{\frac{1}{2}})}{t^{3/2}} \, dt \, d\sigma_{sc} = \frac{\pi a_{TF}^2}{2} \frac{f(t^{\frac{1}{2}})}{t^{3/2}} \, dt \qquad \qquad \frac{d\sigma_{sc}}{dt} = \frac{\pi a_{TF}^2}{2} \frac{f(t^{1/2})}{t^{3/2}} \qquad (1)$$

where t is a dimensionless collision parameter defined by:

$$t \equiv \varepsilon \frac{T}{T_{max}} = \varepsilon^2 \sin^2(\frac{\theta_c}{2}) \qquad (2)$$

$t \equiv \varepsilon^2 \frac{T}{T_{max}} = \varepsilon^2 \sin^2\left(\frac{\theta_c}{2}\right) t \equiv \varepsilon^2 \frac{T}{T_{max}} = \varepsilon^2 \sin^2\left(\frac{\theta_c}{2}\right)$ where T is the transferred energy to the target and T_{max} is the maximum transferred energy as:

$$T_{max} = \frac{4 M_1 M_2}{(M_1 + M_2)^2} E_p \qquad (3)$$

where E_p is the energy of incident and secondary charged particle. ε is the dimensionless energy as:

$$\varepsilon \equiv \frac{a_{TF}}{d_c} = \frac{a_{TF} E}{Z_1 Z_2 e^2} \qquad (4)$$

$\varepsilon \equiv \frac{a_{TF}}{d_c} = \frac{a_{TF}E}{Z_1 Z_2 e^2}$In the above expression, d_c is the unscreened (i.e. Coulomb) collision diameter or distance of closest approach for a head-on collision (i.e. b=0), and a_{TF} is the screening distance.

Lindhard *et al.* considered $f(t^{1/2})$ to be a simple scaling function and the variable t to be a measure of the depth of penetration into the atom during a collision, with large values of t representing small distances of approach. $f(t^{1/2})$ can be generalised to provide a one parameter universal differential scattering cross-section equation for interatomic potential such as screened and unscreened Coulomb potentials. The general form is:

$$f\left(t^{\frac{1}{2}}\right) = \lambda t^{\frac{1}{2}-m}\left[1 + (2\lambda t^{1-m})^q\right]^{-1/q}$$

$$f(t^{1/2}) = \lambda t^{1/2-m}\left[1 + (2\lambda t^{1-m})^q\right]^{-1/q} \tag{5}$$

where λ, m, and q are fitting variables, with λ=1.309, m=1/3 and q=2/3 for the Thomas-Fermi version [11] of $f(t^{1/2})$. The value of $t^{1/2}$ increases with an increase in a dimensionless energy ε, scattering angle in the CM system, and impact parameter. The Coulomb scattering cross-section in the energy region above the displacement threshold energy can be calculated from the following expression:

$$\sigma_{sc} = \int_{t_d}^{t_{max}} \frac{d\sigma_{sc}}{dt} \cdot dt \tag{6}$$

where t_{max} in dimensionless is equal to ε^2 from equation (2) when $\theta=\pi$. t_d is the displacement threshold energy in dimensionless given by equation (4). Displacement threshold energy $T_{threshold}$ is typically in the range between 20 and 90 eV for most metal.

Displacement cross-sections

To estimate the damage cross-sections the NRT formalism of Norgett, Robinson, and Torrens and Robinson [12] is employed as a standard to determine that fraction of the energy of the PKA of the target which will produce damage, e.g. further nuclear displacements. The displacement cross-sections, which indicate the scattering cross-section multiplied by the number of defects, can be evaluated from the following expression:

$$\sigma_{damage} = \int_{t_d}^{t_{max}} d\sigma/dt \times \nu(Z_{target}, A_{target}, T_{target})dt \, \sigma_{damage} =$$
$$\int_{t_d}^{t_{max}} d\sigma/dt \times \nu(Z_{target}, A_{target}, T_{target})dt$$

$$\sigma_{damage} = \int_{t_d}^{t_{max}} \frac{d\sigma_{sc}}{dt} \cdot N_{NRT} dt \tag{7}$$

where N_{NRT} is the number of defects based on the Kinchin and Pease formula [13] modified by Norgett *et al.* and using the Lindhard slowing-down theory, in irradiated material calculated by:

$$N_{NRT} = \frac{0.8 \cdot T_{damage}}{2 \cdot T_{threshold}} \tag{8}$$

The constant 0.8 in the formula is the displacement efficiency given independent of the PKA energy, the target material, or its temperature. The value is intended to compensate for forward scattering in the displacement cascade of the atoms of the lattice. T_{damage} is the "damage energy" transferred to the lattice atoms reduced by the losses for electronic stopping in the atom displacement cascade and is given by Norgett, Robinson, and Torrens.

$$T_{damage} = \frac{T}{1 + k_{cascade} \cdot g(\varepsilon)} \tag{9}$$

where T is the transferred energy to target atom given by Equation (2) as:

$$T = T_{max} \cdot \frac{t}{\varepsilon_p^2} \tag{10}$$

where ε_p is the dimensionless projectile energy given by Equation (4) and the projectile energy E_p. The parameters $k_{cascade}$, and $g(\varepsilon)$ are as follows:

$$k_{cascade} = 0.1337 Z_{target}^{1/6} (Z_{target} / A_{target})^{1/2} \tag{11}$$

$$g(\varepsilon) = \varepsilon + 0.40244 \cdot \varepsilon^{3/4} + 3.4008 \cdot \varepsilon^{1/6} \tag{12}$$

ε is the dimensionless transferred energy given by Equations (4) and (10). Note that this calculation does not include the self-healing of lattice defects.

DPA values

DPA value is calculated from the following expression:

$$DPA = (\sum_i \sigma_{damage, i} d_i \rho) / (\rho \cdot V) \tag{13}$$

where d_i is the travelling length of incident charged particles and secondary ones in the target calculated by using SPAR code [14]. ρ and V is the atomic density and volume of the target, respectively.

DPA calculations using PHITS and other codes

Based on the above formalisms, we calculated DPA distributions in thick Cu and W for various beams listed in Table 1 and compared to calculated results using FLUKA, MARS15 and SRIM codes. Beam area was 1 cm² and target geometry was cylinder with 5 cm radius and each depth. All the calculated results were normalised by the number of incident particles.

Case A: Proton into Cu using PHITS and FLUKA

Figure 2 shows calculated results for 14, 50, 200 and 800 MeV protons. Displacement threshold energy $T_{threshold}$ was 30 eV in PHITS and 40 eV in FLUKA for Cu. For the proton beams in the energy range from 10 MeV to 1 GeV, the PHITS results agree with those of FLUKA within a factor of two. In higher energy, nuclear reactions occur before the stopping range is reached and DPA values produced by PKA directly created by the secondary are increased with energy. For 800 MeV, well-developed hadronic cascades are appeared.

Case B: Neutron into Cu using PHITS and FLUKA

Figure 3 shows calculated results for 14, 50, 200 and 800 MeV neutrons. PHITS results also agree with those of FLUKA within a factor of two because the production of secondary particles in PHITS is almost the same as that in FLUKA. Note that neutron cannot create the radiation damage in the model. Secondary charged particles created by nuclear elastic and nonelastic scattering contribute to the damage calculation.

Case C: ^{76}Ge into W using PHITS, MARS15 and SRIM

Figure 4 shows calculated results by using PHITS, SRIM and MARS15. We selected "Quick Calculation of Damage" as the SRIM option for DPA calculations. The damage calculated with this option is from the statistical estimates based on the Kinchin-Pease formalism. SRIM treats only Coulomb scattering for the projectile and cannot produce "secondary particles" from nuclear reactions. MARS15 code is Monte Carlo transport code for an accurate description of radiation effects in numerous applications at high-power beam facilities. The improved PHITS results were close to SRIM and MARS15 results for DPA values produced by PKA directly created by the ^{76}Ge projectiles. In the 130 MeV/u ^{76}Ge and tungsten system, Coulomb scattering created by the ^{76}Ge projectiles is more dominant than that created by the "secondary particles" produced by nuclear reactions.

Figure 2: Calculated results for 14, 50, 200 and 800 MeV protons into a thick Cu target using PHITS and FLUKA
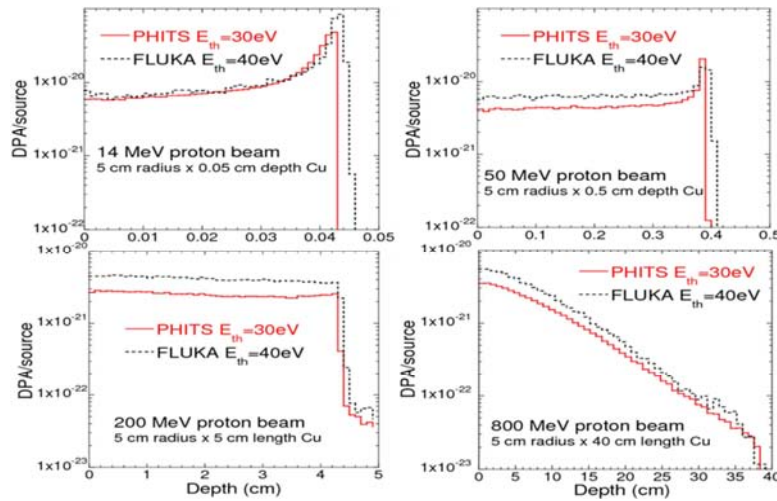
Figure 3: Calculated results for 14, 50, 200 and 800 MeV neutrons into a thick Cu target using PHITS and FLUKA
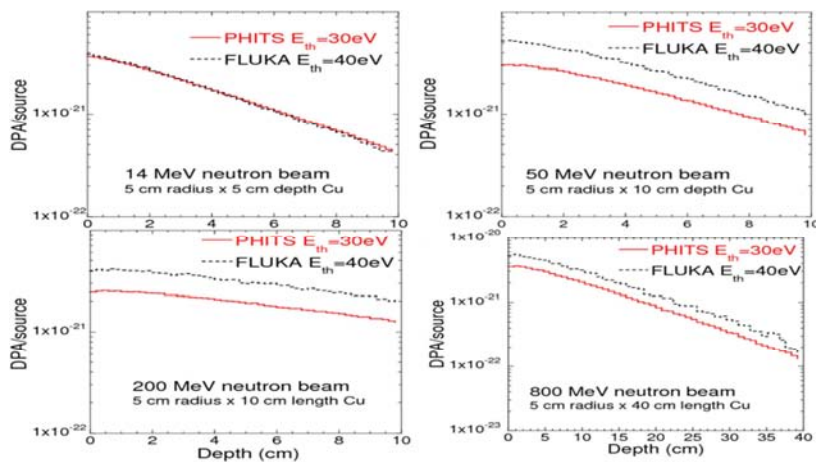
Figure 4: Calculated results for 130 MeV/u ^{76}Ge into W target using PHITS, SRIM and MARS15
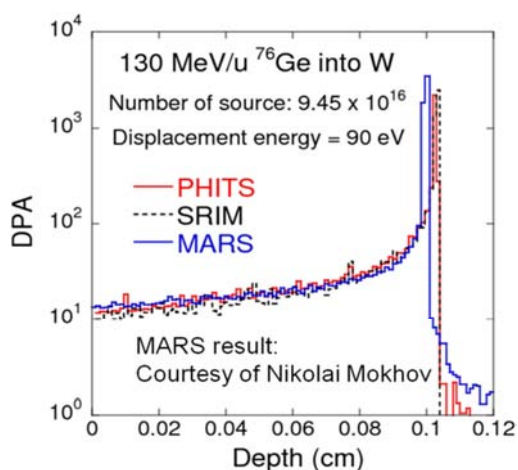
Summary

The PHITS code was further developed to include the displacement damage model. The screened Coulomb scattering and the nuclear reaction model were used to evaluate the energy of the target PKA created by the projectile and the secondary particles. These latter include all particles created from the sequential nuclear reactions. It was found that the PKA created by the secondary particles is more dominant than a target PKA created by the projectile in DPA calculations for proton and neutron induced reactions at energies above 20 MeV. Recently, radiation damage models in other codes such as FLUKA, MARS, and MCNP have also been developed. As there are few experimental data in this high-energy region, an intercomparison among Monte Carlo codes such as FLUKA, MARS, and MCNP used in the radiation damage calculation is one way to improve models or have a consistent approach. As an example, for the reactions between 130 MeV/u ^{76}Ge ions and tungsten, it was found that DPA values calculated with the PHITS are in good agreement with those of SRIM and MARS. For the neutron and proton beams in the energy range from 10 MeV to 1 GeV, the PHITS results agree with those of FLUKA within a factor of two. Further intercomparison among the codes such as MARS, FLUKA, MCNP and PHITS should be carried out, as well as measurements of displacement damage cross-sections. In the future, there is a need to consider new DPA values that go beyond the standard proposed by Norget, Robinson and Torrens (NRT) in 1975.

Acknowledgements

References

[1]   Facility for Rare Isotope Beams websites at: http://www.frib.msu.edu/.

[2]   J-PARC websites at: http://j-parc.jp/index-e.html.

[3]   European Spallation Source websites at: http://ess-scandinavia.eu/.

[4]   J.F. Ziegler, "The Stopping and Range of Ions in Solids", by J.F. Ziegler, J.P. Biersack, U. Littmark, Pergamon Press, New York, 1985, http://www.srim.org/.

[5]   K. Niita, N. Matsuda, Y Iwamoto, H. Iwase, T. Sato, H. Nakashima, Y. Sakamoto, L. Sihver (2010), "PHITS: Particle and Heavy Ion Transport code System, Version 2.23", JAEA-Data/Code, 2010-022, http://phits.jaea.go.jp/.

[6]   N.V. Mokhov, "The MARS Code System User's Guide", Fermilab-FN-628 (1995); N.V. Mokhov, S.I. Striganov, "MARS15 Overview", *Proc. of Hadronic Shower Simulation Workshop, Fermilab,* September 2006, AIP Conf. Proc. 896, pp. 50-60 (2007); http://www-ap.fnal.gov/MARS/.

[7]   A. Fassò, A. Ferrari, J. Ranft, P.R. Sala (2005), "FLUKA: a multi-particle transport code", CERN-2005-10, INFN/TC_05/11, SLAC-R-773.

[8]   L.S. Water (2002), (Ed.), "MCNPX User's Manual version 2.4.0", LA-CP-02-408, Los Alamos National Laboratory, Los Alamos, New Mexico.

[9]   Y. Iwamoto, K. Niita, T Sawai, R.M. Ronningen, T. Baumann (2012), "Improvement of radiation damage calculation in PHITS and tests for copper and tungsten irradiated with protons and heavy-ions over a wide energy range", *Nucl. Instr. and Meth. B 274,* 57-64.

[10]   J. Lindhard, V. Nielsen, M. Scharff, P.V. Thomsen (1965), Mat. Fys. Medd. Dan. Vid. Selsk., Vol. 138, No. A1815.

[11]   K.B. Winterbon, P. Sigmund, J.B. Sanders (1970), Mat. Fys. Medd. Dan. Vid. Selsk. 37 no. 14.

[12]   M.J. Norgett, M.T. Robinson, I.M. Torrens (1975), "A proposed Method of Calculating Displacement Dose Rates", *Nucl. Engineering and Design*, 33, 50-54.

[13]   G.H. Kinchin, R.S. Pease (1955), *Rep. Progr. Phys., 18, 1.*

[14]   T.W. Armstrong, K.C. Chandler (1973), ORNL-4869, Oak Ridge National Laboratory.

EASY-II (12): A system for modelling of n, d, p activation and transmutation processes

Jean-Christophe Sublet[1], James Eastwood[2], Guy Morgan[2], Arjan Koning[3], Dimitri Rochman[3]
[1]UK Atomic Energy Authority, Culham Science Centre, UK,
[2]Culham Electromagnetics Ltd, Culham Science Centre, UK,
[3]Nuclear Research and Consultancy Group, The Netherlands

Abstract

EASY-II (12) is designed as a functional replacement for the previous European Activation System, EASY-2010. It has extended nuclear data and new software, FISPACT-II, written in object-style Fortran to provide new capabilities for predictions of activation, transmutation, depletion and burn-up. The new FISPACT-II code has allowed us to embed many more features in terms of energy range, up to GeV; incident particles: alpha, gamma, proton, deuteron and neutron; and neutron physics: self-shielding effects, temperature dependence, pathways analysis, sensitivity and error estimation using covariance data. These capabilities cover most application needs: nuclear fission and fusion, accelerator physics, isotope production, waste management and many more. In parallel, the maturity of modern general-purpose libraries such as TENDL-2011 encompassing thousands of target isotopes, the evolution of the ENDF format and the capabilities of the latest generation of processing codes PREPRO, NJOY and CALENDF have allowed the FISPACT-II code to be fed with more robust, complete and appropriate data: cross-sections with covariance, probability tables in the resonance ranges, kerma, dpa, gas and radionuclide production and 24 decay types. All such data for the five most important incident particles are placed in evaluated data files up to an incident energy of 200 MeV. The resulting code and data system, EASY-II (12), includes many new features and enhancements. It has been extensively tested and also benefits from the feedback from extensive validation and verification activities performed with its predecessor.

Introduction

FISPACT-II [1] is a completely new inventory code initially designed to be a functional replacement for Fispact-2007. This new code is written in object-style Fortran 95 and has extended physical models, a wider range of irradiation options and improved numerical algorithms compared to the old code. Users familiar with the old code will be able for most cases to use the new code with their existing control input files. Some new keywords have been added to deal with the new capabilities, and some of the old keywords have become obsolete.

The major change introduced in this first release of FISPACT-II was the addition of the reading and processing of alternative ENDF-format library data sets. This has caused a major overhaul of the data input parts of the software and a huge expansion of the number of nuclides and reactions that can be treated. Sensitivity and error prediction capabilities have been extended, and better fission yield data and cross-section data in more energy groups up to higher energies can now be used. The present version can also handle more irradiating projectiles (α, γ, n, p, d) and provides additional diagnostic outputs (kerma, dpa and gas appm rates) if the ENDF-format library contains the required input data. The new code can also connect to any version of EAF-formatted libraries [2].

The new inventory code when associated with a set of nuclear data libraries (EAF-2007, EAF-2010 or TENDL-2011 [3]), plus decay, biological, clearance and transport indices libraries, forms the European Activation System EASY-II (12) (Figure 6).

The models

The FISPACT-II code follows the evolution of the inventory of nuclides in a target material that is irradiated by a time-dependent projectile flux ϕ, where the projectiles may be neutrons, protons, deuterons, α-particles or γ-rays. The material is homogeneous, infinite and infinitely dilute and the description of the evolution of the nuclide numbers is reduced to the stiff-ode Equation (1) for N_i the number of atoms of nuclide i [4]. The key characteristics of the system of inventory equations are that they are linear, stiff and sparse.

$$\frac{dN_i}{dt} = -N_i(\lambda_i + \sigma_i\varphi) + \sum_{j \neq i} N_j(\lambda_{ij} + \sigma_{ij}\varphi) \tag{1}$$

Here λ_i and σ_i are respectively the total decay constant and cross-section for reactions on nuclide i. σ_{ij} is the cross-section for reactions on nuclide j producing nuclide i, and for fission it is given by the product of the fission cross-section and the fission yield fractions. λ_{ij} is the constant for the decay of nuclide j to nuclide i.

The stiffness of the system of equations limits the choice of numerical methods. The code uses the Livermore solver for ordinary differential equations LSODES [5] to solve the stiff ode set. LSODES implements Gear's method and uses the Yale sparse matrix package to handle the Jacobian matrices. This numerical solver compares advantageously with the previous EXTRA ode solver, written in 1976, and used in Fispact-2007. FISPACT-II has a wrapper ode module around LSODES that automatically sets storage and parameters for that solver, improving portability and reducing the need for user input.

Note that FISPACT-II differs from Fispact-2007 in that it does not employ the equilibrium approximation for short-lived nuclides, and includes actinides self-consistently in the rate equations [Equation (1)] rather than as a source term. The new code has been shown to be able to handle short (1ns) time interval and high flux cases that caused problems for older codes.

Pathways

The reaction network may be described either by the rate equations or as the sum of paths and loops, which we refer to as pathways. The inventory of a given nuclide computed using the rate equations can equivalently be found by a linear superposition of contributions of flows along the pathways to that nuclide. Pathways analysis is used in identifying significant nuclides and reactions, and in performing sensitivity and uncertainty analyses.

Pathways analysis uses directed graph algorithms implemented using breadth-first tree searches with pruning for finding routes from a parent to chosen descendants, and for the assembly and solution of a subset of the rate equations for nuclides on a pathway to get the flow along that pathway. Pathways analyses may be performed for single and multiple step irradiation scenarios, and where the cross-sections are time dependent.

Uncertainty estimates

Pathways analysis identifies the pathways from the initial inventory nuclides to the (target) dominant nuclides at the end of the irradiation phase, and provides the number of atoms of each nuclide produced by reactions and decays along each pathway. These, together with uncertainties derived from the covariances in the reaction cross-sections and decay half-lives associated with the edges of the pathways are used in FISPACT-II to provide estimates of the uncertainties. The uncertainties are then computed for significant radiological quantities, e.g. number density, decay heat, dose rate, inhalation or ingestion hazards.

More accurate uncertainty estimates which may also include covariance between different reaction cross- sections can be undertaken by combining pathways analysis with monte-carlo sensitivity calculations.

Nuclear data libraries

FISPACT-II requires connection to several data libraries before it can be used to calculate inventories. While any libraries in the correct format could be used, the code has been designed to use the European Activation Files, a recommended source of cross-section data in the EAF format. The following libraries are required: cross-section data for projectile-induced reactions, uncertainty data for neutron-induced reactions, decay data, fission yields, biological hazard, legal transport, clearance and gamma absorption data. It is the user choice to select from the 2007 or 2010 library versions. There are nine standard energy group structures that may be used with the EAF libraries.

Alternatively, any libraries in the correct ENDF-6 format could be used. The development of FISPACT-II over the last few years has run in parallel with the development of the TALYS-based Evaluated Nuclear Data Library (TENDL) Project and those European libraries are also a recommended source of cross-section data [3].

Cross-sections

The TENDL-2011 library [3] is the current recommended evaluated data source for use in any type of nuclear technology applications (Figures 1-3). The principal advances of this new library are in the unique target coverage, 2 424 nuclides; the upper energy range, 200 MeV; variance and covariance information for all nuclides; and the extension to cover all important projectiles: neutron, proton, deuteron, alpha and gamma, and last but not least the proven capacity of this type of library to transfer regularly to technology the feedbacks of extensive validation, verification and benchmark activities from one release to the next.

Figure 1: Sample neutron library cross-sections from the TENDL-2011 pendf, 200 MeV library data
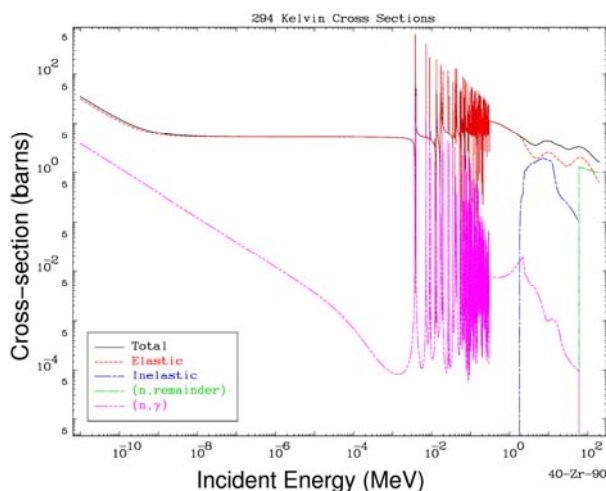
TENDL-2011 is the fourth generation of such a library and as such has benefited from the previous releases and from the EAF-2010 V&V processes.

Figure 2: TENDL-2011 pendf, 200 MeV, gas production
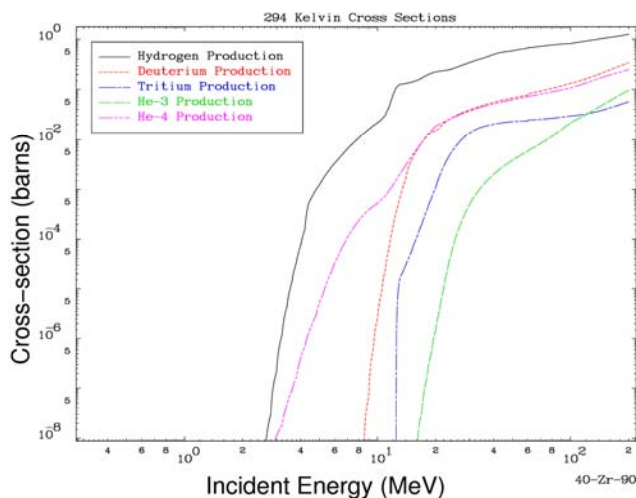
The cross-section data are provided in two universal group structures: a CCFE (709) scheme for the neutron-induced cross-sections and a CCFE (162) scheme for the non-resonant p, d, α and γ-induced cross-sections. The data format used is fully compliant with the ENDF-6 manual specification handled on an isotopic basis and so allows many existing utility codes to further manipulate, visualise or check any aspects of the pre-processed files. The data files are produced using a complex but robust, complementary sequence of modules of the processing codes NJOY-99, PREPRO-2010 and CALENDF-2010.

Figure 3: TENDL-2011 pendf, 200 MeV, γ cross-sections
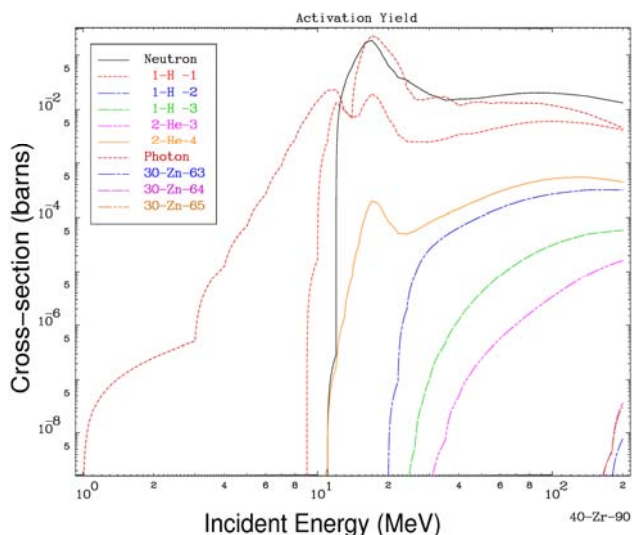
Fission yields

The fission yield data need to be provided for each actinide and incident particle. Only 19 of the many nuclides that undergo fission have any fission yield data in JEFF-3.1.1 and these cover only a reduced energy range. For the remainder, the UKFY-4.1 library then further extends the range before a neighbouring fission yield is used. This UKFY-4.1 library using Wahl's systematics is also used for all other particle-induced fission yields.

Variance-covariance

Above the upper energy of the resolved resonance range, for each of the 2 424 isotopes a Monte Carlo method in which the covariance data come from uncertainties of the nuclear model calculations is used. All information on cross-section covariance is stored in the MF=33 or 40 formats, starting at the end of the resonance range up to 200 MeV. Short-range, self-scaling variance components are also specified for each MT type. The data format used to store the variance-covariance information has been made fully compliant with the ENDF-6 format description and the files are read directly by FISPACT-II (12) without any further intermediate processing.

Self shielding of resonant channels

The CALENDF-2010 [6] nuclear data processing system is used to convert the evaluation defining the cross-sections in ENDF-6 format (i.e. the resonance parameters, both resolved and unresolved) into forms useful for applications. Those forms used to describe neutron cross-section fluctuations correspond to "cross-section probability tables", based on Gauss quadrature and effective cross-sections. FISPACT-II iteratively solves for the dilution cross-section (which depends on mixture fractions and total shielded cross-section) and the shielded cross-section for nuclides in the mixture (which depends on dilution cross-section and probability table data) [1] [6].

Figure 4: Self-shielding effects for different dilutions
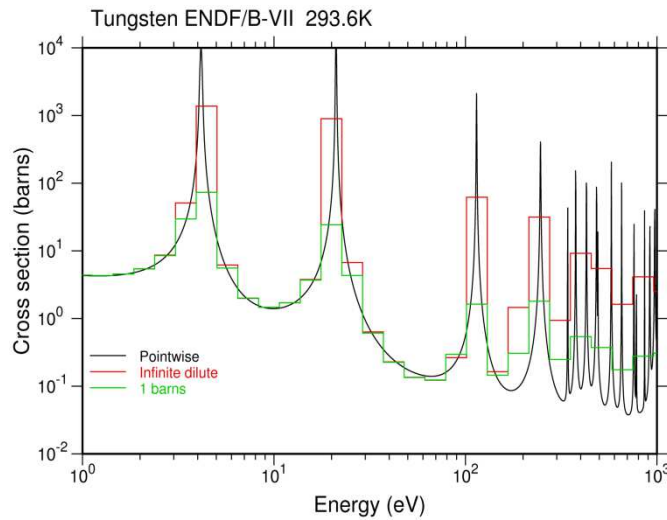
Figure 5: CALENDF improves the cross-section description in the URR energy range
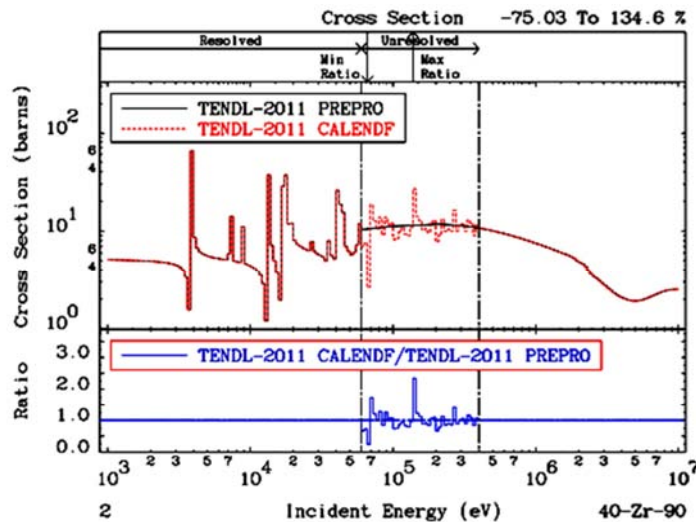
CALENDF-2010 provides probability tables in the energy range from 0.1 eV up to the end of the resolved or the unresolved resonance range. Probability table data in 709 energy group format are provided for 2 143 isotopes of the TENDL-2011 library. These data are used to model dilution self-shielding effects from channel, isotopic or elemental interferences. Doppler broadening effects are included and the tables are given at three temperatures: 293.6, 600 and 900 degree Kelvin.

The dilution cross-sections computed using the CALENDF data are applied either as scaling factors to the library cross-section data or as replacements over the energy ranges for which the probability table data are available [1]. This ability to self-shield, in much the same way as is done in deterministic transport codes and in Monte Carlo codes for the unresolved resonance range (URR) is believed to be unique among inventory codes.

Decay data

In addition to cross-sections, the other basic quantities required by an inventory code are information on the decay properties (such as half-life) of all the nuclides considered. FISPACT-II is able to read the data directly in ENDF-6 format; it requires no pre-processing to be done. The now well-verified and validated EAF_dec_2010 library based primarily on the JEFF-3.1.1 and JEF-2.2 radioactive decay data libraries, with additional data from the latest UK evaluations, UKPADD-6.10, contains 2 233 nuclides. However, to handle the extension in incident particle type, energy range, number of targets and many more decay data are needed. A new 3873-nuclide decay library dec_2012 has been assembled from EAF_dec_2010 complemented with all of JEFF-3.1.1 and a handful of ENDF/B-VII.1 decay files.

Radiological data

The radiological data for the increased number of nuclides present in the TENDL-2011 data are computed in the same manner as described for the EAF data. The new hazards, clearance and transport data are respectively for 3 647, 3 873 and 3 872 nuclides, compared to 2006, 2233 and 2233 for the EAF data.

Figure 6: EASY-II (12): FISPACT-II and TENDL-2011
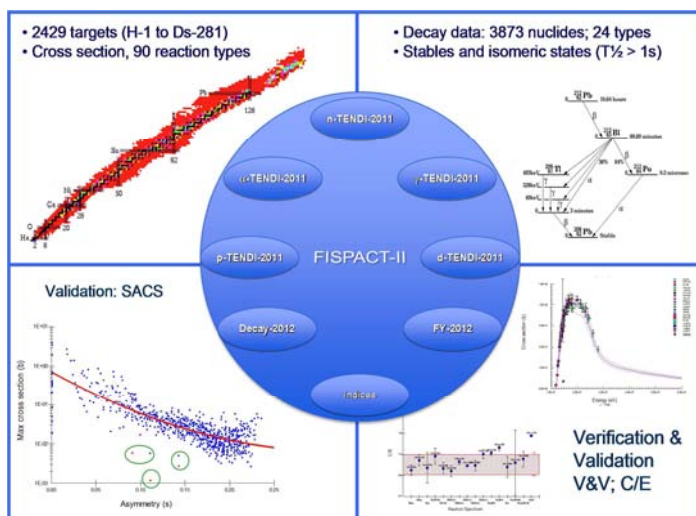
Verification and validation

Verification and validation (V&V) is a critical, yet often overlooked, part of scientific computer code development. Careful software lifecycle management under configuration control has been used for the code, unit and integration tests and validation tests. FISPACT-II is distributed with over 400 input/output regression tests that preserve and extend the validation heritage of Fispact-2007. Further V&V processes are being actively deployed in support of EASY-II.

Conclusion

EASY-II (12) is a new versatile multi-particle inventory code package aimed at satisfying all activation-transmutation requirements for facilities in support of any nuclear technology: stockpile and fuel cycle stewardship, materials characterisation, and life cycle management. It has been developed and tested for magnetic and inertial confinement fusion, fission Generation-II,-III,-IV plant generations; high-energy and

accelerator physics; medical applications, isotope production; earth exploration and astrophysics.

Acknowledgements

References

[1] J-Ch. Sublet, J.W. Eastwood, J.G. Morgan (2012), "The FISPACT-II User Manual", CCFE-R(11)11.

[2] EASY-II European Activation SYstem, http://www.ccfe.ac.uk/EASY.aspx.

[3] TENDL-2011, http://www.talys.eu/tendl-2011.

[4] H. Bateman, "The solution of a system of differential equations occurring in the theory of radio-active transformations", *Proc. Camb. Phil. Soc., 15:423*, 1910.

[5] K. Radhakrishnan, A.C. Hindmarsh (1993), "Description and use of LSODE, the Livermore solver for ordinary differential equations", *Technical Report LLNL Report UCRL-ID-113855, LLNL.*

[6] J-Ch. Sublet, P. Ribon, M. Coste-Delclaux (2011), "CALENDF-2010: User Manual", CEA-R-6277, ISSN 0429-3460, CEA.

Current status of accelerator benchmarks in OECD/NEA radiation shielding experiments database SINBAD

Ivan Kodeli[1], Pedro Ortego[2], Robert E. Grove[3], Akifumi Yamaji[4]
[1]Jožef Stefan Institute, Ljubljana, Slovenia,
[2]SEA, Madrid, Spain,
[3]ORNL, Oak Ridge, US,
[4]OECD/NEA, Issy-les-Moulineaux, France

Abstract

In order to preserve and make available the information on the performed radiation shielding benchmarks the Data Bank of the OECD Nuclear Energy Agency (OECD/NEADB) and the Radiation Safety Information Computational Center (RSICC) at Oak Ridge National Laboratory (ORNL) started the Shielding Integral Benchmark Archive and Database (SINBAD) Project in the early 1990s. The SINBAD database now comprises 100 shielding benchmarks, also covering accelerator shielding benchmarks in addition to fission reactor shielding and fusion blanket neutronics. Recently, a thorough revision of six of the 23 accelerator benchmark experiments was completed in order to provide detailed verification of the completeness and consistency of the benchmark information, in particular concerning the evaluation of the experimental sources of uncertainty. This review process is expected to provide users with an easier choice and help them make better use of the experimental information and is planned to be extended to other available benchmarks.

The OECD NEA Working Party on Scientific Issues of Reactor Systems (WPRS) Expert Group on Radiation Transport and Shielding (EGRTS) was created in 2011 and its mandate is to monitor, steer and support the continued development of the SINBAD database. Co-ordination of the SATIF-11 Workshop is part of the mandate of EGRTS and the development of the accelerator benchmark database is done in a close co-operation with the SATIF expert group. Proposals and assistance in new benchmark compilations are welcome.

SINBAD is available at no charge from RSICC and from the NEA Data Bank. Since its beginnings SINBAD has been used by nuclear data evaluators, computer code developers, experiment designers and university students.

Introduction

The SINBAD project started in the early 1990s as a collaboration between the OECD NEA Data Bank (OECD/NEADB) and the Radiation Safety Information Computational Center (RSICC) at the Oak Ridge National Laboratory (ORNL) with the goal of preserving the information on the performed radiation shielding benchmarks and making them available in a standardised form to the international community. The SINBAD database now comprises 100 shielding benchmarks, divided into three categories, covering both low-and intermediate-energy particles applications: fission reactor shielding (46 benchmarks), fusion blanket neutronics (31), and accelerator shielding (23) benchmarks. In addition to the characterisation of the radiation source, description of shielding set-up, instrumentation and the relevant detectors, most sets in SINBAD contain also the deterministic or probabilistic (Monte Carlo) radiation transport computer model used for the interpretation of the experiment and, where available, results from uncertainty analysis. The set of primary documents used for the benchmark compilation and evaluation are provided in computer readable form. Table 1 lists the accelerator shielding experiments presently included in SINBAD.

The OECD NEA Working Party on Scientific Issues of Reactor Systems (WPRS) Expert Group on Radiation Transport and Shielding (EGRTS) was created in 2011 and its mandate is to monitor, steer and support the continued development of the SINBAD database. Co-ordination of the SATIF-11 Workshop is part of the mandate of EGRTS and the development of the accelerator benchmark database is done in close co-operation with the SATIF expert group. Proposals and assistance in new benchmark compilations are welcome.

The database is intended for different users, including nuclear data evaluators, computer code developers, experiment designers and university students. SINBAD is available at no charge from RSICC and from the NEA Data Bank.

Present status of the accelerator benchmarks, quality review and future plans

Since the experimental data currently available in SINBAD are of varying quality, a thorough revision and classification of the benchmark experiments according to the completeness, reliability and consistency of information was undertaken recently. A series of 34 experiments, among them 6 accelerator experiments, mostly of relevance for fusion neutronics and for accelerator shields were already, or are currently being revised and reclassified. The six of the 23 accelerator benchmark experiments which have already gone through the revision process are listed in Table 2. The review concentrated on the verification of the description of the experimental set-up, the neutron source specifications, the detector characteristics, the geometry and precise material composition of the components. The main criteria for the judgment of the quality of the experiment were the completeness and the consistency of the experimental information (on the geometry, materials, the procedure to derive data-unfolding, etc.), in particular concerning the evaluation of the experimental sources of uncertainty. New or improved inputs for computer codes such as MCNPX and PHITS were prepared and the sensitivity analyses were performed to estimate the impact of the approximations used in the computational model. The following two guidelines were pursued when preparing the computational models:

Table 1: Accelerator shielding experiments in SINBAD

Benchmark	Shielding material	Projectile	Measured quantity	Computer code input
Transmission of n & γ generated by 52 MeV p	C (< 64.5 cm thick), Fe (< 57.9 cm), H_2O (< 101 cm), concrete (< 115 cm)	52 MeV protons on C target	NE213 scintillator	MCNPX
Transmission of n & γ generated by 65 MeV p	Concrete, Fe, Pb, graphite (10 to 100 cm thick)	65 MeV protons on Cu target	NE213 scintillator	No
Transmission of medium energy neutrons through concrete shields (1991)	Concrete	a 75-MeV proton beam incident on a stopping-range Cu assembly	7.6-cm-diameter x 7.6-cm-long NE-213 scintillator	Yes, MCNPX
Neutron production from thick targets of C, Fe, Cu and Pb by 30- and 52-MeV protons(1982)	Stainless steel 316	30- and 52-MeV protons incident on C, Fe, Cu, and Pb targets	NE 213 scintillator	Yes, MCNPX
TIARA 40 and 65 MeV Neutron transmission through iron, concrete and polyethylene	Fe (130 cm), concrete (< 200 cm), polyethylene (up to 180 cm)	43 and 68 MeV protons on Li-7 target	BC501A, Bonner ball, fission counters, TLD, SSNTD	MORSE-CG, HETC-KFA2, DORT,MCNP4B, LAHET HMCNP
Radioactivity induced by GeV-protons & spallation neutrons (2001)	B, C, Al, Fe, Cu, Nb, HgO, Pb, Pb, acrylic resin, SS-316, Inconel	2.83 and 24 GeV protons on mercury target	HPGe	No
Intermediate-and high-energy accelerator shielding benchmarks	C, Al, and Fe	113 and 800 MeV protons	BC-418 plastic scintillators	No
ROESTI I, II and III	Fe and Pb (100 cm thick)	200 GeV/c hadrons (2/3 p$^+$,1/3 π^+) (Roesti I&III), 24 GeV/c p$^+$ (Roesti II)	In, S, Al, C foils, RPL	Yes, FLUKA92
CERF bonner sphere response to charged hadrons	Polyethylene/Cd/Pb	120 GeV/c positive hadrons(1/3 p and 2/3 π)	Bonner sphere - a spherical centronics SP9 3He counter	Yes, FLUKA
CERF Radionuclide production (~2003)	steel, Cu, Ti, concrete, light materials such as C composites and B- nitride	120 GeV/c mixed hadrons (1/3 p, 2/3 π^+)	High-purity germanium (HPGe) for gammas	Yes, FLUKA
CERF residual dose rates (2003)	Al, Cu, Fe, Ti, concrete	120 GeV/c mixed hadrons (1/3 p , 2/3 π^+)	Nal crystal	Yes, FLUKA
CERF shielding experiment at CERN (2004)	cylindrical Cu target	120 GeV/c mixed hadron (1/3 p, 2/3 π^+)	NE213 organic liquid scintillator	Yes, MARS15
CERN 200 and 400 GeV/c protons activation experiments (1983)	Cu targets	200 GeV/c and 400 GeV/c extracted protons	Thermo-, photo-luminescent and optical absorption glass dosimeters, Al, Au, S, Cu foils & plastic scintill.	No
RIKEN quasi-monoenergetic neutron field (70-210 MeV)	Air	70 – 210 MeV protons on ^{7}Li	NE213 scintillator (TOF)	No
KENS p-500 MeV shielding experiment at KEK	Concrete	500MeV protons on thick W target	Activation of Bi, Al, In and Au foils	Yes, MARS14
HIMAC He, C, Ne, Ar, Fe, Xe and Si ions on C, Al, Cu and Pb targets	C, Al, Cu and Pb targets	100-800 MeV/ nuc. He, C, Ne, Ar, Fe, Xe & Si ions	NE213 & NE102A scintillators	Yes, MCNPX
HIMAC/NIRS high-energy neutron (up to 800 MeV)	Fe (up to 100 cm)	400 MeV/nucleon C ions on Cu target	Neutron spectra by self-TOF, NE213	Yes, PHITS
HIMAC/NIRS high-energy neutrons (< 800 MeV)	Concrete (up to 250 cm)	400 MeV/nucleon C ions on Cu target	Self-TOF, NE213, Bi and C foils	Yes, PHITS
BEVALAC experiment - Nb Ions on Nb & Al targets	Nb (0.51 and 1 cm thick) and Al (1.27 cm thick)	272 & 435 MeV/nucl. Nb ions	NE-102 scintillator	No
MSU 155 MeV/nucleon He & C ions on Al target	Al (13.34 cm)	155 MeV/nucleon He and C ions	BC-501, NE213 (TOF)	Yes, MCNPX
PSI – high-energy neutron spectra generated by 590-MeV protons on Pb target	Pb target (60 cm)	590 MeV protons	NE213 (TOF)	Yes
ISIS deep penetration of neutrons through concrete & Fe	Concrete (120 cm) and Fe (60 cm)	800 MeV protons on Ta target	C, Bi, Al, In$_2$O$_3$ foils, n & γ dosimeters	MCNPXe
TEPC-FLUKA comparison for aircraft dose	Air	Co60 (γ), 0.5 MeV n source, AmBe source, CERN/CERF (120 GeV p & π on Cu)	TEPC	No

Table 2: SINBAD accelerator benchmarks with quality review completed

Benchmark	Summary of quality assessment
MSU 155 MeV/nucleon He & C ions on Al targets	MCNPX model prepared, experiments are adequate for benchmarking of calculation models and codes
Transmission of n & γ generated by 52 MeV p	MCNPX model prepared, experimental information should be recovered; experimental uncertainty needed on: proton energy, density, H content in concrete, unfolding process
ISIS deep penetration of neutrons through concrete & Fe	MCNPX model prepared, experiment is adequate for benchmarking purposes
HIMAC/NIRS high-energy neutrons (< 800 MeV)	PHITS model prepared, experimental information needed, reduction in unfolding uncertainty, estimation of experimental uncertainty should be obtained before these experiments could be used for benchmarking processes
HIMAC/NIRS high-energy neutron (up to 800 MeV)	PHITS model prepared, large measurement uncertainties, unfolding uncertainty and parameter uncertainties needed, experiment is not adequate for benchmarking purposes
HIMAC He, C, Ne, Ar, Fe, Xe and Si ions on C, Al, Cu and Pb targets	MCNPX model prepared, experiments are adequate for benchmarking purposes

- Calculation should be able to reproduce the experiment as exactly as reasonably possible, avoiding unnecessary approximations.

- As much as possible the calculations should be compared to pure measured data. Often "processed" measured data are referred to as "measured" (e.g. time-of-flight experiments). In this case the involved computational approximations and uncertainties should be carefully evaluated.

This review process is expected to provide the users with an easier choice and help them make better use of the experimental information.

Conclusions

The SINBAD database currently contains compilations and evaluations of 100 benchmark experiments, among them 23 cover accelerator shielding cases. Several new experiments have been compiled and need final review.

Since the experimental data currently available in SINBAD are of varying quality, a revision and classification of the benchmark experiments according to the completeness and reliability of information is being undertaken in order to provide users with easier choices and help them make better use of the experimental information. A series of 34 experiments, among them 6 accelerator experiments, mostly of relevance for fusion neutronics and for accelerator shields were already, or are currently being revised and reclassified.

The SINBAD database is now widely used for code and data validation. Materials covered include: Air, N. O, H_2O, Al, Be, Cu, graphite, concrete, Fe, Pb, Li, Ni, Nb, SiC, Na, SS, W, V and mixtures thereof. Over 40 organisations from 14 countries and 2 international organisations have contributed data and work in support of SINBAD.

Acknowledgements

References

[1] P. Miller, P. Nagel, M. Salvatores, E. Sartori (1988), Shielding Experimental Benchmark Base at the Nuclear Energy Data Bank, *Proc: 7th Int. Conf. on Rad. Shielding, Bournemouth,* UK, NEACRP-L-310.

[2] A.K. McCracken (AEEW), E. Sartori (NEADB), A Proposed Structure for a Shielding Experimental Benchmark Data Bank, NEACRP-A-1020, 1989.

[3] H. T. Hunter, D. T. Ingersoll, R. W. Roussin, C. O. Slater, E. Sartori, I. Kodeli (1996), SINBAD-Shielding Integral Benchmark Archive and Database, *Proc. ANS Topical Meeting on Rad. Prot.&Shielding, Cape Cod*, Massachusetts.

[4] I. Kodeli, E. Sartori, B. Kirk (2006), "Recent Accelerator Experiments Updates in Shielding INtegral Benchmark Archive Database (SINBAD)", *Nuclear Instruments and Methods in Physics Research A 562, 725-728.*

[5] I. Kodeli, E. Sartori, B. Kirk (2006), SINBAD Shielding Benchmark Experiments Status and Planned Activities, *Proc. ANS 14th Biennial Topical Meeting of Rad. Protection &Shielding Division,* Carlsbad, New Mexico, USA, 3-6 April 2006.

[6] I. Kodeli, A. Milocco, A. Trkov (2009), Lessons Learned From The TOF-Benchmark Intercomparison Exercise Within EU Conrad Project (How Not to Misinterpret a TOF-Benchmark), *Nuclear Technology*, Vol. 168, 965-969.

[7] A. Milocco, A. Trkov, I. Kodeli (2010), The OKTAVIAN TOF experiments in SINBAD: Evaluation of the experimental uncertainties, *Annuals of Nuclear Energy 37, 443–449.*

[8] A. Milocco, I. Kodeli, A. Trkov (2010), The 2010 Compilation of SINBAD: Quality Assessment of the Fusion Shielding Benchmarks, *Proc. NEMEA-6 Scientific workshop on Nuclear Measurements, Evaluations and Application,* Krakow, Poland, 25-28 October 2010.

[9] B. L. Kirk, R. E. Grove, I. Kodeli, J. Gulliford, E. Sartori (2011), Shielding Integral Benchmark Archive and Database (SINBAD) 14th *Int. Symposium on Reactor Dosimetry (ISRD-2011)*.

[10] I. Kodeli, A. Milocco, P. Ortego, E. Sartori, 20 Years of SINBAD (Shielding Integral Benchmark Archive and Database), to be published in *Progress in Nuclear Science and Technology*.

Session III: Dosimetry, Medical and Industrial Accelerators

Chair: Syuichi Ban

Shielding design calculations for ESS activated target system

D. Ene, F. Mezei
ESS-AB, Sweden

Abstract

The European Spallation Source (ESS) is a European common effort in designing and building a next generation large-scale user facility for studies of the structure and dynamics of materials. The ESS target, moderators and reflectors system through interactions with 5 MW proton beam (2.5 GeV, 20 Hz) will produce long pulse (2.8 ms width) neutrons in subthermal and thermal energy range. These neutrons are further transported to a variety of neutron scattering instruments.

The aim of this work is to assess the strategy to be used for the safe handling and shipping of the ESS target and associated shaft. For safe maintenance, during operation as well as handling, transport and storage of the components of the ESS target station after their lifetime, detailed knowledge is required about the activation induced by the impinging protons and secondary radiation fields. The Monte Carlo transport code MCNPX2.6.0 was coupled with CINDER90 version 07.4 to calculate the residual nuclide production in the target wheel and associated shaft. Dose equivalent rates due to the residual radiation were further calculated with the MICROSHIELD and MCNPX codes using photon sources resulting from CINDER. Various decay times after ceasing operation of the target components were considered. The activation and decay heat density distributions of the target system together with the derived dose rates were analysed to assess the best strategy to be used for their safe removal and transport to a hotcell, eventual dismantling, storage on-site and shipping off-site as intermediate level waste packages. The derived photon sources were used afterwards to design the shielded exchange flasks that are needed to remove and transport the target after its lifespan to a hotcell. Design of a multi-purpose cask able to accommodate the different highly activated components of the ESS target station and ship them to external conditioning facility is intended to be developed. For this purpose, the photon source term of target and shaft was derived taking into consideration previously estimated decay time on-site prior the cask loading. The main criterion used for optimisation of the thickness and material selection of the shielding of the flasks, in agreement with Swedish legislation and ADR provisions, is that the dose rate must not exceed 2 mSv h[-1] on the outer surface and 0.1 mSv h-1 at a distance of 1 m.

The calculated parameters for the shield of the target will be used for detailed design and manufacturing of the exchange flask. Obtained results for the off-site shipping cask are discussed in order to derive the requirements to be fulfilled for the type B(U) package design approval.

Neutron exposure accelerator system for biological effect experiments (NASBEE)

Masashi Takada[1], So Kamada[1]
[1]National Institute of Radiological Sciences, Japan

Abstract

The neutron exposure accelerator system for biological effect experiments (NASBEE) has been developed to study biological effects of fast neutrons. NASBEE has been used to experimentally obtain several endpoints of the biological effects to fast neutrons. NASBEE neutron beams are characterised as energy spectrum, absorbed dose energy distribution and space distribution. The neutron energy spectrum extends to 9 MeV and a broad peak at 2.3 MeV. Neutron and photon absorbed doses occupy 82% and 18%, respectively, of the NASBEE neutron beam. We also developed narrowly-collimated neutron beams for irradiating fast neutrons to only lungs of mice. Absorbed dose distributions and beam profile of the collimated neutron beam were measured. For application of NASBEE, we innovated a real-time and non-destructive method of beam profile measurement on a target under large beam current irradiation. NASBEE has been widely used for not only biological study but also for physical and biological dosimetry.

Introduction

It is important to evaluate the biological effects of neutrons because the general public is exposed to neutrons in a variety of settings, in several radiation fields, for example, around nuclear reactors and accelerators, at nuclear accidents such as the Tokaimura nuclear accident in Japan, in radiation therapy (Boron Neutron Capture Therapy: BNCT, charged particle therapy) and at aviation altitudes, and in the international space station. The radiation weighting factor, w_R, for protection quantity is based on relative biological effect (RBE) data of life shortening due to cancer induction from in vivo investigations.

The National Institute of Radiological Sciences (NIRS) in Japan has started the biological study for neutrons. Biological study for high-energy neutrons of 10 MeV [1] [2] has been completed [3] [4]. To investigate biological sensitivity to fast neutrons in vivo, we constructed the neutron exposure accelerator system for biological effect experiments (NASBEE) at NIRS [5] [6]. NIRS has studied several biological effects: carcinogenesis (myeloid leukaemia, cancers of the mammary gland, lung, liver, brain, and intestine), age-dependent cancer risk, and lifespan shortening using NASBEE neutron beams. Neutron energy spectrum and absorbed dose distribution are necessary to evaluate the biological effects. Blood, cell and fishes other than mice have been irradiated by neutrons.

In this study, we characterise neutron energy spectrum, absorbed dose energy distribution, and space distribution. Also, focused neutron beams were developed for locally irradiation to mice.

Neutron beam

Configuration of NASBEE

A 2-MV Tandetron accelerator from the high voltage engineering Europe was installed in NIRS. The accelerator produces 4-MeV proton and deuteron beams and has a capability of producing beam currents of 1-mA. Figure 1 shows the configuration of NASBEE. The accelerator was on the first floor; however, neutron targets are in the first basement. Beams were bent down to two irradiation rooms of conventional and SPF rooms, constructed in the first basement.

A 3-mm-thick Be target was used to produce fast neutrons. Same targets, shielding and cooling systems are configured in both irradiation rooms. In the conventional room neutron irradiation is performed without sample limits. Physical neutron specifications were measured in this room. On the other hand, in the SPF room specific pathogen is controlled to minimise several factors inducing biological effects other than radiations and measure biological effects due to only radiations. In the rooms temperature and humidity are, also, controlled for mice.

**Figure 1: NASBEE configuration of accelerator and
two neutron irradiation rooms of conventional and SPF rooms**
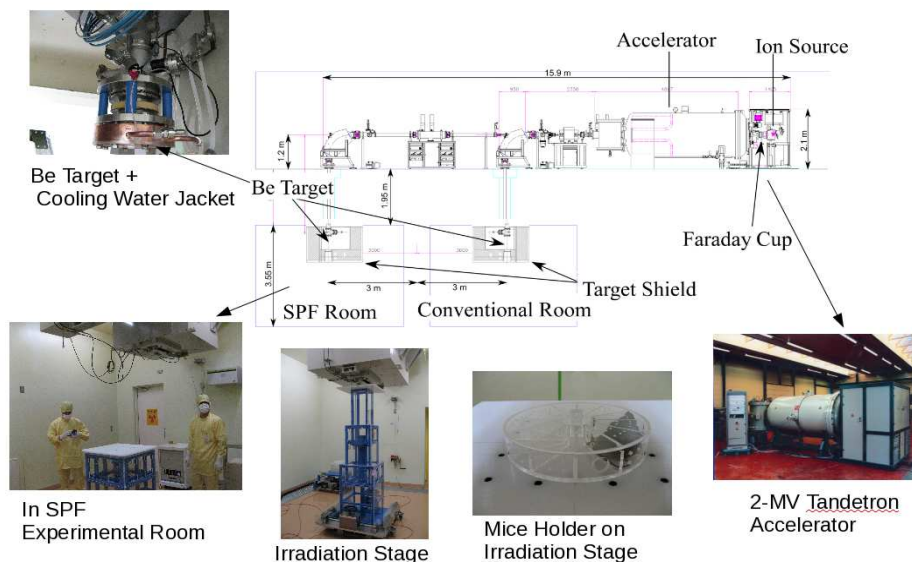
Neutron target

High-intense neutron beam is produced by irradiating 4-MeV deuteron beam into the thick beryllium target. This high-intense neutron beam is required to irradiate 2-Gy neutron beams to mice during 20 minutes, which is shorter than an anaesthesia period of approximately 30 minutes. To produce high-intense neutron beams, the tandetron accelerator with the highest beam currents in the world was installed in NIRS. The accelerator produces proton beams up to 800 µA and deuteron beams up to 500 µA. Proton and deuteron beams are accelerated up to 4 MeV.

Neutrons are produced at the ^{9}Be (d, xn) reactions. The 1.6 kW target heat by deuteron beam is cooled by coolant water with 10-20 litter per minutes, attached at the downstream of the beryllium target.

Neutron energy spectrum

Neutron energy spectrum was measured using an organic liquid scintillator, EJ-399, with a half inch thickness. This scintillator is based on naphthalene and has a particle discrimination property of neutrons and photons. From neutron discriminated pulse height, the energy spectrum was obtained using unfolding technique. Neutron response functions were evaluated with measurement and MCNPX simulations [7]. Figure 2-(A) shows the neutron energy spectrum at NASBEE. The spectrum is normalised with incident deuteron beam current at the target. The neutron spectrum consists of three components: in the low-energy region, mainly scatter neutrons in the irradiation room; from 1 to 4 MeV, neutrons created from the deuteron stripping reaction; in the highest-energy region, neutrons produced at the ^{9}Be(d,n)^{10}B reaction with +4.36-MeV Q-value. Average neutron energies by weighting the neutron energy spectrum with flux, kerma and RBE calculated are 2.3, 3.0 and 2.4 MeV, respectively. Using the keller biological model the RBE value obtained is 3.9 for the NASBEE neutron beam.

Figure 2: (A) Neutron energy spectrum at NASBEE

(A)

(B)
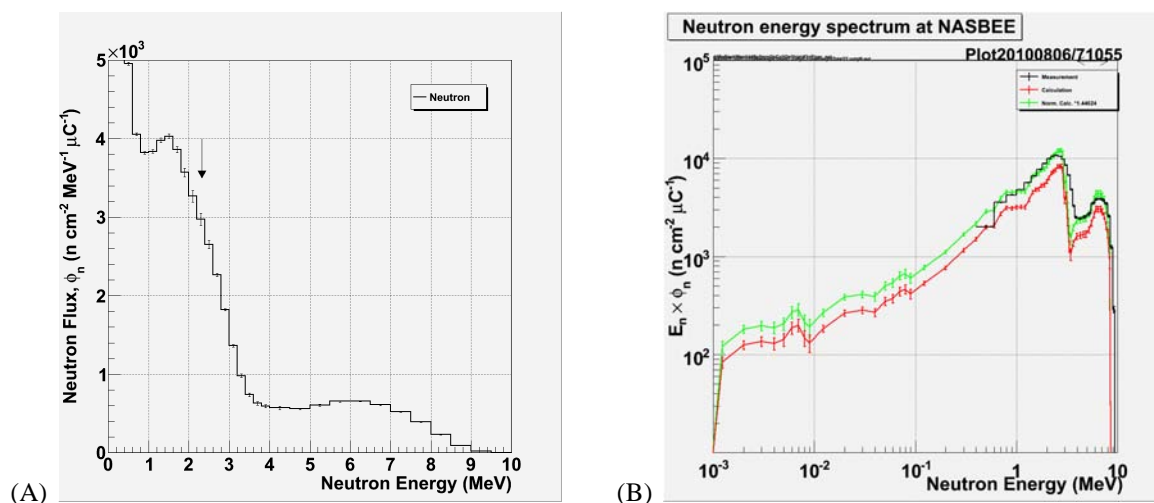
An arrow indicates average neutron energy in flux and (B) simulated neutron energy spectrum from 1 keV to 10 MeV, compared with measured result.

To evaluate lower neutron energy spectrum than the energy limit of particle discrimination, the neutron energy spectrum was simulated using the MCNPX code. In the other experiment, the angular distributions of neutron energy spectrum produced by bombarding 3-MeV deuteron beams into the thick beryllium target were measured using the time-of-flight (TOF) method at Tohoku university. The liquid organic scintillator having particle discrimination of neutron and photon was used. These angular neutron energy spectra without including scatter component were used as source spectrum in the MCNPX neutron transport. In the simulation, these materials are configured; polyethylene collimator, wall and floor in the room, and coolant water and copper holder. Figure 2-(B) shows the simulated neutron energy spectra at a wide range of neutron energy, compared with the measured result. The simulated neutron energy spectrum is smaller than the NASBEE spectrum because of lower incident deuteron energy. The simulated energy spectrum is normalised to the measurement in the energy region from 4 to 8 MeV. This energy spectrum is neutron flux multiplied by neutron energy. The neutron energy is decreased with decreasing neutron energy. The simulated neutron energy spectrum agrees with the measurement.

Photon energy spectrum

NASBEE photon energy spectrum was measured using high purity germanium (HPGe) detector and a liquid scintillator. In the HPGe pulse heights, several photopeaks are produced from the thermal neutron reactions of the n-H, n-Al, n-Fe, n-Be are identified. The energy of these photons extend to 9 MeV. The photon energy spectrum has been analysed.

Absorbed dose distribution

Figure 3 shows absorbed dose distributions of photon and neutron, which were measured using low-pressure proportional counters. The counter measured deposited energies in small site, equivalent to 1 μm tissue. The photon and neutron absorbed dose distributions, which are composed in the NASBEE beam, were discriminated using two types of proportional counters of A150 tissue equivalent and graphite walls [8]. From these absorbed dose distributions the photon and neutron absorbed doses composed of

18% and 82%, respectively, in the NASBEE neutron beam. This photon dose contamination is smaller than the neutron field of nuclear reactors, around 50% photon doses. Based on the microdosimetry technique, the RBE of NASBEE beam evaluated is 3.5 for crypt cell survival.

Also, the depth dose of the NASBEE neutron beam was measured using the low-pressure proportional counter. Maximum neutron dose is measured at near surface. On the other hand, photon doses show maximum values around 30 mm in depth. The neutron and photon depth-dose curves are different from each other.

At NASBEE neutron irradiation, absorbed doses were measured using A150 tissue equivalent ion chamber. At 117 cm from the target surface, the absorbed dose rates measured are 1.56 Gy/C, which is normalised with the deuteron beam current. This measured result agrees with the measured values (1.51 Gy/C) using the low-pressure proportional counters, within measurement uncertainty.

**Figure 3: Neutron and photon absorbed dose distributions,
normalised with incident deuteron beam**
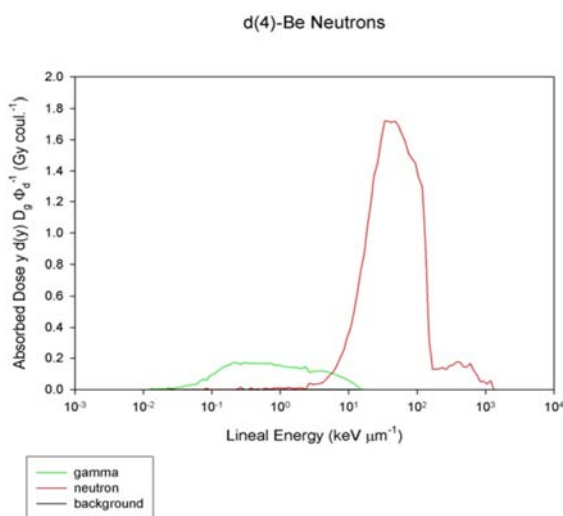
Neutron beam profile

The NASBEE neutron beam profile was measured using neutron activation of an aluminium plate. A large aluminum plate was irradiated by neutrons, followed by an activated aluminium plate being exposed to an imaging plate. This technique has an advantageous about no sensitivity to photons. Measured neutron profiles were shown in Figure 4, compared with a mice sample holder. The neutron beam size is 30 cm in diameter. We confirm that the neutron beam size covers mice and blood samples.

Figure 4: Neutron beam profile, compared with sample holder
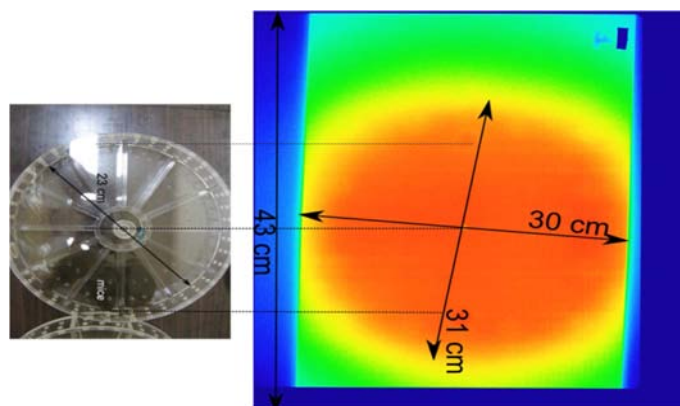
Neutron collimated beam

The NABEE neutron beam was applied to locally irradiate neutrons to only mouse lungs. The biological effects of lungs for alpha emitters of radon were evaluated. Neutron and radon have large RBE values, compared to photon and proton. To study both biological effects of lungs for neutron and radon, neutron beams are locally irradiated to only lungs of mice, which are 4 cm in length. Under local neutron irradiation, the biological effects are negligible due to other organ sources. Using this collimated neutron beam, the biological effects of lungs are experimentally obtained.

The neutron beam was collimated to 4 cm in width with polyethylene and iron blocks between the target and mice. Neutron profiles were measured using the neutron activation of aluminium plate. The neutron beam has a width of approximately 4 cm. Also, neutron and photon absorbed doses were measured using low-pressure proportional counters. Neutron and photon dose distributions were measured, separately. Figure 5 shows neutron and photon absorbed doses measured under the neutron collimator. The ratio of absorbed doses measured is 15 for the inside neutron beam to behind the neutron shields. Neutron absorbed doses are well shielded at a few percentage. Photon doses are only 30% behind the shields. Neutron irradiation carried out locally was completed at NASBEE, and after that, the biological effects were analysed.

Figure 5: Neutron and photon absorbed doses measured using low-pressure proportional counters inside of neutron beam and behind neutron collimator
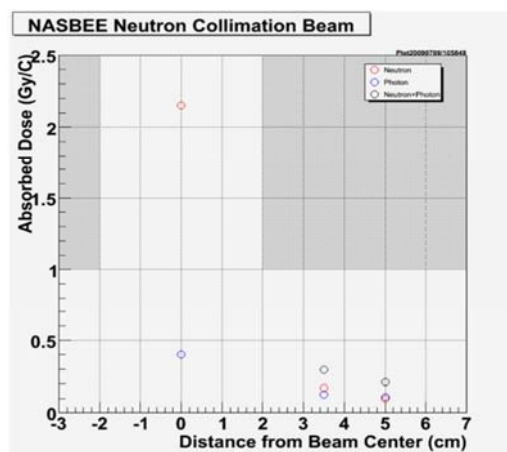
Application of NASBEE

NASBEE has developed beam profile monitor and neutron targets using high-intense neutron beam. We innovated a real-time and non-destructive method of beam profile measurement on a target under large beam current irradiation [9]. This method does not require a complex radiation detector or electrical circuits. The beam profile on a target was measured by observing the target temperature using an infrared-radiation thermometer camera. The target temperatures were increased and decreased quickly by starting and stopping the beam irradiation within 1 s in response speed.

Conclusion

We have characterised the NASBEE neutron beams with the neutron energy spectrum, absorbed dose energy distribution, and space distribution. These distributions are useful for biological study. The results of this study will provide researchers outside of our institute with an opportunity to determine some of the biological effects of fast neutrons.

Acknowledgements

References

[1]   M. Takada *et al*. (2004), "Neutron field produced by 25 MeV deuteron on thick berylium for radiobiological study; energy spectrum", *Radiat. Prot. Dosim., 110 (1/4), 601-606.*

[2]   M. Takada *et al*. (2005), "Neutron irradiation field produced by 25 MeV deuterons bombarding on thick beryllium target for radiobiological study", *Nucl. Instrum. Meth. A545(3), 765-775.*

[3]   Y. Ishida *et al*. (2006), "Dose-response and large relative biological effectiveness of fast neutrons with regard to mouse fetal cerebral neuron apoptosis", *J. Rad. Res. 47(1), 41-47.*

[4]   R. Kanda *et al*. (2006), "Investigation of new cytogenetic biomarkers specific to high-LET radiation using in vivo and in vitro exposed human lymphocytes", *Int. J. Rad. Biol. 82(7), 483-491.*

[5]   M. Suda *et al*. (2009), "Specifications of a Neutron exposure Accelerator System for Biological Effects Experiments (NASBEE) in NIRS", *Rad. Phys. Chem. 78(12), 1216-1219.*

[6]   M. Takada *et al*. (2010), "Neutron exposure accelerator system for biological effect experiments (NASBEE)", *AIP Proc. of the 21st Int. Conf. on the Appl. Accel. Res. Indust.*

[7]   M. Takada *et al*. (2011), "Simulated neutron response functions of phoswich-type neutron detector and thin organic liquid scintillator", *Prog. Nucl. Sci. Tech. 2, 274-279.*

[8]   M. Takada *et al*. (2011), "Differential neutron and gamma-ray absorbed dose distributions at the mono-energetic neutron calibration facility", *Rad. Prot. Dosim. 114(4), 481-490.*

[9]   M. Takada *et al*. (2012), "Innovative real-time and non-destructive method of beam profile measurement under large beam current irradiation for BNCT", *Nucl. Instr. Meth. A689, 22-28.*

Measurement of induced radioactivity in air and water for medical accelerators

K. Masumoto[1], K. Takahashi[1], H. Nakamura[1], A. Toyoda[1], K. Iijima[1],
K. Kosako[2], K. Oishi[2], F. Nobuhara
[1]High Energy Accelerator Research Organization (KEK), Japan,
[2]Shimizu Co. Japan,
[3]Tokyo Nuclear Service Co. Japan

Abstract

Activation of air and water has been evaluated at the 10 and 15 MeV linear electron accelerator facilities. The air present in a glovebox and the water present in the phantom were directly irradiated in front of the beam exit window. The typical irradiation condition was 50 Gy at the isocenter. No activity could be observed at 10 MeV irradiation. At 15 MeV irradiation, the activity of 10-min-half-life ^{13}N was observed in the case of the air in the glovebox, but no activity could be observed in the air sampled from the irradiation room and the maze. Aerosol was also sampled in the irradiation room and the maze by the dust sampler during irradiation and the activity deposited on the high-efficiency particulate air (HEPA) filter was measured using a GM-survey meter. Activity of ^{13}N was observed on the filters for 15 MeV irradiation. Air and water samples were also bombarded by 250 MeV protons and 400 MeV/u carbon, and the irradiation dose was 10 Gy at the isocenter. Upon the ion-chamber monitoring of the air sampled from the glovebox, ^{15}O, ^{13}N, and ^{11}C activities were mainly observed. Upon the dust sampling of the irradiation room and the maze, low activity of ^{13}N was observed on the HEPA filter. At the end of proton and carbon irradiation, the activity of the water was found to be about 10 kBq•cm^{-3} and several kilobecquerel per cubic centimetre, respectively. From the decay analysis of the induced activity in water, ^{15}O, ^{13}N, and ^{11}C were detected. The obtained results of air and water activation were then compared with data calculated by MCNP or PHITS code, coupled with DCHAIN-SP2001. At the 15 MeV linear accelerator, the observed activity of ^{13}N was higher than the calculated activity. A similar trend was observed in the case of proton and carbon irradiation. The reason why the calculated activity was lower than the experimental results needs to be investigated.

Introduction

Accelerators have been widely used in medical applications, especially in cancer treatment. Electron linear accelerators have been used in hospitals for the X-ray irradiation of diseased organs. Particle accelerators have also been used in recent times as a powerful tool for cancer therapy. New regulations for disposing of activated-material components from accelerator facilities were established in Japan in 2012. Activation air and water should also be controlled in the same manner as the facility using non-shielded radioisotopes. In this work, we investigated the activation of air and water in treatment rooms in hospitals for radiation safety management. In the case of photonuclear reaction, several positron emitting radioisotopes such as ^{15}O and ^{13}N can be produced by the bremsstrahlung mechanism at higher than 15 MeV in air. In the case of hadron irradiation, many radioisotopes might be produced by high-energy particles. In this work, we measured the induced activity in air and water caused by the electron and hadron accelerators employed for medical use, in order to determine whether the concentration of radioactivity was below regulated levels.

Experimental

Activation of air and water

Electron accelerator

10 and 15 MeV irradiations for 10 min were performed by Varian Clinac 2 100C and Clinac iX, respectively. Doses were 40 and 60 Gy at the isocenter, respectively.

Proton accelerator

200 MeV proton beam was irradiated for 3.25 min on an area of 0.15 m×0.15 m, and 10 Gy at the isocenter.

Heavy ion accelerator

Carbon beams of 400 MeV/nucleon were irradiated for 2 min on an area of 0.15 m×0.15 m, and 10 Gy at the isocenter.

Measurement of radioactivity in air

Activity in air

A glovebox (0.5×0.5×1.0 m^3) covered with a polyethylene sheet was placed in front of the beam exit window. After irradiation, air in the glove box was collected in a vacuum ionisation chamber (volume 1.5 L). Air samples were also collected from near the glove box in the irradiation room and the maze to the irradiation room. Ionisation current of the ionisation chamber was monitored using a vibrating reed electrometer (Advantest TR8411 and TR8401). An ionisation current of 1.0×10^{-14} A corresponds to the beta activity of 0.063 Bq•cm^{-3}.

Activity in aerosol

Figure 1: Irradiation set-up for activation of air for the electron accelerator (left) and air and water for the proton accelerator (right)

A portable air sampler with a set of HEPA filter (HE-40T) (collection efficiency: 99.6%, particle size 0.09 to 0.8 μm) and charcoal filter (CP-20) was used for aerosol sampling in the irradiation room and the maze to the irradiation room during irradiation. Radioactivity collected on the filter was measured using a GM survey meter (window size: 50 mmφ, TGS-146, Aloka Co.).

Measurement of radioactivity in water

In the case of the electron accelerator, water filled with a water phantom for dose calibration was set in front of the beam exit window and irradiated. After irradiation, the dose rate of the water surface was monitored using a NaI(Tl) survey meter (1.0 φ ×1.0 in, TCS-171, Aloka) and the gamma-ray spectrum was measured using a $LaBr_3$(Ce) scintillation spectrometer (1.5 φ×1.5 in, Canberra).

In the case of the hadron accelerator, two polyethylene tanks (volume: 20L, thickness: 19cm) were set after the glove box in order to stop the beam perfectly. After irradiation, the surface dose rate of the tank was measured using a $LaBr_3$ (Ce) scintillation spectrometer (1.5 φ ×1.5 in, Canberra) and the activity in becquerel per cubic centimetre was calculated. The conversion factor between the dose rate and the activity of water was obtained in advance.

The activity of the water sample was also measured using a Ge-detector (Canberra GR-2018) for detecting gamma-emitting nuclides and a liquid scintillation counter (PerkinElmer 3110TR) for beta-emitting nuclides.

Monte Carlo calculation procedure for determining level of activation of air and water

In the case of the electron accelerator, electron, photon, and neutron distribution were calculated by MCNP5. A plan of irradiation layout for calculation was drawn based on the thickness and density of each material used for the gantry. After calculating the gamma-ray and neutron spectrum using MCNP5, induced activities in the air and water

were calculated using DCHAIN-SP2001. In the case of the particle accelerator, the transportations of incident particles and neutrons were calculated using PHITS, and the activation was calculated using DCHAIN-SP2001.

Results

Results obtained using the electron accelerator
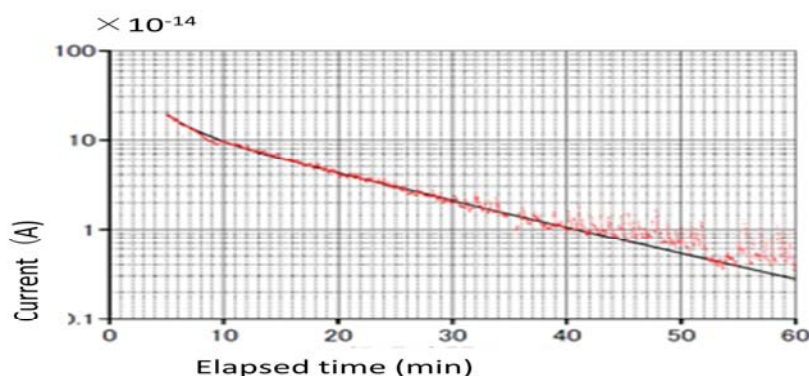
10 MeV irradiation

The ionisation current of air sampled from the glovebox was slightly noisy. However, the ionisation current of air sampled from the irradiation room and the maze to the irradiation room was the same as the background level. No activity was detected in the air filters sampled from the irradiation room and the maze to the irradiation room.

In the case of water, the dose rate of the water sample after irradiation was equal to the background level and no activity was detected by the measurement using a Ge-detector and a liquid scintillation counter. Cooling water was also sampled from the accelerator, and its activity was measured using a Ge-detector and a liquid scintillation counter. However, no activity was detected in the cooling water.

15 MeV irradiation

As a result of the decay analysis of the ionisation current, which is shown in Figure 2, a radioisotope with its half-life of 10 min was only observed in an air sample obtained from the glove box. It seemed to be ^{13}N, which is produced by the (γ, n) reaction of nitrogen in air. Its activity was estimated as 0.87 Bq•cm^{-3} at the end of the irradiation. This value is about a hundred times larger than the calculated value (0.009 Bq•cm^{-3}) obtained by the activation calculation using MCNP5 coupled with DCHAIN-SP2001. The ionisation current of the air sampled from the irradiation room and the maze to the irradiation room was the same as the background level.

Figure 2: Ionisation current of air irradiated by 15 MeV bremsstrahlung

Activities of the filters collected from the irradiation room and the maze to the irradiation room were also measured, and the half-life of the radioactive substance detected was about 10 min in the irradiation room, as shown in Figure 3. Activity concentration was 0.009 and 0.003 Bq•cm^{-3} at the end of irradiation in the irradiation room and the maze. An aerosol of radioactive nitrogen oxide (NO$_x$) may have been produced by the radiation effect.

Figure 3: Radioactivity concentration calculated by the activity collected on a HEPA filter
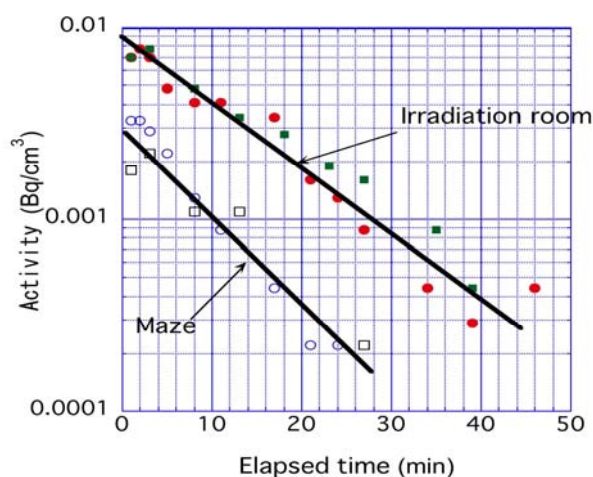
The dose rate of irradiated water, obtained using a NaI (Tl) survey meter, was found to be two times higher than the background level (0.08 μSv/h). A very small annihilation peak was observed using a LaBr$_3$(Ce) spectrometer. It was concluded that the structure material of water phantom was slightly activated.

Results obtained using proton accelerator

Activation of air

The results of the measurement and calculation of the activity concentration of air are shown in Figure 4. Fitting the decay curve of the ionisation current observed in the air sample obtained from the glove box revealed that the following activities of ^{15}O, ^{13}N, and ^{11}C were 1.9, 0.6, and 0.6 Bq•cm^{-3} at the end of irradiation, respectively. On the other hand, the calculated activities of ^{14}O, ^{15}O, ^{13}N, and ^{11}C obtained using PHITS code coupled with DCHAIN-SP2001 were 0.6, 0.7, 0.4, and 0.09 Bq•cm^{-3}, respectively. The difference between the experimental and calculated values at the end of irradiation was small. However, the difference gradually became large because of the difference between the experimental and calculated ^{11}C activity. The ionisation current of the air sampled from the irradiation room and the maze to the irradiation room was equal to the background level.

The activities of the filters collected from the irradiation room and the maze to the irradiation room were also measured, and a half-life of these activities was about 10 min. The activity concentration was 0.05 at and 0.01 Bq•cm^{-3} at the end of irradiation in the irradiation room and the maze, respectively.

Figure 4: Decay curves and calculated values of radioactivity in air irradiated by 250 MeV protons
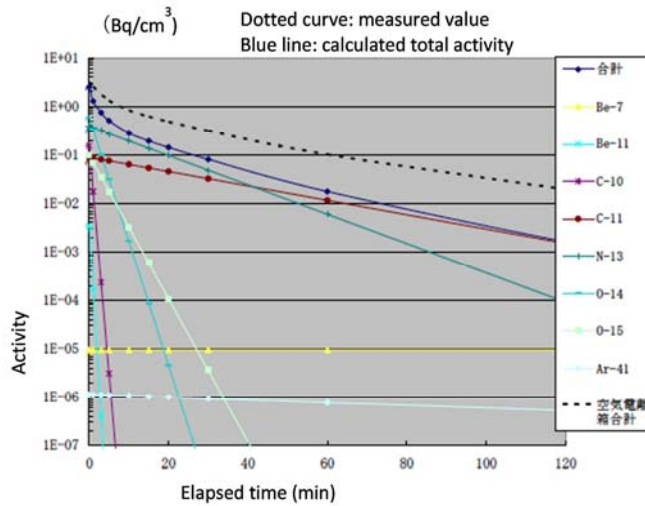
Activation of water

The results from the measurement and calculation of the activity concentration of water are shown in Figure 5. The decay curve analysis of the activity obtained from the surface dose rate of the polyethylene tank showed that the activities of ^{14}O, ^{15}O, ^{13}N, and ^{11}C were 91 000, 12 000, 1 100, and 190 Bq•cm^{-3} at the end of irradiation, respectively.

Figure 5: Decay curves and calculated values of radioactivity in water irradiated by 250 MeV protons
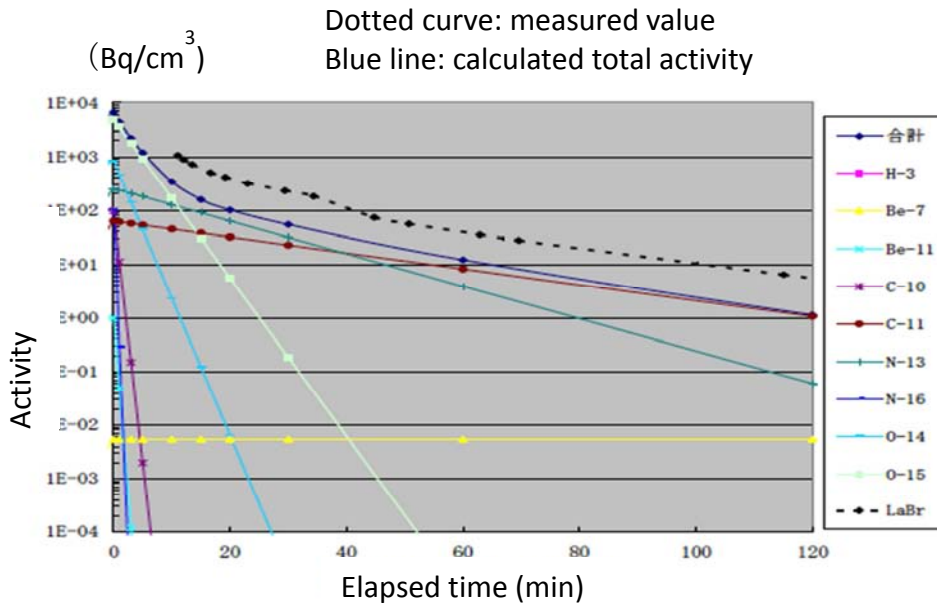
The activities of ^{14}O, ^{15}O, ^{13}N, and ^{11}C obtained using the PHITS code coupled with DCHAIN-SP2001 were 830, 5000, 250, and 63 Bq•cm^{-3}, respectively. The activity of ^{7}Be was 0.039 Bq•cm^{-3}, as determined using a Ge-detector, and it was calculated to be 0.0053 Bq•cm^{-3}. It was found that the calculated activity of each radioisotope was always smaller than its experimental result. No activity was detected using the liquid scintillation counter.

Results obtained from the heavy ion accelerator

Activation of air

The results of the measurement and calculation of activity concentration of air are shown in Figure 6.

We performed irradiation twice and fitted the decay curve for ^{14}O, ^{15}O, ^{13}N, ^{11}C, and ^{41}Ar. Average activities of ^{14}O, ^{15}O, ^{13}N, ^{11}C, and ^{41}Ar were, respectively, 0.8, 1.1, 0.08, 0.09, and 0.006 Bq•cm^{-3} at the end of irradiation. The activities of ^{14}O, ^{15}O, ^{13}N, and ^{11}C obtained using the PHITS code coupled with DCHAIN-SP2001 were 0.003, 0.009, 0.007, 0.012, and 0.000006 Bq•cm^{-3}, respectively. Determined activity levels were lower than those due to proton irradiation, and the activity was mainly due to ^{11}C. The calculated activity of each radioisotope was smaller than the experimental value.
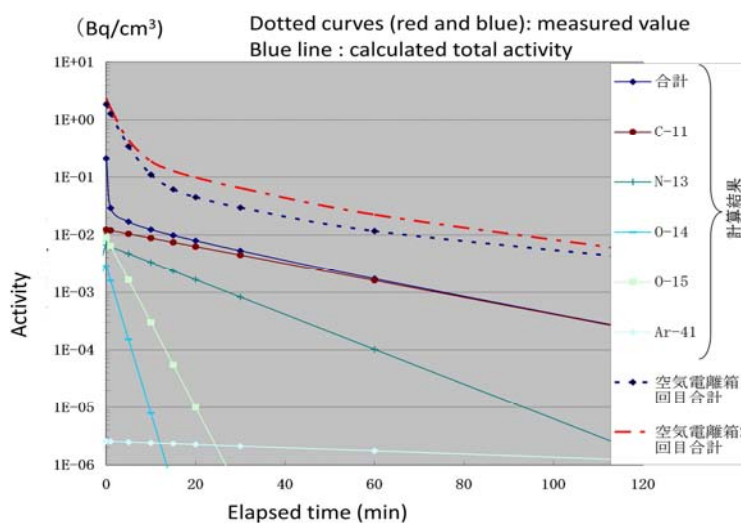
Figure 6: Decay curves and calculated values of radioactivity in air irradiated by 400 MeV/u carbon

The activities of the filters collected from the irradiation room and the maze to the irradiation room were also detected and the half-life of these activities was 10 min. The activity concentration was lower than that of proton irradiation. At the end of irradiation, the activity concentration was about 0.02 Bq•cm^{-3} in the irradiation room.

Activation of water

The results of the measurement and calculation of activity concentration of water are shown in Figure 7. The decay curve analysis of the activity obtained from the surface dose rate of the polyethylene tank showed that the activities of ^{14}O, ^{15}O, ^{13}N, and ^{11}C were 2 100, 2 000, 100 and 180 Bq•cm^{-3} at the end of irradiation, respectively. The activities of ^{14}O, ^{15}O, ^{13}N, and ^{11}C obtained using the PHITS code coupled with DCHAIN-SP2001 were 46, 270, 19, and 34 Bq•cm^{-3}, respectively. In the case of carbon irradiation, the induced activity was lower than that of proton irradiation and ^{11}C became a major contributor to the activity after 20 min of the end of the irradiation. The activity of ^7Be was 0.39 Bq•cm^{-3} using a Ge-detector, and the calculated value was found to be 0.0058 Bq•cm^{-3}. The activity of ^{22}Na was also detected in water, and its concentration was 0.0004 Bq•cm^{-3}, which was only two times larger than the detection limit of our measurement (0.0002 Bq•cm^{-3}). Tritium concentration was found to be 0.28 Bq•cm^{-3} using liquid scintillation counting.

**Figure 7: Decay curves and calculated values of radioactivity
in air irradiated by 400 MeV/u carbon**
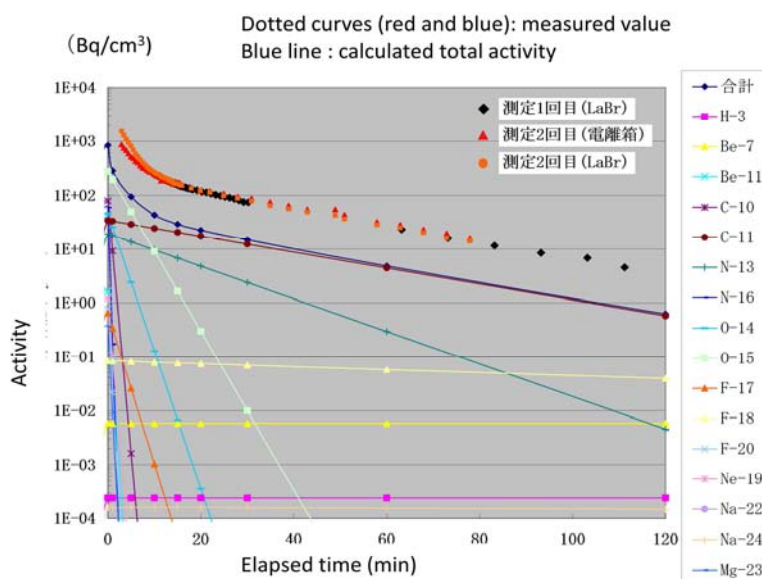
Conclusion

In the case of 10 MeV irradiation residual activity could not be detected in air and water. In the case of 15 MeV irradiation, we observed ^{13}N in the air sampled from the glovebox irradiated in front of the beam exit window and on the filter collected by the air samplers in the irradiation room and the maze. The measured activity concentration of ^{13}N was very small, but it was higher than the value calculated by MCNP5 coupled with DCHAIN-SP2001. It is necessary to verify the irradiation energy for activation and the photonuclear reaction cross-section for the calculation.

In the case of 250 MeV proton activation and 400 MeV/u carbon irradiation, the activation of air was not excessively high and the induced activity was comparable with that induced by 15 MeV irradiation for the electron accelerator. The activity concentration of ^{11}C was seven times higher than the value calculated by PHITS coupled with DCHAIN-SP2001.

The induced activity of water was extremely high. The main radionuclides detected were ^{13}N and ^{11}C, 10 min after irradiation with protons and ^{11}C, 20 min after irradiation with carbon. The activity concentrations of water irradiated by protons and carbon were also higher than the value calculated by PHITS coupled with DCHAIN-SP2001. In these cases, activation cross-sections of light elements induced by the high-energy hadron or reaction models for activation calculation need to be checked.

Session IV: Benchmarking Code/Code and Code/Experimental Data

Chair: Hiroshi Nakashima

Uncertainties in high-energy neutron spectrometry with bonner spheres

V. Mares, C. Pioch, W. Rühm
Helmholtz Zentrum München, Neuherberg, Germany

Abstract

High-energy neutron fields (above 20 MeV), which are typical of secondary cosmic rays and the neutron field outside the shielding of particle accelerators, are especially important in terms of radiation protection due to their large contribution to total dose. A Bonner Sphere Spectrometer (BSS) is one of the most accurate and reliable instruments to measure neutron fluence rates up to several hundreds of MeV. The response functions of BSSs are usually calculated by means of Monte Carlo (MC) codes such as MCNPX, FLUKA, PHITS, MARS, GEANT4, and others. At neutron energies above 20 MeV calculated response functions may be uncertain up to a factor of 2 due to uncertainties in the theory (/model)-based reaction cross-sections on which all transport codes rely. Therefore, experimental calibration of BSSs in high-energy neutron fields is important for response validation.

The uncertainties arising from the use of different transport codes and different INC models are discussed, with special emphasis on a calculational inter-comparison exercise initiated by EURADOS (European Radiation Dosimetry Group). Furthermore, experimental results from response measurements in quasi-monoenergetic high-energy neutron fields at the ring cyclotron facility of the Research Center for Nuclear Physics (RCNP), University of Osaka, Japan, are presented. The response of a complete set of Bonner spheres were for the first time measured at neutron energies of 244 MeV and 387 MeV and compared to calculations using various MC codes and models.

Systematics of thick target neutron yield
for reactions of hundred GeV proton on target

Toshiya Sanami[1], Yosuke Iwamoto[2], Tsuyoshi Kajimoto[3], Nobuhiro Shigyo[4],
Masayuki Hagiwara[1], Hee Seock Lee[5] , Eric Ramberg[6], Aria Sofa[6], Doug Jensen[6],
Anthony Leveling[6], Nikolai Mokhov[6], David Boehnlein[6], Kamran Vaziri[6], Kenji Ishibashi[4],
Yukio Sakamoto[2] and Hiroshi Nakashima[2]
[1]High Energy Accelerator Research Organization, 1-1 Oho, Tsukuba, Ibaraki, Japan,
[2]Japan Atomic Energy Agency, 2-4 Shirakata, Tokai-mura, Naka-gun, Ibaraki, Japan,
[3]Hiroshima University, Kagamiyama, Higashi-Hiroshima, Japan,
[4]Kyushu University, Motooka, Nishi-ku, Fukuoka, Japan,
[5]Pohang Accelerator Laboratory, POSTECH, Pohang, Kyungbuk, Republic of Korea,
[6]Fermi National Accelerator Laboratory, Batavia, IL, US

Abstract

A methodology to obtain neutron energy spectrum for 120 GeV proton on target was developed using a time of flight technique with correction of beam uniformity, at Fermilab Test Beam Facility (FTBF). Experimental data on neutron energy spectra were taken for C, Al, Cu and W targets with emission angles of 15, 30, 45, 90, 120 and 150 degree. The experimental data are compared with the results of multi-particle Monte Carlo codes and a systematic discrepancy was observed.

Skyshine evaluation at high-energy electron accelerator

Hee-Seock Lee, Joohee Oh, Namsuk Jung
Pohang Accelerator Laboratory, POSTECH, Republic of Korea

Abstract

The skyshine effect of neutrons and photons is an important issue for high-energy accelerators to estimate an environmental dose for the public living near facilities. The simple equations and parameters evaluated by several authors like G. Stapleton have been used in many paper and reports.

In this study, equations and parameters were compared with each other to estimate the environmental effect of the PALXFEL operation. The skyshine effect of the 10 GeV electrons striking a thick Cu target was investigated. The PHITS and the FLUKA Monte Carlo codes were used to verify the accuracy of those equations and parameters. The practical geometry like a thick concrete tunnel and a ground condition was considered to evaluate properties of a neutron skyshine and an environmental dose. The ground-shine effect was found to be a little big at the real geometry estimation. This created a discrepancy between this Monte Carlo simulation and the simple equation in estimating an environmental dose. The new equation and parameters are evaluated by the Monte Carlo simulations that use the PHITS and the FLUKA.

Shielding experiment by foil activation method at the anti-proton production target of Fermilab

Yoshimi Kasugai[1], Hiroshi Yashima[2], Norihiro Matsuda[1], Hiroshi Matsumura[3], Nikolai Mokhov[4], Anthony Leveling[4], David Boehnlein[4], Kamran Vaziri[4], Koji Oishi[5], Yukio Sakamoto[1], Hiroshi Nakashima[1]
[1]Japan Atomic Energy Agency, Japan,
[2]Research Reactor Institute, Kyoto University, Japan,
[3]High Energy Accelerator Research Organization, Japan,
[4]Fermi National Accelerator Laboratory, US,
[5]Shimizu Corporation, Japan

Abstract

The shielding experiment was carried out using the Antiproton Production Target Station (Pbar) of Fermilab under the collaboration study of JASMIN: "Japanese and American Study of Muon Interaction and Neutron detection". In the experiment, the neutron flux distributions in the shielding assembly were obtained by means of multi-foil activation method. Neutron spectra in the energy range between 1 and 100 MeV were deduced from the experimental data using the fitting method, which was newly developed in this study. The experimental data were compared with the theoretical calculation of the particle-transportation code: PHITS. The optimum value of neutron attenuation length λ was tentatively deduced by applying the experimental data to the Moyer's model.

Introduction

Intense proton accelerators with the acceleration energy higher than a few tens of GeV have been constructed recently to do research into neutrino and hadron physics. However, systematic experimental shielding data for the proton energies in such high-energy regions have been deficient. Since the current shielding design is based on the extrapolation of the experimental data for the proton energy less than 10 GeV, large safety margin is required for the shielding design due to the ambiguities of the extrapolation.

Shielding data for the energy region higher than 100 GeV are required for the proper interpolation to the higher-energy region in terms of validation of high-energy particle transportation codes, discovery of a macroscopic principle of particle behaviour and estimation of a reasonable margin.

Collaborative research between Japan and US started in 2007 in order to investigate the behaviours of high-energy neutrons and muons associated with the operation of a high-energy proton accelerator. The collaboration was named "JASMIN", which is the abbreviation of "Japanese and American study of muon interaction and neutron detection", and the experiments were carried out in Fermilab; Fermi National Accelerator Laboratory in the US. In the project, mainly two facilities were used: NuMI, Neutrino at the Main Injector, and Pbar, Antiproton production target station. In the NuMI beam line, we investigated the penetration-and-activation features of high-energy muons. The first results on the muon experiments are shown in [1].

In the Pbar station, we obtained systematic experimental data of production-and-attenuation behaviours of secondary neutrons induced by 120 GeV protons in terms of neutron attenuation in the steel-and-concrete shielding, neutron flux distribution and high-energy neutron spectra in the energy range between 1 and 100 MeV.

This paper summarises the experimental procedure and the results at the Pbar station. The first-step analysis was carried out using a particle transportation code with a simple 2-dimensional model. The comparison between the calculations and the experiments is shown and some issues on the further analysis are needed. In future it will be important to determine a neutron attenuation length for the accomplishment of proper shielding designs of high-energy proton accelerators. In order to deduce the attenuation length for steel shielding, we applied our experimental data of neutron flux distributions to the Moyer's approximation model. This paper presents the procedure of the parameter deduction, though the parameter deduced in this work has not yet been finalised.

Experiment

The experiments were carried out at the Pbar station of Fermilab. The configuration of the Pbar station is shown in Figure 1.

Figure 1 shows dimensions in units of cm. It is the drawing before the replacement of the concrete blocks to the brand-new blocks specially fabricated for the experiment in 2010 and will be described in detail in the next section.

The beam line for antiproton production consisted of an antiproton-production target, a collection lens, a pulse magnet and a bema dump. The components were covered by steel and concrete shields with thicknesses of 188 cm and 122 cm, respectively. An air gap, where the utilities of the beam line components had been installed, existed between the steel and concrete shield. The height of the air gap was 179 cm.

The target was bombarded with proton beams injected from the main injector. The proton beam energy was 120 GeV, and the typical beam intensity was 2×10^{12} protons/sec.

The multi-foil activation method was mainly used to measure neutron-flux distributions and high-energy neutron spectra in the shielding configuration. The metal foils of indium, aluminium, niobium and bismuth were placed in the various positions in and out of the shielding assembly. The sample positions are shown in Figure 1.

Figure 1 shows the samples for activation set at the positions marked as squares with crosses. Each position was labelled as FP01-05 (from bottom to top), AG01-05 and CC01-04 (up- to downstream for the proton beam direction). FP means a "filler plate" used for mounting the samples in the steel shield. AG and CC are abbreviations for "air gap" and "concrete cap", respectively.

The foil-samples were irradiated with the secondary neutrons during the beam operation, and some radioactive nuclei were induced in the samples. After the irradiation, the foils were picked up from the Pbar station, and the spectroscopy analysis of the gamma-rays emitted from the foils were performed with germanium detectors in order to measure the reaction rates of the neutron induced reactions. The reactions which we were interested in are tabulated with the half-lives of the products and the threshold energies in Table 1.

Figure 1: Cross-sectional view of the antiproton-production target station of Fermilab
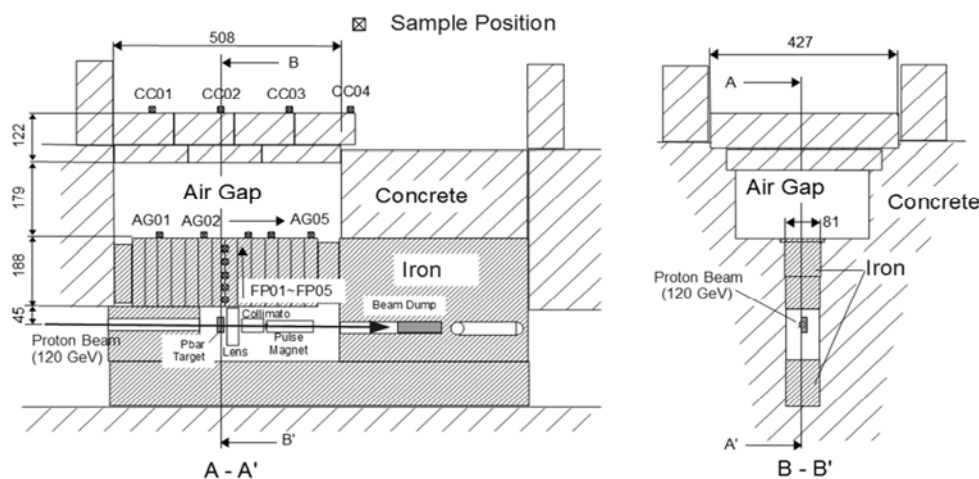
Table 1: Threshold reactions used for the foil activation

Reactions	Half-lives of products	Threshold energies (MeV)
^{115}In(n, 2n)^{115m}In	4.486 h	0.34
^{27}Al(n, α)^{24}Na	14.959 h	3.25
^{93}Nb(n, 2n)^{92m}Nb	10.15 d	9.06
^{209}Bi(n, 4n)^{206}Bi	6.243 d	22.56
^{209}Bi(n, 5n)^{205}Bi	15.31 d	29.63
^{209}Bi(n, 6n)^{204}Bi	11.22 h	38.08
^{209}Bi(n, 7n)^{203}Bi	11.76 h	45.34

A measurement using a Bonner sphere was also carried out on the surface of the concrete shield and a deduction of a neutron spectrum with a wide energy range between 1 eV and 100 MeV succeeded. It should be noted that the neutron spectrum was

consistent with the results of the multi-foil activation method. The details of the Bonner sphere measurement and the result are indicated in [2].

Short history of the experiment

The short history of the experiments at the Pbar station is summarised here.

In the first experiment in November 2007, the foil activation measurement at the air gap and on the concrete-shield surface was carried out. The measurement using a boner sphere was also carried out in the first experiment.

In 2008, we made a new steel palate with some small vacancies for the installation of the activation samples, and the experimental data of neutron attenuation in the steel shield were obtained.

Furthermore, in 2010, we constructed new concrete shielding blocks just for our shielding experiments. The shield thickness of the new blocks was the same as that of the old ones. The new blocks had sample ports for installing activation foils in the concrete blocks. That enabled us to measure neutron attenuation in the concrete shield. The concrete elements and the densities, which are essential data for the calculation analysis using a particle transportation code, were precisely measured.

The concrete blocks of the Pbar station were replaced with the brand-new blocks in November 2010. The activation samples were installed in the sample ports in the new concrete blocks in December 2010, and the radioactivity measurements were carried out in February 2011. The results are summarised in [3].

Analysis

We obtained the reaction-rate data for some threshold reactions in various positions in the shielding assembly. This means that the reaction rate distributions, corresponding to the neutron flux distributions, were obtained. Two examples of the reaction-rate distribution data obtained in this work are shown in Figure 2. The reaction rate distribution of $^{209}Bi(n, 4n)^{206}Bi$ reaction on the surface of the steel shield is shown on the left part of Figure 2, and those in the steel shields, which correspond to the neutron attenuation in the steel shied, are shown on the right part of Figure 2.

The left graph in Figure 2 shows the distribution of the surface of the steel shield as a function of the angles of the sample positions with respect to the proton beam direction from the antiproton-production target, and the right graph shows the neutron attenuation in the steel shield as a function of the steel depth from the bottom of the shield.

Using the set of the reaction-rate data at each measurement position, the neutron spectra with the energy region from 1 to 100 MeV were deduced by means of the fitting method, which was newly developed in this work [4]. The outline of the fitting method is as follows:

Figure 2: Reaction rate distributions of ^{209}Bi(n, 4n)^{206}Bi reaction
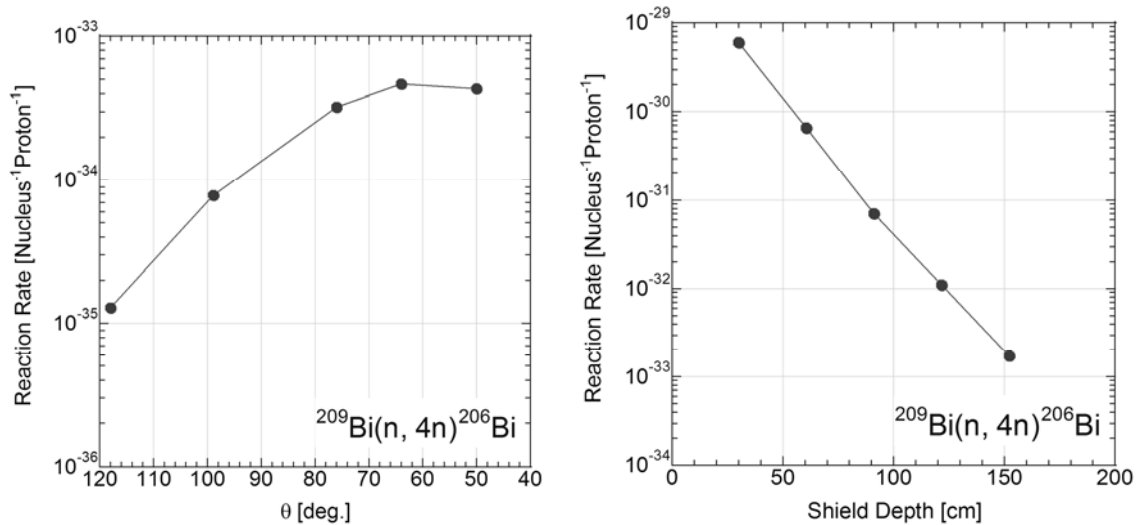
It is empirically assumed that the neutron spectra between 1 and 100 MeV can be expressed as a sum of the two exponential functions:

$$\phi_{fit} = a_1 \exp\left(-a_2 E\right) + a_3 \exp\left(-a_4 E\right), \tag{1}$$

where ϕ_{fit} is a neutron flux in unit of MeV^{-1}, E is a neutron energy in MeV, and a_i(i=1~4) are fitting parameters. The fitting parameters are determined with the non-linear least squares fit to the experimental reaction-rate data. The cross section curves [5-6], which are required in the fitting process, are shown in Figure 3.

Figure 3: Cross-section curves used for deduction of neutron spectra
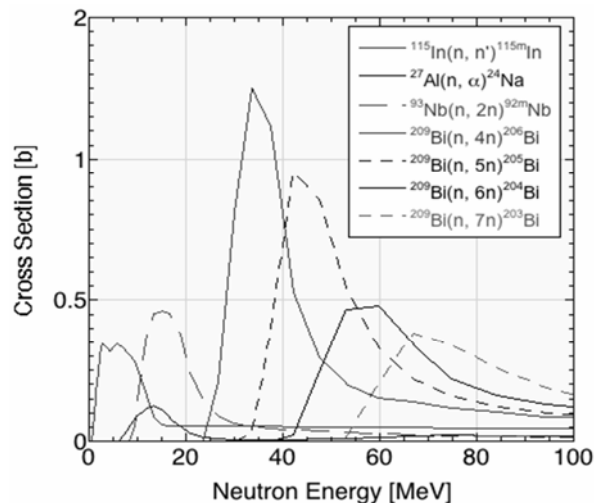
The neutron spectra deduced from the experimental data were compared with the calculation using a Monte Carlo particle transportation code: PHITS. [7] As a first step of the calculation analysis, we used a simplified two-dimensional geometry as an input [8]. Figure 4 shows the experimental and calculated neutron spectra on the line at a 90-degree angle from the antiproton-production target with respect to the proton beam direction.

In the figure, the experimental and calculated neutron spectra are shown with bold and thin lines, respectively. The symbols of FP03, FP04 and FP05 correspond to the neutron spectra in the steel shield at the shield depths of 96.5 cm, 127.0 cm and 157.5 cm from the bottom, respectively. The symbol of AG(θ=90º) means the position on the surface of the steel shield at 90-degree direction from the antiproton production target with respect to the proton-beam direction. There is no experimental data obtained at AG(θ=90º); we could not put the activation sample at AG(θ=90º) because a target-cooling device was already placed there. The experimental data at AG(θ=90º) were deduced by interpolating the data of AG02 and AG03. The bold and thin lines of B6' is the neutron spectrum on the surface of the new concrete shield, respectively, and CC02 is the experimental data at the same position for the old concrete blocks.

The graph in Figure 4 shows that the calculation tends to overestimate the neutron fluxes in the steel shield and on the surface, but it also shows that, on the concrete top, the calculated neutron spectra show good consistency with the experimental one. It should be noted that it is very important to investigate the transition of the deviations from the iron and the concrete shield.

In the figure, we plotted the experimental data at the concrete top for both the old and new concrete blocks. The neutron flux at the concrete top increased after changing the concrete shield. It is very interesting to investigate the reason if the composition of the old concrete shield could be analysed.

We regarded the calculation results shown in this paper as a first step analysis. In the analysis presented in this paper, each beam-line component, such as the antiproton-production target, the collection lens, the collimator and the pulse magnets, can be considered as equivalent secondary-neutron sources. Therefore, it is very important to validate the source terms, which largely depends on how to model the beam-line components.

Figure 4: Experimental and calculated neutron spectra on the line at a 90-degree angle from the antiproton-production target with respect to the proton beam direction
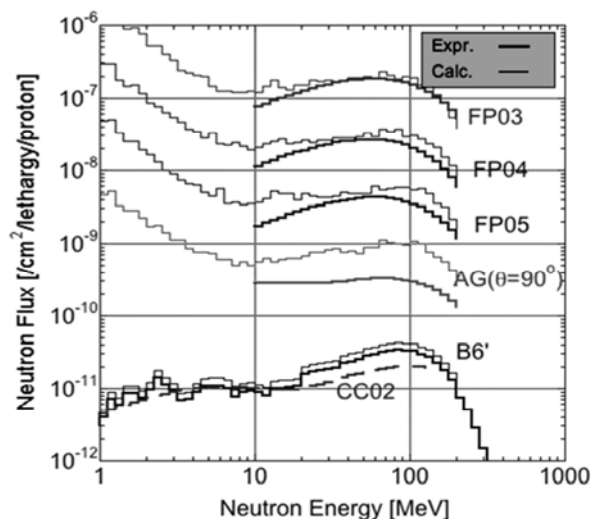
Finally we tried to deduce a neutron attenuation length by applying the Moyer's expression to the experimental reaction-rate distributions obtained in this work. As indicated above, the Pbar station is a multi-source system from the viewpoint of the neutron shielding experiment. The reaction-rate distribution can be expressed as a sum of the contributions of each source using the Moyer's expression as:

$$R_j = \sum_i R_0^{(i)} \frac{e^{-b\theta} e^{-\frac{d}{\lambda \sin \theta_{ij}}}}{r_{ij}^2}, \qquad (2)$$

where, R_j is a reaction rate at a sample (j), d is a shied thickness, r_{ij} is a distance between a neutron source (i) and a sample (j), θ_j is an angle from a neutron source (i) to a sample (j) with respect to the proton beam direction, $R_0^{(i)}$ is a contribution of a source (i), and b and λ are Moyers parameters related to an angular distribution of neutron emission from the neutron source and a neutron attenuation, respectively.

Figure 5: Moyer's model for multi-source system
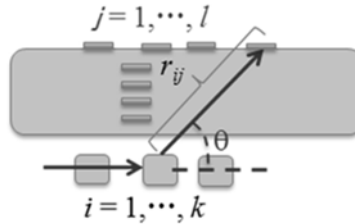
For deduction of a neutron attenuation length of steel shield, the expression (2) was fitted to the experimental reaction-rate data using non-linear least-squares method by adjusting $R_0^{(i)}$ and λ, minimising χ^2 values defined as:

$$\chi^2 = \frac{1}{N} \sum_i \left(\frac{R_{exp}^{(i)} - R_{cal}^{(i)}}{\varepsilon^{(i)}} \right)^2, \qquad (3)$$

where N is a degree of freedom in the fitting process, $R_{exp}^{(i)}$ is the experimental reaction-rate data, $R_{fit}^{(i)}$ is the reaction-rate deduced with the fitting function (2), and $\varepsilon^{(i)}$ is the experimental error. The value of b was fixed in the whole fitting process at 2.3 in the unit of radian^{-1} [9], which has been commonly used in shielding design so far, and the minimum χ^2-values were deduced for a fixed λ by adjusting $R_0^{(i)}$ with the non-linear least square method. The fitting processes were carried out by changing λ from 130 to 150 g/cm^2. The fitting results of ^{209}Bi(n, 4n)^{206}Bi reactions with λ= 145 g/cm^2 are shown in Figure 6, for example. The χ^2-value of the fitting was 3.2. In the fitting, the data at the position of -135 cm, indicated in the right figure, was not used because the position was out of the application range of the Moyer's expression.
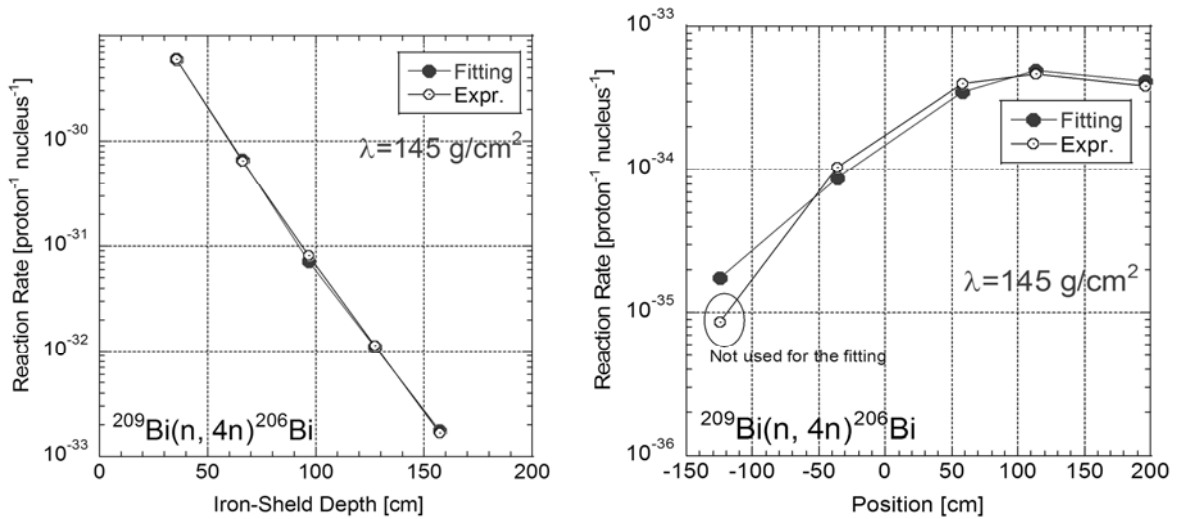
Figure 6: Fitting results of ^{209}Bi(n, 4n)^{206}Bi using Moyer's expression

Figure 7 shows the χ^2-value as a function of λ for ^{209}Bi(n, 4n), (n, 5n) and (n, 6n) reactions. These curves show that the χ^2-values were minimised between λ=140 and 145 g/cm^2. We suppose that this result is tentative. In order to finalise the λ-value deduction, which means obtaining the most optimum λ-value from our experiment, it is necessary to consider the validity of $R_0^{(i)}$-distributions obtained in the fitting from the viewpoint of theoretical calculation.

Using a similar process, the λ- value for the concrete shield will be deduced. In order to do this, we investigate how to treat the "air-gap" in the Moyer model.

Figure 7: Variations of the χ^2-value as a function of λ for ^{209}Bi(n, 4n), (n, 5n) and (n, 6n) reactions
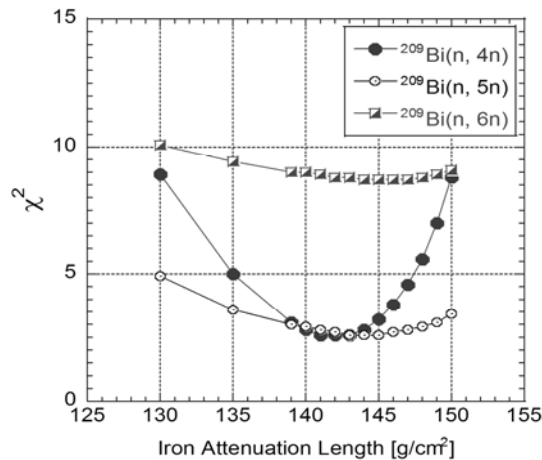
Summary

Experimental shielding data has been obtained at the high-energy accelerator facility with maximum proton acceleration energy over 100 GeV by means of the multi-foil activation method. The neutron spectra at various positions in the shielding assembly were deduced from the experimental reaction-rate data using the fitting method, which is newly developed in this work.

These data are remarkable and essential for validating a particle transportation code in terms of the simplicity of shielding geometry and the well-known constitution of concrete shielding.

The experimental data were compared with the calculation of the PHITS code with the simplified two-dimensional geometry.

We tentatively deduced the optimum values of a neutron attenuation length by applying the experimental reaction-rate distribution to the Moyer's approximation model. The Pbar station is a multi-source system from shielding experiment viewpoints. Therefore, comprehension of the source terms will be essential for obtaining the most optimum value of the attenuation length and for further calculation analysis.

Acknowledgements

References

[1]   H. Nakashima *et al.* (2009), *Nucl. Technol.*, 168, 482-486.

[2]   Y. Kasugai *et al.* (2011), *J. Korean Phys. Soc.*, 59, 2063-2066.

[3]   H. Yashima *et al.* *Progress in Nucl. Sci. and Techonol.*, 2 to be published.

[4]   Y. Kasugai *et al.* (2012), *J. ASTM International (JAI)*, 1550, 675-689.

[5]   F. Maekawa *et al.* (2001), *ASTM Spec. Tech. Publ.*, 1398, 417–424.

[6]   F. Maekawa *et al.* (2005), *Nucl. Sci. Eng.*, 150, 99-108.

[7]   H. Iwase *et al.* (2002), *J. Nucl. Sci. Tecnol.*, 39, 1142–1151.

[8]   N. Matsuda *et al.* (2011), *Progress in Nucl. Sci. and Techonol.*, 1, 57-60.

[9]   G. Stevenson *et al.* (1982), Health Phys., 43, 13-29.

Session V: Source Term and Related Topics

Chair: Hideo Hirayama

Evaluation and applications of shielding parameters for a heavy-ion accelerator facility

Noriaki Nakao[1,2], Hee-Seock Lee[1]
[1]Pohang Accelerator Laboratory (PAL), POSTECH, Nam-gu, Pohang, Republic of Korea
[2]Institute of Technology, Shimizu Corporation, Etchujima, Koto-ku, Tokyo, Japan

Abstract

For the conceptual design of shield for the Rare Isotope Science Project (RISP) in the Republic of Korea, the source term and attenuation length of shielding parameters for a simple exponential formula were determined by means of Monte Carlo simulations using the PHITS code. Simulations were performed for angular and energy spectra of secondary neutrons emitted from an iron target of full stopping thickness or from a thin graphite target bombarded by heavy ions of ^{238}U, ^{86}Kr, or ^{48}Ca (200–270 MeV/u), or by protons (600 MeV) for the in-flight target system. A simulation with 70-MeV proton bombardment was also performed for the isotope separator on-line (ISOL) target system. The simulations of the transmission of high-energy neutrons through 8-m-thick shields of concrete or iron were performed using the neutron-energy spectra for various angles. By fitting the exponential formula to the attenuation profiles, shielding parameters were obtained for various combinations of projectile, target, angle, and shielding material. The parameters were summarised for a point beam loss and for uniform beam loss along the accelerator beam line. Appropriate thicknesses for concrete and iron shields in the heavy-ion accelerator facility can be estimated fairly easily for various conditions.

Introduction

As part of the Rare Isotope Science Project (RISP) in the Republic of Korea, there are plans to use a heavy-ion beam of a few hundred kilowatts of power to achieve effective production of rare isotope (RI) beams using an in-flight target or an isotope separator on-line (ISOL) target system. For such a high-power accelerator facility, it will be necessary to construct a massive shielding wall, probably several meters thick, between the beam line and areas in which personnel work. Because neutrons readily penetrate the matter, the prompt radiation behind a shield consists mainly of neutrons among the secondary particles generated by beam losses at beam dumps, targets, or beam-line components.

Recently, Monte Carlo codes have been widely used to simulate beam interactions and radiation transport at accelerator facilities. However, the simulation of particle transmission with deep penetration through a massive shield generally requires sophisticated techniques and consumes large amounts of computing time. To avoid such complexities in the earlier stages of the conceptual design of the facility, empirical equations with an exponential form, such as the Moyer model [1], are frequently used to evaluate the external dose rate produced by prompt radiation through a massive shield. However, the parameters used in this model generally relate to proton accelerators with energies in excess of several gigaelectron volts [2] [3].

In this work, shielding parameters for heavy ions were investigated by means of a Monte Carlo simulation. Source terms and attenuation lengths for a simple exponential formula were estimated for various targets irradiated by heavy ions or protons with energies of several hundreds of megaelectron volts.

Empirical formula

Generally, the level of prompt radiation behind a massive shield can be expressed approximately by using a simple exponential formula. Images of applicable situations for a beam parallel to the shield and a beam perpendicular to the shield are shown in Figure 1.

For a point beam loss, the dose rate H [μSv/h] arising from prompt radiation at an estimation point can be expressed as follows:

$$H = JH_0 \frac{1}{r^2} \ exp\left(-\frac{d\rho}{\lambda}\right)$$

(1)

where J [W] is the beam injection at the source point, H_0 [(μSv/h) cm^2 /W] is the source term, r [cm] is the distance between the beam loss and the estimation points ($r = a + d$), a [cm] is the part of distance r in space, d [cm] is the part of distance r in the shield, ρ [g/cm^3] is the density of the shielding material, and λ [g/cm^2] is the attenuation length.

Figure 1: Images of applicable situations for point losses of parallel and perpendicular beams

(a) Parallel beam   (b) Perpendicular beam
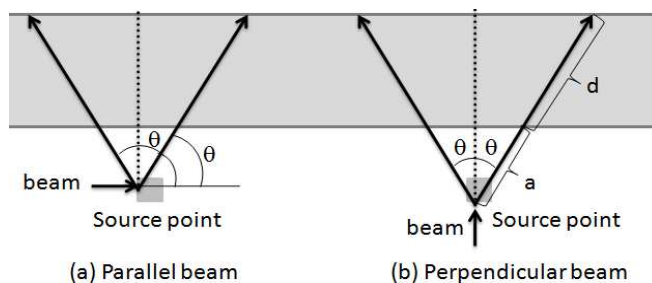
In the case of a multilayer shielding structure, the formula can be adjusted through multiplication by additional exponential parts for the extra materials, as follows:

$$H = JH_0 \frac{1}{r^2} \ exp\left(-\frac{d_1\rho_1}{\lambda_1}\right) exp\left(-\frac{d_2\rho_2}{\lambda_2}\right) \cdots$$

(2)

In the case of uniform beam loss along the beam line, the dose rate behind a massive shield can be expressed as follows:

$$H = \frac{dJ}{dL} \ H_0 \ \frac{1}{r} \ exp\left(-\frac{d\rho}{\lambda}\right)$$

(3)

where dJ/dL [W/m] is the amount of uniform beam loss per unit length and H0 [(Sv/h) cm/(W/m)] is the source term. The other parameters in Equation (3) are the same as those in Equation (1). Equation (3) can be used only for the parallel beam, and the parameters r, d, and a are the distances in the direction perpendicular to the shield.

Monte Carlo simulation

For all Monte Carlo simulations in this work, we used the PHITS code [4] version 2.15. As data libraries for the simulation, we used JENDL-3.3 [5] nuclear data for low-energy neutrons below 20 MeV, and MCPLIB02 [6] for photon production and transportation.

Simulation of secondary neutron production

The characteristics of the targets used for the simulations are listed in Table 1. A thin graphite target of thickness 0.9 g/cm^2 was used as an in-flight target for the RI beam production. The target used in the simulation had a radius of 25 mm, a thickness of 4 mm, and a density of 2.25 g/cm^3. This target thickness is equivalent to a 5-mm-thick target with a density of 1.8 g/cm^3. Thick iron targets were chosen for the estimation of the source term for beam losses at beam-line components due to a beam halo or an operational failure. The thicknesses of these iron targets were chosen to be around 1.1–1.2 times thicker than the stopping range of projectiles, because the maximum flux of high-energy neutrons above 20 MeV is available in the forward direction when the thickness is in the projectile range for the case of heavy ions. The self-shielding effect of high-energy neutrons in the forward direction is not negligible for 600-MeV protons in the 30-cm-thick iron target. However, reducing the radius suppresses the self-shielding effect, not only in the sideways and backward directions, but also in the forward direction. The radius of the iron targets for all projectiles was chosen to be 5 mm, which is short enough to give a negligible neutron self-shielding effect in combination with negligible escape of the primary beam from the sides of the target.

An ISOL target is also used for the RI beam production from 70-MeV protons. As listed in Table 1, the target is of full stopping length and consists of a 3-cm-thick piece of UC$_2$ behind a 4-mm-thick graphite window and with a 5.4-mm-thick graphite dump.

The angular and energy spectra of the secondary neutrons produced from the target–projectile combinations listed in Table 1 were simulated in the energy range above 1 MeV. In the simulation, secondary neutron currents were estimated in the spherical surfaces of parts of the cone shapes for nine angular ranges. Angular and energy spectra of neutrons for various projectile injections for an in-flight target system are shown in Figures 2 and 3 for the iron and the graphite target, respectively. For an ISOL target system, the spectra from the iron and the ISOL targets irradiated by 70-MeV protons are shown in Figure 4.

Table 1: Characteristics of targets used in the simulations

| Projectile	Iron (7.8 g/cm^3)			Graphite (2.25 g/cm^3)			
	Radius [mm]	Thickness [mm]	Range [mm]	Radius [mm]	Thickness [mm]	dE [MeV/u]	E-out [MeV/u]
200 MeV/u ^{238}U	5	2.0	1.7	25	4	167.6	32.4
240 MeV/u ^{86}Kr	5	5.0	4.5	25	4	52.0	188.0
270 MeV/u ^{48}Ca	5	10.0	9.6	25	4	25.9	244.1
600 MeV proton	5	300.0	279	25	4	2.1	597.9
70 MeV proton	5	9.0	7.8				
ISOL target (Graphite 1.8 g/cm^3, UC$_2$: 2.5 g/cm^3)							
70 MeV proton	R=35 mm	Graphite window (4 mm)+UC$_2$ (30 mm)+graphite dump (5.4 mm)					Full stop

Figure 2: Angular and energy spectra of secondary neutrons from an iron target
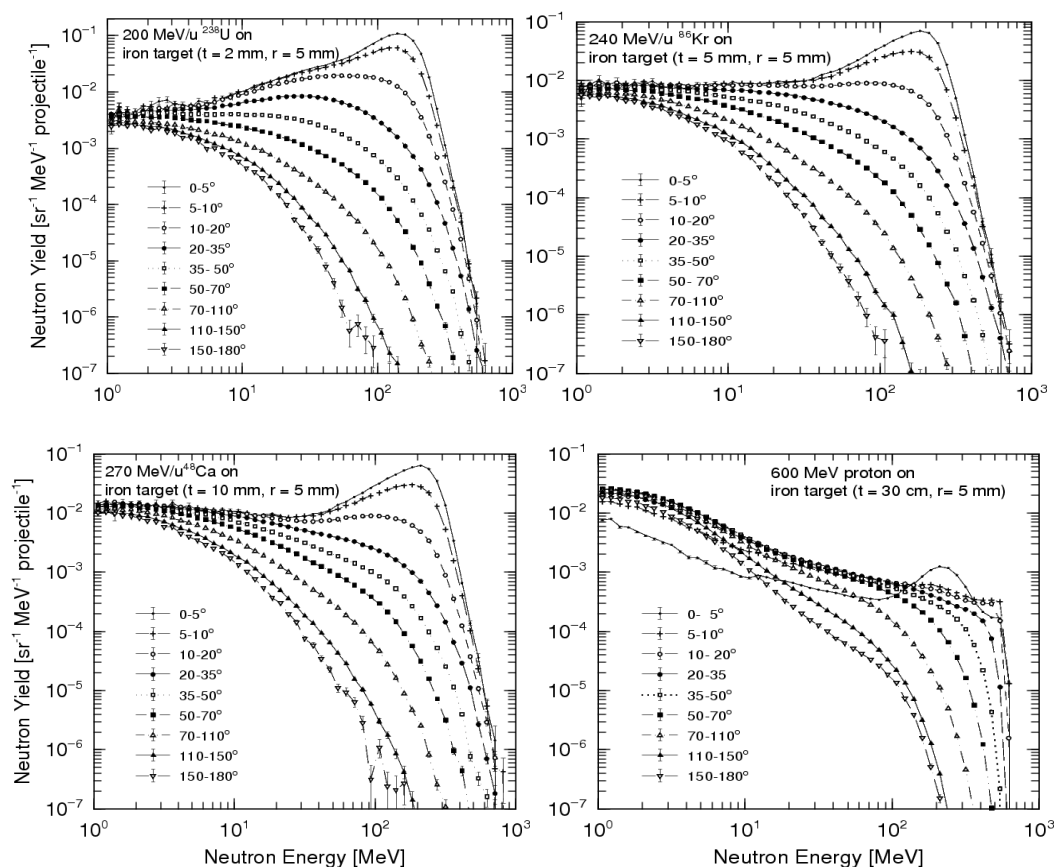
Figure 3: Angular and energy spectra of secondary neutrons from a graphite target
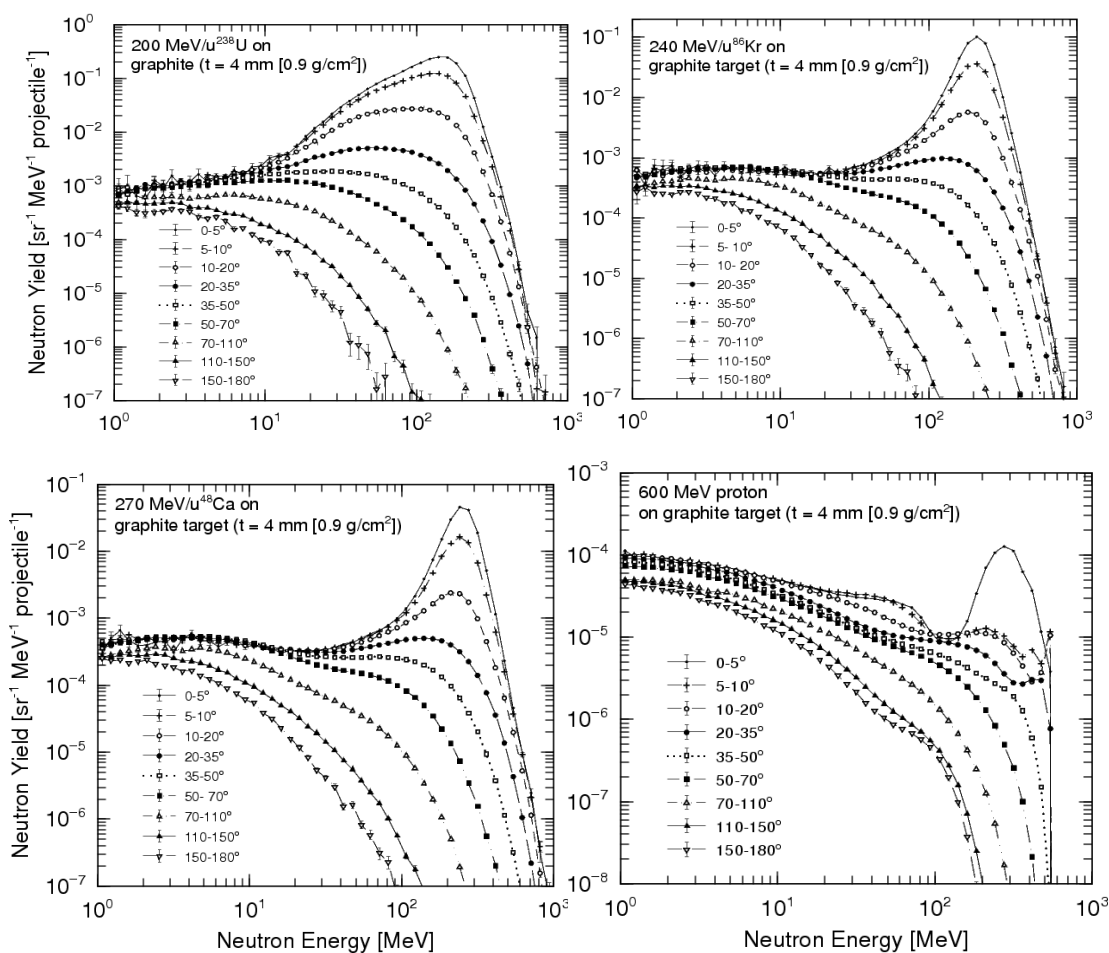
Figure 4: Angular and energy spectra of secondary neutrons from iron and ISOL targets irradiated by 70-MeV protons
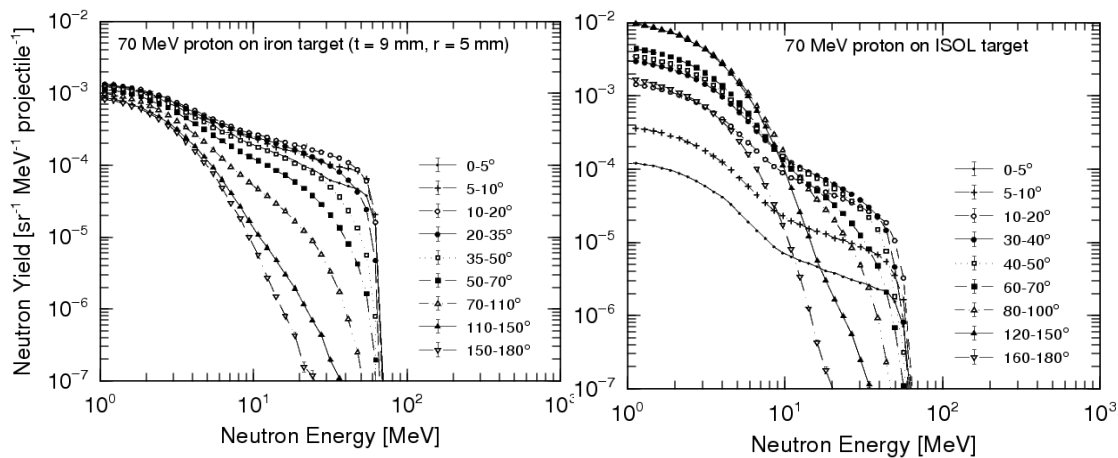
Figures 5(a) and 5(b) show the angular fluxes of high-energy neutrons for the iron and graphite targets, respectively, normalised for a 1-W beam power and integrated above 20 MeV. These figures show that secondary neutrons produced by heavy-ion bombardments have a high degree of forwardness compared with those produced by proton bombardment. For the same beam power, the impact of 600-MeV protons on both targets produced higher fluxes in the sideways and backward directions in comparison with those produced by impact of heavy ions.

Figure 5: Angular flux of high-energy neutrons above 20 MeV for various projectile-target combinations normalised for a 1-W beam injection

(a) Iron target   **(b) Graphite target**
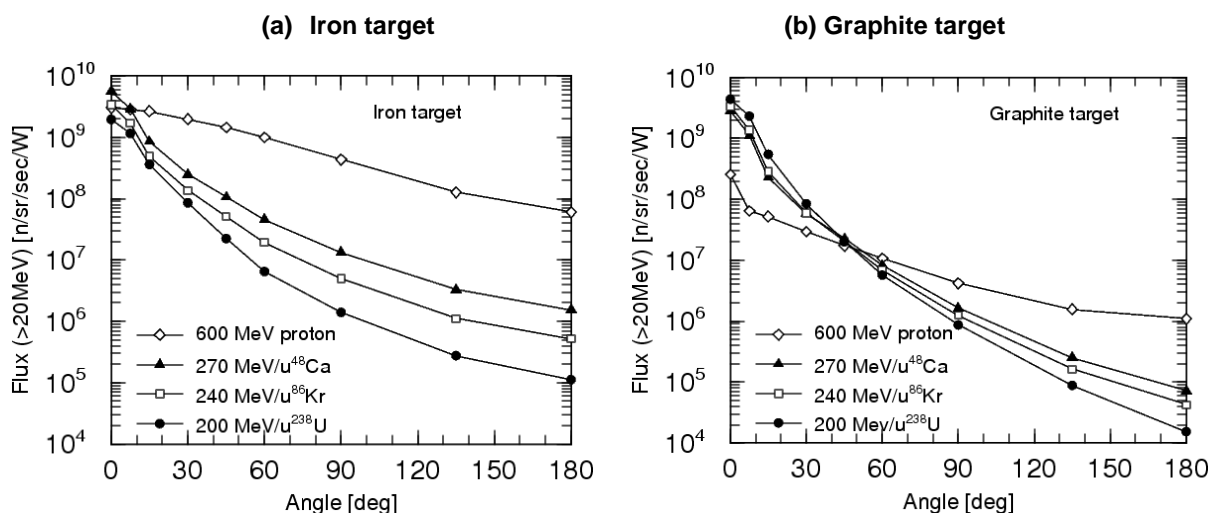
Simulation of neutron attenuation by a massive shield

Having derived the energy spectra of the secondary neutrons, we performed simulations of the transmission of high-energy neutrons above 20 MeV through an 8-m-thick shield using the PHITS Monte Carlo code. A total of 180 transmission simulations were carried out for two targets, five projectiles, nine angles, and two shielding materials. We simulated the injection of a pencil beam of neutrons into the center of the shield slab, and we used an importance method as a variance-reduction technique in the Monte Carlo simulation to obtain good statistics for neutrons in the deep-shielding region. Figure 6 shows two-dimensional neutron-track plots of the shielding transmission simulations with 8-m-thick shields of concrete or iron with neutrons emitted at 0° from an iron target irradiated by a 200-MeV/u ^{238}U beam as an example. The energy spectra of neutrons integrated over planes at the same depth were scored with a surface crossing estimator. Dose rates of high-energy neutrons were estimated from the spectra and from the flux-to-dose conversion factor [7].

Attenuation profiles of the prompt dose rate of high-energy neutrons through the 8-m-thick shields of concrete and iron were obtained for various angles of the neutron sources for all projectile–target combinations. The results for the iron target irradiated by a 200-MeV/u ^{238}U beam are exemplified in Figure 7. As a result of the use of the importance method in the deep-penetration simulation, statistical errors within a few percentage points were obtained, which are sufficiently accurate to permit the estimation of the dose rate through the 8-m thickness. However, the attenuation profiles are strongly dependent on the high-energy part of the source neutron spectra and, because of the strong forwardness of the secondary neutrons emitted as a result of the injection of heavy ions, comparatively poorer statistics are observed in the backward direction, as shown in Figures 2–4. To avoid the risk of underestimating the dose rates, therefore, shielding parameters for 110–150° should be used for the angular direction above 150° for all projectile–target combinations.

Figure 6: Two-dimensional neutron-track plots based on the shielding-transmission simulations using neutrons produced at 0° by irradiation of an iron target by 200-MeV/u ^{238}U

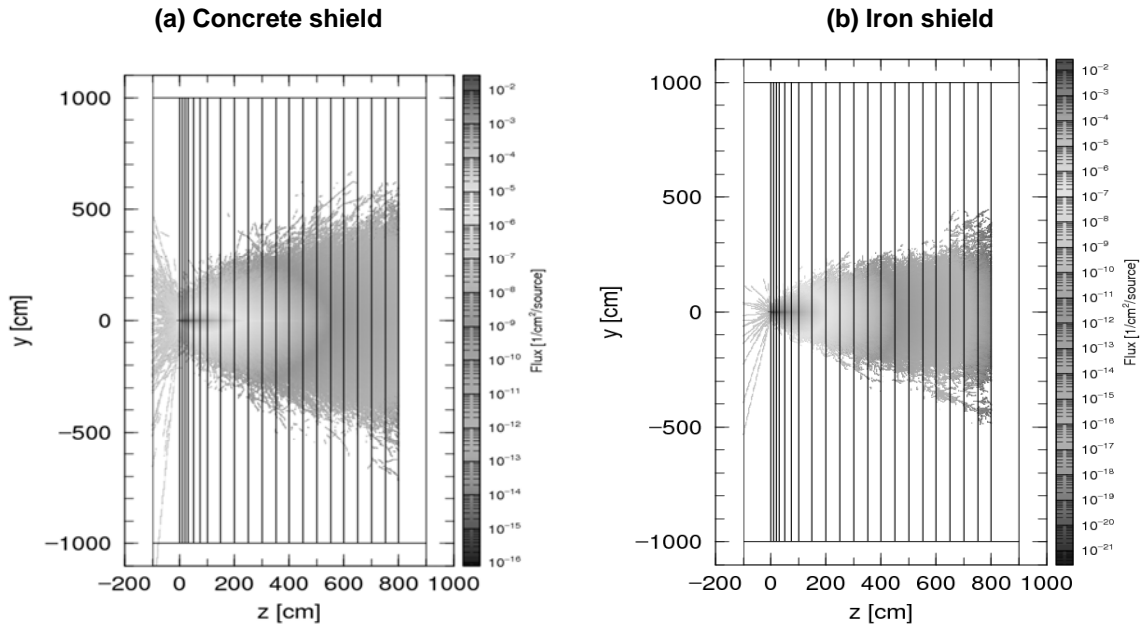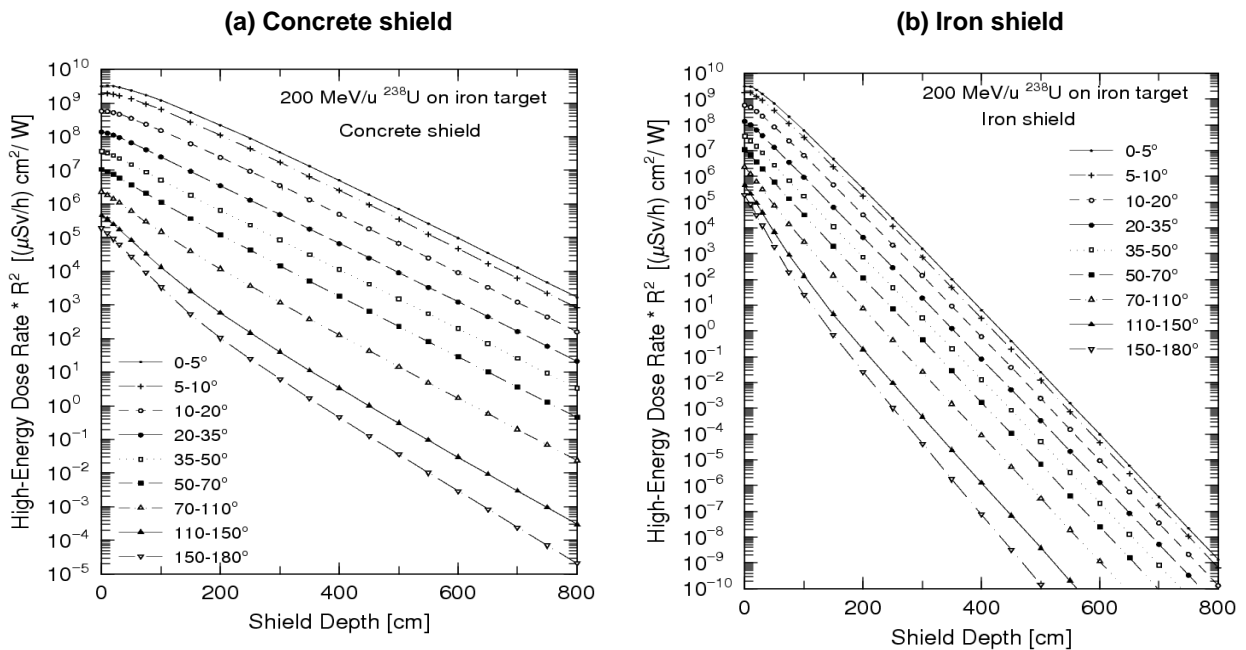### (a) Concrete shield

(b) Iron shield

Figure 7: Attenuation profiles of the dose of high-energy neutrons through shields with irradiation of neutron sources at nine different angles from an iron target by 200-MeV/u ^{238}U

(a) Concrete shield

(b) Iron shield

Relationship between the energy spectrum and the dose rate

Concrete shield

A simulation of transmission of neutrons through an 8-m concrete shield in the range of neutron energies down to the thermal level (0.025 eV) was also performed in the case of neutrons generated by irradiation of an iron target by a 200-MeV/u ^{238}U beam. The neutron-energy spectra down to thermal energy levels at various depths in the concrete shield with the neutron source at 0° are shown in Figure 8. Beyond a thickness of about 200 cm in the concrete shield, an equilibrium state is observed in the neutron-energy spectrum down to thermal energy levels; this keeps the shape of the spectrum independent of the shield depth.

Prompt dose rates were estimated for total neutrons, high-energy neutrons above 20 MeV, and photons, using the energy spectra obtained in the simulation described above. Figure 9 shows a comparison of their attenuation profiles. The three attenuation curves in the region beyond a thickness of about 200 cm show an almost constant slope.

Figure 10 shows the ratios of the total dose (including photons and neutrons) over the whole energy range to the dose of high-energy neutrons passing through the concrete shield for various angles. As can be seen in the figure, all ratios become almost constant after a thickness of 250 cm, and the total prompt dose rates are 1.6–1.9 times those of the high-energy neutrons for all angles. Therefore, by taking a correction factor of 2.0 as a safety margin, the total prompt dose rate behind the concrete shield can be predicted from the results for the high-energy neutrons above 20 MeV.

Iron shield

Using the same source neutrons as described above, we also performed a simulation with 6 m iron shield followed by 2 m concrete shield, and we simulated the neutron-energy spectra down to thermal energy levels at various depths in the two layers of the composite iron-and-concrete shield using a weight window method as a variance-reduction technique in the Monte Carlo simulation. The results are shown in Figure 11. An energy spectrum behind an iron shield generally has a broad peak at around a few hundred kiloelectron volts which consists mainly of inelastically scattered neutrons. Where the iron shield is thicker, the contribution of these neutrons increases, whereas that of high-energy neutrons decreases rapidly. However, placing a concrete shield behind the iron shield reduces the flux of neutrons with energies in the region of a few hundred kiloelectron volts and, finally, the energy spectrum settles to an equilibrium state in the concrete shield.

Additional simulations were performed for 1, 2, 4, 6, and 8 m-thick iron shields followed by a massive concrete shield. Dose-attenuation profiles through the shield were estimated for the total neutrons, high-energy neutrons, and photons; these are shown for the cases of the 2 and 4m-thick iron shields in Figure 12, and for the 6 and 8m-thick shields in Figure 13. The figures show that the curves of the total dose rate start to decrease rapidly after the boundary of the concrete shield and that they finally settle into an equilibrium state in which the attenuation curves for the total neutrons and the high-energy neutrons are parallel. These results permitted the dependence of the required thicknesses of the additional concrete on the thickness of the iron shield to be roughly evaluated and the evaluation is presented in Table 2.

As can be seen in Figures 12 and 13, the contribution of photons accompanied by inelastic reactions is not negligible, especially in the case of a thick iron shield. Even behind the required thickness of concrete, dose rates due to photons remain dominant in cases where the thickness of the iron shield is greater than 4m, and the use of an additional shield for photons should be considered in these cases.

Figure 8: Neutron-energy spectra down to thermal energy levels inside a concrete shield for irradiation of a neutron source at 0° from an iron target by 200-MeV/u ^{238}U
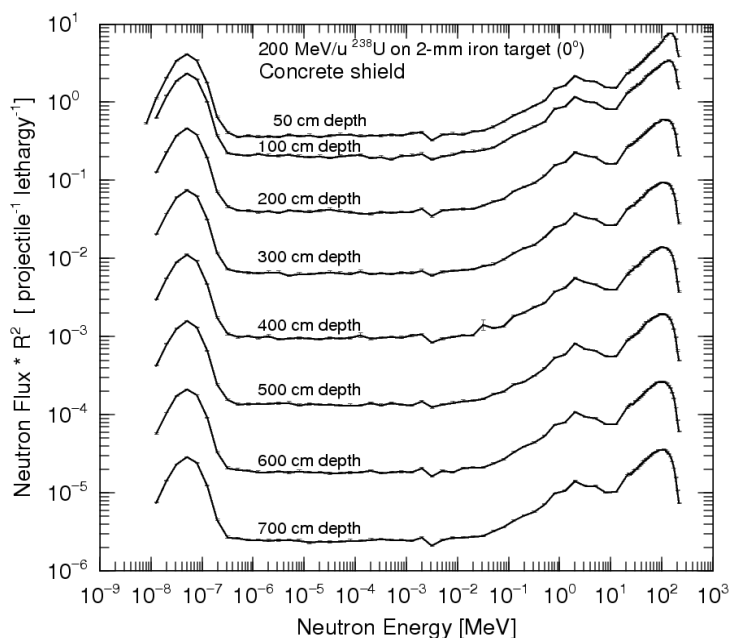
Figure 9: Comparison of attenuation profiles of dose rates of total neutrons, high-energy neutrons above 20 MeV, and photons through a concrete shield for irradiation of neutrons at 0° from an iron target by 200-MeV/u ^{238}U
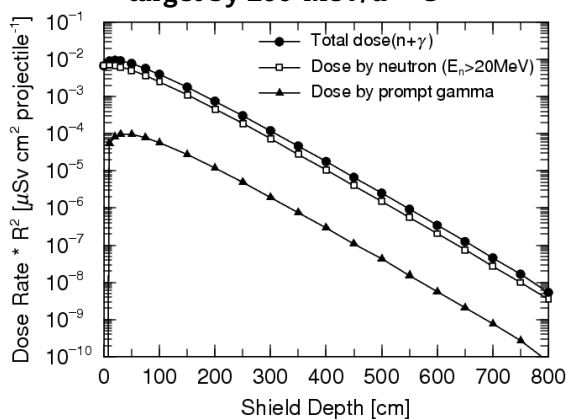
Figure 10: Ratios of total dose to high-energy neutrons through a concrete shield for irradiation of neutrons at various angles from an iron target by 200-MeV/u ^{238}U
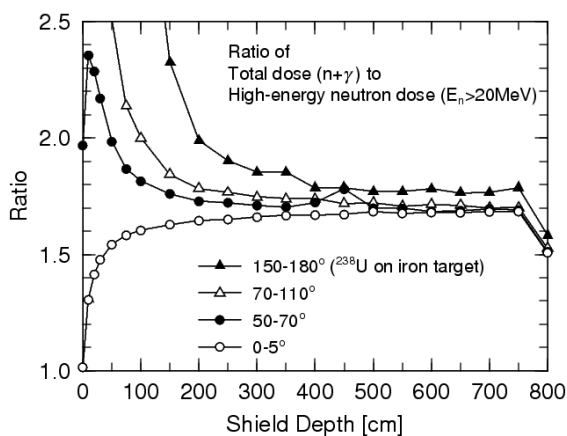
Figure 11: Neutron-energy spectra down to thermal energy levels inside a 6m iron shield followed by a 2 m concrete shield for irradiation of neutrons at 0° from an iron target by 200-MeV/u ^{238}U

Figure 12: Dose-rate attenuation profiles of total neutrons, high-energy neutrons, and photons inside an iron shield of thickness 2 m (left) or 4 m (right) followed by a thick concrete shield for irradiation of neutrons at 0° from an iron target by 200-MeV/u ^{238}U

Figure 13: Dose rate attenuation profiles of total neutrons, high-energy neutrons, and photons inside an iron shield of thickness 6 m (left) or 8 m (right) followed by a thick concrete shield for irradiation of neutrons at 0° from an iron target by 200-MeV/u ^{238}U

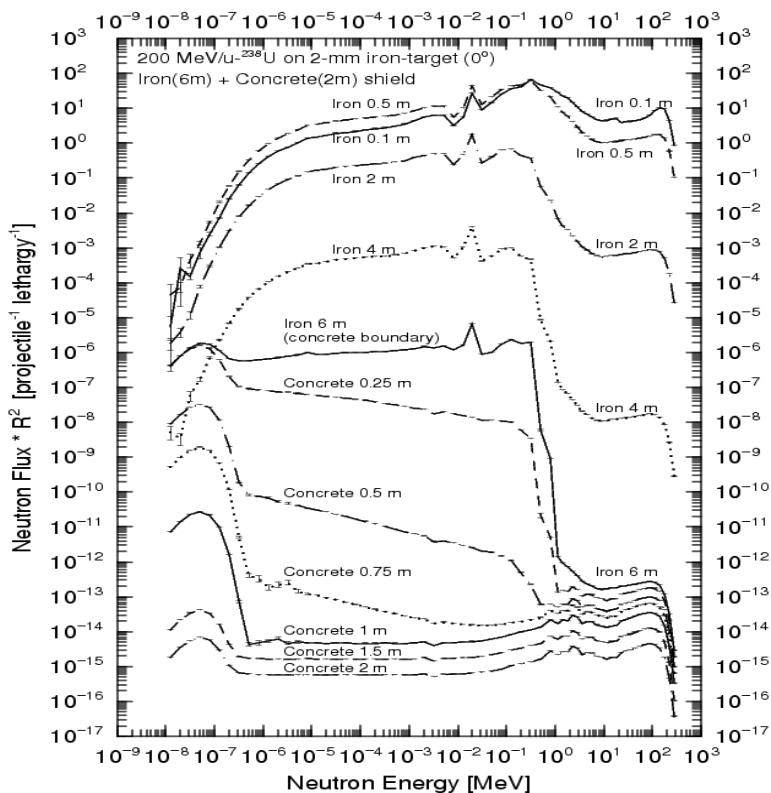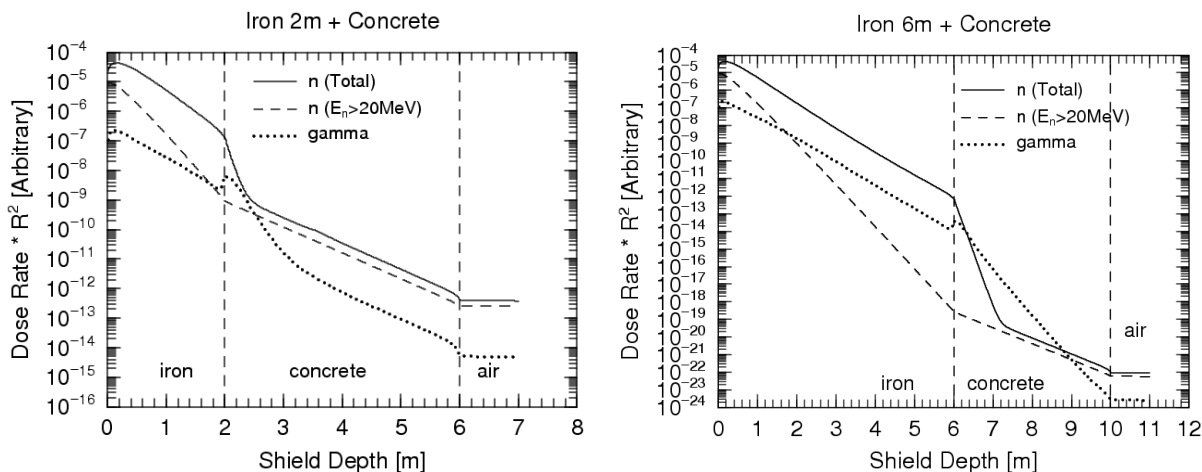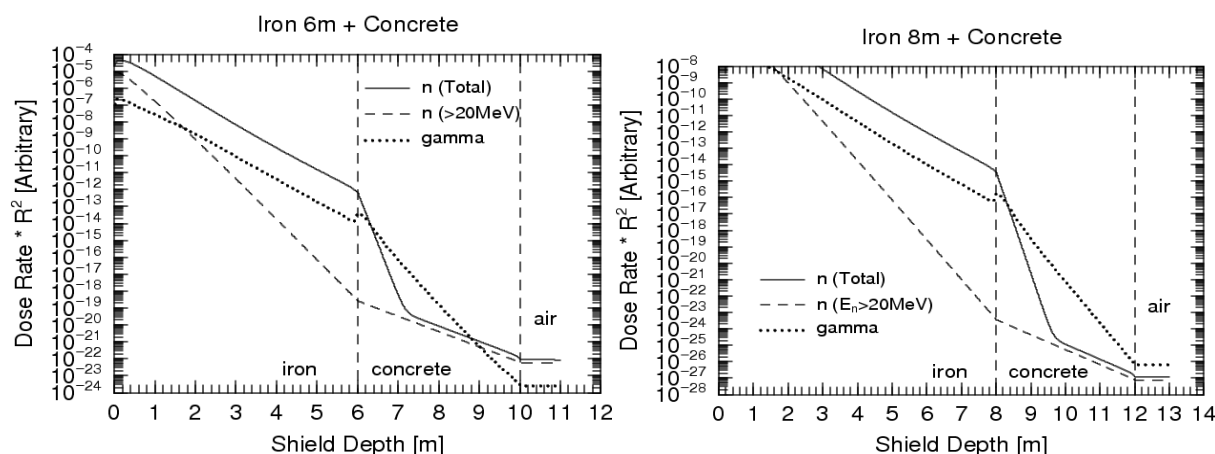**Table 2: Required concrete thickness after various thicknesses of iron shield**

Iron thickness	1 m	2 m	4 m	6 m	8 m
Needed last concrete thickness	0.4 m	0.6 m	0.8 m	1.2 m	1.6 m

Simulation of uniform losses

To estimate the shielding parameters for uniform beam loss, Monte Carlo simulations were performed for the iron target with five projectiles and two shielding materials. Instead of placing multiple beam losses uniformly along the beam line, a point loss and long flux estimators that covered most of the transmitted particles in the beam direction were defined to obtain results physically identical to those for uniform loss.

Surface crossing estimators 2 m wide by 110 m long, i.e. from 10 m backward up to 100 m forward, were placed in the various shield thicknesses. Energy spectra of the transmitted neutrons through an 8 m-thick concrete or iron shield in the energy range above 20 MeV were estimated and the dose rates of high-energy neutrons were obtained at various depths in the concrete and iron shields. Figure 14 shows an example of a two-dimensional dose-rate profile obtained by the simulation.

Figure 14: Two-dimensional dose-rate profiles in the three perpendicular planes (*x*=0, *y*=0 and *z*=0) for a uniform-loss equivalent simulation with a 200-MeV/u ^{238}U parallel beam on an iron target
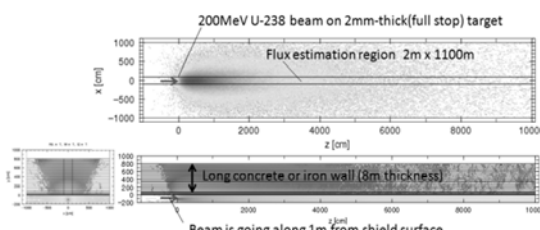
Parameter estimations

The all-attenuation profiles of the prompt dose rates for the point loss that we obtained were fitted using Equation (1) to give the shielding parameters H_0 and λ for high-energy neutrons for various projectile–target combinations and for various angles from the beam direction. The fitting images are exemplified in Figure 15.

The values of H_0 were obtained as values at 0 cm thickness of the shield on the extrapolated fitting lines and, because of a spectrum build-up process, were generally higher for forward angles and lower for backward angles than those for the original data at 0 cm (Figure 15). Finally, the values of H_0 for the high-energy dose were converted into those for the total dose by applying a correction factor of 2.0, as previously discussed.

Two values of H_0 for concrete and iron shields were obtained for one target–projectile combination. Generally, the values for the iron shield were slightly higher than those for the concrete shield because of the steeper slope of the fitted curve in the case of iron. Therefore, the H_0 value for iron was employed for each source term. The maximum difference was less than a factor of two in this work. The shielding parameters that we obtained for point losses are given in Tables 3 and 4 for H_0 and λ, respectively.

The shielding parameters for uniform losses were also estimated by fitting the simulated dose rates with Equation (3). The numerical values of H_0 and λ for five projectiles and two shielding materials are listed in Table 5.

Figure 15: Fitting image for the attenuation profiles of the prompt dose rate in the shield
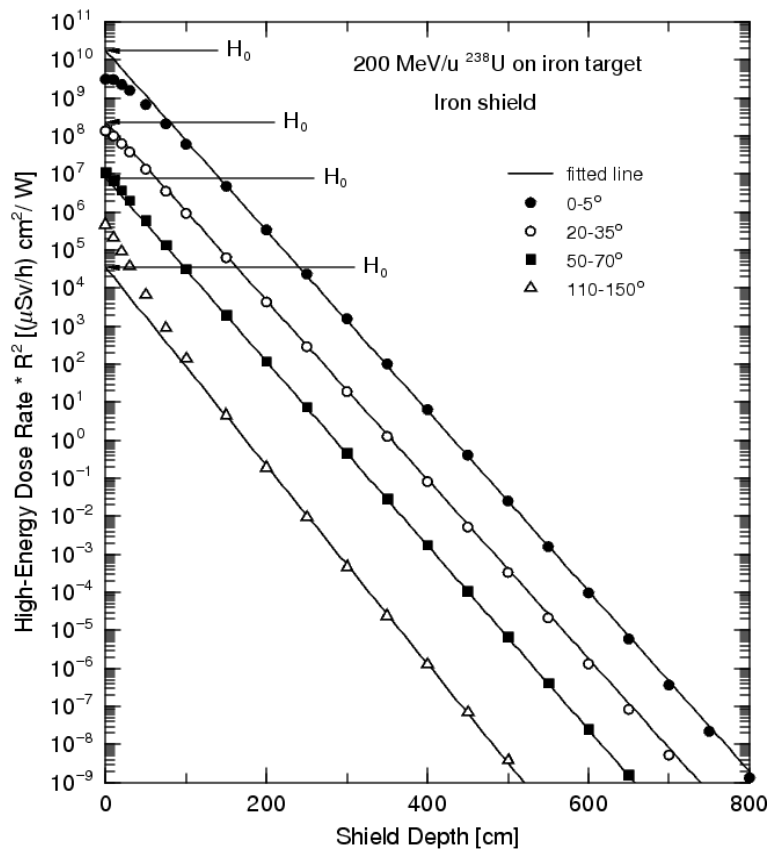
Table 3: Shielding parameter H_0 for various point losses

Target	Beam	$H_0[(\mu Sv/h)\ cm^2/W]$ for point loss							
		0-5°	10°	20°	35°	50°	70°	110°	150-180°
Fe (full stop)	200 MeV/u ^{238}U	3.5E+10	1.8E+10	3.5E+09	4.7E+08	8.7E+07	1.6E+07	1.0E+06	6.9E+04
	240 MeV/u ^{86}Kr	8.1E+10	3.5E+10	6.9E+09	1.0E+09	2.4E+08	5.3E+07	6.1E+06	3.9E+05
	270 MeV/u ^{48}Ca	1.5E+11	6.5E+10	1.3E+10	2.1E+09	5.9E+08	1.4E+08	1.8E+07	1.2E+06
	600 MeV proton	9.7E+10	8.5E+10	6.8E+10	3.8E+10	1.9E+10	7.3E+09	1.4E+09	1.9E+08
	70 MeV proton	1.5E+09	2.6E+09	2.6E+09	1.4E+09	5.4E+08	1.9E+08	2.7E+07	2.2E+06
Graphit (0.9 g/cm^2 thick)	200 MeV/u ^{238}U	8.3E+10	3.7E+10	6.9E+09	7.8E+08	1.1E+08	1.5E+07	7.3E+05	2.4E+04
	240 MeV/u ^{86}Kr	1.1E+11	4.2E+10	7.7E+09	1.1E+09	2.3E+08	3.6E+07	2.2E+06	5.4E+04
	270 MeV/u ^{48}Ca	1.1E+11	4.0E+10	7.0E+09	1.2E+09	3.0E+08	5.4E+07	3.8E+06	1.3E+05
	600 MeV proton	1.0E+10	1.8E+09	1.6E+09	6.7E+08	2.7E+08	9.0E+07	1.5E+07	3.8E+06
ISOL UC$_2$	70 MeV proton	5.4E+07	1.9E+08	6.0E+08	5.6E+08	3.3E+08	1.5E+08	6.3E+07	1.2E+07

∗ Interpolation is recommended for angles where parameters are not given.

Table 4: Shielding parameter λ for various point losses

Shield	Beam	$\lambda[g/cm^2]$ for point loss							
		0-5°	10°	20°	35°	50°	70°	110°	150-180°
Concrete	200 MeV/u ^{238}U	117	117	117	116	114	111	106	96
	240 MeV/u ^{86}Kr	124	123	123	122	119	114	108	101
	270 MeV/u ^{48}Ca	126	126	125	124	120	116	110	102
	600 MeV proton	128	129	128	127	124	119	112	105
	70 MeV proton	63	62	61	60	58	58	54	54
Iron	200 MeV/u ^{238}U	143	143	144	144	142	140	139	130
	240 MeV/u ^{86}Kr	147	147	147	147	145	143	138	134
	270 MeV/u ^{48}Ca	149	149	148	148	146	143	139	135
	600 MeV proton	150	150	150	150	149	145	140	135
	70 MeV proton	88	88	87	85	83	82	79	78

∗ Interpolation is recommended for angles where parameters are not given.

Table 5: Shielding parameters H_0 and λ for various uniform losses

Target	Beam	Concrete shield		Iron shield	
		$H_o[(\mu Sv/h)\ cm/(W/m)]$	$\lambda[g/cm^2]$	$H_o[(\mu Sv/h)\ cm/(W/m)]$	$\lambda[g/cm^2]$
Fe (full stop)	200 MeV/u ^{238}U	3.0E+05	97	1.3E+05	134
	240 MeV/u ^{86}Kr	7.5E+05	99	3.6E+05	136
	270 MeV/u ^{48}Ca	1.6E+06	101	6.8E+05	135
	600 MeV proton	3.4E+07	105	3.7E+07	138
	70 MeV proton	7.3E+05	56	2.8E+05	84

Comparisons of dose-rate results calculated by formula and by simulation

For a simple shielding structure, dose rates calculated by means of the empirical formula were compared with those obtained by simulation with the PHITS code in the case of a distance of 1 m between the target and the shield. A two-dimensional track plot obtained by simulation with a ^{238}U parallel beam is shown in Figure 16. The simulated dose-rate distributions at several depths as a function of the angle for a 600-MeV proton beam and a 200-MeV/u ^{238}U beam are shown in Figure 17, together with the results calculated using Equation (1) with the appropriate parameters.

In the case of the proton beam shown in the figure, the results calculated using the formula agreed well with those obtained by simulation. However, in the case of the ^{238}U beam, the formula sometimes underestimated the results in thick regions at forward angles because of the strong forwardness of neutrons. Therefore, for heavy-ion injection of a parallel beam, the formula can be applied at angles of more than 80° for thicknesses of concrete in excess of 3 m.

Figure 16: Two-dimensional track plots of neutrons with an 8-m concrete shield for a 2 mm-thick iron target irradiated with a 200-MeV/u ^{238}U beam in the direction parallel to the shield surface
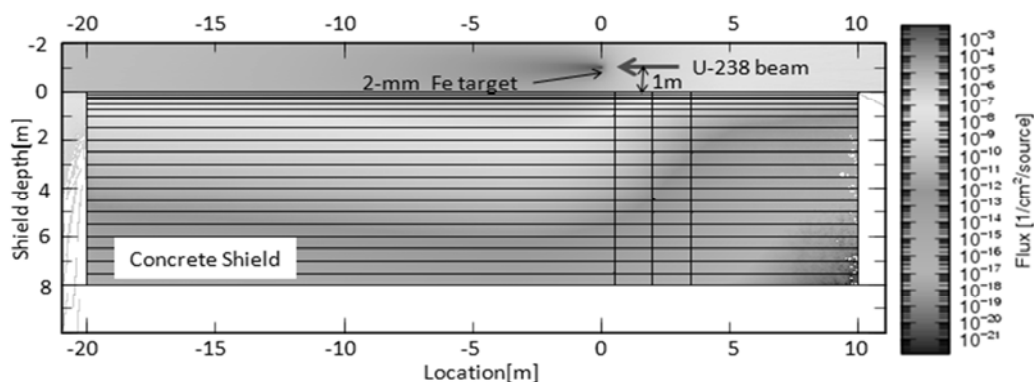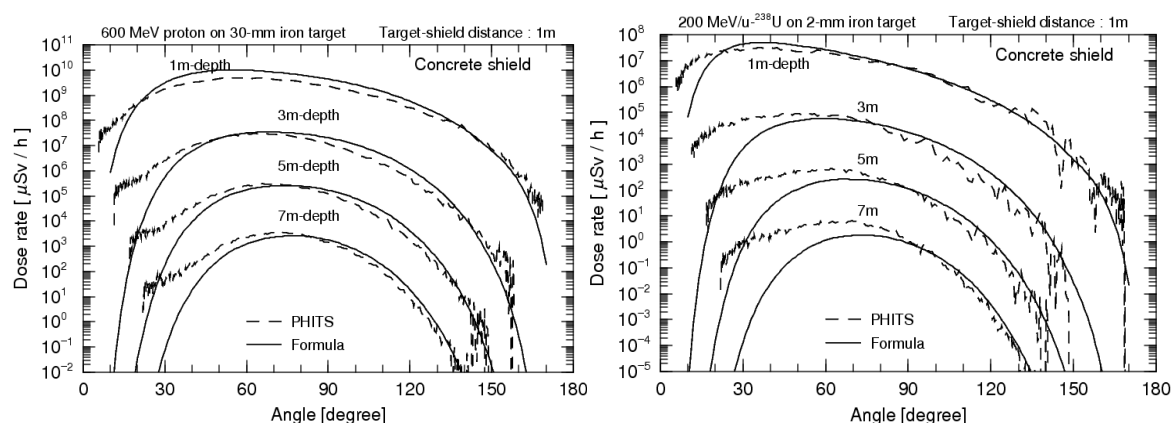
Figure 17: Comparisons of dose-rate distributions obtained by PHITS simulations and by calculations using the formula along the angles from the beam direction at the same shield depth inside an 8 m concrete shield for an iron target irradiated with a 600-MeV proton beam (left) or with a 200-MeV/u ^{238}U beam (right) in the direction parallel to the shield surface

A two-dimensional track plot for the perpendicular beam is shown in Figure 18. The results obtained by simulation and those obtained by the formula, compared as a function of the angle from 0° to 70°, are shown in Figure 19.

For the case of the ^{238}U beam, in the angular range below 10°, the formula gives dose rates that are higher by about a factor of 2 than those given by the simulation. Apart from this, however, the dose rates calculated using the formula generally agreed with those given by simulation over the angular range between 0 and 60° for concrete shields with a thickness of more than 3 m for both the proton beam and the ^{238}U beam.

Figure 18: Two-dimensional track plot of neutrons with an 8-m concrete shield for a 2 mm-thick iron target irradiated by a 200-MeV/u ^{238}U beam in the direction perpendicular to the shield surface
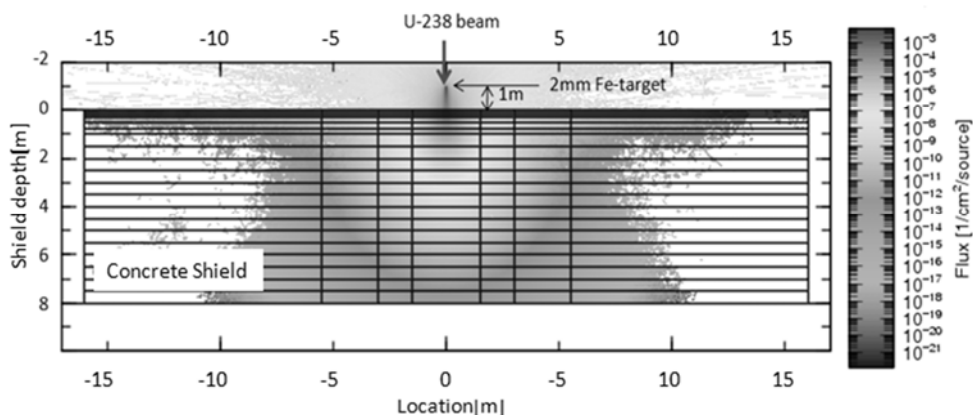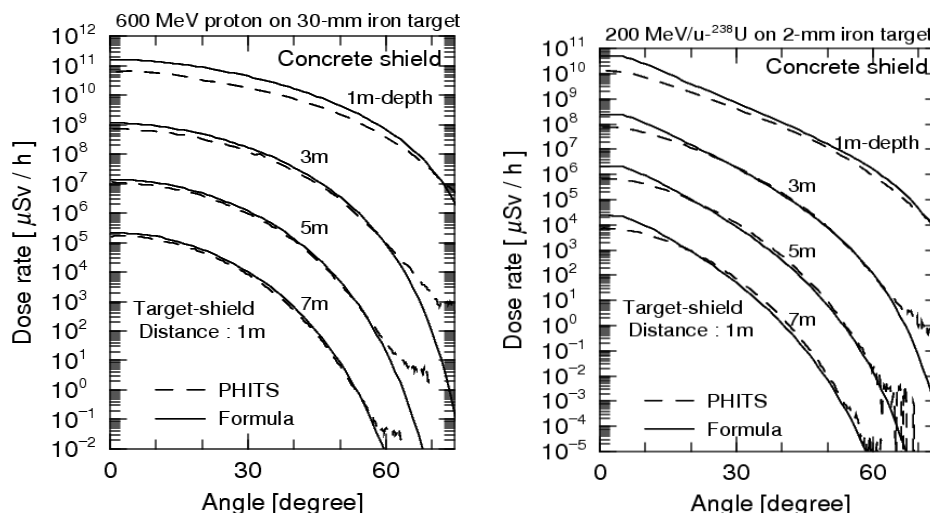
Figure 19: Comparisons of dose rate distributions obtained by PHITS simulation and by calculation with the formula along the angles from the beam direction at the same shield depth inside an 8-m concrete shield for an iron target irradiated with a 600-MeV proton beam (left) or with a 200-MeV/u ^{238}U beam (right) in the direction perpendicular to the shield surface

Conditions and limitations for practical application of the formula

The parameters of the empirical formulae obtained in this work are applicable under the following conditions and with the following limitations.

- The total of the thickness of the concrete shield plus 2.5-times the thickness of the iron shield should be at least 250 cm.

The fitting regions for the attenuation profiles have thicknesses of between 250 and 700 cm for concrete and between 100 and 600 cm for iron; therefore, these parameters should be used for dose estimation points in the region where the thicknesses of the shields are greater than 250 cm for concrete and 100 cm for iron. Because the shielding ability of iron is about 2.5 times greater than that of concrete, the sum of the thickness of the concrete and 2.5 times the thickness of the iron should exceed 250 cm for a multilayer shield.

- An appropriate thickness of concrete should be used for the final shield.

The shielding parameters were estimated on the assumption that the neutron-energy spectrum is in an equilibrium state behind a concrete shield. For the case of a thick iron shield, the required thicknesses of the additional concrete shields are given in Table 2.

- For the point-loss case, the angle to the estimation point should be within the ranges 0–60° for a perpendicular beam, 60-150° for a parallel proton beam, and 80-150° for a parallel heavy-ion beam.

As shown in Figure 20, as the angle from the perpendicular line increases, the portion of the shield in the direct path becomes much longer, so that neutrons passing through the other, shorter, path sometimes contribute markedly (the short-path effect) under actual conditions. Because of the strong forwardness of secondary particles produced by heavy-ion interactions, the short path effect of particles at a small (forward) angle is significant for parallel beams of heavy ions, and the empirical formula gives underestimations in the angular range below 80°. On the other hand, for a perpendicular heavy-ion beam, the short path effect is negligible and the formula applies at comparatively wide angles of up to 60°.

Figure 20: Image showing the direct path and a shorter path to the estimation point
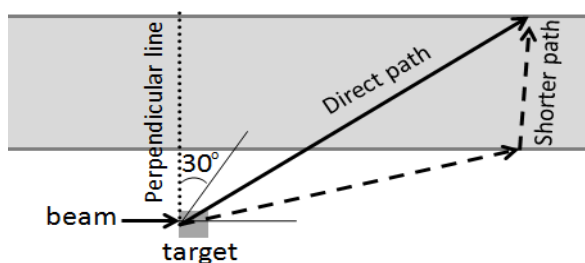
Summary

Shielding parameters for use in an empirical formula for designing shields in a heavy-ion facility were estimated by means of a PHITS Monte Carlo simulation, and the source term and the attenuation length were summarised for various projectiles, targets, angles, and shielding materials. Conditions where the formula applies in terms of the minimum shield thickness, the presence of a final concrete shield, and angular limitations were clarified. The shielding parameters obtained in this work could be very useful in the conceptual design of massive shields for high-power heavy-iron accelerator facilities.

Acknowledgements

References

[1]   B.J. Moyer (1962), *Proc. 1st Int. Conf. Shielding around High Energy Accelerators*, Presses Universitaires de France: Paris, p 65.

[2]   S. Ban *et al.* (1980), "Measurement of Transverse Attenuation Length for Paraffin, Heavy Concrete and Iron Around an External Target for 12 GeV Protons", *Nucl. Instrum. Methods* 174, 271.

[3]   G.R. Stevenson *et al.* (1982), "Determination of Transverse Shielding for Proton Accelerators Using the Moyer Model", *Health Phys.* 43, 13.

[4]   K. Niita *et al.* (2010), "PHITS: Particle and Heavy Ion Transport Code System, Version 2.23", *JAEA-Data/Code* 2010-022.

[5]   K. Shibata *et al.* (2002), "Japanese Evaluated Nuclear Data Library Version 3 Revision-3: JENDL-3.3," J. Nucl. Sci. Technol. 39, 1125.

[6]   H.G. Hughes *et al.* (1996), "Information on the Photon Library MCPLIB02," *Los Alamos National Laboratory Internal Memorandum, X-6: HGH-93-77* and *LA-UR-98-539*.

[7]   A. Ferrari *et al.* (1996), "Fluence to Effective Dose and Effective Dose Equivalent Conversion Coefficients for Photons from 50 keV to 10 GeV", *Radiat. Prot. Dosim.* 67, 245.

Radiation transport and protection calculation for the in-flight fragment separator facility of Rare Isotope Science Project in the Republic of Korea

Mi-Jung Kim[1], J.W. Kim[1], M.J. Kim[1], D.G. Kim[1], J.S. Song[1,2], C.C. Yun[1], S.K. Kim[1]
[1]Institute for Basic Science, Daejeon, Republic of Korea
[2]Department of Physics and Astronomy, Seoul National University, Seoul, Republic of Korea

Abstract

A rare-isotope accelerator facility is planned to be constructed in the Republic of Korea, named as Rare Isotope Science Project (RISP). The facility contains three accelerators: a heavy-ion superconducting linear accelerator as the driver for the in-flight fragment separator (IF) system, a proton cyclotron for the isotope separation on-line (ISOL) system and a superconducting linac for secondary beam acceleration. The driver accelerator will provide uranium beam for the IF system up to 200 MeV/u at a maximum beam power of 400 kW, and the cyclotron a 70-MeV proton beam at 70 kW. The IF system consists of pre- and main separators. An isotope beam of interest is separated in the pre-separator, and then purified for identification in the main separator. A main function of pre-separator is to remove the primary and unwanted fragments by stopping them at a beam dump. Due to the high beam power, it is important to evaluate radiation transport and shielding especially in the pre-separator area. Heat deposition and radiation dose rate in the components of pre-separator have been estimated using PHITS.

Introduction

The Institute for Basic Science was established in 2011, and is the host institution of a next generation rare isotope beam facility in the Republic of Korea. The Rare Isotope Science Project (RISP) was created to carry out the technical design and the construction of the accelerator complex in December 2011. The goal of this accelerator complex is to produce a variety of stable and rare isotope beams to be used for research in both basic and applied sciences.

The rare isotope beams can be produced either by target spallation in the isotope separation on-line(isol) system or projectile fragmentation and fission in the in-flight fragmentation (IF) system. Two different methods produce rare isotope beams of different characteristics, and thereby can provide wider varieties of isotope beams than in other facilities operating only one of the two methods. More diverse users from the basic and applied sciences can be accommodated. Especially high-intensity and high-purity RI beams near the drip line can give us tremendous opportunities to explore the entire universe from microscopic to macroscopic world.

Figure 1: Schematic diagram of the accelerator complex of RISP
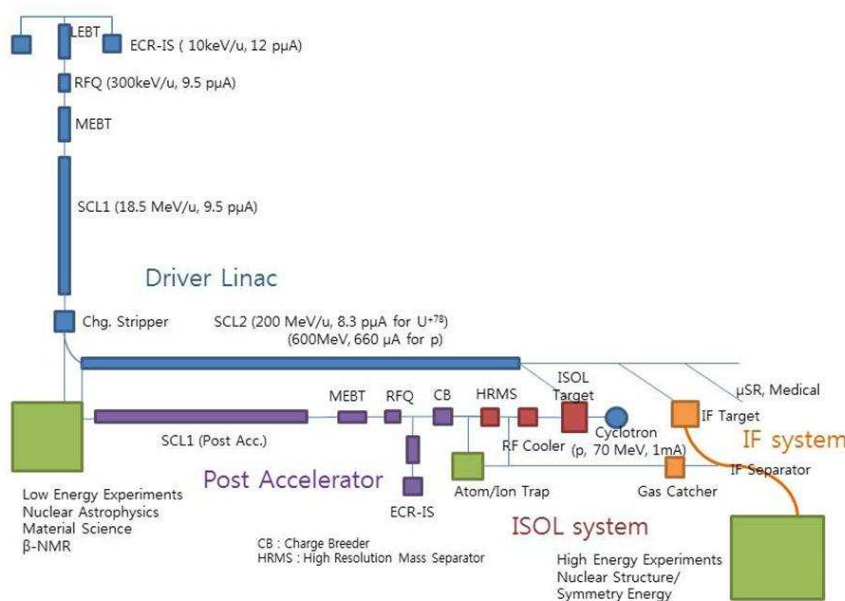
The schematic diagram of the facility is shown in Figure 1. The accelerator complex consists of a heavy ion linear accelerator as the main driver for the IF system, a proton cyclotron as the driver for the ISOL system and a post-accelerator for the ISOL system. The ISOL and the IF systems are to be operated independently. In addition, the RI beams produced in ISOL can be injected into the driver linac for accelerating the RI beams to higher energies, so that the IF system can produce even more exotic rare isotope beams. The advantage of this two-step process needs to be further evaluated. In a future upgrade, the proton beam, which is accelerated up to around 600 MeV by the main linac, can be used for the ISOL system. Table 1 shows the beam specifications of the driver linac. The various kinds of RI beams of proton- and neutron-rich nuclei, which are requested for research, are summarised in Table 2. This list was prepared by the user community of the RISP after the analysis of current research trends and future perspectives of the RI science.

The production and selection of RI beams of interest can induce large amounts of radiation flux and heat in the IF components. The separation of the RI beam of interest from the primary beam non-reacted is an important design issue for the high-power RI beam facility. A major goal in the IF separator design is the delivery of sufficiently pure RI beam to the experimental set-ups. This paper presents some preliminary results of the magnitude of the radiation fields and the estimation of the lifetime of superconducting magnet coils in the high-radiation region of the IF system using PHITS [1].

Table 1: Driver linac beam specification

Ion species	Ion source output		SC linac output			
	Charge	Current(pμA)	Charge	Current(pμA)	Energy(MeV/u)	Power(kW)
proton	1	660	1	660	610	400
^{40}Ar	8	42	18	34	300	400
^{86}Kr	14	22	34-36	18	265	400
^{136}Xe	18	19	47-51	13	235	400
^{238}U	33-34	12	77-81	8	200	400

Table 2: Selected RI beam requirements for RISP research opportunities

RI Beam species	Energy range	Desired intensities [particles/sec]	Research fields
^{80}Ni, ^{76}Fe,^{132}Sn,^{144}Xe	>100 A MeV	> 10^9	nuclear structure
^{80}Ni,^{76}Fe,^{132}Sn,^{144}Xe	5-20 A MeV	>10^8	nuclear structure
^{15}O, ^{14}O	<10 A MeV < 30keV	>10^{10-11} >10^8	nuclear astrophysics material science
^{26m}Al	5-20 A MeV	> 10^{7-8}	nuclear astrophysics
^{45}V	0.613-2.25 A MeV	>$10^7 – 10^9$	nuclear astrophysics
^{39}Si, ^{36}Mg	5-10 A MeV	>10^{7-9}	nuclear Structure
^{68}Ni, ^{106}Sn, ^{132}Sn, ^{149,142}Xe	10-250 A MeV	>10^9	symmetry energy
^{6,8}He, ^{12}Be, $^{24-30}$O	50-100 A MeV	>10^9	nuclear study with polarised target
^{17}N,^{17}B,^{12}B,$^{14-15}$B,$^{31-32}$Al,^{34}K	50-100 A MeV	>10^9	nuclear study with polarised RI beam
^{8}Li, ^{11}Be, ^{17}Ne	< 30 keV	>10^8	material science
$^{133-140}$Sn	<60 keV	>1	atomic physics
^{8}B,^{8}Li,^{9}C,^{11}C,^{15}O	≥ 400 A MeV	>$10^7 ~ 10^9$	medical and bio science

In-flight fragment separator system

Figure 2 shows a schematic view of the IF facility layout. The IF system consists of pre-and main-separators. The pre-separator includes the target system for the production of rare isotope beams by mechanisms such as projectile fragmentation and in-flight fission. The isotope beam of interest passes through the pre-separator, and the remaining beam, which is mostly the primary beam, needs to be dumped in the localised areas. This front-end of pre-separator including a target and beam dump should be well-shielded from the other regions. Most of the parts will be made in detachable modular form so that any malfunctioning can be repaired by taking out the affected module to the designated repair areas. This remote handling will require careful mechanical design on the joining parts as they are related to vacuum sealing and alignment. Modern robot system for remote handling often heavily uses semiconductor devices, which are weak to radiation damage. Major parts of the handling system should use metallic components to avoid fast radiation damage. An efficient approach to the system development would be to adopt established technology at the high-current beam facility in operation such as the MEGAPI collaboration at the PSI and the SNS in the US.

The superconducting magnets in the pre-separator region are exposed to large amount radiation heating and high-level doses. In particular, the first quadrupole magnet set downstream of the target receives the highest level of radiation dose, and still needs to have a large aperture for the large acceptance of isotope beams. High-Tc superconducting magnets have been developed for the FRIB project by the BNL group [2], and we plan to develop a similar magnet also in collaboration with the BNL group.

Figure 2: Layout of the IF separator and the following beam line
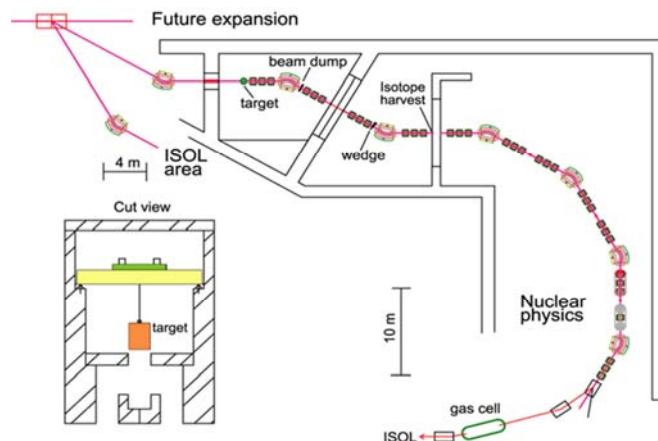
Target and beam dump

The target for in-flight fragmentation needs to endure about 30% of the primary beam power in an average case. The resultant power density inside the target is very high, and thus cooling is critical. The high-power target for in-flight fragmentation has been numerically studied using PHITS, which is a heavy-ion radiation transport code to evaluate the generation of heat and radiation. The highest power density is around 65 MW/cm^3 for a U beam of 200 MeV/u at 400 kW, which is calculated by PHITS, and can be reduced to tens of kW/cm^3 by using a rotating target. The maximum allowable temperature for graphite target is around 1 900^{0}C, but the temperature inside the target goes higher for a single-layer target with a thickness of over 1 mm for the U beam. A multi-slice target with a thickness in the order of 0.1 mm can reduce the temperature by enhancing radiation cooling, but then a structural problem has been observed at high rotating speed [3].

The beam dump is a movable device to select the momentum dispersion of the isotope beam and to completely remove the primary beam. In normal operation, it absorbs about two thirds of the full power of 400 kW, and the short range of the heavy ion beam inside the material results in extremely high power density. The envisioned concept of the beam dump is based on stopping the beam in a water-filled rotating drum, which is similar to the one that has been developed for the FRIB. There are two critical issues in the beam dump. One is material damage to the water container that can severely limit its lifetime, and component failure due to the high-radiation fields. The other is water activation which produces radiologically significant nuclides in the water, for instance ,^{3}H, ^{7}Be, and ^{14}C.

Radiation transport and heating calculation

Set-up geometry of pre-separator for PHITS calculation

Figure 3 shows a 3D model and material compositions of the pre-separator used in PHITS. We use large-aperture superconducting quadrupole triplet magnets and a dipole magnet in the front-end of the pre-separator. High-Tc superconducting coils will be used for those magnets instead of superconducting coils operating at 4 K, considering the efficiency of radiation heat removal. Magnetic fields of those magnets are also included in PHITS calculations, for which the magnetic fields were obtained using beam optics codes such as TRANSPORT. A typical primary beam is U beam of 200 MeV/u at 400kW, which bombards the graphite production target. The optimal target thickness of ~2 mm was determined using LISE++ to have maximum yields of ^{132}Sn isotope beam, which is one of the most important radioactive nuclei.

Figure 3: A 3D pre-separator geometry used in PHITS calculation and material compositions used
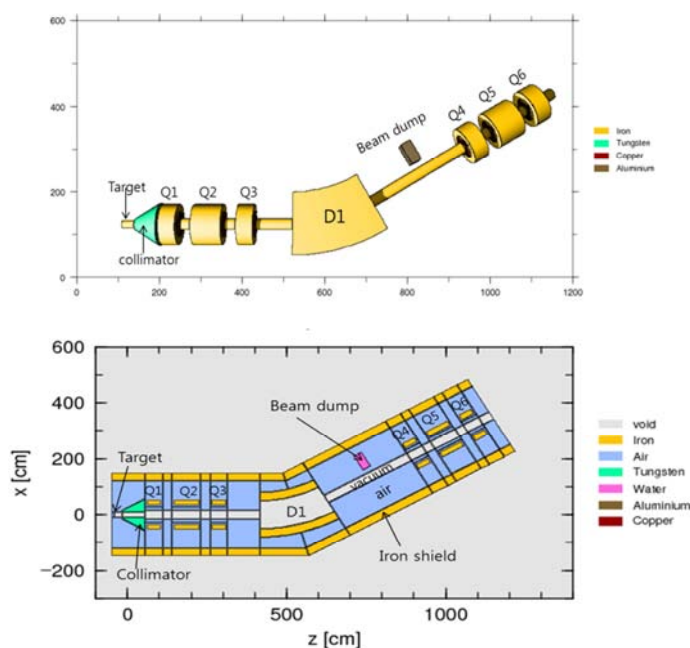
Higher: 3D pre-separator geometry used. Lower: material compositions used.

Calculation of radiation heating and evaluation of lifetime of superconducting coil

Figure 4 shows the distribution of radiation heating in the front-end of the pre-separator area by PHITS calculation in units of MeV/cm3. The projectile fragments produced by a thin target and non-reacted uranium beams are separated by the downstream magnet system. The unwanted beams hit the collimator and the beam dump, which produces intense radiation and deposits the heat on the magnetic elements. By using a cooling system and shielding blocks, heat deposition especially in the superconducting coils should be reduced. To estimate the lifetime of superconducting coils, the heat deposition only to the coil was considered. Figure 5 shows a sectional view of heat distribution in the coil region of the first quadrupole magnet. The average power deposition in the quadrupole magnets is shown as dose rates along the magnet length in MGy/yr in Figure 6. Table 3 shows the maximum energy deposition for the Q1~Q6 magnets. To estimate the approximate lifetime of high-Tc conductor coils, the radiation lifetime of Nb$_3$Sn (500MGy) and the density of copper (8.96 g/cm³) were used instead because data on the high-Tc superconducting magnet

materials are not yet available. Assuming yearly beam operation of 5 600 hours, lifetimes of the coils are estimated as listed in Table 3.

Figure 4: Heating in the pre-separator area when a 400kW, 200MeV/u ^{238}U beam bombards graphite target
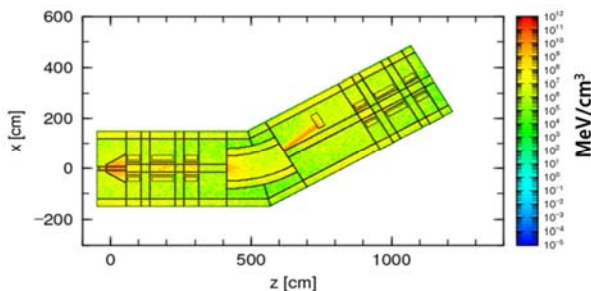

Figure 5: Heat distribution around the coil region of the first quadrupole magnet downstream of the target when ^{238}U beam is used
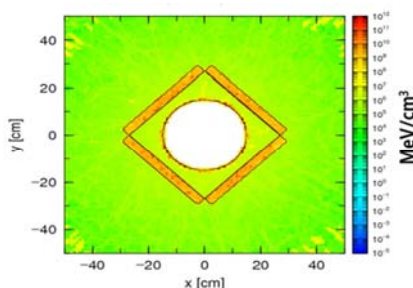
Figure 6: Dose deposition in the quadrupole magnets of the frond-end of pre-separator as a function of the length along the beam
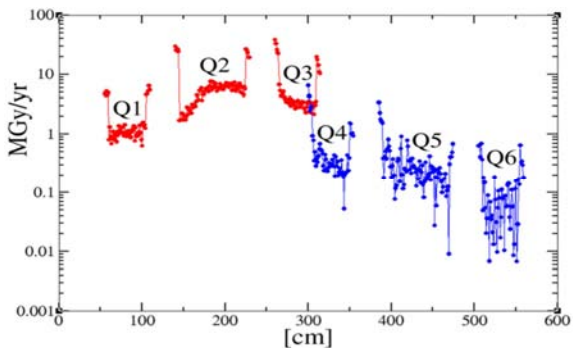
Table 3: Dose rates and lifetime estimation of the six coils when ^{238}U beam is used

	Dose Rates (MGy/yr)	Lifetime (year)
Q1	6.533	77
Q2	29.752	17
Q3	38.348	13
Q4	6.554	76
Q5	3.434	146
Q6	0.640	781

Prompt dose rates

The particle fluxes and the radiation dose rates mainly by neutrons and photons in the pre-separator area were calculated. Figure 7 shows the distribution of prompt dose rates, which can be used to estimate optimum shielding thickness necessary to reduce the radiation dose rates outside the shielding below regulatory limits. The strong radiation fluxes are shown around the target and the beam dump. They can be more effectively reduced by piling up the concrete blocks close to the target and the beam dump. A shielding structure with a remote handling system will also be constructed as shown in Figure 7. Detailed calculations are in progress.

Figure 7: Prompt dose rates for the ^{238}U beam (left); a 3D conceptual view of shielding structure with remote handling system (right)
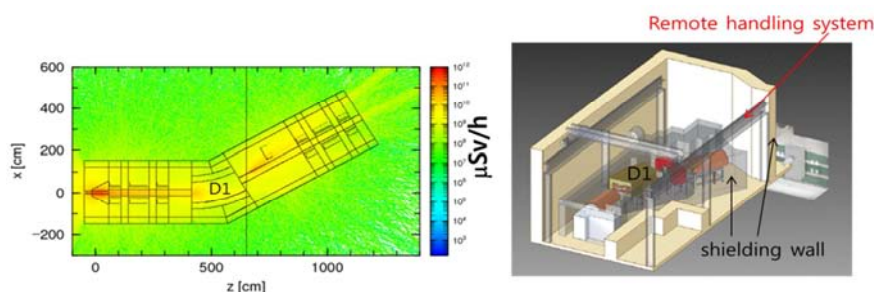
Conclusion

A heavy-ion accelerator facility is planned to be constructed in the Republic of Korea. The next-generation RI beam facility using high-beam power requires elaborated evaluation on the radiation transport and shielding in the area of RI beam production and separation. Some preliminary results were obtained at the front-end of the pre-separator region, where the radiation level is the highest. Heat deposition and radiation dose rate on the components of the pre-separator were calculated using PHITS. The lifetime of the coils in superconducting magnets was then estimated based on assumed beam operation scenario of the facility. More detailed calculation is in progress, and the validation on the Monte Carlo computation is planned by beam experiments in the existing heavy-ion beam facility.

Acknowledgements

References

[1]   K. Niita *et al.* (2011), "Applicability of PHITS Code to Heavy Ion Accelerator Facilities", *Journal of the Korean Physical Society*, Vol. 59, No. 2, pp 1640~1643.

[2]   R. Gupta *et al.* (2011), IEEE *Trans. Appl. Supercond.,* vol. 21, no. 3, pp. 1888-1891.

[3]   W. Mittig (2011), 4th High Power Targetry Workshop, Malmö, Sweden.

Status report of the RIKEN radioisotope beam factory (RIBF)

**Yoshitomo Uwamino, Hisao Sakamoto, Hiroki Mukai, Atsuko Akashio,
Hiroyuki Fukuda and Rieko Higurashi-Hirunuma**
RIKEN Nishina Center for Accelerator-Based Science, Japan

Abstract

The operation of RIKEN Radioisotope Beam Factory (RIBF) was started at the end of 2006 with a heavy-ion injector linac (RILAC), an injector cyclotron (AVF), four ring cyclotrons (RRC, fRC, IRC and SRC), and projectile-fragment separators (RIPS and BigRIPS). After that, an additional new injector heavy-ion linac (RILAC-II) with a 28 GHz superconducting ECR ion source was completed in March, 2011. SRC is the final stage superconducting cyclotron and its maximum energy is 400 MeV/nucleon for lighter ions of hydrogen to Ar and 350 MeV/nucleon for heavier ions up to uranium. The achieved beam intensity is 1 $p\mu A$ for ^{4}He and a few pnA for ^{238}U. A polarised deuteron beam is also available. New developed electron-nucleus scattering equipment is under construction. It is called SCRIT (self-confining radioisotope ion target), and consists of a 150-MeV microtron and a 700-MeV electron synchrotron storage-ring. Uranium photo-fission target system and an ISOL will be constructed for the unstable-nuclide supply. It will realise the electron scattering experiment with unstable nuclides for the first time.

Introduction

The construction of a facility expanding project, RIKEN Radioisotope Beam Factory (RIBF) [1], was completed and the first beam was accelerated at the end of 2006. The first experimental result was obtained [2] at the beginning of the following year. After the construction of the accelerators efforts were made to increase the variety of available beams and their intensities, and to construct detectors.

For the experiment of scattering between electron and unstable nuclide, a novel ion-trap target equipment was discovered with an electron storage ring. It is called SCRIT (self-confining radioisotope ion target), and its construction has started.

Heavy-ion accelerators

Figure 1 illustrates a bird's eye view of the RIBF accelerator complex.

The oldest accelerator of RIBF is the heavy-ion variable frequency linear accelerator, RILAC, which was built in 1980. It has been used as an injector for the RIKEN ring cyclotron, RRC, and has been used alone for the super-heavy element synthesis, such as an element of atomic number 113, and other experiments.

The AVF cyclotron is used for the injector of RRC for light heavy-ions up to nickel. This is also used alone for the production of commercially-distributing radioisotopes.

RRC has been the main accelerator for a long time. It achieved nuclear physics experiment of very short-lived lighter nuclides with the RIKEN projectile fragment separator, RIPS. Many biological and engineering experiments have also been carried out.

In the RIBF Project, three-ring cyclotrons of fRC (fixed-frequency ring cyclotron), IRC (intermediate-stage ring cyclotron) and SRC (superconducting ring cyclotron) [3] were constructed.

SRC is the final stage accelerator, which is the world heaviest (more than 8 000 tonnes) and strongest magnetic-rigidity machine. The magnetic field is 3.8 tesla, and the stored energy is 240 MJ. While the main and the trim coils are superconducting, the iron pole is of room temperature. The valley parts are also covered with 80-cm-thick iron plates which work as an absorber of stray magnetic flux, a magnetic shield and also as a radiation shield.

Figure 1: A bird's-eye view of the RIBF accelerator complex
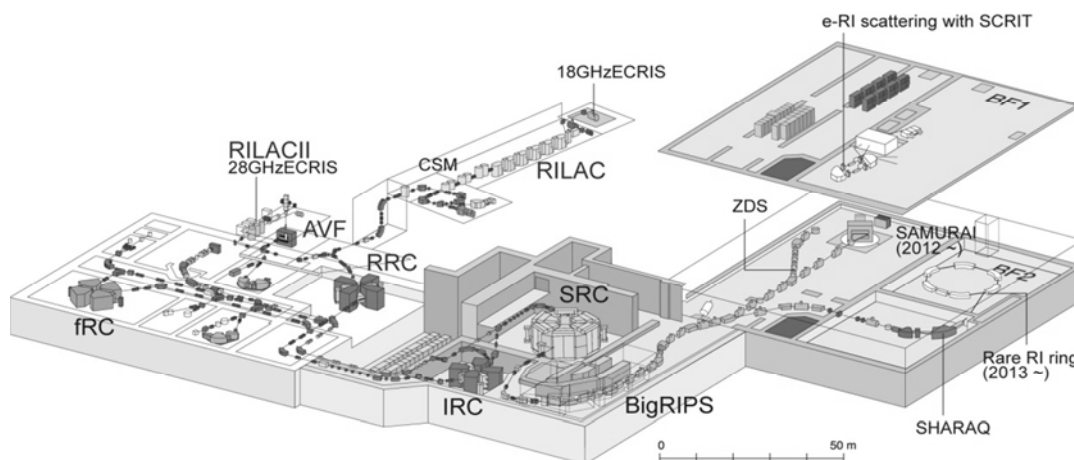
The accelerated beam is conducted into BigRIPS (big RIKEN projectile fragment separator) [4], where any nuclide lighter than uranium can be produced. The secondary unstable beam is delivered to the experimental area.

After the completion of the big project, a 2nd RIKEN linear accelerator, RILAC-II [5], with a 28 GHz superconducting ECR ion source was installed in 2011. RILAC-II supplies high-intensity heavy ion beams to RRC.

To meet the increase of the beam intensity, further improvements have been carried out for safety reasons.

Many superconducting quadrupole magnets are used in the BigRIPS tunnel, and a quench safety system has been installed. When it detects a quench signal or oxygen deficiency, ventilators are actuated and a warning siren goes off.

Since residual radiation level has become high around BigRIPS, pillow-seals that were originally developed at Paul Scherrer Institute in Villigen, Switzerland, have been installed. When the target or the magnets become damaged, the disabled equipment can be taken away without screwing work at vacuum connections.

The acceleration scheme is shown in Figure 2. When uranium or xenon ions are accelerated, RILAC-II, RRC, fRC, IRC and SRC are used. Light heavy-ions, such as deuteron, helium or nitrogen, are injected into RRC by AVF, and the beams are directly injected to SRC bypassing fRC and IRC.

It is possible to perform 3 experiments simultaneously, for example, a super-heavy element experiment with RILAC, radioisotope production with AVF and a high-energy unstable nuclide experiment with RILAC-II to SRC.

The beams listed in Table 1 have been already provided. The intensity of helium, for example, is limited by the license, and the beam loss at the SRC deflector, since a high beam-loss makes maintenance work difficult. The intensity of uranium is limited by the ion source and the damage on the charge stripper foils.

Figure 2: RIBF heavy-ion acceleration scheme
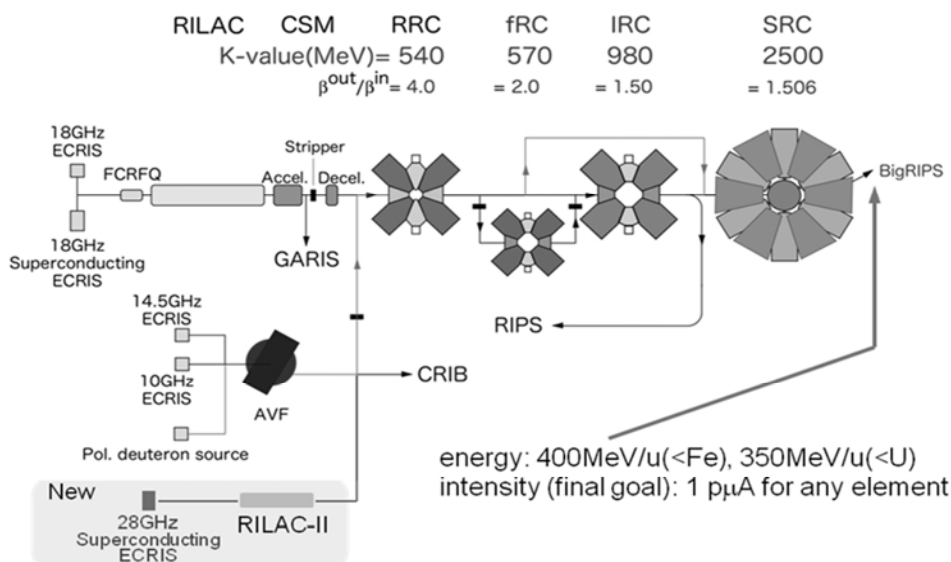
The condition of a stripper foil, which is placed immediately after RRC, is the severest, and a thin rotating carbon foil is used. Damage by the uranium beam is enormous: it may make a big hole after a several-hour operation. The carbon foil stripper was replaced by a helium gas stripping system at the beginning of 2012. The charge state was lowered by this replacement, and a minor alteration was done at fRC.

Table 1: Available beam intensities at present

Ion	Energy (MeV/nucleon)	Intensity (particle-nA)
polarised d	250	120
He-4	320	1000
N-14	250	80
Ca-48	345	200
Kr-86	345	30
Xe-124	345	10
U-238	345	5

Detectors for heavy-ion experiment

Three major detectors have been constructed. In 2007 the zero-degree spectrometer (ZDS) was completed, and the SHARAQ spectrometer (spectroscopy with high-resolution analyser and radio-active quantum beams) was completed in 2009. The construction of SAMURAI spectrometer (superconducting analyser for multi-particles with radio-isotope beams) was completed in March, 2012.

Now, three types of spectrometers are available; zero-degree type (ZDS), small-angle high-resolution type (SHARAQ), and multi-particle (heavy ions, protons and neutrons) type (SAMURAI).

The EURICA (EUroball RIken Cluster Array) detector, which is a high-efficiency gamma-ray spectrometer based on the former Euroball germanium cluster detectors, was installed at ZDS, and major beam time is allocated for the experiment with it.

Electron accelerator facility, SCRIT

The SCRIT facility is under construction [6]. It consists of a 150-MeV microtron and a 700-MeV synchrotron storage-ring. It will realise an electron scattering experiment with unstable nuclides for the first time.

The concept of the SCRIT is shown in Figure 3. Ions are trapped by the electric fields made by the 700-MeV circulating electron bunches and the longitudinal electrodes. Electrons scattered by the trapped nuclides are detected.

The radionuclides whose characteristics are measured are supplied by the ISOL (isotope separator on line) connected to the uranium carbide target as shown in Figure 4.

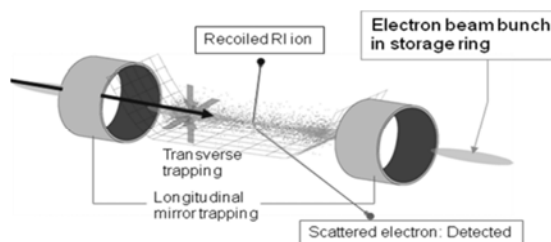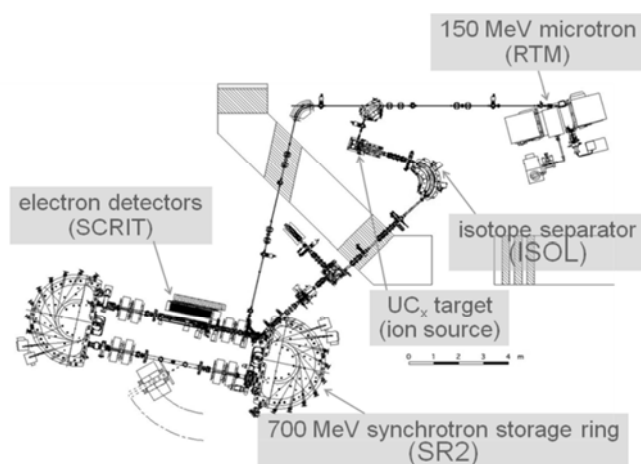### Figure 3: Principle of the ion trapping in an electron storage ring

Figure 4: Layout of the SCRIT facility

The experimental scheme is as follows: Firstly, electrons from the 150-MeV racetrack microtron (RTM) are injected into the synchrotron storage ring (SR2), and accelerated up to 700 MeV. After the storage is finished, the electron beam course is changed to the uranium carbide (UCx) target. A 1-kW electron beam produces intense bremsstrahlung, which causes uranium fission. Fission fragment is extracted from the heated uranium target, separated with the ISOL, and conducted to the SCRIT trapping area.

Summary

RIBF accelerators were almost completed; 28-GHz superconducting ECR ion source and RILAC-II were installed in 2011. Three major detectors were already installed. "Rare-RI ring" for accurate mass spectrometry is under construction, and "SLOWRI" for slow radioisotope beam experiment is still waiting for budget. Improvements on charge stripping are under progress. An electron and unstable-nuclide scattering experiment will start with SCRIT within a year.

References

[1]   Y. Yano (2004), "RI Beam Factory Project at RIKEN", *Cyclotrons* '04, Tokyo, 169.

[2]   T. Ohnishi *et al.* (2010), *J. Phys. Soc. Jap.*, 79, 073201.

[3]   H. Okuno *et al.* (2004), "Magnets for the RIKEN Superconducting Ring Cyclotron", *Cyclotrons* '04, Tokyo, 373.

[4]   T. Kubo *et al.* (2003), *Nucl. Instrum. Methods*, B204, 97.

[5]   O. Kamigaito *et al.* (2009), "Intensity-Upgrade Plans of RIKEN RI-Beam Factory", *HIAT* '09, Venice, 21.

[6]   M. Wakasugi *et al.* (2009), *Eur. Phys. J.* A 42, 453.

Monte Carlo simulation of beam mis-steering at electron accelerators

Mario Santana Leitner[1], Taiee Liang[1,2]
[1]SLAC National Accelerator Laboratory
[2]Georgia Institute of Technology, Nuclear and Radiological Engineering Department

Abstract

The nominal trajectory and shape of a charged beam in a particle accelerator is determined by the electromagnetic fields that are typically provided by electro-magnets. Those components may eventually be incorrectly tuned or they may experience hardware failures, ultimately leading to a mis-steered beam that could even depart from the beam-pipe and hit components or shielding walls that may not be designed to take direct beam hits. In order to reduce the potentially hazardous radiation levels that would then be generated and the damage to certain components, collimators should be installed around the beam-pipe at strategic locations so that any extraneous trajectory is intercepted and spoiled before reaching sensitive areas. Depending on the beam power and size, those collimators might need to be accessorised with a pressurised vessel to detect if the beam has punctured through the collimator part and has thereby bypassed the shielding.

We present a powerful application of the intra nuclear Monte Carlo particle transport code FLUKA to draw the envelope of mis-steered beams. Additionally, simulations with the same code were carried out to parameterise the heat profile of typical mis-steered beams, so as to help assess where and when collimators require burn-through monitors.

Introduction

Accelerator enclosures are usually dimensioned for losses occurring along the beam lines, either on insertion devices like stoppers or beam diagnostics, or in beam impedances such as halo-scraping collimators. The radiation shielding design of an accelerator should also include local shielding to cover the low-occurrence, high-risk scenario of beams being lost outside of their regular trajectory, as illustrated in Figure 1. Indeed, the electro-magnets that guide and focus the beam within its nominal parameters may eventually fail steering the beam towards components or shielding walls that may not be designed to take direct beam hits. Such failures may result from inadequate electric powering of magnets due to operational mistakes (e.g. energy mismatch), or hardware failures (short-circuits, radiation-induced electronic bit-flips, etc.), or installation errors (i.e. inversed polarities). Though infrequent, in absence of local shielding the consequences of such accidents could be severe, and therefore, these also entail long shutdowns for extensive investigations and for the implementation of the corresponding corrective measures.

Figure 1: (A) Accelerator enclosure walls are usually dimensioned for normal losses in the beam line and (B) mis-steered beams must be contained with local shielding to prevent high exposure
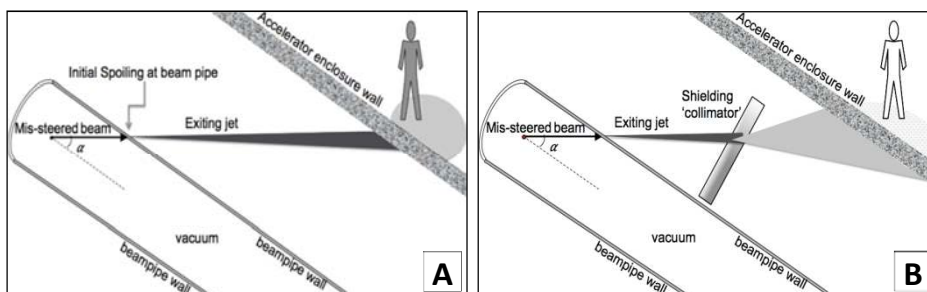
Ray-trace representations containing all possible errant trajectories compatible with plausible mis-steering assumptions should be generated to define the minimum needs of local shielding. Since this process is intrinsically multi-variant, the approximations used in its creation may impact the size and count of the set of necessary shielding units. The following section addresses this topic.

Figure 2: If mis-steered beams exit the beam pipe, the escaping jets may eventually burn-through local shielding (A) and pressurised gas vessels may detect these instances (B)
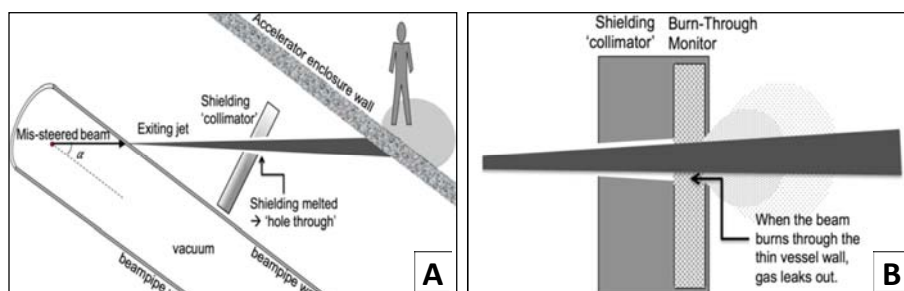
Certain local shielding components are equipped with a gas-pressurised vessel that will be ruptured if the escaping jet carries excessive power density. The pressure drop that would follow would be detected by a gauge that would then trigger a beam-shutoff signal through the personal protection system (PPS). This mechanism alerts if the shielding is drilled through by the escaping jets and thus becoming transparent to

radiation, as sketched in Figure 2. The system entails supplementary costs and operational burden (e.g. periodic gas refilling required to compensate natural gas leaks) and therefore, it should only be put in place if the local shielding may not sustain the maximum credible heat load. The second part of this paper presents some guidelines on this regard.

Ray-tracing techniques–new approach with FLUKA Monte Carlo code

Geometric ray-tracing

Ray-tracing for accelerators is usually done analytically, taking into account consecutive (mis)-kicks from two to three magnets. In many simple cases this geometric technique is very efficient as it makes evident the optimal placement and dimensioning of collimators in terms of the magnet locations and mis-steering rules.

However, this method has some serious limitations. For example, if several magnets within a section of a beam line may fail simultaneously, then the analysis tends to become rather cumbersome, as many logic branches open up, and those need to be redefined as a function of the parameters and positions of the components. Figure 3 shows a screen capture for part of an analytical ray-trace for an FEL machine. In that case there were several consecutive magnets that could eject the beam towards a sensitive zone (experimental area at forward angle). The study was extensive, as it had to ensure the collimators would simultaneously lock multiple solid angles. Moreover, for leakage channels originating in downstream magnets, approximations were necessary to account for the effect of previous magnets, and conservativeness in each of the assumptions had to be proved. In such cases, besides tedious, the method is prone to mistakes, and lengthy reviews may be required each time component locations change, as it often happens during the design phase of most beam-lines. Also, this technique usually considers that trajectories are instantaneously bent at a point (the centre) of the magnet. While the latter assumption is usually sufficiently accurate, in some special cases it may end up underestimating the minimum shielding extents.

Figure 3: Screen capture of an analytical ray-trace study
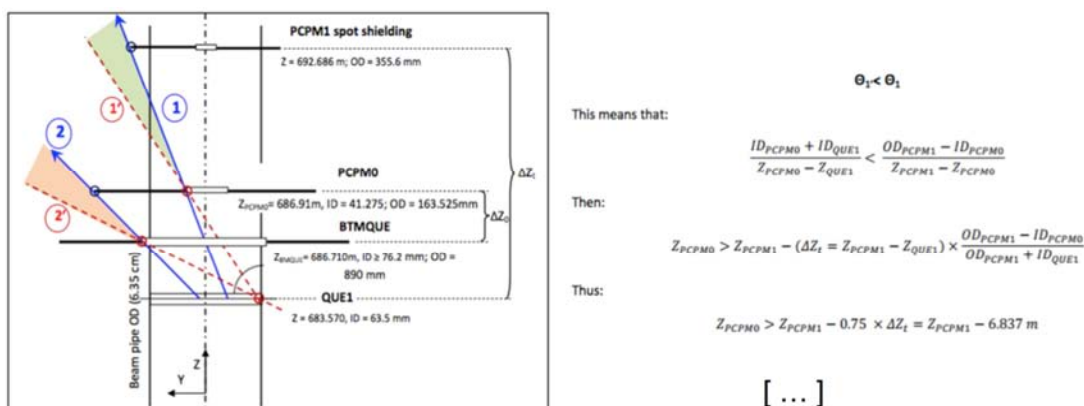
Solid angles of mis-steered rays escaping all collimators are explored as a function of relative locations.

Monte Carlo ray-tracing

State of the art intra-nuclear cascade Monte Carlo (MC) codes like FLUKA [1, 2], MARS [3], or PHITS [4] can track charged particles under magnetic fields. Actually, the beam line optics is often implemented in those codes to determine beam losses and heat loads in components, e.g. amount of beam scraped on a collimator, heat load on it, beam lost on next collimator, etc. On the other hand, the same software is typically used to compute the enclosure thicknesses for those (and other) losses. In such cases it would make sense to utilise the existing geometric and magnetic MC description of the accelerator to draw the ray-trace as well.

The MC ray-tracing concept consists in flooding the system with particles within the credible beam phase-space (energy-position-direction) and having the code track each of those throughout an optics system where magnet strengths may vary anywhere between the limits established in the failure assumptions. Except for local shields and enclosing walls, which are set to a perfectly absorbing material where particles are terminated (e.g. "blackhole" in FLUKA), all components should be assigned vacuum properties so that particles can freely cross them. The resulting envelope of all trajectories is the ray-trace.

This capability has been developed for the FLUKA MC code. Firstly, the geometry of relevant components is defined. This includes regions where magnetic field is present, beam pipe, local shielding and outer walls. Next, the user source routine ("*source.f*") is customised to sample the starting coordinates, the direction and the energy of each particle. Then, the user routine that describes the beam optics ("*magfld.f*") is modified so that the strength of each magnet is randomly adjusted from within its range of variation, as established in the accident scenarios. Since "*magfld.f*" is called at every sub-step along the trajectory of a given particle inside a magnetic region, a condition must be set so that the initialisation of the magnet field strength is performed only upon first entrance to the region. Finally, detectors should be set to score the particle fluence (e.g. "*usrbin*"), and custom scoring should be defined (via "*bxdraw*" routine) to dump the characteristics (energy, starting coordinates, etc.) of particles leaking out of the collimator/local shielding towards the areas of interest.

Figure 4: Left: ray-tracing plot at LCLS-II HXR vertical beam plane for the initial safety collimator design, rays should not reach the end wall behind which there are users, right: hits on the end-wall
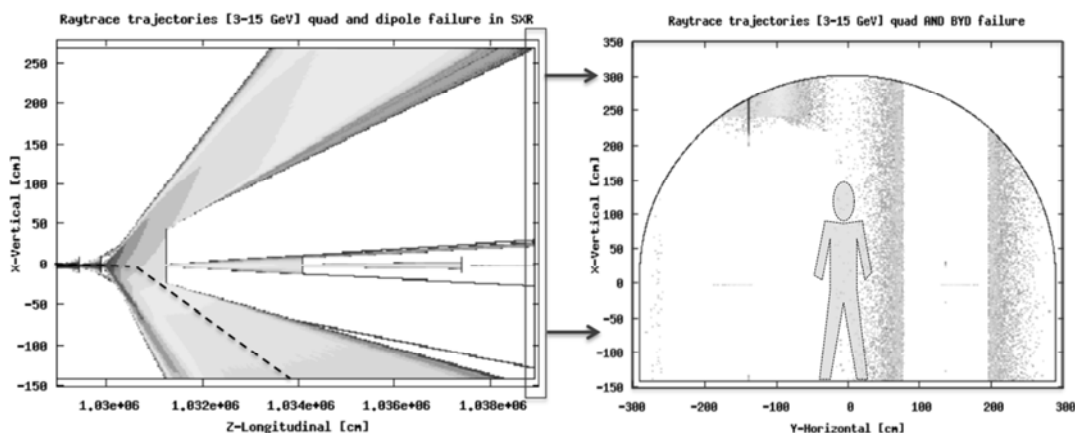
In the MC implementation of the aforementioned analytical ray-trace example, particles were originated uniformly within the beam pipe cross-section, with an angular dispersion consistent with possible kicks from magnets located far upstream. The energy was sampled uniformly between the LCLS limits, 2-15 GeV. The strength of magnets was sampled between minus/plus their nominal values. Fine grid fluence maps on both beam planes and on the end wall (at forward angle) were generated to visualise (with Flair [5]) the envelope of ray-traces and the fluence leakage of particles towards the area of

interest. Figure 4 shows such plots for the collimator setup defined through the analytical ray-trace. It is observed how the MC ray-trace unveils some weak domains through which some particles could potentially escape and hit the end wall.

The MC ray-tracing method offers many assets. Simulations run very fast, typically filling up the beam mis-steering phase-space to a very significant degree within minutes. Hence, alternative beam-line designs can be swiftly explored by simply adjusting the coordinates of magnets and/or shielding, changing energies, etc. and finally re-launching the simulations. The capability to accurately track particles throughout extended beam optics that is offered by the MC method often spares to adopt conservative assumptions which would otherwise be required by the analytical methods, while revealing some weaknesses that may not be apparent with those techniques. Mis-alignments in the positioning of a magnet can easily be considered by adding tolerance-bound random roto-translations in the local coordinate system used in *magfld.f*. Moreover, inclusion of beam spoiling effects at insertion devices is intrinsically possible when using Monte Carlo transport codes like FLUKA. It should be noted that by replacing magnets with mirrors, and 'magfld.f' by "*usrmed.f*" user routine, photon ray-tracing (e.g. FEL) is also possible in FLUKA.

Power density of mis-steered rays

As explained in the introduction, the design of local shielding that intercepts mis-steered rays involves two steps, namely, ray-tracing to determine optimal location, count and size of local shielding and power density estimations of mis-steered rays to decide whether/which shielding requires burn-through monitors. In this section the shape of the mis-steered jets is characterized as a function of beam energy, mis-steering angle and distance from the exit point. The resulting formulae are meant to be used for ulterior calculations that would reveal whether a particular local shielding could potentially be burnt-through for those given conditions. The results of the study are applicable for high-energy (3-15 GeV) electron beams, but the same methodology could in principle be used for other types of machines.
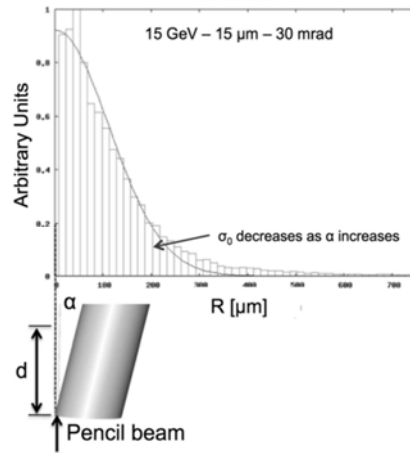
Jet size response function

FLUKA simulations were carried out for pencil beams ($\sigma_B = 0$) of energies between 3 GeV and 15 GeV, mis-steered at various 'large' angles (30-90 mrad) from within a typical beam pipe of thickness 0.0889 cm. Surface 'detectors' were set at several distances, and particles crossing those were scored. For each of those cases, the profile of the particle stream was seemingly fit to a Gaussian jet. An example is sketched in Figure 5.

An equation was found (Equation 1) to express the Gaussian size of the exiting jet for a pencil beam (σ_0) as a function of the beam energy (E_0), the mis-steering angle (α) and the distance from the beam escape point (d):

$$\sigma_0 = a_1 \cdot \left(e^{-a_2 \cdot \alpha} \right) \cdot d + b_1 \cdot e^{-b_2 \cdot \alpha} \tag{1}$$

Where:

$$a_1 = 152.14 \cdot e^{-0.11 \cdot E_0}$$
$$a_2 = 2.4 \cdot 10^{-3} \cdot \ln\left(E_0\right) + 0.0101$$
$$b_1 = 371.98 \cdot e^{-0.17 \cdot E_0}$$
$$b_2 = 0.0396 \cdot e^{-0.135 \cdot E_0}$$

Figure 5: Sketch of simulation set-up and resulting jet size Gaussian fit

Jet size for finite mis-steered beams

The size of the escaping jet will obviously depend on that of the primary mis-steered beam. In the previous section a response function was derived for a pencil beam, i.e. for a beam of $\sigma_B = 0$. By convolving that expression (Equation 1) with the primary beam profile, the jet size (σ_r) can be obtained for any mis-steered beam shape. The process is straightforward for the typical category of Gaussian cylindrical beams. Indeed, the resulting jet size can then simply be described as in Equation 2:

$$\sigma_r^2 = \sigma_B^2 + \sigma_0^2 \qquad (2)$$

This mathematical property is very useful, as it reduces the number of variables in the problem thereby allowing to cleanly express the escaping jet size for any Gaussian beam size with important savings in the number of necessary Monte Carlo simulations, while reducing the complexity of the subsequent fits.

The following sections will expand on this particular, yet key case.

Jet power profile for Gaussian beams

The ultimate goal of this analysis is to obtain parametric formulae to predict the heat load of mis-steered jets in local shielding so that those can be designed accordingly. For that purpose, it is necessary to determine the total energy carried by the exiting jet within a given radius. Since particles in the primary beam suffer inelastic interactions in the beam pipe, the exiting jet will have some energy spread, which needs to be accounted for in the beam shape parameterization.

The earlier fits did not take into consideration the kinetic energy of each event. Now, to obtain the jet power profile (σ_{rE}), that information is used by weighting each particle with its energy. When comparing these with the jet particle profiles, it was found out that the two relate through an angular dependent factor, as shown in Equation 3:

$$\sigma_{rE} = \sigma_r \cdot \{0.1643 \cdot \ln(\alpha) + 0.2137\} \qquad (3)$$

Normalisation constant of the energy-weighted Gaussian jet

In order to compute how much power is carried by the mis-steered jet within some given radius, not only is it necessary to know how focused the jet is (σ_{rE}), but also what fraction of the original mis-steered beam does the exiting jet carry in total, i.e. what is the normalisation constant for the energy-weighted Gaussian, C_{rE}

Further mathematical fits to the data stored in the simulations casts the following result (Equation 4):

$$C_{rE} = \frac{f_E(\alpha, d, E_0)}{0.6827 \cdot \alpha_{rE} \cdot \sqrt{2\pi}} \tag{4}$$

With:

$$f_E(\alpha, d, E_0) = \left[f_1 \cdot e^{-f_2 \cdot d} \right] \cdot \left[\left(f_3 \cdot e^{f_4 \cdot \alpha} \right) \cdot E_0 + f_5 \cdot \ln(\alpha) - f_6 \right] \tag{5}$$

Where the fitting coefficients are:

$f_1 = 1.0588$ $\qquad f_2 = 0.0110$

$f_3 = 0.0005$ $\qquad f_4 = 0.0280$

$f_5 = 0.1490$ $\qquad f_6 = 0.4605$

Finally, the power distribution, $P(r)$, of the mis-steered jet is (Equation 6):

$$P(r) = C_{rE} \cdot e^{-\left(\frac{r^2}{2 \cdot \sigma_{rE}^2} \right)} \tag{6}$$

Where σ_{rE} and C_{rE} are respectively defined in equations, and appear tabulated in Table 1 for some typical values of α and d at $E_0 = 15$ GeV.

Table 1: Example of values σ_{rE} and C for beams of $E_0 = 15$ GeV and $\sigma_B = 30$ μm mis-steered by different angles and measured at distances ranging from 5 to 50 cm

Angle	30 mrad		60 mrad		90 mrad	
d [cm]	σ_{rE} [μm]	C_{rE} * 1E4	σ_{rE} [μm]	C_{rE} * 1E4	σ_{rE} [μm]	C_{rE} * 1E4
5	90.8	4.11	71.8	15.5	90.8	31.5
10	158.1	2.23	117.5	8.95	158.1	19.8
20	294.5	1.07	211.8	4.45	294.5	10.4
30	431.4	0.66	307.0	2.75	431.4	6.52
40	568.4	0.45	402.4	1.88	568.4	4.49
50	705.4	0.32	497.8	1.36	705.4	3.27

Conclusions and future outlook

A beam mis-steering ray-tracing simulation method based on FLUKA code customisation has been presented. The method accurately accounts for magnet failure assumptions as well as other effects such as magnet mis-alignment, or beam interaction with insertion devices. This technique has successfully been used in the design of the safety collimation system of the LCLS-II dump line. Software is being developed to assist in the conversion from MAD [7] beam optics files to FLUKA, so that ray-tracing studies can be expedited.

Spoiling of mis-steered beams at the vacuum pipe has been parameterised as a function of energy, angle, distance to exit point and original beam size. This result will be useful to determine whether local shielding needs to be equipped with burn-through monitors.

Acknowledgements

References

[1]   G. Battistoni, S. Muraro, P.R. Sala, F. Cerutti, A. Ferrari, S. Roesler, A. Fassò and J. Ranft, "The FLUKA code: Description and benchmarking" (2007), *Proc. of the Had. Shower Sim. Workshop* 2006, Fermilab 6-8 Sep. 2006, M. Albrow, R. Raja eds., AIP Conference Proceeding 896, 31-49.

[2]   A. Ferrari, P.R. Sala, A. Fassò, J. Ranft (2005), "FLUKA: a multi-particle transport code", CERN-2005-10, INFN/TC_05/11, SLAC-R-773.

[3]   N. V. Mokhov (1995), "The MARS Code System User Guide, Fermilab-FN-628".

[4]   K. Niita, N. Matsuda, Y. Iwamoto, H. Iwase, T. Sato, H. Nakashima, Y. Sakamoto, L. Sihver, (2010),"PHITS: Particle and Heavy Ion Transport code System, Version 2.23", JAEA-Data/Code 2010-022.

[5]   V. Vlachoudis (2009), "FLAIR: A Powerful But User Friendly Graphical Interface", *Proc. Int. Conf. on Mathematics, Computational Methods & Reactor Physics* (M&C 2009), Saratoga Springs, NY.

[6]   "Linac Coherent Light Source", https://portal.slac.stanford.edu/sites/lcls_public/lcls_ii.

[7]   H. Grote, F. Ch. Iselin, "The MAD Program, User's Reference Manual", CERN/SL/90-13(AP).

Monte Carlo studies for radiation protection of LCLS-II XTOD

**Shanjie Xiao, Mario Santana Leitner, Ludovic Nicolas,
Stan X. Mao and Sayed H. Rokni**
SLAC National Accelerator Laboratory, Menlo Park, California, US

Abstract

The design of LCLS-II X-ray Transport and Diagnostic (XTOD) system does not have the shielding wall separating electron dump line from Front End Enclosure (FEE), therefore any forward radiation may directly challenge the end wall. A series of radiation protection features are designed to protect users behind the end wall from the mixed radiation environment including FEL, spontaneous radiation, bremsstrahlung and possible electron beam in accident. Detailed Monte Carlo studies are implemented for various beamline configurations, considering both normal operation and accidental electron beam loss, and the crucial requirement on the end wall is benchmarked by using both FLUKA and MARS. The leakage of Bremsstrahlung and spontaneous radiation along photon beam pipes into the experimental hall are also studied. It is found that a local safety collimator after the first mirror can help reduce the thickness and cost of the end wall, and a proper collimator system can sufficiently limit radiation leakage through photon beam pipes.

Introduction

The X-ray Transport and Diagnostic (XTOD) systems of Linac Coherent Light Source-II (LCLS-II) at SLAC start just downstream of where electron beams are bent toward the main dump and end just downstream of the main shielding wall separating the LCLS-II tunnel and the new experimental hall. In LCLS-II the x-ray beams are produced from two parallel undulators, which are designed for one to produce hard x-rays (HXR) and the other soft x-rays (SXR). XTOD systems include a set of fixed and insertable mirrors, collimators, diagnostics, and other x-ray instruments needed to characterize x-ray beams and transport them to the experimental hall or to a photon beam stopper. The main shielding wall is designed to protect personnel in the new experimental hall from radiation generated in LCLS-II tunnel, and the mirror and collimator system can filter out undesirable radiation to the level allowing personnel access around beam pipes in the experimental hall. This paper describes FLUKA [1, 2] simulations used to design a proper radiation protection system. Since XTOD systems are still in active evolution, this paper uses the SXR beamline only and focuses on principles, not on final design.

Radiation sources and XTOD layout

Electrons generate bremsstrahlung radiation through collisions with residual gas molecules, certain portion of electron beams is lost on the bending dipoles sending electrons to the main dump, and from time to time, beam intercepts objects such as wire scanners or screens that are inserted into the beam. Analysis shows that 200 mW bremsstrahlung in normal operations is a conservative estimation for XTOD radiation protection design [3], and the corresponding shielding criterion is 0.5 µSv/h behind the main shielding wall.

In accident scenarios, electrons may also be sent to the XTOD system (if permanent magnets are not employed on the electron dump line), and the dose rate behind the main shielding wall should be less than 250 mSv/h under the maximum credible beam (MCB) of 10 kW 15 GeV electrons [3].

On the other hand, bremsstrahlung, spontaneous x-rays and the desired free-electron laser (FEL) x-rays will interact with XTOD mirror sets, and certain amount of radiation will enter the experimental hall from beam pipes. This paper focuses on the leakage of bremsstrahlung since its high energy makes it the main contributor of radiation dose in the experimental hall. The XTOD mirror and collimator system should limit the radiation leakage so as to reduce the dose rate at 30 cm away from beam pipes in the experimental hall to less than 0.5 µSv/h.

The fundamental layout of LCLS-II XTOD systems with both HXR and SXR beamlines are shown in Figure 1. Each beamline has three mirrors, where the second mirror is insertable to select the pathway of x-ray beams. When the second mirror is inserted, x-rays are sent to the branch line parallel to LCLS-II tunnel. Each beamline has also an iron safety collimator, which helps reduce the radiation dose behind the main shielding wall of 3-meter concrete (EH2 wall). A pair of tungsten collimators are applied on each branch line between the last mirror and the main shielding wall. The bremsstrahlung radiation source in the following FLUKA simulations is generated as 15 GeV electrons hitting 0.1 mm titanium foil. All charged particles after the foil are bent out of beam line and dumped, and the simulation results are normalised according to the defined bremsstrahlung power.

Main shielding wall and safety collimator

To help reduce the thickness of EH2 wall as well as its cost, a safety collimator is deployed to scatter and attenuate either bremsstrahlung or electrons. The safety collimator is behind the first mirror, and the farther it is from EH2 wall the more effective it is. The initial SXR configuration set a 30 cm thick iron safety collimator at 15 m upstream of EH2 wall. Figure 2 shows, the plan view distribution (left) and curve along the highest area (right) of the total dose from FLUKA simulations with the radiation source of (a) 200 mW bremsstrahlung in normal operations and (b) 10 kW 15 GeV electrons in accident with MCB. Note that, although particles should first interact with the first mirror, in reality the silicon mirror is ignored in this simulation to have a conservative estimation for the safety collimator thickness.

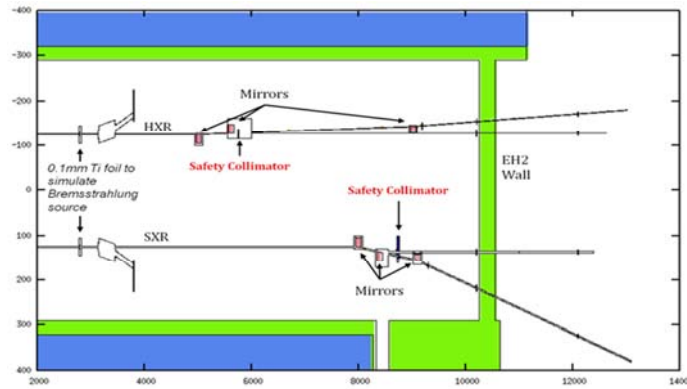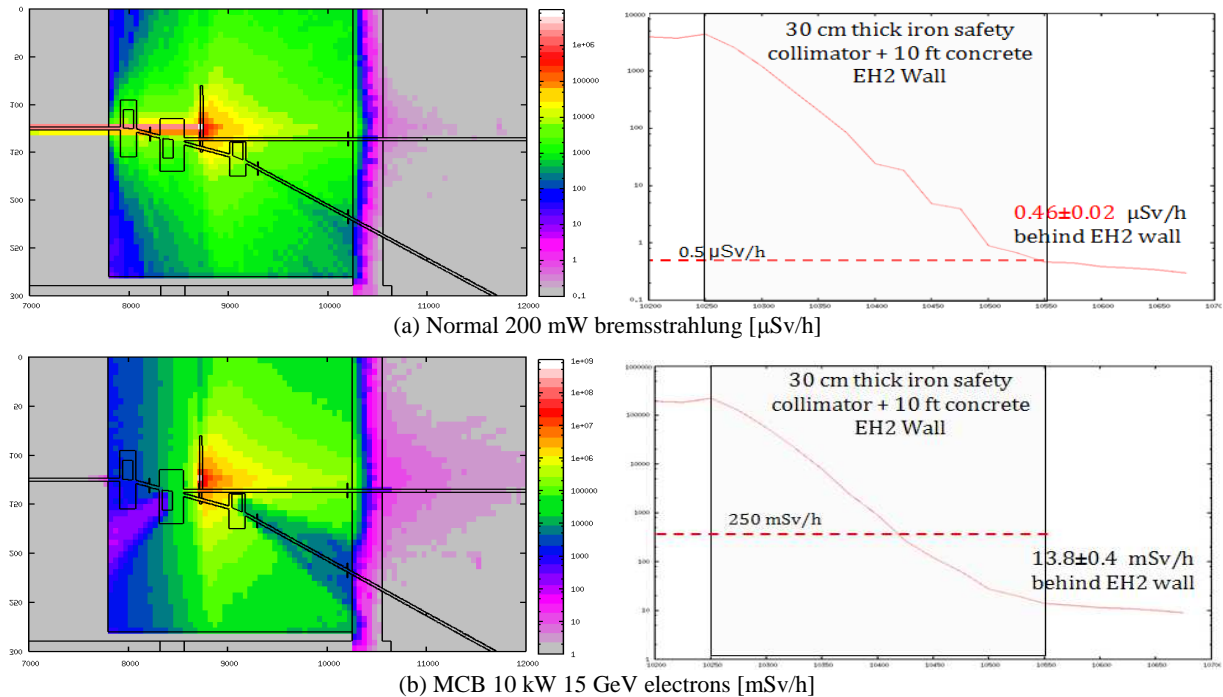**Figure 1: Fundamental layout of LCLS-II XTOD systems**

Figure 2: Total dose distribution of SXR with 30 cm thick safety collimator from FLUKA simulations

(a) Normal 200 mW bremsstrahlung [μSv/h]

(b) MCB 10 kW 15 GeV electrons [mSv/h]

Since the main shielding wall is critical to protect personnel in the experimental hall, the above configuration is benchmarked independently with MARS15 [4]. Figure 3 shows the total dose in an *R-Z* coordinate system, whose *Z* is the primary beam direction. The leftmost *Z* in Figure 3 is the upstream surface of EH2 wall and the vertical line indicates the downstream surface of EH2 wall. The maximum doses behind EH2 wall are 0.6 µSv/h with 200 mW bremsstrahlung in normal operation and 16 mSv/h with 10 kW MCB. The results from FLUKA and MARS simulations match in both normal and accident scenarios, and suggest a slight thicker safety collimator as the dose in normal operations is close to the shielding criterion of 0.5 µSv/h.

Figure 3: Total dose distribution of SXR with 30 cm thick safety collimator from MARS15 simulations

(a) Normal 200 mW bremsstrahlung [µSv/h]   (b) MCB 10 kW 15 GeV electrons [µSv/h]
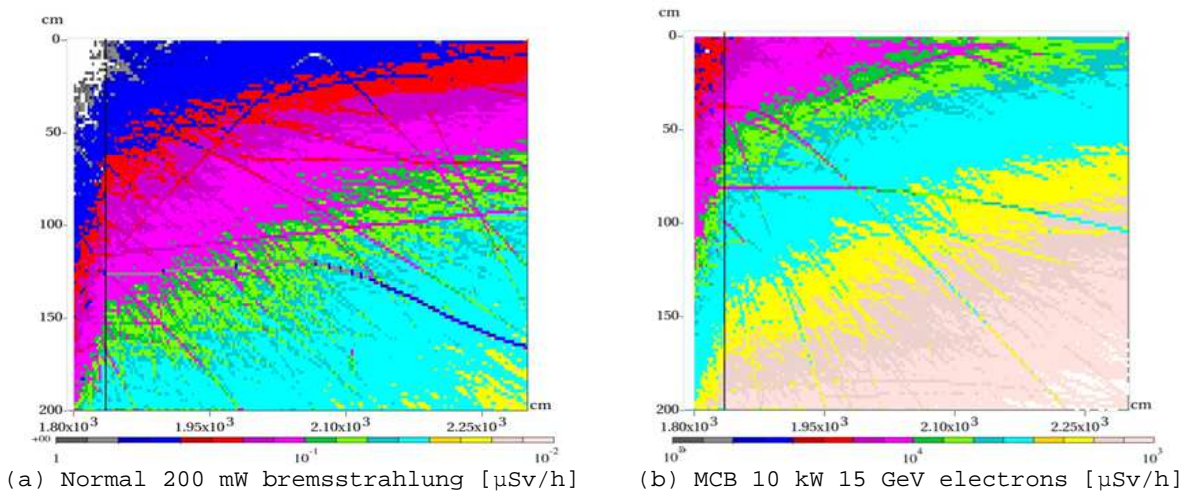
Thus, the latter SXR configuration as shown in Figure 4 adopts a 40 cm thick safety collimator at 17.8 m upstream of EH2 wall. Figure 5 shows the total dose under 200 mW bremsstrahlung in normal operations. The first mirror is included into this simulation to verify the extension of the safety collimator. The maximum dose behind EH2 wall is 0.21 µSv/h, below the criterion of 0.5 µSv/h, and 60% of dose is from muons and photons and neutrons contribute 20% each. As a comparison, the Monte Carlo simulations suggest a combination of 40 cm iron safety collimator and 3 m concrete wall for LCLS-II, while LCLS-I applies two walls with a total of 2.1 m iron and 1.8 m concrete.

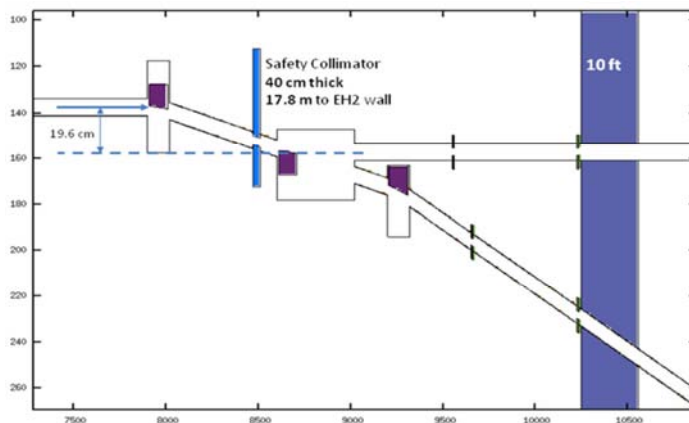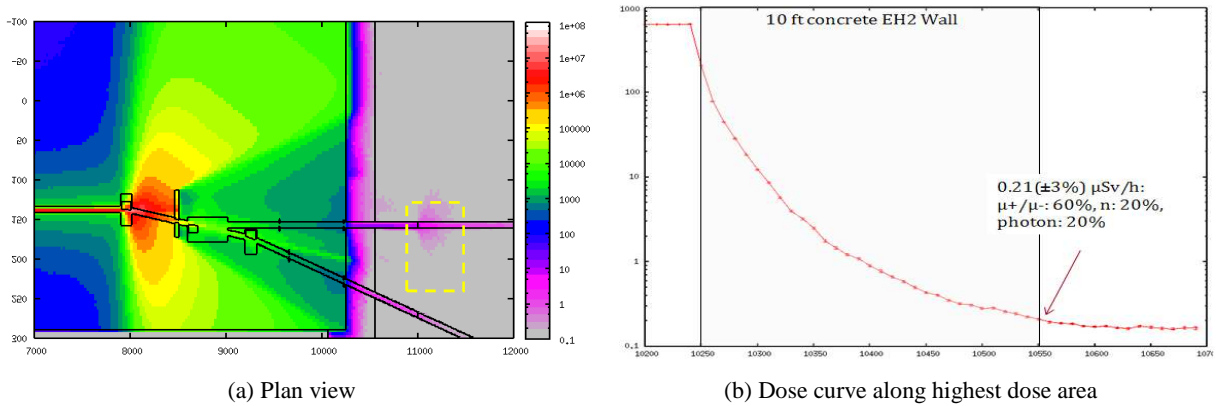**Figure 4: SXR configuration with 40 cm thick safety collimator**

Figure 5: Total dose [μSv/h] with 40 cm thick safety collimator under 200 mW bremsstrahlung

(a) Plan view

(b) Dose curve along highest dose area

Radiation leakage

The radiation leaking through photon beam pipes is another source that may affect the radiation safety in the experimental hall. The clue of the leakage can be found in the dashed area of Figure 5.a, where radiation entering the experimental hall interacts with a target inside beam pipe and generates certain radiation dose around the pipe. This SXR configuration has two collimators between the last mirror and EH2 wall on each branch line, and each mirror reflects x-rays 28 mrad. Each collimator is 8 cm long tungsten with an inner diameter of 3.3 cm and outer diameter of 15 cm. Figure 6 shows the total power of all kinds of particles at different locations along SXR when the second mirror is inserted. With 200 mW bremsstrahlung entering SXR, only 45 nW, mainly secondary electrons, leaks into the experimental hall from the beam pipe close to the primary beam. It is also simulated that when the second mirror is moved out, the leakage along the beam pipe far from the primary beam is less than 45 nW. Therefore the close branch line with the second mirror inserted is the worst scenario in radiation leakage analysis.

Figure 6: Total radiation power along SXR with the second mirror inserted
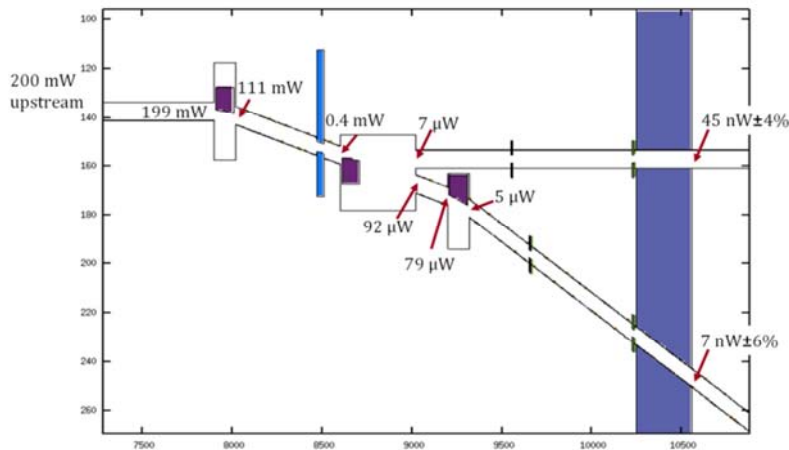
To have a more accurate dose estimation, a two-step simulation was performed: (1) record all particles (location, direction, energy and weight) reaching EH2 from beam pipe into a file; (2) use the recorded particles to simulate radiation dose inside EH2. Figure 7 shows the total dose when the leaked radiation from the SXR close branch line (with the second mirror inserted) interacts with a thin target (1 cm iron) inside the beam pipe.

The total dose is about 1 µSv/h on contact with beam pipe and less than 0.1 µSv/h at 30 cm away, well below the requirement of 0.5 µSv/h.

Figure 7: Total dose [µSv/h] from radiation leakage with the second mirror inserted
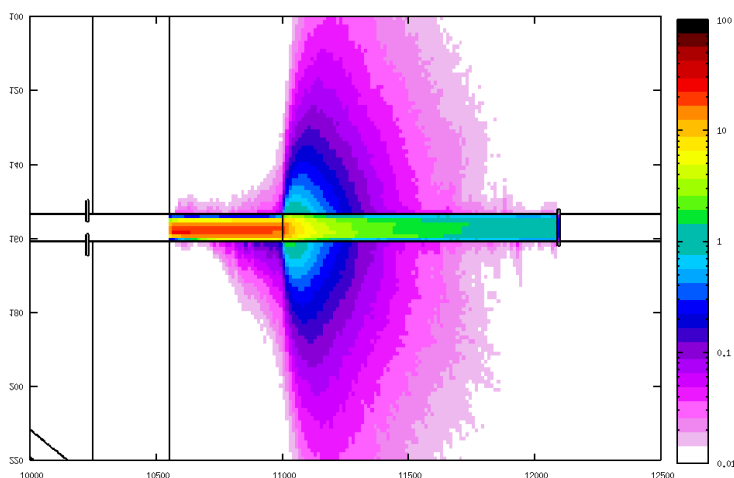
Conclusion

This paper describes various radiation sources which affect radiation safety for personnel in the new experimental hall of LCLS-II. Monte Carlo studies show that the application of local safety dump can help reduce the thickness and complexity of the main shielding wall separating LCLS-II tunnel and experimental hall, and that a proper collimator system can sufficiently limit radiation leakage through photon beam pipes.

Acknowledgements

This work was supported by Department of Energy contract DE-AC02-76-SFO0515.

References

[1]   A. Fassò *et al.* (2005), "*FLUKA: a Multi-particle Transport Code*", CERN-2005-10, INFN/TC_05/11, SLAC-R-77.

[2]   G. Battistoni *et al.* (2007), "*The FLUKA Code: Description and Benchmarking*", AIP Conference Proceeding 896, 31-49.

[3]   S. Rokni *et al.* (2012), "*LCLS-II Preliminary Design Report: Ch.13 Radiological Considerations*", SLAC National Accelerator Laboratory, Menlo Park, CA.

[4]   N.V. Mokov (2003), "Status of MARS Code", Fermilab-Conf-03/053.

Neutron shielding experiment using 244 and 387 MeV mono-energetic neutrons at RCNP

Hiroshi Iwase[1*], Masayuki Hagiwara[1], Yosuke Iwamoto[2], Yoshihiro Nakane[2],
Tatsuhiko Sato[2], Daiki Satoh[2], Hiroshi Yashima[3], Akihiko Masuda[4],
Tetsuro Matsumoto[4], Jun Nishiyama[4], Christian Theis[5], Lukas Jaegerhofer[5],
Eduard Feldbaumer[5], Christian Pioch[6], Vladimir Mares [6], Toshiro Itoga[7],
Yukio Sakamoto[2], Hiroshi Nakashima[2], Atsushi Tamii[8],
Kichiji Hatanaka[8], Takashi Nakamura[9]
[1]High Energy Accelerator Research Organization (KEK), Tsukuba, Japan
[2]Japan Atomic Energy Agency (JAEA), Tokai, Japan
[3]Kyoto University, Kumatori Japan
[4]National Institute of Advanced Industrial Science and Technology (AIST), Japan
[5]Research Organisation for Nuclear Research (CERN), Switzerland
[6]Helmholtz Zentrum München, Neuherberg, Germany
[7]Spring-8 (RIKEN), Japan
[8]Research Center for Nuclear Physics, Osaka University, Ibaraki, Japan
[9]Tohoku University, Aramaki, Japan

Abstract

The RCNP shielding experiment using 244 and 387 MeV mono-energetic neutrons is summarised in the talk. Mono-energetic neutrons of two different energies, 244 and 387 MeV, were produced using a ^{7}Li(p,n) reaction with incident proton energies of 246 MeV and 389 MeV (nominal), respectively. The produced neutrons were collimated using a $10\times12\times350$ cm^3 collimator and transported to the next hall, where the experiment was located.

The first irradiation was performed without shielding blocks. The neutron energy spectra were measured using a NE213 liquid scintillator and bonner ball spheres located 18 m downstream from the target in the hall. Next several neutron dosimeters were irradiated in the neutron fields so that the dose response of the detectors could be checked and calibrated.

The shielding experiment then began by placing a shielding block on the beam axis. The concrete and Fe blocks were $25\times100\times100$ and $10\times80\times80$ cm^3 and had maximum thicknesses of 300 and 100 cm, respectively. Neutron energy spectra behind the shielding blocks were measured by the NE213 scintillator and the bonner spheres. Neutron doses were also measured by several dosimeters. The measured spectra (and doses) are compared with Monte Carlo calculations by FLUKA and PHITS, and the accuracy of models and cross-sections used in the codes are discussed. Finally attenuation length of 244 and 387 MeV mono-energetic neutrons in concrete and Fe are estimated and compared to other data using different incident energies.

NEA PUBLICATIONS AND INFORMATION

The full **catalogue of publications** is available online at www.oecd-nea.org/pub.

In addition to basic information on the Agency and its work programme, the **NEA website** offers free downloads of hundreds of technical and policy-oriented reports.

An **NEA monthly electronic bulletin** is distributed free of charge to subscribers, providing updates of new results, events and publications. Sign up at www.oecd-nea.org/bulletin/.

Visit us on **Facebook** at www.facebook.com/OECDNuclearEnergyAgency or follow us on **Twitter** @OECD_NEA.

Shielding Aspects of Accelerators, Targets and Irradiation Facilities – SATIF-11

Particle accelerators have evolved over the last decades from simple devices to powerful machines and are having an increasingly important impact on research, technology and daily life. Today, they have a wide range of applications in many areas including material science and medical applications. In recent years, new technological and research applications have helped to define requirements while the number of accelerator facilities in operation, being commissioned, designed or planned has grown significantly. Their parameters, which include the beam energy, currents and intensities, and target composition, can vary widely, giving rise to new radiation shielding issues and challenges.

Particle accelerators must be operated in safe ways to protect operators, the public and the environment. As the design and use of these facilities evolve, so must the analytical methods used in the safety analyses. These workshop proceedings review the state of the art in radiation shielding of accelerator facilities and irradiation targets. They also evaluate progress in the development of modelling methods used to assess the effectiveness of such shielding as part of safety analyses.